

The HiggsTools Handbook: Concepts and observables for deciphering the Nature of the Higgs Sector

Abstract

This Report summarizes some of the activities of the HiggsTools Initial Training Network working group in the period 2015-2017. The main goal of this working group was to produce a document discussing various aspects of state-of-the-art Higgs physics at the Large Hadron Collider (LHC) in a pedagogic manner.

The first part of the Report is devoted to a description of phenomenological searches for New Physics at the LHC. All of the available studies of the couplings of the new resonance discovered in 2012 by the ATLAS and CMS experiments [1, 2] conclude that it is compatible with the Higgs boson of the Standard Model (SM) within present precision. So far the LHC experiments have given no direct evidence for any physical phenomena that cannot be described by the SM. As the experimental measurements become more and more precise, there is a pressing need for a consistent framework in which deviations from the SM predictions can be computed precisely. Such a framework should be applicable to measurements in all sectors of particle physics, not only LHC Higgs measurements but also electroweak precision data, etc. We critically review the use of the κ -framework, fiducial and simplified template cross sections, effective field theories, pseudoobservables and phenomenological Lagrangians. Some of the concepts presented here are well known and were used already at the time of the Large Electron-Positron Collider (LEP) experiment. However, after years of theoretical and experimental development, these techniques have been refined, and we describe new tools that have been introduced in order to improve the comparison between theory and experimental data.

In the second part of the Report, we propose ϕ_η^* as a new and complementary observable for studying Higgs boson production at large transverse momentum in the case where the Higgs boson decays to two photons. The ϕ_η^* variable depends on measurements of the angular directions and rapidities of the two Higgs decay products rather than the energies, and exploits the information provided by the calorimeter in the detector. We show that, even without tracking information, the experimental resolution for ϕ_η^* is better than that of the transverse momentum of the photon pair, particularly at low transverse momentum. We make a detailed study of the phenomenology of the ϕ_η^* variable, contrasting the behaviour with the Higgs transverse momentum distribution using a variety of theoretical tools including event generators and fixed order perturbative computations. We consider the theoretical uncertainties associated with both p_{TH} and ϕ_η^* distributions. Unlike the transverse momentum distribution, the ϕ_η^* distribution is well predicted using the Higgs Effective Field Theory in which the top quark is integrated out – even at large values of ϕ_η^* – thereby making this a better observable for extracting the parameters of the Higgs interaction. In contrast, the potential of the ϕ_η^* distribution as a probe of new physics is rather limited, since although the overall rate is affected by the presence of additional heavy fields, the shape of the ϕ_η^* distribution is relatively insensitive to heavy particle thresholds.

Authors

M. Boggia¹, J. M. Cruz-Martinez², H. Frellesvig^{3,4}, N. Glover², R. Gomez-Ambrosio^{2,5},
G. Gonella¹, Y. Haddad^{2,6}, A. Ilnicka^{7,8}, S. Jones^{1,9}, Z. Kassabov^{5,10}, F. Krauss², T. Megy¹,
D. Melini^{11,12}, D. Napoletano², G. Passarino⁵, S. Patel^{13,14,15}, M. Rodriguez-Vazquez¹⁶,
T. Wolf¹⁷

¹ Physikalisches Institut, Albert-Ludwigs-Universität Freiburg, 79104 Freiburg, Germany

² Institute for Particle Physics Phenomenology, Department of Physics, University of Durham, Durham DH1 3LE, UK

³ Institute of Nuclear and Particle Physics, NCSR “Demokritos”, Agia Paraskevi, 15310, Greece

⁴ Institute for Theoretical Particle Physics (TTP), Karlsruhe Institute of Technology, Engesserstraße 7, D-76128 Karlsruhe, Germany

⁵ Dipartimento di Fisica Teorica, Università degli Studi di Torino and INFN, Sezione di Torino, Via Pietro Giuria 1, 10125 Turin, Italy

⁶ High Energy Physics Group, Blackett Lab., Imperial College, SW7 2AZ, London, UK

⁷ Institute for Theoretical Physics, University of Zürich, Winterthurerstrasse 190, 8057 Zürich, Switzerland

⁸ Institute for Particle Physics, Physics Department, ETH Zürich, 8093 Zürich, Switzerland

⁹ Max-Planck-Institut für Physik, Werner-Heisenberg-Institut, Föhringer Ring 6, 80805 München, Germany

¹⁰ Dipartimento di Fisica, Università degli Studi di Milano and INFN, Sezione di Milano, Via Celoria 16, 20133 Milan, Italy

¹¹ Departamento de Física Teórica y del Cosmos, Avenida de la Fuente Nueva S/N C.P. 18071 Granada, Spain

¹² IFIC, Universitat de València and CSIC, Catedrático Jose Beltrán 2, 46980 Paterna, Spain

¹³ DESY, Notkestrasse 85, 22607 Hamburg, Germany

¹⁴ Institute for Theoretical Physics (ITP), Karlsruhe Institute of Technology, Wolfgang-Gaede-Straße 1, D-76131 Karlsruhe, Germany

¹⁵ Institute for Nuclear Physics (IKP), Karlsruhe Institute of Technology, Hermann-von-Helmholtz-Platz 1, D-76344 Karlsruhe, Germany

¹⁶ Laboratoire de Physique Théorique, UMR 8627, CNRS, Université de Paris-Sud, Université Paris-Saclay, 91405 Orsay, France

¹⁷ Nikhef, Science Park 105, 1098 XG Amsterdam, The Netherlands

Acknowledgements

We thank Ramona Gröber for useful comments, and Xuan Chen, Aude Gehrman-De Ridder, Thomas Gehrman, Alex Huss and Tom Morgan for their collaboration in developing the NNLOJET code. We thank Marzieh Bahmani, Giulio Falcioni, Nicolas Gutierrez, Brian Le, Elisa Mariani, Joosep Pata and Cosimo Sanitate for their contributions to the HiggsTools Initial Training Network. We gratefully acknowledge the Research Executive Agency (REA) of the European Union for funding through the Grant Agreement PITN-GA-2012-316704 (“HiggsTools”). M.B. and G.G. acknowledge the German Research Foundation (DFG) and Research Training Group GRK 2044 for the funding and the support.

Contents

| | | |
|-----------|---|-----------|
| I | Towards a theory of Standard Model deviations | 1 |
| I.1 | Introduction | 1 |
| I.2 | The κ -framework | 3 |
| I.3 | Fiducial and simplified template cross sections | 15 |
| I.4 | Effective field theories | 25 |
| I.5 | Pseudoobservables for the LHC | 46 |
| I.6 | Tools and phenomenological Lagrangian | 60 |
| I.7 | Summary | 70 |
| II | ϕ_η^*: A new variable for studying $H \rightarrow \gamma\gamma$ decays | 71 |
| II.1 | Overview | 71 |
| II.2 | Observables for probing Higgs boson recoil | 76 |
| II.3 | Photons | 81 |
| II.4 | Parton Showers | 85 |
| II.5 | Theoretical Predictions | 88 |
| II.6 | Beyond the Standard Model | 115 |
| II.7 | Summary | 124 |
| A | Calculation of the One-Loop Master Integrals | 125 |
| B | Two-loop Feynman Integrals | 132 |

Chapter I

Towards a theory of Standard Model deviations

I.1 Introduction

Before the discovery of the Higgs boson in 2012, the hypothesis under test at the LHC was the Standard Model (SM) with the Higgs boson mass, m_H , being the unknown parameter. Therefore, bounds on m_H were derived through a comparison of theoretical predictions with high-precision data. Now, after the discovery, the SM is fully specified and the unknowns are constrainable deviations from the SM. Of course, the definition of SM deviations requires a characterization of the underlying dynamics. So far, all of the available studies of the couplings of the new resonance conclude that it is compatible with the Higgs boson of the SM with our current precision, and, as of yet, there is no direct evidence for new physics phenomena beyond the SM at the LHC.

This chapter is devoted to a description of phenomenological searches for New Physics (NP) at the LHC. Some of the concepts presented here are well known and were used already at the time of the Large Electron-Positron Collider (LEP). Now, after years of developments both on the experimental and the theoretical sides, these techniques have been refined, and new tools have been introduced in order to improve the comparison of theory to experiment.

In this work, different approaches are revisited, with special emphasis on the relations and connections between them, showing their limits, and how they complement each other. In the following we will introduce their main definitions, necessary for a complete comprehension of the chapter. The technical details will be largely covered in the following sections.

The κ -framework

The κ -framework was proposed shortly after the discovery of the Higgs boson in order to try a systematic and model-independent search for SM deviations. It is used at Leading Order (LO) and accommodates for factorisable Quantum Chromodynamic (QCD) corrections but not for Electroweak (EW) ones. The κ -framework will be covered in Section I.2, where its use during the Run 1 of the LHC is discussed and its limitations highlighted.

Fiducial and Simplified Template Cross Sections

Fiducial cross sections are useful observables for particle physics, but they have always been a source of disagreement between theorists and experimentalists. The reason is that the phase space defined by the theory is not the same as the one of the detector and additionally, different detectors operate at their maximum efficiency in different regions of the phase space. The Simplified Template Cross Sections (STXSs) are one of the possible answers to this problem. They provide a gain in experimental sensitivity by introducing a small theoretical model dependence. STXSs are defined in greater detail in Section I.3.

Effective Field Theories (EFTs)

EFTs come into play when the solutions to a quantum field theory are provided as expansions in a small coupling constant and ratio of scales. Among these theories the Standard Model EFT (SMEFT) is an example. In such theories an infinite number of higher dimensional operators must be included, which means that the theory is (strictly) non-renormalisable. Nevertheless,

if v is the Higgs vacuum expectation value and E is the typical scale at which the process is measured, the EFT amplitudes are expanded in powers of v/Λ and of E/Λ , where Λ is the scale of new physics. This expansion is computable to all orders and the introduction, order-by-order, of an increasing number of counter-terms can eliminate the UV divergences, which makes the theory renormalisable order-by-order in the E/Λ perturbative expansion. An overview of EFTs is presented in Section I.4 introducing definitions, descriptions and methodologies.

Pseudoobservables (POs)

Pseudoobservables were introduced to allow a better interplay between theory and experiment. They answer the urgent need of extending the parameters of the κ -framework to something with a more rigorous theoretical interpretation. Another main advantage of POs is that they deliver results which do not have to be totally unfolded by experiments to a model-dependent parameter space. POs could also be the solution to the issue posed by the κ -framework of not being able to describe theoretically any eventual SM deviations (being only able to *parametrise* but not to *explain* such measurements), and at the same time, POs make it possible to get closer to quantities that are well defined QFT objects. POs had been already used for LEP analysis, and they have gained new relevance now given their close connection with EFTs. They are addressed in Section I.5 as a natural continuation of Section I.4.

Phenomenological Lagrangians

Several models have been built that aim at producing observable NP effects based on phenomenological Lagrangians constructed by adding a limited number of additional interactions to the SM Lagrangian. Theoretical tools and Monte Carlo (MC) generators with such implementations are already available. Section I.6 offers an insight into this topic, together with a discussion of the challenges faced when dealing with Next-to-Leading Order (NLO) corrections. Finally, there are a couple of finer points in terminology that are worth keeping in mind:

- 1) technically speaking leading-order defines the order in perturbation theory where the process starts. Sometimes, however, “LO” is used in the literature to denote tree level (as opposed to loop contributions).
- 2) The resonant (often called “signal”) and the non-resonant (often called “background”) are parts of a physical process (which may contain more than one resonant part). Typically whenever we write $i \rightarrow X \rightarrow f$ we mean the X -resonant part of a process with initial state i and final state f . However, we should keep in mind that separating and defining “signals” and “backgrounds” is not trivial. For example, Vh production at LO in QCD with $V \rightarrow jj$ and Vector Boson Fusion (VBF) are not clearly separated. At Next-to-Next-to-Leading Order (NNLO) QCD everything becomes much more complicated and even the definition of Vh , $V \rightarrow jj$ and VBF is ambiguous.

I.2 The κ -framework

I.2.1 Concept and description

Theory and experiment aim at the same goal but, surprisingly, they often find it hard to communicate with each other. The search for a common language to be used by experimentalists to express their results and by theorists to interpret them has become more and more urgent after the observation of a massive neutral boson [1,2], that is identified as being compatible with the quantum fluctuations of a field whose Vacuum Expectation Value (VEV) breaks the EW symmetry. This is the well-known Brout-Englert-Higgs mechanism of Refs. [3–8] and the LHC resonance has been interpreted so far in terms of the SM Higgs boson.

The Higgs boson couplings to the other known particles play a central role in the investigation of the properties of this state, since they are predicted very accurately by the SM and its extensions. They also influence the Higgs boson production and decay rates: this is why an interim framework called the κ -framework was proposed in Ref. [9] to parameterise small deviations from the predicted SM Higgs boson couplings and widths, for a recent review see Ref. [10]. The basic assumptions are:

- The signals observed in the different search channels originate from a single narrow resonance with a mass near 125 GeV.
- The zero-width approximation is used, meaning that the total width of the resonance is narrow enough to be negligible with respect to the mass. In this case, the signal cross section can be decomposed (for all $i \rightarrow H \rightarrow f$ channels) as

$$\sigma_i \cdot \text{BR}^f = \frac{\sigma_i \cdot \Gamma_f}{\Gamma_H}, \quad (\text{I.1})$$

where σ_i is the production cross section for $i \rightarrow H$ with $i = (ggF, \text{VBF}, WH, ZH, t\bar{t}H)$ and BR^f is the decay Branching Ratio (BR) for $H \rightarrow f$ with $f = (ZZ, WW, \gamma\gamma, \tau\tau, bb, \mu\mu)$. Γ_f and Γ_H are the partial and total decay widths of the Higgs boson respectively.

The couplings cannot be directly measured by the experiments and events collected in the detector undergo an unfolding procedure, in order for us to be able to extract the information from some measurable observable(s). Typically, the measured observable is $\sigma \times \text{BR}$, which is defined within a certain acceptance and with some specific experimental cuts, and this leads to some model dependence.

Obviously, it is not possible to fit the experimental data within the context of the SM while treating Higgs couplings as free parameters. Once the value of the Higgs boson mass is specified, the couplings are specified as well. For this reason, it is only possible to test the overall compatibility of the SM with the data. This kind of study can be used to extract or constrain deviations in the measured couplings with respect to the the SM ones.

Some of the available approaches introduce specific modifications in the structure of the couplings: besides including all the available higher order corrections in the model, they add additional terms to the Lagrangian, the so-called “anomalous couplings”. This gives rise to modifications of the tensor structure of the amplitude leading not only to a modification of the coupling strengths, but also of the kinematic distributions. This approach has turned out to be a difficult one when it comes to reinterpreting the results. An additional assumption is then made to simplify the framework:

- The tensor structure of the couplings is assumed to be the same as in the SM predictions, only modifications of coupling strengths are taken into account. This implies that the observed state is assumed to be a CP-even scalar.

The framework is built in such a way that the predicted SM Higgs cross section and partial decay widths are dressed with scaling factors κ_j , as shown in Table I.1. The cross section σ_i and the partial decay width Γ_f scale with κ_i^2, κ_f^2 when compared to SM predictions.

$$\sigma_i \cdot \text{BR}^f = (\sigma_i \cdot \text{BR}^f)_{\text{SM}} \cdot \frac{\kappa_i^2 \cdot \kappa_f^2}{\kappa_H^2}. \quad (\text{I.2})$$

In the SM, all the κ_i are unity by definition and therefore, the best available (i.e. highest possible perturbative order) predictions are recovered. However, when $\kappa_i \neq 1$ higher-order accuracy is in general lost due to the factorisation of Eq.(I.2) does not necessarily hold beyond LO. This will be illustrated later on with an example.

The κ are sometimes confused with the actual couplings in the Lagrangian. They are the same at tree level, but not the same once radiative corrections are taken into account. As an example we consider the process $gg \rightarrow t\bar{t}H(bb)$. At tree level one can say that the squared matrix elements are proportional to the coupling of the interactions:

$$|\mathcal{M}|^2 \propto (g_{tH}g_{bH})^2, \quad (\text{I.3})$$

and then, assuming that the total width of the Higgs boson stays unchanged, $\Gamma_H \equiv \Gamma_H^{\text{SM}}$, one would have $\kappa_i = g_{tH}$ and $\kappa_f = g_{bH}$.

Another quantity that can be expressed in this framework and is a common experimental observable, is the *signal strength* μ . Consider a specific process $i \rightarrow H \rightarrow f$. For the production ($i \rightarrow H$) the signal strength μ is defined as

$$\mu_i = \frac{\sigma_i}{\sigma_{i\text{SM}}}, \quad (\text{I.4})$$

whereas, for the decay ($H \rightarrow f$) we have

$$\mu_f = \frac{\text{BR}^f}{\text{BR}_{\text{SM}}^f}. \quad (\text{I.5})$$

By definition, in the SM $\mu_i = 1$ and $\mu_f = 1$. The only thing that can be measured experimentally is the product of μ_i and μ_f , since it is not possible to separate them without further assumptions. In terms of the κ -framework we obtain the following expression:

$$\mu \equiv \mu_i \mu_f \equiv \frac{\kappa_i^2 \kappa_f^2}{\kappa_H^2}. \quad (\text{I.6})$$

To summarize, the original κ -framework is a simplified picture which shows its limitations when more precise data necessitate the inclusion of higher order QCD and EW corrections. In many cases, the QCD corrections do not completely factorise and their impact in the context of the SMEFT can be sizeable, as was shown in Ref. [11].

Keeping this in mind, let us first discuss the LO strategy, which was applied during the analysis of the LHC Run 1 data. Different production processes and decay modes probe different coupling modifiers. Together with the individual modifiers related to the coupling of the Higgs boson with different particles, two *effective* modifiers need to be introduced to describe loop induced processes: the modifier κ_g to describe the ggF production process and κ_γ for the $H \rightarrow \gamma\gamma$ decay.

| Production | Loops | Interference | Effective scaling factors | Resolved scaling factors |
|--|-------|--------------|---------------------------|---|
| $\sigma(ggF)$ | ✓ | $t-b$ | κ_g^2 | $1.06 \cdot \kappa_t^2 + 0.01 \cdot \kappa_b^2 + 0.07 \cdot \kappa_t \kappa_b$ |
| $\sigma(\text{VBF})$ | — | — | — | $0.74 \cdot \kappa_W^2 + 0.26 \cdot \kappa_Z^2$ |
| $\sigma(WH)$ | — | — | — | κ_W^2 |
| $\sigma(qq/qg \rightarrow ZH)$ | — | — | — | κ_Z^2 |
| $\sigma(gg \rightarrow ZH)$ | ✓ | $t-Z$ | — | $2.27 \cdot \kappa_Z^2 + 0.37 \cdot \kappa_t^2 - 1.64 \cdot \kappa_Z \kappa_t$ |
| $\sigma(t\bar{t}H)$ | — | — | — | κ_t^2 |
| $\sigma(gb \rightarrow tHW)$ | — | $t-W$ | — | $1.84 \cdot \kappa_t^2 + 1.57 \cdot \kappa_W^2 - 2.41 \cdot \kappa_t \kappa_W$ |
| $\sigma(qq/qb \rightarrow tHq)$ | — | $t-W$ | — | $3.40 \cdot \kappa_t^2 + 3.56 \cdot \kappa_W^2 - 5.96 \cdot \kappa_t \kappa_W$ |
| $\sigma(b\bar{b}H)$ | — | — | — | κ_b^2 |
| Partial decay width | | | | |
| Γ_{ZZ} | — | — | — | κ_Z^2 |
| Γ_{WW} | — | — | — | κ_W^2 |
| $\Gamma_{\gamma\gamma}$ | ✓ | $t-W$ | κ_γ^2 | $1.59 \cdot \kappa_W^2 + 0.07 \cdot \kappa_t^2 - 0.66 \cdot \kappa_W \kappa_t$ |
| $\Gamma_{\tau\tau}$ | — | — | — | κ_τ^2 |
| Γ_{bb} | — | — | — | κ_b^2 |
| $\Gamma_{\mu\mu}$ | — | — | — | κ_μ^2 |
| Total width ($\text{BR}_{\text{BSM}}=0$) | | | | |
| Γ_H | ✓ | — | κ_H^2 | $0.57 \cdot \kappa_b^2 + 0.22 \cdot \kappa_W^2 + 0.09 \cdot \kappa_g^2 +$ $0.06 \cdot \kappa_\tau^2 + 0.03 \cdot \kappa_Z^2 + 0.03 \kappa_c^2 +$ $0.0023 \cdot \kappa_\gamma^2 + 0.0016 \cdot \kappa_{(Z\gamma)}^2 +$ $0.0001 \cdot \kappa_s^2 + 0.00022 \cdot \kappa_\mu$ |

Table I.1: Higgs boson production cross sections σ_i , partial decay widths Γ_f , and total decay width (in the absence of BSM decays) parametrised as a function of the κ coupling modifiers, including higher-order QCD and EW corrections to the inclusive cross sections and decay partial widths. The coefficients in the expression for Γ_H do not sum exactly to unity because some negligible contributions are not shown. Table from Ref. [12].

This is possible since it is expected that other Beyond the SM (BSM) particles which might be present in the loop do not change the kinematics of the process. The study of these processes can therefore be approached by either using effective coupling modifiers, which provide sensitivity to the presence of BSM particles in the loops, or using *resolved* coupling modifiers corresponding to the SM particles.

I.2.2 The κ -framework in the experiments

The measurement of the properties of the Higgs boson is one of the main goals of the two LHC general purpose experiments: ATLAS, described in Ref. [13], and CMS, described in Ref [14].

For the interpretation of results in the light of a combination it is mandatory to have a global overview of the current situation and to understand how the κ -framework has been used by the experiments so far. In the following we review the combination of measurements performed by the ATLAS and CMS experiments, which was presented in Ref. [12], with a focus on the constraints on the couplings.

The analysis used the data collected by the detectors from pp collisions at the LHC in 2011

and 2012, corresponding to an integrated luminosity of approximately 5 fb^{-1} at $\sqrt{s} = 7 \text{ TeV}$ and 20 fb^{-1} at $\sqrt{s} = 8 \text{ TeV}$. They considered multiple production processes: gluon fusion, vector boson fusion, and associated production with a W or a Z boson or a pair of top quarks, and the $H \rightarrow ZZ, WW, \gamma\gamma, \tau\tau, bb$ and $\mu\mu$ decay modes.¹ Two formalisms were used to interpret the results: the signal strength μ , related to the yields, and the κ -framework for the couplings. Usually, Higgs cross section measurements are given in two ways:

- Fiducial cross-section: this has basically no input from the signal Monte Carlo (MC), so it can be compared to any theory calculation, provided that it can reproduce the cross-section within these specific cuts
- Signal strength (μ). In this case,
 - The event yield after cuts is computed.
 - This is extrapolated to the full phase space using signal Monte Carlo (typically POWHEG [15] + JHUGen [16–19] + Pythia8 [20] + Geant4 [21]) in the full detector simulation to compute acceptance and efficiency.
 - The result is compared with the best theory predictions, e.g. Next-to-Next-to-Next-to-Leading Order (N3LO) QCD for production in the gluon fusion channel, and Prophecy4f, from Refs. [22–24], for decays with four fermions in the final state.

To directly measure the individual coupling modifiers, an assumption for the Higgs boson width is necessary. It is predicted to be approximately 4 MeV in the SM, which is assumed to be small enough for the Narrow Width Approximation (NWA) to be valid and for the Higgs boson production and decay mechanisms to be factorised.

The relations among the coupling modifiers, the production cross-sections and the partial decay widths of Table I.1 are used as a parametrisation to extract the coupling modifiers from the measurements. Changes in the values of the couplings will lead to a change of the Higgs boson width. To characterise this variation a new modifier κ_H is introduced, defined as $\kappa_H^2 = \sum_j \text{BR}_{\text{SM}}^j \kappa_j^2$. If we only allow for SM decays of the Higgs boson, the relation $\kappa_H^2 = \Gamma_H / \Gamma_{H;\text{SM}}$ holds, otherwise Γ_H can be expressed as:

$$\Gamma_H = \frac{\kappa_H^2 \cdot \Gamma_{H;\text{SM}}}{1 - \text{BR}_{\text{BSM}}}, \quad (\text{I.7})$$

where BR_{BSM} indicates the total branching fraction into BSM decays. Since Γ_H is not experimentally constrained in a model-independent manner with sufficient precision, only ratios of coupling strengths can be measured in the most generic parametrisation considered in the κ -framework. The individual ATLAS and CMS analysis of the Higgs boson production and decay rates are combined using the profile likelihood method.

Intermezzo: profile likelihood method

The statistical data treatment used in the combination is the same as that used by the single analysis and described in Ref. [25]. Let us consider a kinematic variable x and the corresponding histogram of values $\mathbf{n} = (n_1, \dots, n_n)$. The expectation value in a bin i can be written as

$$E[n_i] = \mu s_i + b_i, \quad \text{where} \quad s_i = s_{\text{tot}} \int_{\text{bin } i} f_s(x, \theta_s) dx, \quad b_i = b_{\text{tot}} \int_{\text{bin } i} f_b(x, \theta_b) dx, \quad (\text{I.8})$$

and μ determines the strength of the signal process, with $\mu = 0$ being the background-only hypothesis and $\mu = 1$ the nominal signal hypothesis.

¹Note that the definition of the $H \rightarrow ZZ(WW)$ decay requires some additional information.

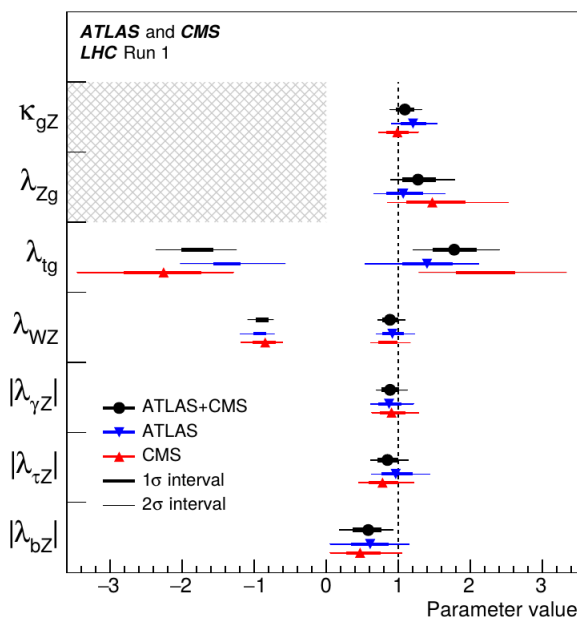


Fig. I.1: Best fit values of ratios of Higgs boson coupling modifiers, as obtained from the generic parametrisation. The single results from each experiment are also shown. The thick error bars indicate the 1σ interval and the thin lines the 2σ one. The hatched areas indicate the non-allowed regions for the parameters that are assumed to be positive without loss of generality. For those parameters with no sensitivity to the sign, only the absolute values are shown. Figure from Ref. [12].

The functions $f_s(x, \theta_s)$ and $f_b(x, \theta_b)$ are the probability density functions of the variable x for signal and background characterised by the set of parameters $\vec{\theta}_s$ and $\vec{\theta}_b$. The quantities s_{tot} and b_{tot} are the total mean numbers of events for signal and background: s_{tot} is not considered to be an adjustable parameter but rather fixed to the value predicted by the nominal signal model.

In addition to the histogram of interest \mathbf{n} , supporting measurements are usually made to help constrain the nuisance parameters. Therefore for a control sample where mainly background is expected, we may find a histogram $\mathbf{m} = (m_1, \dots, m_M)$ for a particular kinematic variable, where the expectation value of m_i is

$$E[m_i] = u_i(\theta). \quad (\text{I.9})$$

Here the u_i are calculable quantities that depend on $\theta = (\theta_s, \theta_b, b_{tot})$. This is often done to obtain information on the parameter b_{tot} .

In each bin, the number of events follows the Poisson distribution and the likelihood function is the product of those probabilities for every bin,

$$\mathcal{L}(\mu, \theta) = \prod_{j=1}^N \frac{(\mu s_j + b_j)^{n_j}}{n_j!} e^{-(\mu s_j + b_j)} \prod_{k=1}^M \frac{u_k^{m_k}}{m_k!} e^{-u_k}. \quad (\text{I.10})$$

The likelihood function is then used to build a so-called “test statistic”

$$\Lambda(\mu) = \frac{\mathcal{L}(\mu, \hat{\theta})}{\mathcal{L}(\hat{\mu}, \hat{\theta})}, \quad (\text{I.11})$$

where $\hat{\theta}$ indicates the value of θ that maximizes L for a specific value of μ (conditional maximum-likelihood estimator for θ), while $\hat{\mu}$ and $\hat{\theta}$ are the unconditional maximum likelihood estimates of the parameter values.

Likelihood fits are then performed to obtain the values for the parameters of interest. The actual data is used for the observed values and Asimov datasets, see for instance Ref. [25], are used for the expected values. Asimov datasets are pseudo-data distributions equal to the signal plus background predictions for a given value of the parameters. By definition, when the Asimov dataset is used to estimate the parameters, the “true” values are obtained.

Often, not all of the parameters need to be estimated and in these cases a *profile likelihood* analysis is performed, which means that the parameters one is not interested in are written as a function of the parameters of interest.

The combination is based on simultaneous fits to the data from both experiments taking into account the correlations between systematic uncertainties within each experiment and between the two experiments. Almost all input analysis are based on the concept of event categorisation. This consists of classifying the events in different categories, based on their kinematic properties.

This categorisation increases the sensitivity of the analysis and also allows separation of the different production processes on the basis of exclusive selections that identify the decay products of the particles produced in association with the Higgs boson: W or Z boson decays, VBF jets, etc. A total of approximately 600 exclusive categories addressing the five production processes explicitly considered are defined for the five main decay channels.

The signal yield in a category k , $n_{\text{signal}}(k)$, can be expressed as a sum over all possible Higgs boson production processes i , with cross section σ_i and decay modes f , with branching fraction BR^f :

$$\begin{aligned} n_{\text{signal}}(k) &= \mathcal{L}(k) \cdot \sum_i \sum_f \left\{ \sigma_i \cdot A_{i;\text{SM}}^f(k) \cdot \epsilon_i^f(k) \cdot \text{BR}^f \right\} \\ &= \mathcal{L}(k) \cdot \sum_i \sum_f \mu_i \mu_f \left\{ \sigma_{i;\text{SM}} \cdot A_{i;\text{SM}}^f(k) \cdot \epsilon_i^f(k) \cdot \text{BR}_{\text{SM}}^f \right\}, \end{aligned} \quad (\text{I.12})$$

where $\mathcal{L}(k)$ represents the integrated luminosity, $A_{i;\text{SM}}^f(k)$ the detector acceptance assuming SM Higgs boson production and decay, and $\epsilon_i^f(k)$ the overall selection efficiency for the signal category k . Finally μ_i and μ_f are the production and decay signal strengths, respectively.

It can be seen that the measurements are only sensitive to the products of the cross sections and branching fractions, $\sigma_i \cdot \text{BR}^f$. The overall statistical methodology is the same as used by the single experiments.

The parameters α are estimated via the profile likelihood ratio test statistics $\Lambda(\alpha)$, which depend on one or more parameters as well as on the nuisance parameters, θ , which reflect various experimental and theoretical uncertainties. The likelihood functions are constructed using products of signal and background Probability Density Functions (PDFs) of the discriminating variables. The probability density functions are obtained from simulations in the case of the signal and from both data and simulation for the background case.

Three parametrisations of experimental results have been performed in the combination: two are based on cross-sections and branching fractions, one is based on ratios of couplings modifiers. The $\sigma \cdot \text{BR}$ for $gg \rightarrow H \rightarrow ZZ$ channel is parametrised as a function of $\kappa_{gZ} = \kappa_g \cdot \kappa_Z / \kappa_H$ (where κ_g is the effective coupling modifier). The measurement of VBF and ZH production probes $\lambda = \kappa_Z / \kappa_g$, the measurements of $t\bar{t}H$ production processes are sensitive to $\lambda_{tg} = \kappa_t / \kappa_g$. The three decay modes $H \rightarrow WW$, $H \rightarrow \tau\tau$ and $H \rightarrow bb$ probe the three ratios $\lambda_{WZ} = \kappa_W / \kappa_Z$, $\lambda_{\tau Z} = \kappa_\tau / \kappa_Z$ and $\lambda_{bZ} = \kappa_b / \kappa_Z$, relative to the $H \rightarrow ZZ$ branching fraction.

| $S\bar{F}_1 F_2$ | $h\bar{f}_i f_j$ | $\chi\bar{f}_i f_j$ | $\phi^+ \bar{u}_i d_j$ | $\phi^- \bar{d}_j u_i$ |
|------------------|---|--|---|---|
| C_L | $-\frac{1}{2s} \frac{m_{f,i}}{M_W} \delta_{ij}$ | $-\frac{i}{2s} 2I_{W,f}^3 \frac{m_{f,i}}{M_W} \delta_{ij}$ | $\frac{1}{\sqrt{2s}} \frac{m_{u,i}}{M_W} V_{ij}$ | $-\frac{1}{\sqrt{2s}} \frac{m_{d,j}}{M_W} V_{ji}^\dagger$ |
| C_R | $-\frac{1}{2s} \frac{m_{f,i}}{M_W} \delta_{ij}$ | $\frac{i}{2s} 2I_{W,f}^3 \frac{m_{f,i}}{M_W} \delta_{ij}$ | $-\frac{1}{\sqrt{2s}} \frac{m_{d,j}}{M_W} V_{ij}$ | $\frac{1}{\sqrt{2s}} \frac{m_{u,i}}{M_W} V_{ji}^\dagger$ |

Table I.2: Scalar-fermion couplings in the SM, from Ref. [26].

Other parametrisations were performed in the combination analysis with more specific and more restrictive assumptions.

I.2.3 Limitations of the κ -framework

One problem that arises at higher orders is the violation of unitarity. Unitarity is connected to the renormalisability of a theory, and the introduction of coupling modifiers for the Higgs spoils unitarity and renormalisability.

Example $H \rightarrow b\bar{b}$ decay width

To show why the κ -framework cannot be considered a fully consistent theoretical framework, we give an example of the problems arising when we try to compute an observable at NLO precision in this framework. We consider a ‘‘simplified κ -framework’’ phenomenological Lagrangian, similar to the Lagrangian that is discussed in Section I.6.2.

We define this simplified theory as follows: we start from the SM (following here the conventions of Ref. [26]), and we modify all the fermionic couplings to scalar particles, multiplying them by a common factor κ_{ffS} . In this simplified framework, the generic scalar-fermion vertex is given by

$$\begin{array}{c} \text{---} h \text{---} \\ \swarrow \quad \searrow \\ \bar{F}_1 \\ F_2 \end{array} = ie \kappa_{ffS} \left(C_L \frac{1 - \gamma_5}{2} + C_R \frac{1 + \gamma_5}{2} \right), \quad (\text{I.13})$$

where the values of the coefficients C_L and C_R are specified in Table I.2. As for the observable that we want to compute, we consider the Higgs decay width into a pair of bottom quarks, i.e. $\Gamma(H \rightarrow b\bar{b})$. The Born matrix element for the decay process reads as follows:

$$\mathcal{M}_0 = \frac{e m_b \kappa_{ffS}}{2s M_W} \bar{u}(p) v(k), \quad (\text{I.14})$$

and we can see how the LO SM decay width is modified using this simple phenomenological model: it is rescaled by a factor κ_{ffS}^2 coming from the square of Eq. (I.14). This rescaling reflects the effects of the κ -framework on the fermion-fermion-Higgs coupling. To achieve a more accurate theoretical prediction, we must include contributions containing higher powers of the coupling constant α . The NLO matrix element can be cast in the following form, see for example Ref. [27],

$$\mathcal{M} = \mathcal{M}_0 \left[1 + \frac{\alpha}{4\pi} \left(\delta_{\text{loop}} + \delta_{\text{CT}} \right) \right], \quad (\text{I.15})$$

where δ_{loop} contains the contributions due to loops with internal gauge and Higgs bosons, and δ_{CT} the counterterm contributions coming from the renormalisation procedure.

In this example, the purpose is not to show the complete derivation of the NLO decay width, but we want to highlight the NLO inconsistency of the κ -framework. To this end, we take

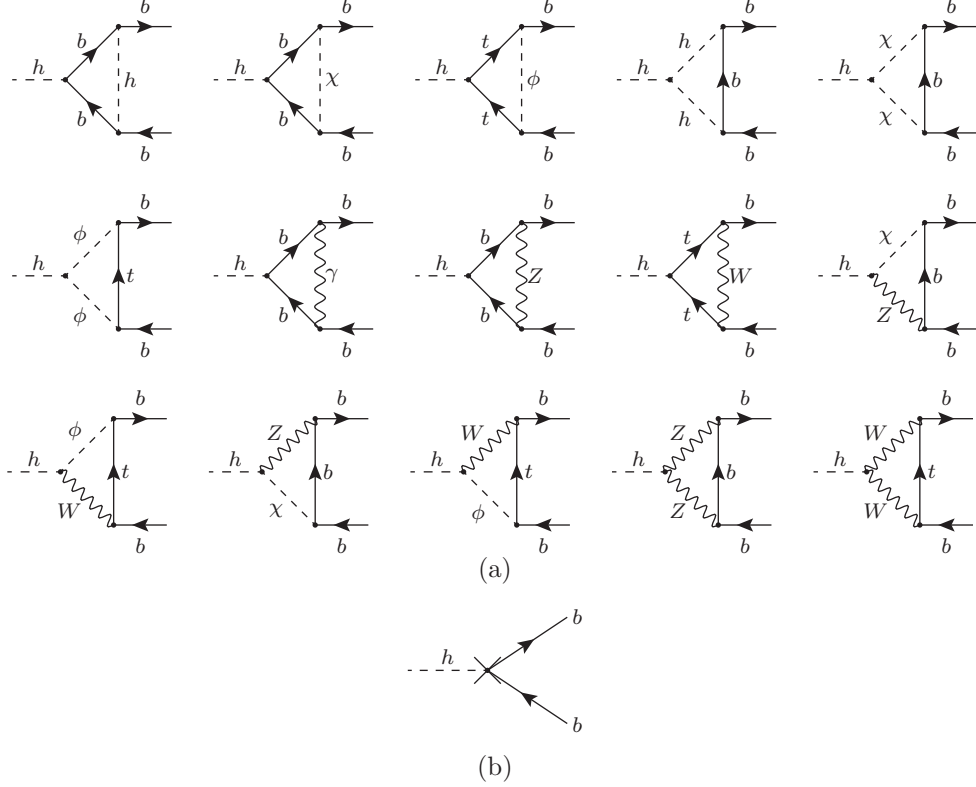


Fig. I.2: (a) Loop contributions to the Higgs decay into a bottom quark pair. (b) Counterterm contribution to the Higgs decay into a bottom quark pair.

advantage of the following simplifications: firstly, we drop QCD contributions, and we focus on the EW corrections.

Then, by means of dimensional regularisation, we identify the UV divergent contributions in the NLO matrix element, and we drop the UV finite part. This allows us to overlook the problems related to the infrared (IR) and collinear structure of the loop amplitude (involving the inclusion of the real emission process $H \rightarrow b\bar{b}(\gamma, g)$). Finally, we neglect effects induced by the quark-mixing matrix V in the W -boson couplings of Table I.2, setting $V_{ij} = \delta_{ij}$.

For the renormalisation procedure, we adopt the on-shell scheme, as presented in Ref. [28]. In this scheme, each renormalised mass is related to the corresponding physical mass, defined as the real part of the particle propagator pole.

Considering EW corrections, δ_{loop} of Eq. (I.15) contains contributions coming from the diagrams reported in Fig. I.2a and δ_{CT} , the counterterm contribution reported in Fig. I.2b.

The UV-divergent part of δ_{loop} turns out to be (in the MS scheme)

$$\delta_{\text{loop}}|_{\text{UV}} = \frac{1}{36 s^2 M_W^2} \frac{2}{4-D} (26 M_W^2 + M_Z^2 + 18 \kappa_{ffS}^2 m_t^2), \quad (\text{I.16})$$

where D is the number of space-time dimensions considered to regularise the loop integrals, and the factor $2/(4-D)$ shows the divergent contribution. To motivate this result, we can separate the loop contributions into four different classes, ordered as they appear in Fig. I.2a:

- I. scalar-exchange diagrams, where a scalar particle is exchanged between the two outgoing b quarks,
- II. diagrams with two scalars running in the loop,

- III. diagrams with one internal gauge boson line (exchanged by outgoing particles, or emitted by the incoming Higgs),
- IV. diagrams with two gauge boson lines running in the loop.

As can be seen by naive power counting, type-II and type-IV diagrams are UV finite and do not contribute to δ_{loop} . Conversely, type-I and III render UV contributions² that are respectively proportional to κ_{ffS}^3 and κ_{ffS} , leading to κ_{ffS}^2 and κ_{ffS}^0 terms in Eq. (I.16).

The counterterm contribution, written in terms of renormalisation constants, is given by

$$\begin{aligned} \frac{\alpha}{4\pi}\delta_{\text{CT}} = & -\frac{\delta Z_{AA}}{2} + \frac{\delta Z_H}{2} - \frac{s}{2c}\delta Z_{ZA} - \frac{1}{2s^2 M_W^2}\delta M_W^2 \\ & - \frac{c^2}{2s^2}\delta M_Z^2 + \frac{1}{s^2 M_Z^2}\delta M_W^2 + \frac{\delta m_b}{m_b} + \frac{\delta Z_{33}^{d,L} + \delta Z_{33}^{d,R}}{2}, \end{aligned} \quad (\text{I.17})$$

where the renormalisation constants are fixed by the scheme chosen in the renormalisation procedure. In the on-shell scheme, the field renormalisation constants δZ_{AA} , δZ_H , $\delta Z_{33}^{d,L(R)}$ are related respectively to the one-loop self-energies of the photon, the Higgs boson, and the bottom quark. Consequently, in the considered framework, we expect κ_{ffS}^2 contributions in the renormalisation constants δZ_H and $\delta Z_{33}^{d,L(R)}$, due to the presence of scalar-fermion couplings in the one-loop self-energies of the Higgs boson and the bottom quark.

The expression for the constant δZ_{AA} , related to the photon self-energy, in which the modified couplings do not appear, will reproduce the SM result. Repeating the same argument, we can argue that among the other constants, only δm_b will present a κ_{ffS}^2 term. This is reflected in the expressions of the renormalisation constants, and their UV divergent parts:

$$\delta Z_i|_{\text{UV}} = \frac{2}{4-D} \frac{\alpha}{4\pi} dZ_i, \quad (\text{I.18})$$

with,

$$\begin{aligned} dM_Z^2 &= \frac{1}{6M_W^2 s^2} \left[-3M_Z^2 \left(\sum_l m_l^2 + 3 \sum_q m_q^2 \right) - 70M_W^2 M_Z^2 + 22M_W^4 + 47M_Z^4 \right], \\ dZ_{AA} &= -\frac{23}{3}, \quad dZ_{ZA} = \frac{4M_W}{M_Z s}, \\ dM_W^2 &= -\frac{1}{6s^2} \left[7M_W^2 - 6M_Z^2 + 3 \left(\sum_l m_l^2 + 3 \sum_q m_q^2 \right) \right], \\ dZ_H &= \frac{1}{2M_W^2 s^2} \left[-\kappa_{ffS}^2 \left(\sum_l m_l^2 + 3 \sum_q m_q^2 \right) + 2M_W^2 + M_Z^2 \right], \\ dm_b &= \frac{m_b}{24M_W^2 s^2} \left[9\kappa_{ffS}^2 (m_b^2 - m_t^2) + 2M_W^2 + 7M_Z^2 \right], \\ dZ_{33}^{d,L} &= -\frac{1}{36M_W^2 s^2} \left[9\kappa_{ffS}^2 (m_b^2 + m_t^2) + 26M_W^2 + M_Z^2 \right], \\ dZ_{33}^{d,R} &= -\frac{1}{18M_W^2 s^2} \left(9m_b^2 \kappa_{ffS}^2 - 2M_W^2 + 2M_Z^2 \right). \end{aligned} \quad (\text{I.19})$$

The compensation of divergent terms between loop diagrams and counterterms, when performing the renormalisation procedure is a delicate mechanism. We will see how the presence of κ -dependent terms spoils the cancellation of the divergent part.

²Except for the W -exchange diagram, which is UV-finite because of the $\gamma^\mu(1-\gamma_5)$ structure of the W coupling to two fermions.

Indeed, the UV component of the counterterm contribution, obtained inserting Eq. (I.19) into Eq. (I.17), is the only source of divergences that might compensate the UV component of δ_{loop} given in Eq. (I.16), rendering the one-loop matrix element UV finite and thus valuable for the evaluation of the decay width.

The substitution leads to

$$\delta_{\text{CT}}|_{\text{UV}} = -\frac{1}{36 s^2 M_W^2} \frac{2}{4-D} \left[26M_W^2 + M_Z^2 - 9 \left(\sum_l m_l^2 + 3 \sum_q m_q^2 \right) + 9 \kappa_{ffS}^2 \left(2m_t^2 + \sum_l m_l^2 + 3 \sum_q m_q^2 \right) \right], \quad (\text{I.20})$$

and we see that the one-loop corrected transition matrix element of Eq. (I.15) gets a UV divergent contribution

$$\mathcal{M}|_{\text{UV}} = \frac{\alpha}{4\pi} \frac{\mathcal{M}_0}{4s^2 M_W^2} \frac{2}{4-D} (1 - \kappa_{ffS}^2) \left(\sum_l m_l^2 + 3 \sum_q m_q^2 \right), \quad (\text{I.21})$$

which in general does not vanish for $\kappa_{ffS} \neq 1$.

Another unsatisfactory aspect of using the κ -framework is that it cannot describe deviations in differential distributions. This happens because global factors can predict how many times the Higgs decays in a specific channel, but not how the kinematics of the decay products are affected. Of course new physics could modify these differential distributions, but it would not be captured by the overall factors.

The κ -framework is well motivated if one is looking for large deviations from the SM, as was the case in Run 1. The kappas parametrise these deviations and, if something new would be found, they would point which direction one should look into. ATLAS and CMS did not find any large differences in what was predicted by the SM, therefore the next step would be looking for small deviations.

I.2.4 Extrapolation on achievable experimental accuracy in future Runs

It starts to become clear that defining a theoretical framework able to describe possible deviations in the Higgs sector is not straightforward. If one wants to be as model independent as possible, an EFT approach may be the answer. EFTs will be extensively discussed in Section I.4, however, here we demonstrate how the testable hierarchies of scales are limited by the experimental accuracy.

The maximum testable hierarchy of scales is determined by two ‘‘sources’’: the assumption of a maximum size of underlying couplings and the experimental precision³ In the EFT approach and for observables close to the on-shell Higgs region, the higher dimensional operators are ordered by factors $g^2 m_H^2 / \Lambda^2$ (where Λ is the scale of the momentum cut-off of the theory), i.e. the only relevant scale for ‘‘on-shell’’ Higgs production is given by m_H .

This scale should be well separated from the experimentally accessible scale, in our case the EW scale $\Lambda \gg v$. The applicability of an EFT approach is, however, limited when the hierarchy of scales is not guaranteed. Because hadron colliders do not have a well-defined partonic energy, strategies relying on boosted objects and large recoils are the most critical.

While it is not clear that a marginal separation of scales invalidates the EFT approach, such observables clearly pose a challenge.

For this reasons, interpreting LHC physics in terms of an effective theory involves a delicate balance between energy scales. It is possible to roughly estimate the physics scales which can

³The problem for the interpretation of results in terms of an EFT during Run 1 was indeed the limited experimental accuracy, see Ref. [29].

be probed, and see if the deviation from the SM Higgs production and decay rates lies within the experimental accuracy. For instance in the energy region around the Higgs peak,

$$\left| \frac{\sigma \times \text{BR}}{(\sigma \times \text{BR})_{\text{SM}}} - 1 \right| = \frac{g^2 m_H^2}{\Lambda^2}. \quad (\text{I.22})$$

The accuracy on a rate measurement can then be translated into a threshold for new physics as

$$\left| \frac{\sigma \times \text{BR}}{(\sigma \times \text{BR})_{\text{SM}}} - 1 \right| = \frac{g^2 m_H^2}{\Lambda^2} > \Delta. \quad (\text{I.23})$$

This translates into the following relation:

$$\Lambda < \frac{g m_H}{\sqrt{\Delta}}. \quad (\text{I.24})$$

The precise value of the experimental accuracy Δ depends on the process under consideration. If we assume a value of $\Delta = 10\%$ (which roughly covers the current experimental accuracy), then for a weakly interacting theory with $g^2 \sim 1/2$, one can probe scales up to $\Lambda \approx 280$ GeV. This means that for weakly coupled new physics and with current experimental accuracy, it is not possible to test very high energy scales. However, for a more strongly interacting theory with $g \sim 1$ (but $g < 4\pi$, which is the theoretical limit for preserving unitarity), one can probe higher scales up to $\Lambda \approx 400$ GeV.

The increased statistics and Higgs production cross sections at Run 2 will enable us to add a wide range of distributions and off-shell processes to the Higgs observables, which can probe higher energy scales $\Lambda \gg m_H$. It is important to note that, if we look at differential observables, and in particular in the tails of the distributions, Eq. (I.24) has to be modified by substituting $m_H \rightarrow p_T$. Depending on the p_T regions that are reconstructed by the experiment, we will be able to access also different Λ values. Of course, we have to keep in mind that when we move towards higher Q^2 , the accuracy on the measurement will drastically decrease, and the value of Δ has to be reconsidered.

Intermezzo: Higgs off-shellness

In the NWA, $\Gamma_H \ll m_H$, the Higgs cross section factorises into on-shell production and on-shell decay, so the Higgs cross section can be written as:

$$\sigma_{i \rightarrow H \rightarrow f} = \sigma_{i \rightarrow H} \times \text{BR}_{H \rightarrow f} \propto \frac{\sigma_{i \rightarrow H} \Gamma_{H \rightarrow f}}{\Gamma_H}, \quad (\text{I.25})$$

and in terms of couplings

$$\sigma_{i \rightarrow H \rightarrow f} \propto \frac{g_i^2 g_f^2}{\Gamma_H} \sim \frac{g_i^2 g_f^2}{\sum_j g_j^2}, \quad (\text{I.26})$$

which means that the measurements in individual channels are complicated through dependence on the global Higgs properties due to the width. The width of the 125 GeV Higgs boson is predicted to be very small (4 MeV) compared to other heavy EW particles such as Z , W or top (~ 2 GeV). This is because the width is calculated by summing over all the decays, and the Higgs mostly decays to b quarks which are light compared to the EW scale

$$\Gamma_H \sim \left(\frac{m_b^2}{m_{EW}^2} \Gamma_{EW} \right). \quad (\text{I.27})$$

So what are the differences when looking at the resonance and at the tails? In the resonance region, the propagator (ignoring differences between fixed width, running width and complex pole),

$$\frac{1}{(s - M_X^2) + (i\Gamma_X M_X)} \quad (\text{I.28})$$

is dominated by the width in the denominator, so

$$\sigma_{i \rightarrow X \rightarrow f}^{on} \sim \frac{g_i^2 g_f^2}{\Gamma_X}. \quad (\text{I.29})$$

In the off-shell region instead, the cross section does not depend on the width so that,

$$\sigma_{i \rightarrow X \rightarrow f}^{off} \sim g_i^2 g_f^2. \quad (\text{I.30})$$

For a detailed discussion of off-shell Higgs physics see Refs. [30–33].

To summarise, the κ -framework has been used in Run 1 to interpret and deliver results, but a new era is approaching, where the limitations of this interim framework are becoming more and more evident. The lack of consistency when going to higher perturbative orders and the inability of the framework to describe BSM effects that modify the kinematic distributions cannot be neglected.

On one hand, the increasing experimental accuracy demands higher theoretical precision. On the other hand, the higher statistics and energies of the LHC Run 2 will allow us to study off-shell processes and distributions that will require a robust theoretical description of differential quantities.

The need for different frameworks is compelling, and in the following part of this chapter possible solutions will be offered, both on the experimental and the theoretical side. In general, the search for new physics at the LHC is performed via:

- A search for new states: resonances or more complicated structures searches. In this case, it is fundamental to have descriptive SM MC generators to achieve discoveries, i.e. the discovery in this case is data driven. Further on we will need precision for characterisation.
- Alternatively, a search for new interactions: deviations are expected to be small making this intrinsically a precision measurement. There is also a need for predictive MC generators in this case, and additionally accurate theoretical predictions for both background (SM) and signal (EFT) hypotheses.

Having said that, we should keep in mind that the matter content of the SM has been experimentally verified and evidence for other light states has not yet been found. Therefore, SM measurements can always be interpreted as searches for deviations from the $\text{dim} = 4$ SM Lagrangian predictions.

I.3 Fiducial and simplified template cross sections

I.3.1 Introduction

In this chapter we describe the set of approaches used by the LHC experiments to present their future results on the Higgs boson. The former, attempt to optimize the results based on the following requirements:

- The measured quantities should be directly comparable to theory.
- The measurements should be independent of the underlying theoretical assumptions.
- The experimental and theoretical errors should be factorisable.

The κ -framework discussed in Section I.2 was the first proposed method to address these requirements. Still, some limitations to its validity motivate going beyond this useful, but over-simplified, approach. For this purpose, a new framework is presented in this section.

I.3.2 Fiducial cross sections

As mentioned above, experiments should report quantities that are independent of theory, such that the result is comparable with theories other than the one that is more favoured at the time of the experiment. To have to redo an analysis for each new theoretical improvement is simply not feasible.

Let us, as an example, consider a measurement of a signal strength (see Section I.2). If an experiment was to report its measurements in terms of

$$\mu_i^f = \frac{(\sigma_i \cdot \text{BR}^f)^{\text{exp}}}{(\sigma_i \cdot \text{BR}^f)^{\text{theo}}}, \quad (\text{I.31})$$

the results, and their errors, would be based on the theoretical prediction available at the time of the experiment. And thus the measurement would have to be repeated each time an improved formulation of the theory becomes available. Reporting only μ_i^f , does not allow for a proper disentanglement of theoretical and experimental contributions to the reported errors.

One solution to this problem is to present experimental measurements of $\sigma_i \cdot \text{BR}^f$, which do not contain a strong assumption on the theoretically expected value. With such clean measurements, it is possible to deduce parameters in a way which is as theory-independent as possible.

Another area in which theoretical and experimental considerations become entangled, is the *unfolding* procedure used to correct for detector effects and to extrapolate them outside the detector phase space. Also here, it is desirable to report the results in a way that is independent on particular assumptions on the detector.

Experimentally, cuts are usually applied in order to increase the signal over background ratio, and to get a better sensitivity on the quantities of physical interest. All these cuts are applied to objects constructed from signals coming directly from the detector, eventually caused by the interaction of the physical particles with the detector material.

Levels

The phase space of signals in the detectors is called the *detector level*. Phase spaces defined for particles before their interaction with the detector are called *truth levels*. The definition of truth levels is ambiguous and relies on a theoretical model.

One could define a level formed by particles with a relatively long lifetime ($\gtrsim 10^{-10}$ s), which typically are the particles which interact with the detector. This is usually referred

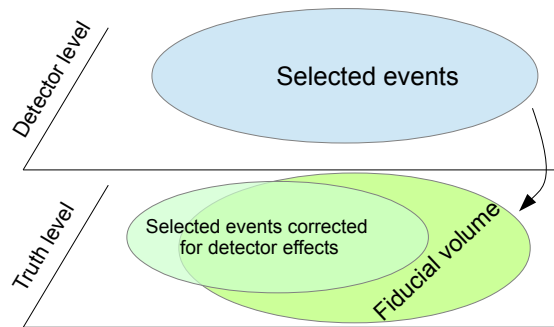


Fig. I.3: Schematic representation of the unfolding procedure. Events selected at detector level, with cuts enhancing the S/B ratio (blue ellipse). A correction is then applied to take into account particle interactions with the detector (light green ellipse). A fiducial volume at truth level is then defined in order to compare the measurement with a theoretical prediction (green ellipse).

to as *particle level*. The theoretical description of the particle level depends on shower and hadronisation modelling.

It is also possible to define a level based on partons, the *parton level*, by considering particles before shower hadronisation. This level describes only elementary particles which exist in theoretical calculations, i.e. as defined in the Lagrangian. As an example, gluons and quarks are valid objects at the parton level, while at the particle level the corresponding objects are jets.

If an experiment corrects a measurement to parton level, it must assume a theoretical model for showering and hadronisation, as well as a model for interaction of stable particles with the detector. At the particle level, only the latter has to be assumed. Thus parton level descriptions depend more on theoretical assumptions than the particle level.

Another thing to take into account is the detector efficiency. Detectors do not allow the measurement of all the particles produced in collisions due to gaps and supporting structures. Even when particles do interact with the detectors, they may not leave a clear enough trace to allow the object to be reconstructed correctly. Events whose reconstruction is not possible are usually discarded. When correcting a measurement to truth level, only detector level events which passed detector level cuts are unfolded.

To compare with a particular theoretical prediction, cuts on truth level objects have to be applied too. The set of cuts defines a volume in the truth level phase space, which is usually referred to as the *fiducial volume*. In general, events which pass truth level cuts could also fail to be reconstructed at detector level, and vice versa. To correct for this effect, a theoretical assumption has to be made on the correction of truth levels which were lost in detector level selections. The larger the fraction of events from the fiducial volume that are reconstructed at detector level, the smaller the theoretical contribution to the correction.

In summary, if it is possible to define a truth level as close as possible to the detector level, the theoretical model dependence of such a level is minimised. This is the idea which defines *fiducial cross sections*, introduced in Ref. [34]. Fiducial cross sections are cross sections unfolded to particle level in a fiducial volume defined by some cuts that are as close as possible to the ones applied at detector level (but are applied on particle level objects instead). Such

cross sections are the measurements with the least theoretical assumptions.

Experimentally, cross sections can be defined in terms of directly measurable quantities, such as:

- Total cross sections

$$(\sigma_i)_{\text{exp}} = \frac{N_{\text{ev},if}}{\text{BR}^f \mathcal{A}_{if} \epsilon_{if} \mathcal{L}}.$$

- Total cross sections with fixed final state

$$(\sigma_i \times \text{BR}^f)_{\text{exp}} = \frac{N_{\text{ev},if}}{\mathcal{A}_{if} \epsilon_{if} \mathcal{L}}.$$

- Fiducial cross sections with fixed final state

$$(\sigma_i \times \text{BR}^f \times \mathcal{A}_{if})_{\text{exp}} = \frac{N_{\text{ev},if}}{\epsilon_{if} \mathcal{L}}.$$

where \mathcal{A} is the fiducial acceptance (i.e. a factor to extrapolate the measurement to the full particle level phase space), ϵ is the experimental efficiency (which includes all of the unfolding factors), \mathcal{L} is the luminosity, BR^f is the branching ratio for final state f , i determines a particular bin and/or initial state, and $N_{\text{ev},if}$ is the number of events counted at detector level. Apart from the luminosity and the collected number of events, all of these factors depend on a given theoretical model.

It is thus clear that fiducial cross sections, which have the fewest correction factors, depend least on the underlying theory assumptions. It is also possible to extract differential fiducial cross sections:

$$\frac{d\sigma^{\text{fid}}}{\sigma^{\text{fid}}} = \frac{dN_{\text{ev}}}{N_{\text{ev}}} \cdot \frac{\epsilon_{dN}}{\epsilon_N},$$

where dN_{ev} is the number of events in a particular bin, and ϵ_{dN} the experimental efficiency for this bin. In general, the measured and fiducial cross sections are related by,

$$\sigma_i^{\text{fid}} = \sum_j \mathcal{A}_{ij} \sigma_j, \tag{I.32}$$

where σ_i^{fid} are the fiducial cross sections, \mathcal{A}_{ij} contains the factors which define the fiducial volumes and σ_j are the measured cross sections. The indices i and j specify the production mode, decay channel, or a bin of a differential cross section.

From the theoretical point of view, fiducial cross sections are particle level predictions of a particular theoretical model, with the same fiducial cuts as those applied by the experiments for the observable of interest. Typically, fixed order theoretical calculations are implemented in a Monte Carlo event generator, in order to be able to apply the cuts on particle level objects and compare the result to the available measurements.

Fiducial measurements are, in principle, the cleanest possible way to compare data with theory and generally all event selections which depend only on kinematic cuts allow the extraction of fiducial cross sections. However, in order to increase sensitivity, experiments often use cuts which involve complex techniques, such as multivariate techniques (MVA) in the form of boosted decision trees (BDT) or neural networks (NN).

This type of cuts are generally needed to produce precise measurements, but are hard to reproduce in theoretical calculations. So, although minimally theory-dependent fiducial cross sections are fundamental to understand specific processes, which usually have a clean experimental signature, their application for studying the whole range of Higgs physics is limited.

| Cuts definition | ATLAS | CMS |
|-----------------------|---|---|
| Lepton definition | | |
| Electrons | $p_T > 7 \text{ GeV}, \eta < 2.47$ | $p_T > 7 \text{ GeV}, \eta < 2.5$ |
| Muons | $p_T > 6 \text{ GeV}, \eta < 2.7$ | $p_T > 5 \text{ GeV}, \eta < 2.4$ |
| Event selection | | |
| Leptons p_T cuts | $p_T > 20, 15, 10, 10 \text{ GeV}$ | $p_T > 20, 10, 7(5), 7(5) \text{ GeV}$ |
| Invariant masses cuts | $50 \text{ GeV} < m(l^+, l^-) < 106 \text{ GeV}$ | $40 \text{ GeV} < m(l^+, l^-) < 120 \text{ GeV}$ |
| | $12 \text{ GeV} < m(l^-, l'^+) < 115 \text{ GeV}$ | $12 \text{ GeV} < m(l^-, l'^+) < 120 \text{ GeV}$ |
| | $118 \text{ GeV} < m(l^+, l^-, l'^-, l'^+) < 129 \text{ GeV}$ | $105 \text{ GeV} < m(l^+, l^-, l'^-, l'^+) < 140 \text{ GeV}$ |
| | $m(l^+, l^-) > 5 \text{ GeV}$ | $m(l^+, l^-) > 4 \text{ GeV}$ |
| Lepton separation | $\Delta R(l_i, l_j) > 0.1(0.2)$ for same(opposite) sign | $\Delta R(l_i, l_j) > 0.02$ for every $i \neq j$ |

Table I.3: Some of the differences in the definition of fiducial volumes for ATLAS, defined in Ref. [35] and CMS, defined in Ref. [36] for the $H \rightarrow 4l$ analysis.

Of course the definitions of the physical objects have to be shared between the various experiments and fiducial volumes have to be the same in order for all quantities to be comparable. This is not obvious, since each experiment could be in principle most sensitive to an observable in a different region of the phase space than others.

As an example, in the ATLAS and CMS analysis of $H \rightarrow 4l$, published in Refs. [35,36], the fiducial cuts are similar but not precisely the same - see Table I.3. Global combinations can be done by correcting to a common fiducial volume. This procedure introduces a small theoretical dependence, but the benefits of the combinations are much larger, as discussed in Section I.2.2.

In some cases, it is necessary to simply extrapolate the measurement to a larger phase space, because the definition of minimally-theory dependent fiducial phase space is not possible. In that case, the formula for the fiducial cross section becomes:

$$(\sigma_i)_{\text{exp}}^{\text{fid}} = \frac{N_{\text{ev},if}}{\alpha_{if}\epsilon_{if}\mathcal{L}}, \quad (\text{I.33})$$

where we introduced the factor α_{if} which extrapolates the measurement to the larger fiducial phase space. A study of the extrapolation and unfolding factors can be found in Ref. [36] from the CMS analysis of $H \rightarrow 4l$ and is reported in Table I.4 with the notation used in this section.

Table I.4 shows that the acceptance factors depend strongly on the Higgs production modes, and that the unfolding factors are compatible within their errors, because the different production modes have very different kinematics and final states. Thus, it makes sense to report Higgs fiducial cross sections in large fiducial volumes in terms of Higgs production modes.

A last thing to notice is that in Eq. (I.33), the experimental and theoretical uncertainties factorise. In fact, a naive calculation of the relative error on the fiducial cross section gives:

$$\frac{\Delta\sigma^{\text{fid}}}{\sigma^{\text{fid}}} = \frac{\Delta N_{\text{ev}}}{N_{\text{ev}}} \oplus \frac{\Delta\epsilon_{if}}{\epsilon_{if}^2} \oplus \frac{\Delta\alpha_{if}}{\alpha_{if}^2}. \quad (\text{I.34})$$

When a more precise measurement becomes available, there is no need to repeat the analysis from the beginning. Only the extrapolation factors α_{if} need to be re-computed, starting from the unfolded distribution. To summarise, the new framework for Higgs physics should:

- Measure cross sections.
- Unfold cross sections to fiducial volumes, taking advantage of positive aspects of fiducial measurements while not renouncing to maximise experimental sensitivity.

| Signal process | α_{if} | ϵ_{if} |
|---|-------------------|-------------------|
| Higgs production modes | | |
| ggH | 0.422 ± 0.001 | 0.681 ± 0.002 |
| VBF | 0.476 ± 0.003 | 0.678 ± 0.005 |
| WH | 0.342 ± 0.002 | 0.672 ± 0.003 |
| ZH | 0.348 ± 0.003 | 0.679 ± 0.005 |
| ttH | 0.250 ± 0.003 | 0.685 ± 0.010 |
| Non-SM models | | |
| $q\bar{q} \rightarrow H(J^{\text{CP}} = 1^-)$ | 0.238 ± 0.001 | 0.642 ± 0.002 |
| $q\bar{q} \rightarrow H(J^{\text{CP}} = 1^+)$ | 0.283 ± 0.001 | 0.651 ± 0.002 |
| $gg \rightarrow H \rightarrow Z\gamma^*$ | 0.156 ± 0.001 | 0.667 ± 0.002 |
| $gg \rightarrow H \rightarrow \gamma^*\gamma^*$ | 0.238 ± 0.001 | 0.671 ± 0.002 |

Table I.4: Fiducial volume and detector/unfolding efficiencies and their errors, for $H \rightarrow 4l$. Table from Ref. [36].

- Yield cross section measurements in terms of production modes, since acceptance factors depend on them.

The simplified template cross section (STXS) framework, introduced in Ref. [37] is designed to take these considerations into account. It tries to combine the ease with which signal-strength-like fits are performed experimentally with the theoretical needs of fitting to well defined and calculable predictions, aiming to find a good compromise between theory-independence of the measurements and their experimental sensitivity. The STXS framework will be explained in detail in the next section.

I.3.3 Simplified template cross section framework

STXSs are fiducial cross sections defined in simplified fiducial volumes. The definition of the fiducial volumes allows the use of advanced experimental techniques, thereby gaining in experimental sensitivity, at the cost of a small dependence on the theoretical model. This is necessary, since at the moment all the measurements on Higgs boson cross sections are dominated by statistical uncertainty. Also the combination of different decay channels reduces the statistical uncertainty. This has been shown, for example, in Ref. [38], where the combination reduced the statistical error on the production cross section by a factor of 1.4.

$$\begin{aligned}
\frac{\Delta\sigma}{\sigma}(H \rightarrow \gamma\gamma) &= 35\%, & \frac{\Delta\sigma}{\sigma}(H \rightarrow ZZ) &= 23\%, \\
\frac{\Delta\sigma}{\sigma}(H \rightarrow \gamma\gamma \oplus H \rightarrow ZZ) &= 17\%.
\end{aligned}
\tag{I.35}$$

Combining the different Higgs decay channels would further improve the precision of the measurements. This is the main difference between the usual fiducial differential cross sections and the STXS framework. While fiducial measurements maximise the independence on the theoretical modelling, simplified cross sections maximise the experimental sensitivity. Instead of using fully differential distributions, cross sections are divided into sub-cross sections, called *bins*. How to choose such *bins* is an interesting topic in its own right and is discussed in Section I.3.4.

The definition of the physics objects in the STXS fiducial volume, is aimed at taking advantage of combinations. It is independent of the Higgs decay modes in such a way that

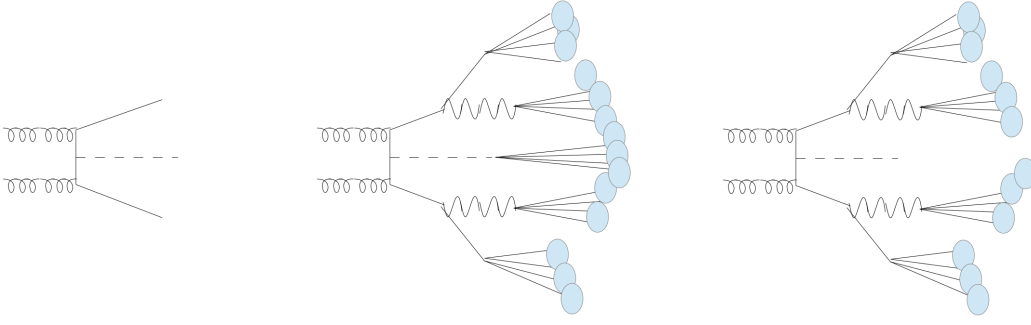


Fig. I.4: Parton level (left), usual particle level definition (center) and corresponding particle level definition for STXSs (right), for the $t\bar{t}H$ production mode. Blue blobs represent particles with long lifetime ($\gtrsim 10^{-10} s$).

combinations do not introduce further theory dependent factors. In STXS, the particle level is defined with undecayed Higgs bosons while jets are reconstructed from the particles which are not associated with the Higgs decay. The formula connecting single channel measurements to the STXS is:

$$\begin{aligned}
\sigma_i^f(\text{exp}) &= A_{f,\alpha_1}^i \sigma_i^{\alpha_1} \\
\sigma_i^f(\text{exp}) &= A_{f,\alpha_1\alpha_2}^i \sigma_i^{\alpha_1\alpha_2} \\
&\dots \\
\sigma_i^f(\text{exp}) &= A_{f,\alpha_1\alpha_2\dots\alpha_n}^i \sigma_i^{\alpha_1\alpha_2\dots\alpha_n},
\end{aligned}
\tag{I.36}$$

where $i=\{ggF, VBF, VH, t\bar{t}H, b\bar{b}H, tH\}$ and $f=\{\bar{b}b, \gamma\gamma, ZZ, WW, \tau\tau\}$ denote production and decay modes respectively, $\sigma_i^{\alpha_1}$, $\sigma_i^{\alpha_1\alpha_2}$, $\sigma_i^{\alpha_1\alpha_2\dots\alpha_n}$ are the STXSs and the $A_{f,\alpha_1\alpha_2\dots\alpha_n}^f$ are efficiency/acceptance factors for each STXS.

Each line of Eq. (I.36) is called a *stage*. The first *stage* or *stage(0)* is very close to the signal strength measurements performed during Run 1 of the LHC. The indices α_k indicate the *bin* divisions and the sum over repeated indices is understood.

Every bin of *stage(n)* is split into smaller bins in *stage(n+1)*. The sub-bins are defined in independent regions of the full fiducial phase space. This is repeated at every stage. The procedure could be repeated recursively, but given the prediction for the amount of data that LHC experiments are going to collect during Run 2 and the HL-LHC phases, only stages up to *stage(2)* will have enough statistical significance. Notice that the structure of Eq. (I.36) is identical to Eq. (I.32), which allows the factorisation of the experimental and theoretical contributions from the total uncertainty.

I.3.4 STXSs *bins* and the $t\bar{t}H$ binning proposal

The STXS framework is incomplete without a definition of a *bin*. The binning aims to reduce the theoretical dependence of the measurement within each bin so that limits derived from a certain *bin* do not strongly depend on a particular theoretical model.

A *bin* should therefore be defined through cuts on truth level objects. If, for instance, the cut would be on the transverse momentum of the reconstructed object, the theoretical uncertainty would need to be convoluted with other effects and thereby be enlarged.

Another aspect to take into account is the identification of regions where BSM physics has a higher probability of being observed. Separating such phase space regions from the SM

dominated ones, would increase the chance of seeing potential deviations from the SM. Since no big deviation from the SM has been observed, BSM effects are expected to have the largest impact in the tails of distributions or in extreme kinematic regions. For example, one could put a cut on Higgs transverse momentum, p_{TH} , beyond which no SM events are expected (for a given integrated luminosity). All entries in such a bin would then be sign of BSM physics.

The binning depends on the integrated luminosity and on experimental systematic uncertainties, therefore it can only be fully understood a posteriori. To allow the framework to be more flexible, the combination of bins is possible. In case a bin is found to be not significant, it can be combined with others to increase the global significance. Of course, not all bins can be combined with all the others, but only adjacent ones.

The best solution is then starting with a very general binning, similar to the one used during LHC Run 1. This is called *stage(0)*. Then, by taking into account more recent measurements and expected results, a second stage can be already defined for most processes. The current proposal can be found in Ref. [37] where the gluon fusion, vector boson fusion and associated vector boson production modes for the Higgs have been studied up to *stage(1)*, and hints for a future stage are given.

The $t\bar{t}H$ production mode has not been studied in depth yet. It has a more complicated topology than the other channels, and the cross section is relatively small. It is difficult then, given a reasonable luminosity, to have enough events to fill a lot of *bins*. This means that the statistical experimental uncertainty will be big, which allows for a relaxation of the theoretical independence criterion. As an exercise, we are going to propose a possible *binning* for $t\bar{t}H$ production mode up to *stage(2)*.

Stage(0) has been already defined in Ref. [37], as inclusive $t\bar{t}H$ production with Higgs pseudo-rapidity (Y_H) less than 2.5. The cut on Y_H avoids an extrapolation to the full phase space. Similar to all production modes, this bin is the most similar to a Run 1-like signal strength measurement.

Top quark pair associated production with a Higgs allows direct access to the top-Higgs interaction. One could naively expect that NP would show up at high energies, hence a kinematic region which deserves consideration is the boosted regime. This is the phase space where the Higgs and one (or two) top(s) are produced at high transverse momentum, ideally much larger than their mass, but realistically starting from around 200 GeV.

Boosted analysis usually have a smaller background contamination, as explained in Ref. [39]. On the other side, objects with high transverse momentum are less likely to be produced than objects with mild/low p_T . Furthermore, the region with $p_{TH} < 200$ GeV is sensitive to the CP properties of the top-Higgs interaction, see Ref. [40].

Finally, a reasonable choice for the first *stage* of $t\bar{t}H$ production mode seems to be the definition of a boosted *bin* more sensitive to potential NP phenomena, and unboosted bins sensitive to CP properties. Since the former would probably contain few events, the latter topology could be divided in even smaller bins.

Using the transverse momentum of the Higgs to define fiducial sub-volumes, we could define the *bins*:

$$\begin{aligned}
 & \text{bin}(0) : & 0 < p_{TH} < 100 \text{ GeV} \\
 \text{stage}(1) & \text{bin}(1) : & 100 \text{ GeV} < p_{TH} < 200 \text{ GeV} \\
 & \text{bin}(2) : & 200 \text{ GeV} < p_{TH}
 \end{aligned} \tag{I.37}$$

where *bin(2)* contains the boosted category where NP effects are more probable. Although not a requirement for a high energy top-Higgs interaction, most of the boosted analysis require at least one top quark to be boosted to reduce background contamination.

It has been shown in Ref. [41] that the general contribution arising from $\text{dim} = 6$ operators to the Yukawa-like interaction between fermions and the Higgs boson, is:

$$\mathcal{L} \propto \bar{f} \left(a_f + b_f \gamma^5 \right) f H, \quad (\text{I.38})$$

where f is the fermion (top quark in our case), a_f and b_f are two real factors. In Ref. [40] the top quark Yukawa interaction has been studied for $t\bar{t}H$ production mode.

Another distribution which is sensitive to the Yukawa coupling is the rapidity difference between the two tops, $\eta(t, \bar{t})$. In particular, the region with $0 < \eta(t, \bar{t}) < 2$ is most sensitive, the region with $2 < \eta(t, \bar{t}) < 4$ has a smaller dependence, while the region $4 < \eta(t, \bar{t}) < 6$ has no sensitivity and low statistics. A second stage seems possible (and useful when enough statistics will be available).

In principle, top quarks are not available among the objects we defined in the fiducial space, but strategies exist to define “pseudo-tops” in a way which is as theory independent as possible. Furthermore, when removing Higgs decay products from the list of particles from which jets are constructed, we are left with a $t\bar{t}$ -only signature, for which such algorithms are optimised. The use of pseudo-tops is currently a standard procedure in many experimental analysis, e.g., Ref. [42].

The second stage we propose is then:

$$\begin{aligned} \text{bin}(0) : & \quad 0 < |\Delta\eta(t, \bar{t})| < 2 \\ \text{stage}(2) \quad \text{bin}(1) : & \quad 2 < |\Delta\eta(t, \bar{t})| < 4 \\ \text{bin}(2) : & \quad 4 < |\Delta\eta(t, \bar{t})| < 6 \end{aligned} \quad (\text{I.39})$$

Compared to other production modes, $t\bar{t}H$ has a clearer signature, therefore its staging and binning has been more focused on finding regions sensible to BSM effects. And there is no need for defining bins with cuts which allow to distinguish it from other production channels, as it is the case for VBF, studied in Ref. [37]. The final staging and binning we propose for Higgs boson associated production with top pairs is shown in Fig. I.5. Summarising the choice of bins, we have:

- One bin where the Higgs is boosted and hypothetical NP can be reached with a higher probability because of the high energies involved.
- Other bins sensitive to the CP characteristics of the Yukawa interaction.

After the definition of *stages* and *bins*, we end up with well defined measured quantities which have a small residual theoretical dependence.

The next step is to interpret such measurements within a particular theory model through the extraction of Wilson coefficients. This is a difficult step, since different theories contain different coefficients, and there can be a large number of them, making a simultaneous fit to all of them a priori impossible. Additionally, if an experiment would perform a fit to Wilson coefficients of a chosen theory, the results would be valid only for this particular theory (and for all theories which can be matched to it).

Instead of fitting Wilson coefficients directly, one could fit objects, such as Pseudo-Observables (POs), which are well defined from both the theoretical and the experimental points of view. These objects should be general enough (and fewer in number) to allow for variety of different theoretical models to be studied. The POs framework will be described in Section I.5.

In summary, STXSs and BR measurements, together with physical POs, allow a wide variety of Higgs measurements to be studied in a well defined theoretical framework.

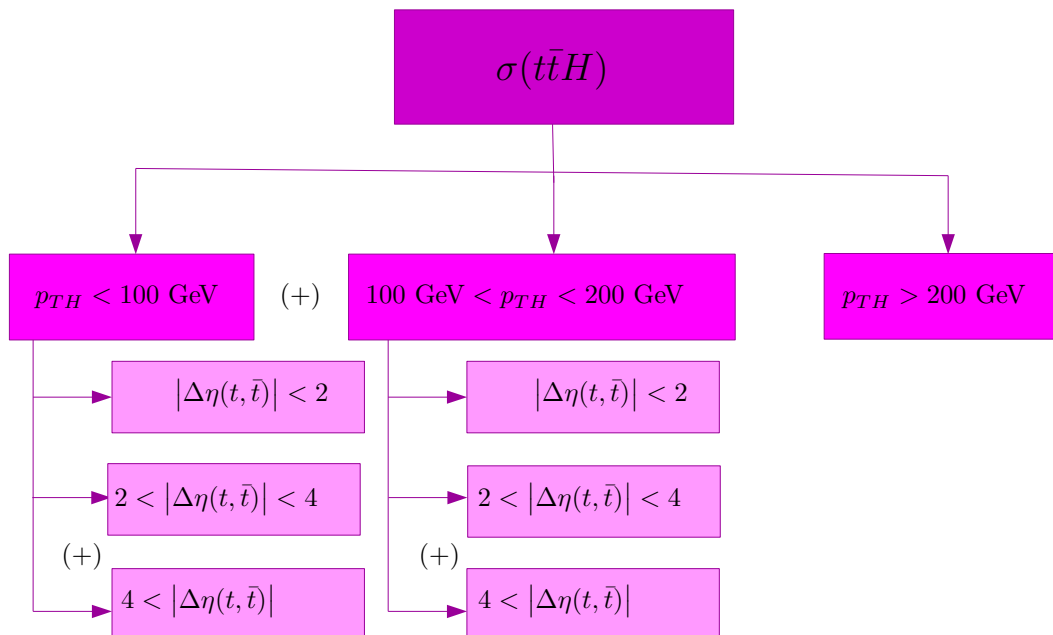


Fig. I.5: Staging and binning for the $t\bar{t}H$ production mode. p_{TH} is the transverse momentum of the Higgs boson, $|\Delta\eta(t, \bar{t})|$ is the absolute rapidity difference between the two tops. The “+” sign means that the bins can be added together.

I.3.5 Interplay with pseudo-observables

For Higgs production and decay modes, a list of Pseudo-Observables already exists, proposed in Refs. [43, 44]. As discussed in Section I.3.3, STXSs are divided according to the various production modes.

In order to maximally disentangle measurements from theory assumptions, a good option is to connect the STXSs with POs of Higgs decays, which introduces fewer theoretical-experimental correlations than interpreting them directly through POs of Higgs production.

In Ref. [44] Higgs EW production modes were written in terms of Higgs POs. Most of these POs also contribute to Higgs decays. This allows for a direct connection between VBF and VH production modes (and therefore their STXSs) and the Higgs EW decays. Note that POs coming from the second order terms of the momentum expansion around physical poles cannot be directly connected to POs of Higgs decays and only describe the production processes.

Such effects also appear in off-shell decay cross sections and distributions, where the kinematic regime (high transferred momentum) is similar. QCD POs are not generally available yet, only a few have been introduced for production modes, which are modifiers of the ggH and $t\bar{t}H$ production rates.

Since POs come from a momentum expansion around physical poles, such as vector boson masses, the validity of using POs has to be checked carefully. Of course, transferred momentum

is not directly accessible from an experimental point of view, but other variables can be used, which are related through kinematic constraints. For instance, for the VH production mode $q \rightarrow p_{TZ}$ for $p_{TZ} \rightarrow \infty$, while for VBF production $q \rightarrow p_{T\text{forward-jet}}$, where q is the transferred momentum, as defined in Ref. [44]. Once the missing POs are defined, an important task will be to find the variables which allow us to infer the value of the transferred momentum and thereby check the validity of the approximation.

In the case of the $t\bar{t}H$ production mode, the problem is more complex, since many POs can be defined (taking into account the decays of the top quarks) while there is limited information from the measurements (i.e. approximately 10 correlated STXS bins of Section I.3.4).

From the definition of the POs that will be given in Section I.5, the amplitudes depend linearly on POs. Therefore cross section-like observables have a quadratic dependence, since integration over phase space does not change this behaviour. For this reason, a theoretical prediction for the expected number of events can be written in the form:

$$N^{\text{ev}} = X_{ij} k_i k_j, \quad (\text{I.40})$$

where k_i is a vector of POs and X_{ij} is a matrix of coefficients that can be computed with MC simulations. This is in general true for every theory which introduces a linear dependence on a coefficient at scattering amplitude level. For a STXS bin, the procedure is the same, although the factors X_{ij} are different.

Using the notation of section Section I.3.3, then for $stage(n)$ with a bin described by a_1, \dots, a_n :

$$\sigma_i^{a_1 \dots a_n} = C_{i, a_1 \dots a_n}^{lm} k_l k_m, \quad (\text{I.41})$$

where $C_{i, a_1 \dots a_n}^{lm}$ are factors computed theoretically. The question one should ask is *which values of $\{k_i\}$ are more likely, given the experimentally observed $\sigma_i^{a_1 \dots a_n}$?* To try to answer this question, a number of technical tools and results are needed:

- MC generators producing theoretical predictions for various NP scenarios.
- Detector level simulations of NP models, in order to verify their independence from the data correction.
- All the relations between observables and theory parameters.
- A software framework to perform the fit.

All these aspects introduce additional technical difficulties which will be discussed in Section I.6.4.

I.4 Effective field theories

I.4.1 Introduction

At the heart of effective field theories lies the idea of adding a series of higher dimensional operators to a Lagrangian. In principle, adding operators of mass dimension bigger than four to a Lagrangian in four space-time dimensions renders the latter non-renormalizable in the classical sense. However, if this effective Lagrangian is interpreted as a series expansion in operator dimensions, it can be shown that the new Lagrangian is renormalizable order by order in such expansion.

This result is closely related with the Wilsonian interpretation of ultraviolet divergences, where the higher dimensional operators are suppressed by powers of some energy scale (a *cut-off* scale). This way, they can be understood as a collection of non-local operators, parametrising the effects of the local, renormalizable, operators of the theory in the UV regime.

For this reason, such an effective Lagrangian can be used to parametrize SM deviations and ultimately lead to the development of an improved version of the Standard Model, valid in higher energy regimes. Any effective Lagrangian, describing SM deviations, can be written as

$$\mathcal{L}_{\text{Eff}} = \mathcal{L}_{\text{SM}} + \sum_{n>4} \sum_i \frac{a_i}{\Lambda^{n-4}} \mathcal{O}_i^{(n)}, \quad (\text{I.42})$$

where $\mathcal{O}_i^{(n)}$ are higher dimensional operators, built out of SM fields, Λ is the cut-off scale for the effective theory, and the a_i are the Wilson coefficients for the new operators, acting as effective couplings. In this section we will discuss how to build such a Lagrangian and make predictions with it.

I.4.2 Fermi Effective Theory

Fermi Theory can be seen as the prototype of all EFTs, and as such, we will briefly discuss it in this section. The first Lagrangian for weak interactions was written by Fermi in 1934, based on the electromagnetic one, \mathcal{L}_{em} . Its purpose was to explain the neutron decay, also known as β -decay, $n \rightarrow p + e^- + \bar{\nu}_e$. After many theoretical efforts Fermi wrote an effective four-fermion Lagrangian

$$\mathcal{L}_F = \frac{G_F}{\sqrt{2}} J^\mu(x) J_\mu^\dagger(x), \quad (\text{I.43})$$

where the J^μ are point-like interaction currents. In particular, $J^\mu(x) = L^\mu(x) + H^\mu(x)$, where $L^\mu(x)$ is the weak *leptonic* current and $H^\mu(x)$ the weak *hadronic* current. This theory considers the proton and the neutron fields to be fundamental and does not take parity violation into account. Although it violates the unitarity of the scattering matrix and it is not renormalisable, Fermi theory proved to be a good effective theory with phenomenological success. Now we understand that the Fermi theory is a low-energy version of a Yang-Mills QFT. However, the theory of EW interactions did not appear as a UV completion of Fermi theory, and in fact it took much longer before the connection between the two was properly understood, for a discussion on this connection see ref. [45].

The decades after Fermi theory was proposed, namely the 40's and the 50's were times when particle physicists were extremely active. Many small experiments were taking place all around the world and experimental methods were developing very fast. This way parity violation was discovered, the V-A structure was detected, as well as $SU(2)$ symmetry and neutral currents, all these led to the postulation and experimental confirmation of the EW theory.

Without these experimental discoveries, Fermi and his theory colleagues would have been challenged to discover the SM starting only from the Fermi theory of β -decay and fundamental

principles. In this case, a natural way forward could have been to enhance the theory by adding higher dimensional operators, which respect the known symmetries, as proposed in ref. [46]. Then, it would be possible to make predictions with this new theory and see in which manner the latter deviate from experiments. This way, information about previously unknown symmetries such as $SU(2)$ could have been revealed. Theorists may then have written :

$$\mathcal{L}_F = G_F \bar{\psi} \psi \bar{\psi} \psi + \sum_{i,j} \underbrace{(\bar{\psi} \mathcal{O}_i \psi)(\bar{\psi} \mathcal{O}_j \psi)}_{\mathcal{O}_{i,j}=\text{any other fields}} = G_F \bar{\psi} \psi \bar{\psi} \psi + a_{\square} G_F^2 \bar{\psi} \psi \square \bar{\psi} \psi + \dots \quad (\text{I.44})$$

History did not happen like this, but this example illustrates how the theoretical effort done nowadays in the search for the *underlying theory* complements what we know at the energies accessible for us. This procedure by which we add higher dimensional operators to our low-energy theory in a model-independent way is the so called “bottom-up” approach.

I.4.3 EFT: Top-down approach

In practise, EFT comes in two different flavours, the bottom-up approach that we just outlined, and the top-down approach. In this section, we will focus on the latter.

The top-down approach is model dependent: it represents a scenario where we want to study a particular high-energy or UV-complete theory and we try to infer the behaviour and footprints of this theory in the experimentally accessible low energy regime. One can understand this technique by looking at the Fermi theory where the UV completion was the SM, or more concretely, the theory of EW interactions. Back then, the energy regime of the SM was far beyond what could be probed experimentally, therefore, if one would have wanted to test the validity of the SM at energies of say, the order of 10 GeV, what would be the best strategy to follow?

The first observation is that particles heavier than the energy regime accessible by our experiments will not be created. Therefore we can remove them from our theory, since we do not expect them to appear. However, particles are not always on-shell, and, heavy particles that are not directly produced in the experiment can nevertheless contribute via loop corrections. This has the direct implication that we cannot simply remove them from the theory by setting the masses to infinity and/or the couplings to zero. We have to integrate out the relevant degrees of freedom using legitimate QFT methods.

The technique of removing heavy particles but keeping the consistency of the QFT, goes back to the early 80’s [47], in the context of quantum gravity, and makes use of a technique called Background Field Method (BFM) to integrate out the heavy states in the path integral.

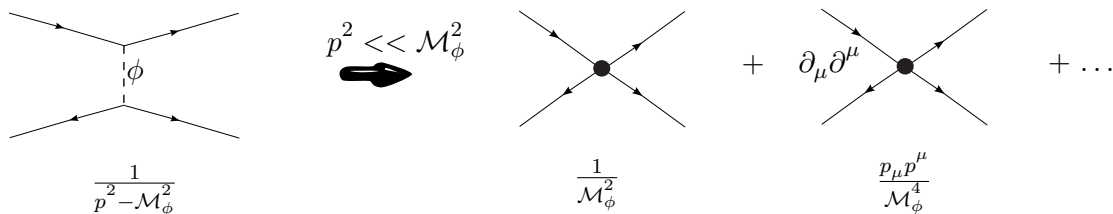


Fig. I.6: In the top-down approach the heavy particles (a scalar ϕ field in this case) are *integrated out* by taking the limit $M_\phi^2 \gg |p^2|$. This way the propagator contracts to become a vertex.

After we identify the the cut-off scale of the UV theory, and integrate out the particles above this scale, the last step is to make predictions for the low energy regime using the new and simplified effective scenario.

To understand how heavy particles are integrated out, we can do a simple exercise: imagine some heavy singlet under $SU(2)$, represented by a scalar field S with a mass M_S much bigger than the SM masses and construct the singlet extension of the SM (SESM). This SM extension was born in the 80's as a dark matter candidate, in Ref. [48], it is also often used in the context of Higgs physics and LHC phenomenology see for instance Refs. [49–53], as well as more exotic scenarios: to guarantee the stability of the EW vacuum at very high energies, in Ref. [54], or to describe baryogenesis, in Ref. [55, 56],

$$\begin{aligned}\mathcal{L}_{UV} &= \mathcal{L}_{SM} + \mathcal{L}_S, \\ \mathcal{L}_S &= \frac{1}{2}(\partial_\mu S)(\partial^\mu S) - \frac{1}{2}M_S^2 S^2 - \lambda_1 S^4 - \frac{\lambda_{12}}{2}S^2(2vH + H^2 + 2\phi^+\phi^- + \chi^2),\end{aligned}\quad (\text{I.45})$$

where φ is the scalar doublet of the SM and ϕ, χ the unphysical Goldstone fields. To remove the heavy field S from the Lagrangian, we have to *integrate it out*. This can be done either by diagrammatically or by using functional methods. Here we will outline the latter.

To integrate out the field S , we write down a path integral over that field. This can be understood as keeping all SM fields fixed (also called “background fields”) with the heavy ones being dynamic. The effective action then becomes:

$$S_{\text{eff}} = \exp\left\{i \int d^4x \mathcal{L}_{eff}\right\} \sim \int \mathcal{D}S \exp\left\{\frac{i}{2} \int d^4x \left[\frac{1}{2}(\partial_\mu S)(\partial^\mu S) - M_S^2 S^2 - S^2 F(\varphi)\right]\right\}. \quad (\text{I.46})$$

For the interested reader, this procedure is discussed in detail in Refs. [57, 58] in the context of a heavy Higgs in the SM. Here we just show the basic steps.

$$\begin{aligned}\exp\left\{i \int d^4x \mathcal{L}_{eff}\right\} &= \int \mathcal{D}S \exp\left\{\frac{-i}{2} \int d^4x \int d^4y S(x)(\partial_x^2 + M_S^2 + F(x))\delta(x-y)S(y)\right\} \\ &= \exp\left\{\mathcal{D}et \left[(\partial_x^2 + M_S^2 + F(x))\delta(x-y)\right]^{-\frac{1}{2}}\right\} \\ &= \exp\left\{-\frac{1}{2}\mathcal{T}r\{\ln(\partial_x^2 + M_S^2 + F(x))\delta(x-y)\}\right\}.\end{aligned}\quad (\text{I.47})$$

Now we can take the *decoupling limit* $M_S \rightarrow \infty$

$$\begin{aligned}\mathcal{T}r\left\{\ln\left[(-\partial_x^2 - M_S^2 - F(x))\delta(x-y)\right]\right\} &= \int d^4x \int \frac{d^4p}{(2\pi)^4} \ln\left(-(\partial_x + ip)^2 - M_S^2 - F(x)\right) \\ &= \int d^4x \int \frac{d^4p}{(2\pi)^4} \ln\left(p^2 - M_S^2 - 2ip_\mu \partial_x^\mu - \partial_x^2 - F(x)\right) \\ &= -\sum_{n=1}^{\infty} \frac{1}{n} \int d^4x \frac{d^4p}{(2\pi)^4} \left(\frac{2ip_\mu \partial_x^\mu + \partial_x^2 + F(x)}{p^2 - M_S^2}\right)^n + \text{const.} \\ &= \int d^4x \frac{d^4p}{(2\pi)^4} \left[\frac{F(x)}{p^2 - M_S^2} + \frac{(F(x))^2}{2(p^2 - M_S^2)^2} + \frac{F(x)\partial_x^2 F(x) + F(x)^3}{3(p^2 - M_S^2)^3} + \mathcal{O}(M_S^{-4})\right] + \text{const.},\end{aligned}\quad (\text{I.48})$$

where we used the following identity,

$$\ln(-\partial_x^2 - M_S^2 - F(x))\delta(x-y) = \ln(-\partial_x^2 - M_S^2 - F(x)) \int \frac{d^4p}{(2\pi)^4} e^{ip(x-y)} =$$

$$= \int \frac{d^4 p}{(2\pi)^4} e^{ip(x-y)} \ln(-(\partial_x + ip)^2 - M_S^2 - F(x)).$$

Written in a more compact way:

$$\begin{aligned} & \mathcal{T}r\{\ln [(-\partial_x^2 - M_S^2 - F(x)) \delta(x-y)]\} \\ &= \frac{-i}{16\pi^2} \int d^4 x \left[I_{01} F(x) + \frac{I_{02}}{2} F(x)^2 + \frac{I_{03}}{3} \left(F(x) \partial_x^2 F(x) + F(x)^3 \right) \right], \end{aligned} \quad (\text{I.49})$$

with the momentum integrals defined as,

$$\begin{aligned} I_{kl} g_{\mu_1 \dots \mu_{2k}} &= \frac{(2\pi\mu)^{4-D}}{i\pi^2} \int d^D p \frac{p_{\mu_1} \dots p_{\mu_{2k}}}{(p^2 - M_S^2)^l} \\ &= g_{\mu_1 \dots \mu_{2k}} \frac{(-1)^{(k+l)} \Gamma(l-k-\frac{D}{2})}{2^k \Gamma(l)} (4\pi\mu^2)^{\frac{4-D}{2}} M_S^{D+2k-2l}. \end{aligned} \quad (\text{I.50})$$

Substituting the integrals of Eq.(I.4.3) in the expression in Eq.(I.4.3), and this in \mathcal{L}_{eff} we find:

$$\begin{aligned} \mathcal{L}_{eff} &= \frac{1}{32\pi^2} \left[c_1(\varphi^\dagger \varphi) + c_2(\varphi^\dagger \varphi)^2 + c_3(\varphi^\dagger \varphi) \partial_x^2(\varphi^\dagger \varphi) + c_4(\varphi^\dagger \varphi)^3 \right] \\ &= \frac{1}{32\pi^2} \left[-\frac{\lambda_{12}^2}{3M_S^2} (\varphi^\dagger \varphi) \partial_x^2(\varphi^\dagger \varphi) - \frac{4\lambda_{12}^3}{3M_S^2} (\varphi^\dagger \varphi)^3 \right] + \mathcal{O}(M_S^{-4}). \end{aligned} \quad (\text{I.51})$$

In the last step we have used the Appelquist-Carazzone theorem of Ref. [59] to remove some of the operators whose Wilson coefficients are mass-suppressed. Observe that in this case, the scale of new physics is: $\Lambda^2 = M_S^2$, however if we were working with the mass eigenbasis instead of with the weak eigenbasis, the scale would have to be extracted from:

$$M_S^2 = \Lambda^2 \sum_{n=0} \xi_n \left(\frac{M_W^2}{\Lambda^2} \right)^n, \quad (\text{I.52})$$

where ξ_n is a parameter dependent on the model we are studying. We can see that the difference between both scales is sub-leading, however the question of the scale choice is a non-trivial one and should be carefully addressed before choosing the cut-off for the EFT calculation.

1.4.3.1 The Background Field Method

To quantize a gauge theory in the conventional approach it is necessary to choose a gauge and the corresponding Faddeev-Popov ghost Lagrangian. Then, when the gauge has been fixed, the Feynman rules can be read from the Lagrangian which is, by construction, not invariant any more under a gauge transformation of the fields and requires the Becchi-Rouet-Stora-Tyutin (BRST) global supersymmetry introduced in the mid-1970s in Ref. [60]. Consequently, quantities with no direct physical meaning, like Green's functions, are not gauge invariant. On the other hand, the gauge dependence consistently cancels when computing physical quantities like the S -matrix.

The Background Field Method introduced in Refs. [61–66] is a technique that was developed in the 80's in the context of quantum gravity, to preserve some degree of gauge invariance in every step of the calculation; for instance, in any gauge theory the gauge-fixing term can be chosen to involve only the quantum fields and not the classical ones.

Another benefit of working with the BFM at the one-loop level, comes from the fact that it is possible to take apart, for a generic field ϕ of the theory, a classical field $\hat{\phi}$ and its quantum

fluctuation ϕ . The so-called background field $\hat{\phi}$ can only appear on external lines, while the quantum field ϕ only as an internal line in loops. Then, considering the generating functional

$$Z[J] = \int \mathcal{D}\phi \exp i\{S[\phi] + J \cdot \phi\} \quad (\text{I.53})$$

of the Green's functions of the considered theory (for simplicity here, ϕ is a scalar field and we do not consider a gauge theory), it is possible to define the analogous functional

$$\tilde{Z}[J, \hat{\phi}] = \int \mathcal{D}\phi \exp i\{S[\hat{\phi} + \phi] + J \cdot \phi\}, \quad (\text{I.54})$$

obtained by the substitution $\phi \rightarrow \hat{\phi} + \phi$ in the action. Here, the background field $\hat{\phi}$ can be considered as an additional source. When defining the generating functional for the One Particle Irreducible (1PI) Green's functions of the theory

$$\begin{aligned} \Gamma[\bar{\phi}] &= W[J] - J \cdot \bar{\phi}, \\ W[J] &= -i \ln Z[J], \quad \bar{\phi} = \frac{\delta W}{\delta J}, \end{aligned} \quad (\text{I.55})$$

a similar functional can be defined in presence of the background field $\hat{\phi}$,

$$\begin{aligned} \tilde{\Gamma}[\tilde{\phi}, \hat{\phi}] &= \tilde{W}[J, \hat{\phi}] - J \cdot \tilde{\phi}, \\ \tilde{W}[J, \hat{\phi}] &= -i \ln \tilde{Z}[J, \hat{\phi}], \quad \tilde{\phi} = \frac{\delta \tilde{W}}{\delta J}. \end{aligned} \quad (\text{I.56})$$

Applying the previous definitions one recovers the main result of Ref. [63], that

$$\tilde{\Gamma}[0, \hat{\phi}] = \Gamma[\hat{\phi}]. \quad (\text{I.57})$$

This equation provides an alternative way to compute the generating functional of 1PI Green's functions Γ by using the background field functional $\tilde{\Gamma}[\tilde{\phi}, \hat{\phi}]$, i.e. the conventional functional in presence of the background field $\hat{\phi}$.

Functional derivatives of $\tilde{\Gamma}[\tilde{\phi}, \hat{\phi}]$ with respect to $\tilde{\phi}$ would generate 1PI Green's functions with external ϕ field, in presence of the background field $\hat{\phi}$. Since the latter does not appear in the functional integral, it cannot be present in the internal lines of the Green's functions. Moreover, since the functional $\tilde{\Gamma}[0, \hat{\phi}]$ in Eq. (I.57) does not depend on $\tilde{\phi}$, it cannot generate Green's functions with external ϕ lines, but only with external $\hat{\phi}$ lines. These considerations explain why $\hat{\phi}$ and ϕ are called “background” and “quantum” fields respectively, and why they can only appear respectively on external and loop lines.

For this reason, the BFM provides a good bookkeeping framework that can be used when integrating out heavy degrees of freedom from the path integral: when performing the path integral over the heavy fields (reported in Eq. (I.58)), we have a solid argument to state that only the Lagrangian terms that are bilinear in the integration variable Φ matter for the computation of the one-loop effective action. Then,

- couplings with exactly one quantum field are not relevant for one-loop diagrams (however, terms with one *heavy* quantum field are retained in the functional integration, in couplings with two quantum fields, of which only one is heavy),
- couplings with more than two quantum fields are only needed beyond one loop (analogously to the previous remark, in this case terms containing more than two heavy fields are retained, given that no more than two quantum fields are present).

After the application of the BFM, to work at the one-loop level, the action of Eq.(I.54) contains only linear and bilinear terms in the quantum heavy field. Linear terms can be shifted away by a redefinition of the heavy quantum field, and the functional integral over the heavy quantum field can be performed by means of Gaussian integration. This has been used, for example, in Refs. [57, 58] in the context of the SM.

I.4.3.2 The Covariant Derivative Expansion

A very similar, equivalent, approach was first proposed by Mary K. Gaillard in Ref. [67] and went relatively unadvertised until 2012 when an EFT review, Ref. [68], put it back on the scope. This approach is known as the Covariant Derivative Expansion (CDE). It relies on the same physical ideas as the BFM but focusses on the steps needed to derive $\Gamma[\hat{\phi}]$.

Given the action of a theory with a heavy field Φ and a lighter one ϕ : $S[\phi, \Phi]$ the effective action after integrating out the heavy field at the cut-off scale μ , can be written in terms of a path integral, just as we did in Eq. (I.46)

$$e^{iS_{eff}[\phi](\mu)} = \int \mathcal{D}\Phi e^{iS[\phi, \Phi]}. \quad (\text{I.58})$$

Up to this point, everything is similar to the example shown in Eqs. (I.45)-(I.51). The CDE approach introduces an elegant way of solving this path integral analytically in a gauge-invariant way.

To solve (I.58), we use the saddle point approximation, namely, we do a Taylor expansion of the exponent on the r.h.s. such that we can solve the path integral term by term of the power expansion, in particular we expand around the minimum of the action:

$$\begin{aligned} \frac{\delta S}{\delta \Phi} = 0 &\Rightarrow \Phi_c[\phi] \\ S[\phi, \Phi_c + \eta] &= S[\Phi_c] + \frac{1}{2} \frac{\delta^2 S}{\delta \Phi^2} \Big|_{\Phi_c} \eta^2 + \mathcal{O}(\eta^3) + \dots \end{aligned} \quad (\text{I.59})$$

this way, the path integral becomes easier to solve,

$$\begin{aligned} e^{iS_{eff}} &= \int \mathcal{D}\eta e^{iS[\phi, \Phi_c + \eta]} \\ &\approx e^{iS[\Phi_c]} \left[\det \left(- \frac{\delta^2 S}{\delta \Phi^2} \Big|_{\Phi_c} \right) \right]^{-1/2} \\ S_{\text{eff}} &\approx S[\Phi_c] + \frac{1}{2} \text{Tr} \log \left(- \frac{\delta^2 S}{\delta \Phi^2} \Big|_{\Phi_c} \right). \end{aligned} \quad (\text{I.60})$$

Eq. (I.60) can be applied to any UV action that we want to solve. If we want to find a more explicit expression, we observe that almost any Lagrangian can be cast in the following form,

$$\mathcal{L} = \underbrace{\Phi^\dagger B}_{B(\phi(x))} + B^\dagger \Phi + \Phi^\dagger (-D^2 - m^2 - \underbrace{U}_{U(\phi(x))}) \Phi + \mathcal{O}(\Phi^3, \Phi^4, \dots). \quad (\text{I.61})$$

Solving the equation of motion for Φ we find:

$$\Phi_c = \frac{B}{D^2 + m^2 + U} + \mathcal{O}(\Phi^2). \quad (\text{I.62})$$

In order to simplify this expression, we make an inverse mass expansion of Φ_c :

$$\Phi_c \approx \frac{1}{m^2} B + \frac{1}{m^2} (-D^2 - U) \frac{1}{m^2} B + \frac{1}{m^2} (-D^2 - U) \frac{1}{m^2} (-D^2 - U) \frac{1}{m^2} B + \dots \quad (\text{I.63})$$

The name CDE comes from the fact that we leave D^2 contracted rather than making it explicit and expanding in powers of $\left(\frac{\partial^2}{m^2}\right)$. Replacing Φ_C in (I.61), we find the effective Lagrangian at tree level:

$$\mathcal{L}_{\text{eff,tree}} = \underbrace{B^\dagger \frac{1}{m^2} B}_{\text{dim-6 operator}} + \underbrace{B^\dagger \frac{1}{m^2} (-D^2 - U) \frac{1}{m^2} B}_{\text{dim-8 operator}} + \text{higher dim. ops.} \quad (\text{I.64})$$

To find the one-loop part of the effective Lagrangian, we have to solve the last term in (I.60). The details about the calculation of the functional trace and log can be found in Ref. [68], as well as tables of “universal” results and many detailed examples. Repeating these examples would be an useful exercise for the reader interested in functional methods. Here, however, we simply focus on the physical content rather than on the algebra, and we will not repeat the derivations.

As discussed earlier, both the CDE and BFM methods rely on fixing the heavy fields while making the light ones dynamic. Looking at the diagrammatic interpretation of the method (see Fig. I.7) one can rapidly realize a flaw, namely the diagrams with heavy fields inside the loops are not being taken into account. It can be argued that the contribution of these diagrams to the Wilson coefficients of interest is generally small, however it is not advisable to use the previous equations without making sure of the size of the neglected contribution.

This problem was first pointed out in Ref. [69] and further discussed in Ref. [70]. Later, the authors of the original CDE paper proposed the following solution in Ref. [71]. Eq. (I.60) for the one-loop effective action,

$$S_{\text{eff}} \approx \underbrace{S[\Phi_C]}_{\text{tree-level}} + \underbrace{\frac{i}{2} \text{Tr} \log \left(-\frac{\delta^2 S}{\delta \Phi^2} \Big|_{\Phi_C} \right)}_{\text{one-loop}}, \quad (\text{I.65})$$

has to be corrected by adding a non-local term,

$$\Gamma[\phi] = S_{\text{eff}}[\phi] + \underbrace{\frac{i}{2} \log \det \left(\frac{-\delta^2 S}{\delta \phi^2} \right)}_{\text{non-local term}}, \quad (\text{I.66})$$

which accounts for the neglected terms. Unfortunately it is no longer possible to find a universal result since the non-local term depends on the tadpoles and self energies of the particular theory that we are studying. In that case, the remaining non-universal loop diagrams can be solved diagrammatically, as it was done for example in Ref. [70].

The connection with Fermi theory is now clear: the UV theory in this case is the electroweak sector of the SM, and the energy scale above which we will *cut* is related to the mass of the heavy particles, M_W . We can thus apply either the BFM or the CDE and integrate out the W bosons from our theory, shrinking the propagator to a point, and the full diagram becomes a vertex, as shown in Fig. I.6.

⁴This seems counter-intuitive, but there are many examples where an expansion in powers of $\frac{\partial^2}{m^2}$ is more useful, due to the x integration in $\int dx \mathcal{L}$

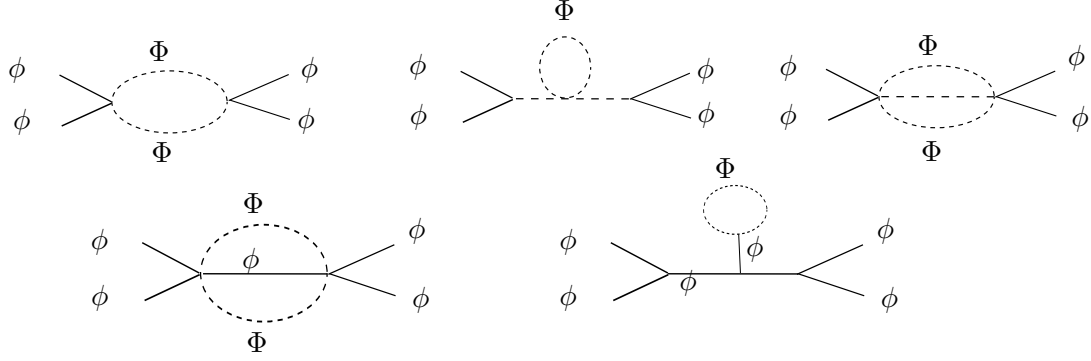


Fig. I.7: Diagrammatic interpretation of the BFM. Diagrams with mixed heavy and light fields, like the ones in the bottom row, are not taken into account by the *naive* CDE method.

I.4.3.3 Matching of the UV and SM scales

After deriving the effective Lagrangian, there is one more step necessary before we can make predictions. As we know from a general QFT, the masses and couplings are not constant, and their precise value depends on the scale we are looking at. We commonly say that these parameters *run* with the scale.

Therefore the value of the effective couplings that we extracted using the previous methods has to be evolved down to the scale of interest to us. As an illustration, in the singlet example of Eq. (I.51), the coefficients in front of the dim = 6 operators,

$$(\varphi^\dagger \varphi) \partial_x^2 (\varphi^\dagger \varphi), \quad (\varphi^\dagger \varphi)^3, \quad (\text{I.67})$$

at the scale $\Lambda^2 = M_S^2$ are given by

$$c_1(M_S) = \frac{1}{32\pi^2} \frac{-\lambda_{12}^2}{3},$$

$$c_2(M_S) = \frac{1}{32\pi^2} \frac{-4\lambda_{12}^3}{3},$$

respectively. In order to find these coefficients at the scale of our experiment (which might be M_W, m_b, m_H, \dots , depending on the process we are looking at) there are two possible approaches:

- The fastest and most commonly used approach relies on the Renormalisation Group (RG) flow equations, see for example Ref. [72]. At LO, one has

$$c_i(M_W) \neq c_i(\Lambda), \quad \Rightarrow \quad c_i(M_W) = c_i(\Lambda) - \sum_j \frac{1}{16\pi^2} \gamma_{ij} c_j(\Lambda) \log \frac{\Lambda}{M_W} \quad (\text{I.68})$$

where γ_{ij} is the anomalous dimension matrix. The full equation is:

$$\frac{dc_i(\mu)}{d\log\mu} = \sum_j \frac{1}{16\pi^2} \gamma_{ij} c_j.$$

- The other possible approach is more rigorous: we can perform the full renormalisation of the newly found effective Lagrangian, in Eq. (I.51), and the values of the coefficients at the new scale will be fixed at the point when we choose the renormalisation scheme and the set of input parameters. For the example of a heavy singlet, the full procedure was carried out in Ref. [70]. Further details on the renormalisation procedure will be given in Section I.4.6 in the context of the bottom-up approach.

After we have computed the values of $c_i(M_W)$ we can start to make predictions for physical processes with the effective theory. However, as pointed out in Ref. [73], the effective operator expansion is only slowly converging at best. The agreement between the SMEFT and a range of UV-complete models depends sensitively on the appropriate definition of the matching and can be systematically improved through an appropriate matching procedure at the one loop level; matching schemes based solely on leading logarithms are not useful for any kind of precision physics.

I.4.4 Fine points in EFT

It is important to note that the EFT that we are discussing here is the “continuum EFT” introduced by Georgi in Refs. [74, 75]. The main question is: how can an EFT be constructed without appealing to a cut-off that will prevent us from using dimensional regularisation? For top-down constructions, the initial momentum splitting of the fields in a Wilsonian EFT and the integration over the heavy modes, is replaced in a continuum EFT by the following steps,

- First, start with a dimensionally-regularised theory with Lagrangian density $\mathcal{L}(\phi, \Phi)$ where ϕ are the light fields and Φ the heavy ones.
- Then, evolve the theory to a lower scale using RG flow equations, Eq. (I.4.3.3).
- When below some scale, say M , the EFT is changed to a new one without the Φ -fields $\mathcal{L}(\phi) + \Delta\mathcal{L}(\phi)$ where $\Delta\mathcal{L}$ encodes a “matching correction” that includes any new non-renormalisable interactions that may be required. The matching condition is defined so that the physics of the light fields is the same in the two theories at the boundary M . At leading order this condition is trivial: it represents the continuity of the couplings at the matching scale. At NLO and beyond this is not the case any more.
- For explicit calculations, $\Delta\mathcal{L}$ is expanded in a complete set of local operators.

To summarise, in the construction of a Wilsonian EFT, the heavy fields are first integrated out of the underlying high-energy theory and the resulting Wilsonian effective action is then expanded in a series of local operator terms. The cutoff in a Wilsonian EFT plays a double role: first, it explicitly separates the low-energy physics from the high-energy physics; and second, it regulates divergent integrals in the calculation of observable quantities.

In the construction of a continuum EFT, the heavy fields initially remain in the underlying high-energy theory, which is first evolved down to the appropriate energy scale. The continuum EFT is then constructed by completely removing the heavy fields from the high-energy theory, as opposed to integrating them out; and this removal is compensated for by an appropriate matching calculation. For a detailed description see Ref. [76].

I.4.5 EFT Bottom-Up approach

If we think about the phenomenological application of EFTs, we can say that the top-down option generates the following chain: UV complete theory \rightarrow EFT (preferably at NLO) + Parton Shower \rightarrow data analysis \rightarrow experimental fit to Wilson coefficients. Whilst in the bottom-up approach instead the chain is: SM data analysis \rightarrow observable \rightarrow EFT at NLO fit to Wilson coefficients.

An EFT can be used also in those cases in which we do not integrate out explicitly the heavy degrees of freedom. Once we have a theory which describes quite well the physics on the scale which we explore, we can build up new interactions which would account for the small deviations. This requires the assumption that the “real” NP (i.e. new resonances), lie high above the currently available experimental scale. Note that this description is model independent - we do not make any a priori assumptions about the underlying UV theory. The SMEFT approach

| Field | ϕ | Ψ | $F_{\mu\nu}$ | \mathcal{D}_μ |
|-------|--------|---------------|--------------|-------------------|
| $[M]$ | 1 | $\frac{3}{2}$ | 2 | 1 |

Table I.5: The mass dimensions of the fields in Lagrangian.

| Field | SU(3) | SU(2) | U(1) |
|-----------|-------|-------|----------------|
| φ | 1 | 2 | $\frac{1}{2}$ |
| L_L | 1 | 2 | $-\frac{1}{2}$ |
| e_R | 1 | 1 | -1 |
| Q_L | 3 | 2 | $\frac{1}{6}$ |
| u_R | 3 | 1 | $\frac{2}{3}$ |
| d_R | 3 | 1 | $\frac{1}{3}$ |

Table I.6: Gauge representations for the SM. A singlet is denoted by 1, a doublet by 2 etc.

is therefore very different to studies of specific models such as supersymmetry or compositeness. Nevertheless, the two approaches are complementary and they can each benefit from the other. For reviews we refer to Refs. [47, 75, 77–92].

To consistently build the EFT operators, we start by taking all fields and derivatives which are present in the renormalisable theory and combine them in the gauge and Lorentz invariant way building the higher-dimension operators.

If we do so with the SM fields we would find that the only operator with dimension 5 which can be built is the neutrino Majorana mass term,

$$(\tilde{\varphi}^\dagger l_i)^T C (\tilde{\varphi}^\dagger l_j), \quad (\text{I.69})$$

which was first described by Weinberg in Ref. [93]. Since neutrinos cannot be directly observed at the LHC, this operator is mostly explored in neutrino experiments and is generally not included in the SMEFT description.

If we combine fields further we find out that there are many more operators arising at $\text{dim} = 6$. As a first example, there are the the four fermion interactions which we saw in the Fermi theory, see Table I.8. These four fermion interactions are nowadays used to study deviations from SM predictions in B meson decays, but can appear as well in many other SM processes.

Considering the whole particle content of the SM, there are many other operators that can be built at $\text{dim} = 6$. Let us first note that the square of the Higgs doublet, $\varphi^\dagger \varphi$, is both Lorentz and gauge invariant, as can be read from Table I.6. From Table I.5 we easily conclude that $\varphi^\dagger \varphi$ has mass dimension 2, and therefore, multiplying any of the SM terms by $\varphi^\dagger \varphi$ produces terms of dimension 6. This way, we can obtain the following terms (see Table I.7):

- Scalar interactions, $(\varphi^\dagger \varphi)^3$ (class φ^6 of Table I.7).
- Gauge boson kinetic terms multiplied by $\varphi^\dagger \varphi$ (class $X^2 \varphi^2$).
- Yukawa couplings multiplied by $\varphi^\dagger \varphi$ (class $\psi^2 \varphi^3$).

Since φ can be expanded around the constant VEV (v), these operators generally lead to modifications of the SM couplings. For example, in the SM, the cubic Higgs coupling is fully

| X^3 | | φ^6 and $\varphi^4 D^2$ | | $\psi^2 \varphi^3$ | |
|--------------------------|--|---------------------------------|---|-----------------------|---|
| Q_G | $f^{ABC} G_\mu^{A\nu} G_\nu^{B\rho} G_\rho^{C\mu}$ | Q_φ | $(\varphi^\dagger \varphi)^3$ | $Q_{e\varphi}$ | $(\varphi^\dagger \varphi)(\bar{l}_p e_r \varphi)$ |
| $Q_{\tilde{G}}$ | $f^{ABC} \tilde{G}_\mu^{A\nu} G_\nu^{B\rho} G_\rho^{C\mu}$ | $Q_{\varphi\Box}$ | $(\varphi^\dagger \varphi)\Box(\varphi^\dagger \varphi)$ | $Q_{u\varphi}$ | $(\varphi^\dagger \varphi)(\bar{q}_p u_r \tilde{\varphi})$ |
| Q_W | $\varepsilon^{IJK} W_\mu^{I\nu} W_\nu^{J\rho} W_\rho^{K\mu}$ | $Q_{\varphi D}$ | $(\varphi^\dagger D^\mu \varphi)^* (\varphi^\dagger D_\mu \varphi)$ | $Q_{d\varphi}$ | $(\varphi^\dagger \varphi)(\bar{q}_p d_r \varphi)$ |
| $Q_{\tilde{W}}$ | $\varepsilon^{IJK} \tilde{W}_\mu^{I\nu} W_\nu^{J\rho} W_\rho^{K\mu}$ | | | | |
| $X^2 \varphi^2$ | | $\psi^2 X \varphi$ | | $\psi^2 \varphi^2 D$ | |
| $Q_{\varphi G}$ | $\varphi^\dagger \varphi G_{\mu\nu}^A G^{A\mu\nu}$ | Q_{eW} | $(\bar{l}_p \sigma^{\mu\nu} e_r) \tau^I \varphi W_{\mu\nu}^I$ | $Q_{\varphi l}^{(1)}$ | $(\varphi^\dagger i \overleftrightarrow{D}_\mu \varphi)(\bar{l}_p \gamma^\mu l_r)$ |
| $Q_{\varphi \tilde{G}}$ | $\varphi^\dagger \varphi \tilde{G}_{\mu\nu}^A G^{A\mu\nu}$ | Q_{eB} | $(\bar{l}_p \sigma^{\mu\nu} e_r) \varphi B_{\mu\nu}$ | $Q_{\varphi l}^{(3)}$ | $(\varphi^\dagger i \overleftrightarrow{D}_\mu^I \varphi)(\bar{l}_p \tau^I \gamma^\mu l_r)$ |
| $Q_{\varphi W}$ | $\varphi^\dagger \varphi W_{\mu\nu}^I W^{I\mu\nu}$ | Q_{uG} | $(\bar{q}_p \sigma^{\mu\nu} T^A u_r) \tilde{\varphi} G_{\mu\nu}^A$ | $Q_{\varphi e}$ | $(\varphi^\dagger i \overleftrightarrow{D}_\mu \varphi)(\bar{e}_p \gamma^\mu e_r)$ |
| $Q_{\varphi \tilde{W}}$ | $\varphi^\dagger \varphi \tilde{W}_{\mu\nu}^I W^{I\mu\nu}$ | Q_{uW} | $(\bar{q}_p \sigma^{\mu\nu} u_r) \tau^I \tilde{\varphi} W_{\mu\nu}^I$ | $Q_{\varphi q}^{(1)}$ | $(\varphi^\dagger i \overleftrightarrow{D}_\mu \varphi)(\bar{q}_p \gamma^\mu q_r)$ |
| $Q_{\varphi B}$ | $\varphi^\dagger \varphi B_{\mu\nu} B^{\mu\nu}$ | Q_{uB} | $(\bar{q}_p \sigma^{\mu\nu} u_r) \tilde{\varphi} B_{\mu\nu}$ | $Q_{\varphi q}^{(3)}$ | $(\varphi^\dagger i \overleftrightarrow{D}_\mu^I \varphi)(\bar{q}_p \tau^I \gamma^\mu q_r)$ |
| $Q_{\varphi \tilde{B}}$ | $\varphi^\dagger \varphi \tilde{B}_{\mu\nu} B^{\mu\nu}$ | Q_{dG} | $(\bar{q}_p \sigma^{\mu\nu} T^A d_r) \varphi G_{\mu\nu}^A$ | $Q_{\varphi u}$ | $(\varphi^\dagger i \overleftrightarrow{D}_\mu \varphi)(\bar{u}_p \gamma^\mu u_r)$ |
| $Q_{\varphi WB}$ | $\varphi^\dagger \tau^I \varphi W_{\mu\nu}^I B^{\mu\nu}$ | Q_{dW} | $(\bar{q}_p \sigma^{\mu\nu} d_r) \tau^I \varphi W_{\mu\nu}^I$ | $Q_{\varphi d}$ | $(\varphi^\dagger i \overleftrightarrow{D}_\mu \varphi)(\bar{d}_p \gamma^\mu d_r)$ |
| $Q_{\varphi \tilde{W}B}$ | $\varphi^\dagger \tau^I \varphi \tilde{W}_{\mu\nu}^I B^{\mu\nu}$ | Q_{dB} | $(\bar{q}_p \sigma^{\mu\nu} d_r) \varphi B_{\mu\nu}$ | $Q_{\varphi ud}$ | $i(\tilde{\varphi}^\dagger D_\mu \varphi)(\bar{u}_p \gamma^\mu d_r)$ |

Table I.7: Bosonic operators of the Warsaw basis. Table from Ref. [94].

determined by the λ - quartic coupling constant and VEV, while the $(\varphi^\dagger \varphi)^3$ operator changes this relation. Similarly the SM Yukawa couplings depend only on the particle mass and VEV, while using operators of the form $v^2 \bar{l} \varphi e$ modifies this dependence.

There are other classes of operators which are not simply multiplications of the SM ones. For instance:

- The cubic field strength operators (class X^3 in Table I.7), which need to be multiplied by the appropriate structure constants ($SU(3)$ or $SU(2)$) in order to be gauge invariant.
- The magnetic dipole operators, which combine the Higgs doublet, fermions and gauge fields in a way not present in the SM. This is the class $\psi^2 X \phi$ in Table I.7.

Looking at Table I.5 and Table I.6, we can think of other classes of $\dim = 6$ operators which we can write down, e.g. $D^4 \varphi^2$ or $X D^2 \varphi^2$. However, these can be reduced into the other classes of operators mentioned above using the Equations of Motion (EoM) and Fierz identities. Why and how the other classes of operators can be reduced to the presented minimal basis (i.e. a complete and non-redundant set of higher-dimensional operators) is described in Ref. [94].

The general form of the SMEFT Lagrangian reads:

$$\mathcal{L} = \mathcal{L}_{SM} + \frac{a_5}{\Lambda} \mathcal{O}_5 + \sum_i \frac{a_6^{(i)}}{\Lambda^2} \mathcal{O}_6^{(i)} + O(\Lambda^{-3}) \quad (\text{I.70})$$

where the dimensionless coefficients a_i are the Wilson coefficients of the higher dimensional operators, which are suppressed by powers of the mass scale, Λ , such that each term in the Lagrangian has a mass dimension equal to 4. As we can recall from the example from the previous section, Λ plays the analogous role as the W boson mass in the Fermi theory. Indeed, the meaning of the Λ is the common scale above which we expose the heavy degrees of freedom of the full theory. Since we do not make any assumption about the NP (other than it is well separable from SM, and obeys Lorentz and gauge invariance), we do not automatically identify it with the onset of new resonances.

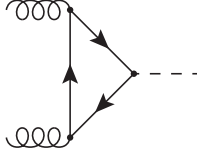
| $(\bar{L}L)(\bar{L}L)$ | | $(\bar{R}R)(\bar{R}R)$ | | $(\bar{L}L)(\bar{R}R)$ | |
|---|---|------------------------|---|------------------------|--|
| Q_{ll} | $(\bar{l}_p \gamma_\mu l_r)(\bar{l}_s \gamma^\mu l_t)$ | Q_{ee} | $(\bar{e}_p \gamma_\mu e_r)(\bar{e}_s \gamma^\mu e_t)$ | Q_{te} | $(\bar{l}_p \gamma_\mu l_r)(\bar{e}_s \gamma^\mu e_t)$ |
| $Q_{qq}^{(1)}$ | $(\bar{q}_p \gamma_\mu q_r)(\bar{q}_s \gamma^\mu q_t)$ | Q_{uu} | $(\bar{u}_p \gamma_\mu u_r)(\bar{u}_s \gamma^\mu u_t)$ | Q_{tu} | $(\bar{l}_p \gamma_\mu l_r)(\bar{u}_s \gamma^\mu u_t)$ |
| $Q_{qq}^{(3)}$ | $(\bar{q}_p \gamma_\mu \tau^I q_r)(\bar{q}_s \gamma^\mu \tau^I q_t)$ | Q_{dd} | $(\bar{d}_p \gamma_\mu d_r)(\bar{d}_s \gamma^\mu d_t)$ | Q_{td} | $(\bar{l}_p \gamma_\mu l_r)(\bar{d}_s \gamma^\mu d_t)$ |
| $Q_{lq}^{(1)}$ | $(\bar{l}_p \gamma_\mu l_r)(\bar{q}_s \gamma^\mu q_t)$ | Q_{eu} | $(\bar{e}_p \gamma_\mu e_r)(\bar{u}_s \gamma^\mu u_t)$ | Q_{qe} | $(\bar{q}_p \gamma_\mu q_r)(\bar{e}_s \gamma^\mu e_t)$ |
| $Q_{lq}^{(3)}$ | $(\bar{l}_p \gamma_\mu \tau^I l_r)(\bar{q}_s \gamma^\mu \tau^I q_t)$ | Q_{ed} | $(\bar{e}_p \gamma_\mu e_r)(\bar{d}_s \gamma^\mu d_t)$ | $Q_{qu}^{(1)}$ | $(\bar{q}_p \gamma_\mu q_r)(\bar{u}_s \gamma^\mu u_t)$ |
| | | $Q_{ud}^{(1)}$ | $(\bar{u}_p \gamma_\mu u_r)(\bar{d}_s \gamma^\mu d_t)$ | $Q_{qu}^{(8)}$ | $(\bar{q}_p \gamma_\mu T^A q_r)(\bar{u}_s \gamma^\mu T^A u_t)$ |
| | | $Q_{ud}^{(8)}$ | $(\bar{u}_p \gamma_\mu T^A u_r)(\bar{d}_s \gamma^\mu T^A d_t)$ | $Q_{qd}^{(1)}$ | $(\bar{q}_p \gamma_\mu q_r)(\bar{d}_s \gamma^\mu d_t)$ |
| | | | | $Q_{qd}^{(8)}$ | $(\bar{q}_p \gamma_\mu T^A q_r)(\bar{d}_s \gamma^\mu T^A d_t)$ |
| $(\bar{L}R)(\bar{R}L)$ and $(\bar{L}R)(\bar{L}R)$ | | B -violating | | | |
| Q_{ledq} | $(\bar{l}_p^j e_r)(\bar{d}_s^k q_t^j)$ | Q_{duq} | $\varepsilon^{\alpha\beta\gamma} \varepsilon_{ijk} [(d_p^\alpha)^T C u_r^\beta] [(q_s^j)^T C l_t^k]$ | | |
| $Q_{quqd}^{(1)}$ | $(\bar{q}_p^j u_r) \varepsilon_{ijk} (\bar{q}_s^k d_t)$ | Q_{ququ} | $\varepsilon^{\alpha\beta\gamma} \varepsilon_{ijk} [(q_p^{\alpha j})^T C q_r^{\beta k}] [(u_s^i)^T C e_t]$ | | |
| $Q_{quqd}^{(8)}$ | $(\bar{q}_p^j T^A u_r) \varepsilon_{ijk} (\bar{q}_s^k T^A d_t)$ | Q_{qqq} | $\varepsilon^{\alpha\beta\gamma} \varepsilon_{jmn} \varepsilon_{km} [(q_p^{\alpha j})^T C q_r^{\beta k}] [(q_s^m)^T C l_t^n]$ | | |
| $Q_{lequ}^{(1)}$ | $(\bar{l}_p^j e_r) \varepsilon_{ijk} (\bar{q}_s^k u_t)$ | Q_{duu} | $\varepsilon^{\alpha\beta\gamma} [(d_p^\alpha)^T C u_r^\beta] [(u_s^i)^T C e_t]$ | | |
| $Q_{lequ}^{(3)}$ | $(\bar{l}_p^j \sigma_{\mu\nu} e_r) \varepsilon_{ijk} (\bar{q}_s^k \sigma^{\mu\nu} u_t)$ | | | | |

Table I.8: Fermionic operators of the Warsaw basis. Table from Ref. [94].

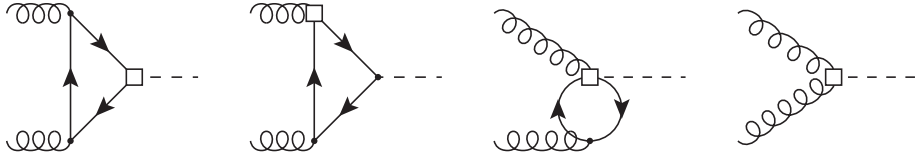
It is also important to note that there is not a one-to-one correspondence between coefficients and measurements, since one operator can contribute to many observables and one observable may depend on more than one operator.

Examples: SMEFT at LO

Let us show this with the example of gluon fusion Higgs production at LHC. At LO in the SM, there is just one diagram that contributes to this process:

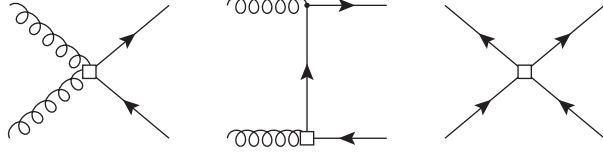


In the SMEFT, there are contributions from three different dimension 6 operators:

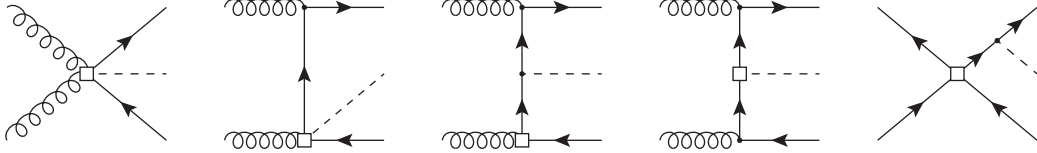


$$\begin{aligned}
- \frac{c_1}{\Lambda^2} \mathcal{O}_1 &\sim \frac{\alpha_s}{\pi v} a_g H G_{\mu\nu}^a G^{\mu\nu a} \quad \rightarrow \text{Higgs-gluon-gluon coupling} \\
- \frac{c_2}{\Lambda^2} \mathcal{O}_2 &\sim \frac{m_t}{v} a_t t\bar{t}H \quad \rightarrow \text{Higgs-}t\bar{t} \\
- \frac{c_4}{\Lambda^2} \mathcal{O}_4 &\sim \frac{g_s m_t}{2v} a_{tg} (v + H) G_{\mu\nu}^a (\bar{t}_L \sigma^{\mu\nu} T^a t_R + \text{h.c.}) \quad \rightarrow \text{chromomagnetic operator}
\end{aligned}$$

Another example is top pair production, where there is a contribution from the chromomagnetic operator $\bar{Q}_L H \sigma^{\mu\nu} T^a u_R G_{\mu\nu}^a + h.c.$:



or $t\bar{t}H$ associated production:



Observe that we have always inserted precisely one EFT operator per diagram. The motivation for this will be discussed later.

I.4.6 SMEFT at NLO

SMEFT is an active area of research that is moving towards NLO predictions. NLO in the SMEFT is important for two reasons: from a phenomenological point of view NLO is important for capturing potentially large QCD K-factors in total rates, gaining greater sensitivity. In this way we can verify stability of differential information beyond leading order with consistent estimates of the scale uncertainty. This programme has already been started with Refs. [95,96].

Thus, interpreting the data using theoretical results developed beyond LO can often be crucial for the SMEFT. NLO calculations (not only NLO QCD) should be used if they are available, as argued in Ref. [97]. NLO calculations help characterize (and reduce) theoretical uncertainties and allow the consistent incorporation of precise measurements in the SMEFT. NLO interpretations of the data will be critical in the event that deviations from the SM emerge over the course of LHC operations.

From a more formal point of view we can say that, although different in the UV, the SM and SMEFT are both examples of a QFT; therefore, NLO SMEFT requires renormalisation. Details of renormalisation in the SMEFT can be found in Refs. [97,98]. However, we stress that consistent removal of UV poles in SMEFT, i.e. closure of SMEFT under renormalisation, requires starting from a basis of higher dimensional operators, that respects the full gauge symmetries. Inevitably, the renormalisation scheme will be a mixed one, on-shell for the SM parameters and $\overline{\text{MS}}$ for the Wilson coefficients.

One question often raised concerns the “optimal” parametrization of the $\text{dim} > 4$ basis; once again, all sets of gauge invariant, dimension $d > 4$ operators, none of which is redundant, form a basis and all bases are equivalent. For a formal definition of redundancy see Sect. 3 of Ref. [99].

I.4.6.1 Renormalisation abridged

It is worth discussing how the problems described in Section I.2.3. in particular in Eq. (I.20), are solved in the SMEFT. Consider again the process $H \rightarrow \bar{b}b$ at NLO in SMEFT. Ultraviolet poles in self-energies and transitions, e.g. the H self-energy etc, are eliminated by extending the usual definition of counterterms for fields and SM parameters,

$$\delta Z_i = \frac{1}{\epsilon} \frac{g^2}{16\pi^2} \left[\delta Z_i^{(4)} + g_6 \delta Z_i^{(6)} \right], \quad (\text{I.71})$$

more details can be found in Ref. [98]. Here we use the $\overline{\text{MS}}$ prescription where $\bar{\epsilon}^{-1} = 2/(4 - D) - \gamma - \ln \pi - \ln \mu_R^2$, γ is the Euler-Mascheroni constant, g is the $SU(2)$ coupling constant and μ_R is the renormalisation scale. Furthermore, $g_{4+2k} = 1/(\sqrt{2}G_F\Lambda^2)^k$, where G_F is the Fermi coupling constant. Note that we have made no attempt to go beyond $\text{dim} = 6$. Extension of the basis for $\text{dim} > 6$ has been considered in Refs. [100–103].

First we define combinations of Wilson coefficients as follows:

$$\begin{aligned} a_{ZZ} &= s_W^2 a_{\phi B} + c_W^2 a_{\phi W} - s_W c_W a_{WB}, \\ a_{AA} &= c_W^2 a_{\phi B} + s_W^2 a_{\phi W} + s_W c_W a_{\phi B}, \\ a_{AZ} &= 2c_W s_W (a_{\phi W} - a_{\phi B}) + (2c_W^2 - 1) a_{\phi WB}. \end{aligned} \quad (\text{I.72})$$

We present the result for the renormalisation of the Higgs mass, in the limit where only m_t is kept finite (5-flavour scheme). The SM counterterm is simple,

$$\delta Z_{m_H}^{(4)} = \frac{3}{2} \frac{M_W^2}{m_H^2} \frac{1 + 2c_\theta^4}{c_\theta^4} - \frac{3}{2} \frac{4m_t^4 - m_H^2 m_t^2 - m_H^4}{M_W^2 m_H^2} - \frac{1}{2} \frac{1 + 2c_\theta^2}{c_\theta^2}, \quad (\text{I.73})$$

where $c_\theta = M_W/M_Z$. For $\text{dim} = 6$ there are more terms and we write

$$\delta Z_{m_H}^{(6)} = \sum_{i \in A} C_i a_i, \quad (\text{I.74})$$

where $\{A\} = \{AA, ZZ, AZ, \phi D, \phi \square, \phi, t\phi\}$. The result is as follows:

$$\begin{aligned} C_{AA} &= -\frac{9 - 8s_\theta^2}{c_\theta^2} s_\theta^2 \\ &\quad - 3 \frac{4m_t^4 - m_H^2 m_t^2 - m_H^4}{M_W^2 m_H^2} s_\theta^2 + 3 \frac{M_W^2}{m_H^2} \frac{1 + 10c_\theta^4}{c_\theta^4} s_\theta^2, \\ C_{ZZ} &= -\frac{3 + c_\theta^2 + 8c_\theta^4}{c_\theta^2} \\ &\quad - 3 \frac{4m_t^4 - m_H^2 m_t^2 - m_H^4}{M_W^2 m_H^2} c_\theta^2 + 3 \frac{M_W^2}{m_H^2} \frac{4 + c_\theta^2 + 10c_\theta^6}{c_\theta^4}, \\ C_{AZ} &= -3 \frac{4m_t^4 - m_H^2 m_t^2 - m_H^4}{M_W^2 m_H^2} c_\theta s_\theta \\ &\quad + 3 \frac{s_\theta}{c_\theta} \frac{M_W^2}{m_H^2} \frac{1 + 10c_\theta^4}{c_\theta^2} - \frac{s_\theta}{c_\theta} (1 + 8c_\theta^2), \\ C_{\phi D} &= -\frac{1}{8} \frac{5 - 4c_\theta^2}{c_\theta^2} \\ &\quad + \frac{3}{8} \frac{8m_t^4 - 2m_H^2 m_t^2 - 7m_H^4}{M_W^2 m_H^2} + \frac{3}{4} \frac{M_W^2}{m_H^2} \frac{3 - 2c_\theta^4}{c_\theta^4}, \\ C_{\phi \square} &= -\frac{1 + 2c_\theta^2}{c_\theta^2} \\ &\quad - \frac{12m_t^4 - 3m_H^2 m_t^2 - 11m_H^4}{M_W^2 m_H^2} + 3 \frac{M_W^2}{m_H^2} \frac{1 + 2c_\theta^4}{c_\theta^4}, \end{aligned}$$

$$\begin{aligned}
C_\phi &= -33 - 3 \frac{M_W^2}{m_H^2} \frac{1 + 2c_\theta^2}{c_\theta^2}, \\
C_{t\phi} &= -3 \frac{8m_t^2 - m_H^2}{M_W^2 m_H^2} m_t^2.
\end{aligned}
\tag{I.75}$$

This example is enough to show the complexity of renormalisation in the SMEFT. In fact, this is only the first step of the renormalisation procedure since M_W, m_H and m_t are the renormalized masses but we still need a new set of lengthy equations (not reported here) of the form $m_H = m_H(\text{IPS})$ etc, where IPS stands for the input parameter set, in order to connect these quantities with experimentally measured ones and so, complete the finite renormalisation procedure.

Further, UV poles in Green's functions with three or more legs contain residual $\text{dim} = 6$ divergences that can only be removed by introducing a mixing of Wilson coefficients,

$$a_i = \sum_j Z_{ij} a_j^{\text{ren}}, \quad Z_{ij} = \delta_{ij} + \frac{1}{\epsilon} \frac{g^2}{16\pi^2} \delta Z_{ij}.
\tag{I.76}$$

For $H \rightarrow \bar{b}b$ we will have non-zero entries when $a_{b\varphi}$ mixes with the other 25 Wilson coefficients (without neglecting light quark masses) introduced in Table I.7 and in Table I.8. For instance, the mixing of $a_{b\varphi}$ with $a_{t\varphi}$ is given by

$$\frac{3}{4} \frac{m_t^2}{M_W^2} - \frac{3}{2} \sum_{i=u,c} \frac{m_i^2}{M_W^2}.
\tag{I.77}$$

It is worth noting again that the renormalisation of Wilson coefficients is performed in the $\overline{\text{MS}}$ -scheme, i.e. giving a residual dependence on the renormalisation scale.

Operator mixings are important: mixing means that in general the Wilson coefficients at low scale are related. One immediate consequence is that assumptions about some coefficients being zero at low scales are in general not valid. A global point of view is required and contributions from individual couplings may not make sense and only their sum is meaningful. Note also that operator mixing is not symmetric. A simplified example is as follows: consider the sub-set $\{a_{t\phi}, a_{tg}\}$. Starting with $a_{tg} = 1$ and $a_{t\phi} = 0$ at 1 TeV one obtains $a_{tg} = 0.98$ and $a_{t\phi} = 0.45$ at m_t , see Ref. [95].

The cancellation of UV divergences from all the $\text{dim} = 6$ operators in the Warsaw basis gives a highly non-trivial check on the calculation. The logarithmic corrections could have been deduced from the RG analysis. However, the calculation of the full NLO calculation identifies non-logarithmic terms which would be otherwise missed and which are not always negligible.

We can summarise the situation as follows: NLO is the first order where a non-trivial SMEFT structure becomes manifest. A nice example of SMEFT scale dependence can be found in Ref. [95]. Another example can be found in Ref. [104] where it is shown that SMEFT parameters contributing to LEP data are formally unbounded when the accuracy of loop corrections is reached. In other words, the number of SMEFT parameters contributing at one-loop is larger than the number of available measurements.

The size of these loop effects is generically a correction of the order of a few percent compared to leading effects in the SMEFT, but even so, multiple large numerical coefficients have been found at this order. Furthermore, in Ref. [11] it has been shown that there are contributions from $\text{dim} = 6$ operators, which alter the gbb vertex and introduce sizeable corrections to the hbb vertex which are unrelated to the SM corrections and cannot be anticipated through a renormalisation-group analysis.

We will skip here all technical details related to the treatment of IR/collinear divergences necessary for computing $H \rightarrow \bar{b}b\gamma(g)$ in the SMEFT. Once a finite S -matrix has been obtained we can start making approximations, LO SMEFT, NLO SMEFT in the PTG scenario⁵ and the full NLO SMEFT. Note that the LO SMEFT involves the following Wilson coefficients:

$$a_{\varphi W}, \quad a_{\varphi D}, \quad a_{\varphi \square}, \quad a_{b\varphi}, \quad (\text{I.78})$$

but only the combination

$$a_{\varphi W} - \frac{1}{4}a_{\varphi D} + a_{\varphi \square} - a_{b\varphi} \quad (\text{I.79})$$

appears when computing observables. In the NLO SMEFT additional Wilson coefficients will be present, i.e. we will have more “generalized” kappas and more sub-amplitudes, and some of them will not factorize onto the SM LO/NLO amplitudes.

The renormalisation procedure continues until all UV poles have been eliminated. Therefore, we will have the following scheme:

- Compute the (on-shell) decay $h(P) \rightarrow A_\mu(p_1) A_\nu(p_2)$; the amplitude, containing only one Lorentz structure, is made UV finite by mixing a_{AA} with a_{AA}, a_{ZZ}, a_{AZ} and a_{QW} .
- Compute the (on-shell) decay $h(P) \rightarrow A_\mu(p_1) Z_\nu(p_2)$; the amplitude, containing only one Lorentz structure, is made UV finite by mixing a_{AZ} with a_{AA}, a_{ZZ}, a_{AZ} and a_{QW} .
- Compute the (on-shell) decay $h(P) \rightarrow Z_\mu(p_1) Z_\nu(p_2)$. The amplitude contains a part proportional to $g^{\mu\nu}$ (\mathcal{D}) and a part proportional to $p_2^\mu p_1^\nu$ (\mathcal{P}). Mixing of a_{ZZ} with other Wilson coefficients makes \mathcal{P} UV finite, while the mixing of $a_{\varphi \square}$ makes \mathcal{D} UV finite.
- Continue until there are no Wilson coefficients left free, so that UV finiteness follows from gauge cancellations, which follow from having selected a “basis”.

I.4.7 Predictions using the Dimension 6 Lagrangian

I.4.7.1 Amplitudes in SMEFT

Any amplitude for $1 \rightarrow 2$ processes, in the SMEFT, can be written in the following way, as proposed in Ref. [98]:

$$\mathcal{A} = \sum_{n=N}^{\infty} g^n \mathcal{A}_n^{(4)} + \sum_{n=N_6}^{\infty} \sum_{\ell=0}^n \sum_{k=\ell}^{\infty} g^n g_{4+2k}^\ell \mathcal{A}_{n\ell k}^{(4+2k)}, \quad g_{4+2k} = \frac{1}{(\sqrt{2}G_F\Lambda^2)^k}, \quad (\text{I.80})$$

where g is the $SU(2)$ coupling constant, and $g_{4+2k} = g_6^k$ is the new coupling constant. Λ is the scale of new physics. N is the number of vertices at leading order (i.e. 1 for $H \rightarrow VV$, 3 for $H \rightarrow \gamma\gamma$ etc.), and N_6 is 1 for tree initiated processes and $N - 2$ for loop initiated ones.

As we can see from Eq. (I.80), there is more than one expansion parameter for the amplitude, and this is a key fact to consider when doing EFT predictions. Namely, the power counting for the perturbative expansion grows simultaneously in two directions: we can go to higher loops, like in the SM perturbation theory, or we can go to higher orders in the $1/\Lambda$ expansion. Because both the former and the latter corrections depend on the size of Λ it is a priori not possible to determine which are more relevant, as sketched in Fig. I.8.

Even when we consider going to higher orders in perturbation theory, but restricting ourselves to dimension 6, there is the question of how many operator insertions should we include at each level. For example: if a tree level diagram with one $\text{dim} = 6$ operator is “LO

⁵For a definition of potentially-tree-generated (PTG) operators see Ref. [99]

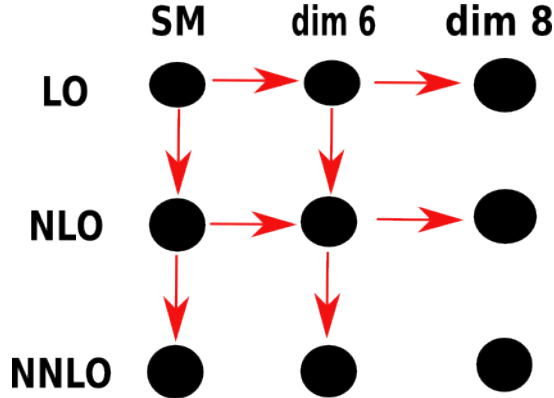


Fig. I.8: The power counting in perturbative SMEFT grows in two directions: higher loops, and higher dimensional operators.

EFT” and a one-loop diagram with one $\text{dim} = 6$ operator and one SM operator is “NLO EFT”, where do we put a diagram with tree topology but two $\text{dim} = 6$ operators?.

Traditionally, the community works with only one $\text{dim} = 6$ operator per diagram, both at tree and loop level, since each of these vertices is suppressed by two powers of the cut-off scale ($1/\Lambda^2$), which we consider to be *big enough*. However this raises the question of which terms shall we keep or discard when squaring the amplitude (terms with only one operator insertion squared will become sizeable to the interference term of those that we just neglected with the SM, i.e. of order $1/\Lambda^4$). This last fact will be discussed thoroughly in the next section.

Moreover, in the SM, when a particular process is calculated, a common practice is that a theoretical error is assigned. It can be subtle to assign such an error if we do not have an estimate for the missing higher order perturbative terms in the SM, and this part of the calculation is often overlooked, since there are allegedly enough hints perturbative expansions are legit. However, the need to include theoretical errors when perturbatively expanding the SMEFT is tied to the fact that different truncations of such expansions can be constructed, and to the fact that no assumption is done on the size of the Wilson coefficients of the UV theory nor the scale Λ , and it becomes even more necessary than in the SM case.

In particular, suppose that at some point in the future, we observe some deviation from the SM. Then, if the experimental precision allows, we could be able to test one-loop corrections and/or $\text{dim} = 8$ effects. If, on the other hand, no deviation from the SM is observed and limits on the $\text{dim} = 6$ coefficients are set through a LO procedure, we think that one-loop effects can be used to express a rough estimate of the corresponding MHOU (SMEFT truncation).

To be more precise, the higher order corrections in SMEFT are normally classified as follows:

- $gg_6 \mathcal{A}_{111}^{(6)}$ defines LO SMEFT
- $g^3 g_6 \mathcal{A}_{311}^{(6)}$ defines NLO SMEFT, or the Missing Higher Orders Uncertainty (MHOU) for LO EFT. g_6 stands for a single $\text{dim} = 6$ operator insertion, and it is therefore known as *linear EFT term*.
- $gg_8 \mathcal{A}_{112}^{(8)}, g^3 g_6^2 \mathcal{A}_{321}^{(6)}$ defines the MHOU for NLO SMEFT. g_6^2 stands for 2 $\text{dim} = 6$ operator insertions, and it is called *quadratic EFT term*.

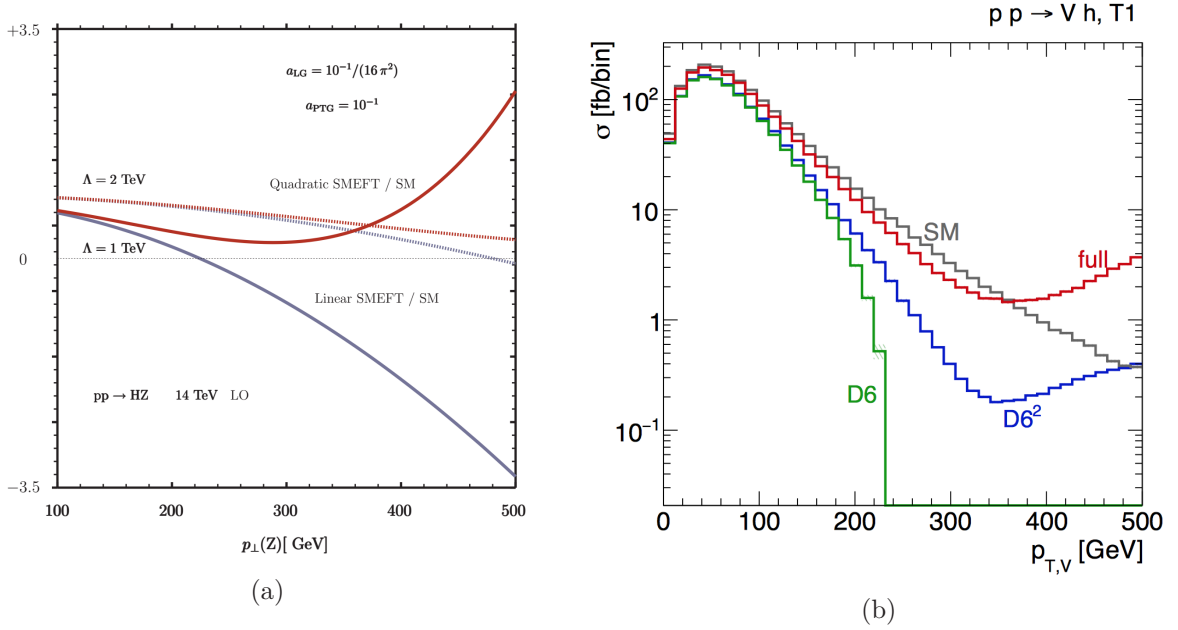


Fig. I.9: The transverse momentum distribution of the vector boson in Vh production. In Fig. I.9a, different ratios of SMEFT and SM cross sections are depicted, the blue lines represent cross sections where only the linear EFT terms are considered, while the red lines include also quadratic contributions. Solid and dashed functions represent two different choices for the Λ scale. In Fig. I.9b, we see a similar prediction, obtained by means of the top-down approach, where the effective Lagrangian for a UV vector triplet model is studied. This figure is taken from Ref. [105] with permission from the authors.

Written in a more schematic way we have the following situation:

$$\begin{aligned}
 |\mathcal{A}|^2 &= |\mathcal{A}_{SM} + \mathcal{A}_{\text{dim6}} + \mathcal{A}_{\text{dim8}} + \dots|^2 = \\
 &= |\mathcal{A}_{SM}|^2 + \underbrace{|\mathcal{A}_{SM} \times \mathcal{A}^{(6)}|}_{\text{“linear EFT”}} + \underbrace{|\mathcal{A}^{(6)}|^2}_{\text{“quadratic EFT”}} + \underbrace{|\mathcal{A}_{SM} \times \mathcal{A}^{(8)}|}_{\text{not available (th.uncertainty)}} + \dots \quad (\text{I.81})
 \end{aligned}$$

I.4.7.2 To square or not to square?

In order to make predictions with the effective Lagrangian, it is necessary to calculate amplitudes and cross sections. Amplitudes in SMEFT can generically be expressed as in Eq. (I.80). As we discussed previously, the square term $|\mathcal{A}_{\text{dim6}}|^2$ is of the order of $1/\Lambda^4$, just as the interference term of $\text{dim} = 8$, which is usually unavailable. For this reason, it can be argued that it is inconsistent to include just part of the $1/\Lambda^4$ terms. However, it is interesting to analyse the impact of the inclusion of the squared term in the differential observables in Fig. I.9.

In the following, we will refer as “linear SMEFT” to the case where only the interference term is considered, and we will refer to “quadratic SMEFT” in the case where $|\mathcal{A}_{\text{dim6}}|^2$ is also included. In Fig. I.9a, the transverse momentum spectra of the Z boson from ZH production is showed, in scenarios with two scales $\Lambda = 1, 2 \text{ GeV}$ (solid and dashed lines respectively) and in linear and quadratic SMEFT (blue and red lines respectively). The linear SMEFT for $\Lambda = 1 \text{ GeV}$ starts to have negative cross sections above $p_T \approx 200 \text{ GeV}$, which is cured by the inclusion of squared terms, which make the distribution positive by definition. It is also clearly visible that both approaches deviate significantly at higher p_T . This behaviour signals the breakdown of the EFT approximation.

In Fig. I.9b, where again the p_T spectra of the associated vector boson are presented, four cases were plotted: SM, full theory of a UV triplet vector boson of mass 591 GeV and the low-energy EFT for the previous theory, comparing both linear and linear-plus-quadratic contributions. The linear and quadratic realisations have very similar behaviour at low p_T , but at higher p_T the linear approximation breaks down. The quadratic EFT, although being far from the full theory, reproduces the behaviour better.

Since the effective operators should be used to describe small deviations from the SM, the situation in which the inclusion of $|\mathcal{A}_{\text{dim6}}|^2$ which should be actually suppressed, becomes necessary, shows the end of the validity regime of the EFT. Once the SMEFT amplitudes are known, both linear and quadratic SMEFT observables can be generated, and in that case, the comparison of their behaviour is a good check for the validity of EFT approximation and the difference of them should definitely be included into the theoretical uncertainty. Additionally there are other contributions of order $1/\Lambda^4$ that should also be studied and included in the theoretical uncertainty.

The example of how the inclusion of the $|\mathcal{A}_{\text{dim6}}|^2$ term can change the behaviour of SMEFT prediction, calls for a more detailed look on the validity of the approach. Although we roughly describe Λ as the “scale of new physics”, it is evident from the previous example, that it does not correspond to the breakdown of the approach, since in Fig. I.9a problems started at $p_t \approx 200$ GeV, well below 1 TeV. One of the usual checks of the validity of a perturbative expansion is a study of perturbative unitarity. Perturbative unitarity is in general violated in EFT, however it can be used to check energies lower than Λ , since above EFT should be definitely replaced by the full theory.

To summarise: experiments occur at finite energy and “measure” an effective action $S^{\text{eff}}(\Lambda)$; whatever QFT should give low energy $S^{\text{eff}}(\Lambda)$, $\forall \Lambda < \infty$. One also assumes that there is no fundamental scale above which $S^{\text{eff}}(\Lambda)$ is not defined and $S^{\text{eff}}(\Lambda)$ loses its predictive power in a process where the scale E approaches Λ ; indeed, $E = \Lambda$ requires ∞ renormalized parameters.

I.4.7.3 SMEFT validity and unitarity

The SMEFT behaviour is similar to that of renormalisable theories that satisfy unitarity in perturbation theory; a perturbative expansion in E/Λ always becomes difficult at high enough energy, and the applicability of the SMEFT will break down in the “tails” of kinematic distributions (or new physics will be seen before the breakdown). Therefore, projecting data into the SMEFT will have a large intrinsic uncertainty, i.e we do not know what exactly is going on because the SMEFT interpretation becomes a series where the expansion parameter is close to 1 and/or the perturbative unitarity bound is saturated.

The range of validity of the perturbative expansion in SMEFT is poorly known and unitarity conditions can be used to get additional information. Having said that, EFTs could enjoy some range of non-perturbative validity before new physics is manifest (which goes under the name of classicalization, asymptotic safety, etc ...).

Finally, one should keep in mind that these are not statements that unitarity is violated in the SMEFT. Unitarity *would be violated*, if we could trust the perturbative expansion, which we cannot. Perturbative unitarity bounds can be computed, but the bounds also imply that loops *must* be important.

To give a brief example, we consider the scattering of longitudinally polarized W bosons. In the SM,

$$T_{\text{SM}}(W_L^+ W_L^- \rightarrow W_L^+ W_L^-) \sim -\frac{G_F m_H^2}{4\sqrt{2}\pi} \quad s \rightarrow \infty. \quad (\text{I.82})$$

Unitarity is not violated, since the amplitude is constant in limit of large s . In the SMEFT,

$$T_{\text{SMEFT}}(W_L^+ W_L^- \rightarrow W_L^+ W_L^-) \sim -\frac{1}{32\pi} g_6 G_F (a_{\phi D} + 2a_{\phi\Box}) \frac{s}{\Lambda^2} + \mathcal{O}(1), \quad (\text{I.83})$$

where g_6 is the common coupling of $\text{dim} = 6$ SMEFT operators and a_X are specific Wilson coefficients. The SM contributes to the constant part, while the part growing with s is driven by the new higher dimension interactions. From these equations, we can, by imposing $T_{\text{SMEFT}} = 1$, estimate the scale at which perturbative unitarity is broken, s_C :

$$\begin{aligned} |T_{\text{SMEFT}}| &\sim \frac{1}{32\pi} g_6 G_F (a_{\phi D} + 2a_{\phi\Box}) \frac{s}{\Lambda^2} < 1 \\ s_C &< \frac{32\pi}{g_6 G_F (a_{\phi D} + 2a_{\phi\Box})} \Lambda^2. \end{aligned} \quad (\text{I.84})$$

Note, that from this equation it is not obvious that the scale s_C is smaller than Λ^2 . However, it makes no sense to talk about EFT for s_C above Λ^2 . Thus, in general, we can define number of scales in EFT, at which we suspect the breakdown of the approximation will occur, and they should be studied case by case, to find the one which leads to the strongest constraints. Performing calculations above these scales, although still possible, should be treated with extreme caution.

Finally, imposing a form-factor-like suppression to EFT coefficients in order to avoid unitarity violations at scales $E \sim \Lambda$ corresponds (at best) to choosing some specific UV model; in particular form-factors introduce a second cut-off scale which a priori has nothing to do with the scale appearing in front of the Wilson coefficients.

In principle, one could introduce a cut-off to forbid unphysical events manually (a prescription also partially used by ATLAS and CMS, known as ‘‘event clipping’’). Such a cut-off could also be motivated theoretically by the argument that these events could have never arisen in a UV-complete theory. However, this leads to a sharp edge in the distribution which does not resemble any sensible approximation to a UV-complete theory, see Ref. [106] for details and for a description of EFT, perturbative unitarity and unitarization.

Ref. [107] indicates that the two phenomena of tree-unitarity violation and the onset of new physics are separate in practice in QCD-like theories with different numbers of colors and flavours. Unitarity violation happens in elastic scattering well below the energy where the QCD degrees of freedom are produced. In such a case, there is no other option but that the apparent unitarity violation must be solved within the effective field theory without recourse to the new degrees of freedom.

I.4.8 Amplitudes in SMEFT, asymptotic behaviour

To fully understand the ‘‘linear’’ vs. ‘‘quadratic’’ problem we provide the asymptotic behaviour of the helicity amplitudes for the process $q\bar{q} \rightarrow HZ$ as a function of the HZ invariant mass. From Table I.9 it is easy to understand when and why the linear approach starts giving unphysical results.

| Helicity | SM | one insertion | two insertions |
|----------|----------------------------|--|--|
| $- + -$ | $\frac{G_F M_Z^3}{M_{HZ}}$ | $\frac{M_Z M_{HZ}}{\Lambda^2}$ | $\frac{M_Z M_{HZ}}{G_F \Lambda^4}$ |
| Wilson | — | $a_{ZZ}, a_{\phi q}^{(1)}, a_{\phi q}^{(3)}$ | $a_{AA}, a_{AZ}, a_{ZZ}, a_{\phi D}, a_{\phi \square}, a_{\phi q}^{(1)}, a_{\phi q}^{(3)}$ |
| $- + 0$ | $G_F M_Z^2$ | $\frac{M_{HZ}^2}{\Lambda^2}$ | $\frac{M_{HZ}^2}{G_F \Lambda^4}$ |
| Wilson | — | $a_{\phi q}^{(3)}, a_{\phi q}^{(1)}$ | $a_{AA}, a_{AZ}, a_{ZZ}, a_{\phi D}, a_{\phi \square}, a_{\phi q}^{(3)}, a_{\phi q}^{(1)}$ |
| $- + +$ | $\frac{G_F M_Z^3}{M_{HZ}}$ | $\frac{M_Z M_{HZ}}{\Lambda^2}$ | $\frac{M_Z M_{HZ}}{G_F \Lambda^4}$ |
| Wilson | — | $a_{ZZ}, a_{\phi q}^{(1)}, a_{\phi q}^{(3)}$ | $a_{AA}, a_{AZ}, a_{ZZ}, a_{\phi D}, a_{\phi \square}, a_{\phi q}^{(1)}, a_{\phi q}^{(3)}$ |

Table I.9: LO EFT helicity amplitudes for the process $q\bar{q} \rightarrow HZ$. For each helicity amplitude, the perturbative order and the involved Wilson coefficients are reported.

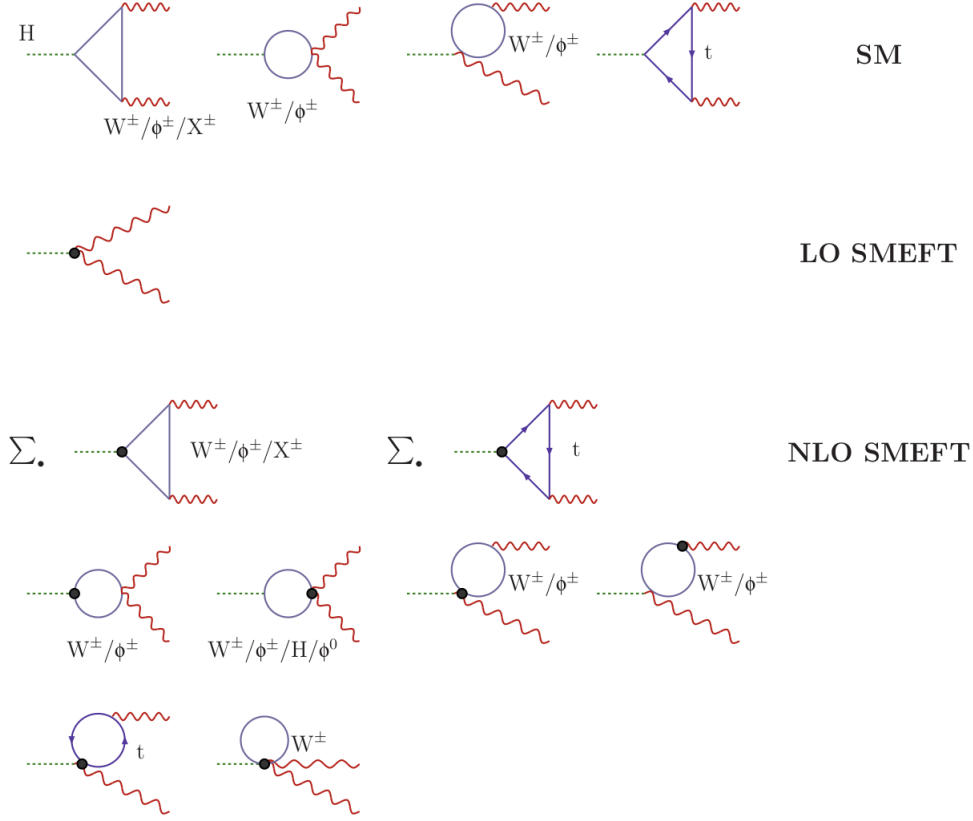


Fig. I.10: Original figure from Ref. [46]. Diagrams contributing to the amplitude for $H \rightarrow \gamma\gamma$ in the R_ξ -gauge: SM (first row), LO SMEFT (second row), and NLO SMEFT. Black circles denote the insertion of one dim-6 operator. Σ_\bullet implies summing over all insertions in the diagram (vertex by vertex). For triangles with internal charge flow ($t, W^\pm, \phi^\pm, X^\pm$) only the clockwise orientation is shown. Non-equivalent diagrams obtained by the exchange of the two photon lines are not shown. Higgs and photon wave-function factors are not included. The Fadeev-Popov ghost fields are denoted by X .

I.5 Pseudoobservables for the LHC

I.5.1 Pseudoobservables from the LEP times

The LEP collider was operating between 1990 and 2000, in the same tunnel that is now used by the LHC; at the beginning it was operating at a c.m. energy close to the Z boson mass, more precisely at $|\sqrt{s} - M_Z| < 3 \text{ GeV}$, and on its second run the energy was raised in order to produce also W boson pairs, reaching 209 GeV.

With each successive energy upgrade of the LEP collider, some hope re-emerged that the discovery of the Higgs boson was about to happen. Just prior to the planned shutdown of LEP in 2000, few events that resembled a Higgs boson with a mass of $\sim 115 \text{ GeV}$ were observed. This led to the extension of the final LEP run by a few months. But in the end the data was inconclusive and insufficient to justify another run and the final decision to shut down and dismantle LEP was taken. This way it was possible to make room for the new Large Hadron Collider. The analysis of the direct search for the Higgs boson at LEP resulted in a final lower bound of the Higgs mass 114.4 GeV at the 95% confidence level.

The concept of POs was born in the frame of the LEP analysis, see for instance Refs. [108, 109], as a counterpart to the traditional Fiducial Observables (FOs), also called Realistic Observables (ROs). The POs were designed to have two main features:

- to allow comparison between experiments (i.e. independent of the various detector cuts)
- to be as independent as possible of changes in the underlying theory.

For this purpose, it was needed to find a set of quantities that are well defined in QFT and as independent as possible of detector fiducial volumes. To start the discussion on the POs used at LEP we define the matrix element for a Z boson decaying into a fermion pair:

$$\mathcal{M}_{Z \rightarrow f\bar{f}} = \bar{u}_f \not{\epsilon}_Z (\mathcal{G}_V^f + \gamma_5 \mathcal{G}_A^f) v_f, \quad (\text{I.85})$$

where $\mathcal{G}_{V/A}^f$ are complex valued effective coefficients, which absorb all correction factors and are evaluated at a scale $Q^2 = -M_Z^2$.

The strategy followed a LEP in defining the POs was, first of all, to de-convolute the initial state QED radiation and the final state QED/QCD radiation. This is possible given our good understanding of the structure of radiation: therefore, we can define a *radiator*, e.g. for initial state QED radiation, such that the observed cross section becomes

$$\sigma(s) = \int_0^{1-x_{cut}} dx H(x, s) \sigma_0((1-x)s), \quad (\text{I.86})$$

where σ_0 is the de-convoluted cross section and $H(x, s)$ is the radiator absorbing the corrections. One can think of this radiator as similar to the parton distribution functions, PDFs, so important nowadays for the LHC strategy. Furthermore, around the Z peak, σ_0 only contains the Z resonant part of the amplitude.

Observe that this approximation will only work if we know the corrections that we are neglecting, or at least have a good estimate of their size. This was the case at LEP but opens a debate in the case of the SMEFT analysis, where we still define POs but we do not have such a good knowledge of the SMEFT-extended radiator. For instance Bremsstrahlung has a very important effect for a circular electron-positron collider.

This way, after we subtract the real emission and the non-resonant part from the process, we are left with a kernel which looks more like the Breit-Wigner (BW) function we expect, for instance for $f\bar{f} \rightarrow Z$ we have:

$$\sigma_{f\bar{f}}(s) = \sigma_0^{f\bar{f}} \frac{s^2 \Gamma_Z^2}{(s - M_Z^2)^2 + s^2 \Gamma_Z^2 / M_Z^2}, \quad \sigma_0^{f\bar{f}} = \frac{12\pi}{M_Z^2} \frac{\Gamma_e \Gamma_f}{\Gamma_Z^2}. \quad (\text{I.87})$$

The partial and total Z widths were defined as POs (i.e. $\Gamma_Z, \Gamma_f, \Gamma_e$), with additional definitions of:

$$\begin{aligned} \Gamma_{\text{hadr}} &= \Gamma_u + \Gamma_d + \Gamma_c + \Gamma_s + \Gamma_b, & \Gamma_{\text{inv}} &= \Gamma_Z - \Gamma_e + \Gamma_\mu + \Gamma_\tau + \Gamma_{\text{hadr}}, \\ R_l &= \frac{\Gamma_{\text{hadr}}}{\Gamma_e}, & R_{b,c} &= \frac{\Gamma_{b,c}}{\Gamma_{\text{hadr}}}, & \sigma_{\text{hadr}} &= \frac{12\pi}{M_Z^2} \frac{\Gamma_e \Gamma_{\text{hadr}}}{\Gamma_Z^2}. \end{aligned} \quad (\text{I.88})$$

These partial and total widths were calculated including the final state QCD and QED corrections.

Another class of POs used at LEP are the ones connected to distributions, such as forward-backward asymmetries and polarisations. The assumption for this de-convoluted POs was that QED and QCD corrections were subtracted from the experimental data. From the theoretical point of view they can be calculated from the differential cross section,

$$\frac{d\sigma_f}{d\Omega} = \frac{\alpha}{4\pi} \cos(\theta) \beta_f \left[(1 + \cos(\theta)^2) F_1(s) + 4\mu_f^2 (1 + \cos(\theta)^2) F_2(s) + 2\beta_f \cos(\theta) F_3(s) \right], \quad (\text{I.89})$$

where $\beta_f^2 = 1 - 4\mu_f^2$ with $\mu_f^2 = m_f^2/s$, while $F_i(s)$ are form factor functions which depend on reduced γ/Z propagator ratio, effective Z couplings and electric charges, both for electron and final state fermions. Then asymmetries and polarisations can be expressed by the form factors, e.g.

$$\mathbf{A}_{FB}^f(s) = \frac{3}{4} \frac{\beta_f F_3(s)}{F_1(s) + 2\mu_f^2 F_2(s)}. \quad (\text{I.90})$$

The definitions of POs were significantly simplified in the limit of massless fermions and vanishing Γ_Z^2 terms, yielding:

$$\mathbf{A}_{FB}^f = \frac{3}{4} \mathcal{A}_e \mathcal{A}_f, \quad \mathbf{A}_{LR}^e = \mathcal{A}_e, \quad \mathbf{P}^f = -\mathcal{A}_f, \quad \mathbf{P}_{FB}(\tau) = -\frac{3}{4} \mathcal{A}_e, \quad (\text{I.91})$$

where \mathcal{A}_f is defined as:

$$\mathcal{A}_f = \frac{2 \operatorname{Re}[\mathcal{G}_V^f (\mathcal{G}_A^f)^*]}{|\mathcal{G}_V^f|^2 + |\mathcal{G}_A^f|^2}, \quad (\text{I.92})$$

and the couplings \mathcal{G} were defined in Eq. (I.85).

The experiments performed fits to the POs described above, and then were able to combine them to present legacy LEP results. Fig. I.11a shows the combined measurement for the total Z width, from the analysis of the four LEP experiments. The table in Fig. I.11b shows the set of combined POs measurements, altogether known as EW Precision Data (EWPD). These were measured with an unprecedented precision, and up to now they still represent a strong constraint on all BSM models. Additionally, due to their theoretical connection with the unknown Higgs and top quark masses, they pointed at the correct mass ranges, which were then confirmed by direct observation of these particles.

I.5.1.1 LEP summary

The rationale for the deconvolution is based on the fact that all experiments used different kinematic cuts and selection criteria, while an objective requirement was put forward by the scientific community for having universal results expressed in terms of the on-shell Z region.

Assuming a structure function representation for the initial fermions, in turn, allows us to deconvolute the measurements and to access the hard scattering at the nominal peak. The transition from FO's to PO's involves certain assumptions that reflect our understanding of QED effects but, within those assumptions, there is a well-defined mathematical procedure.

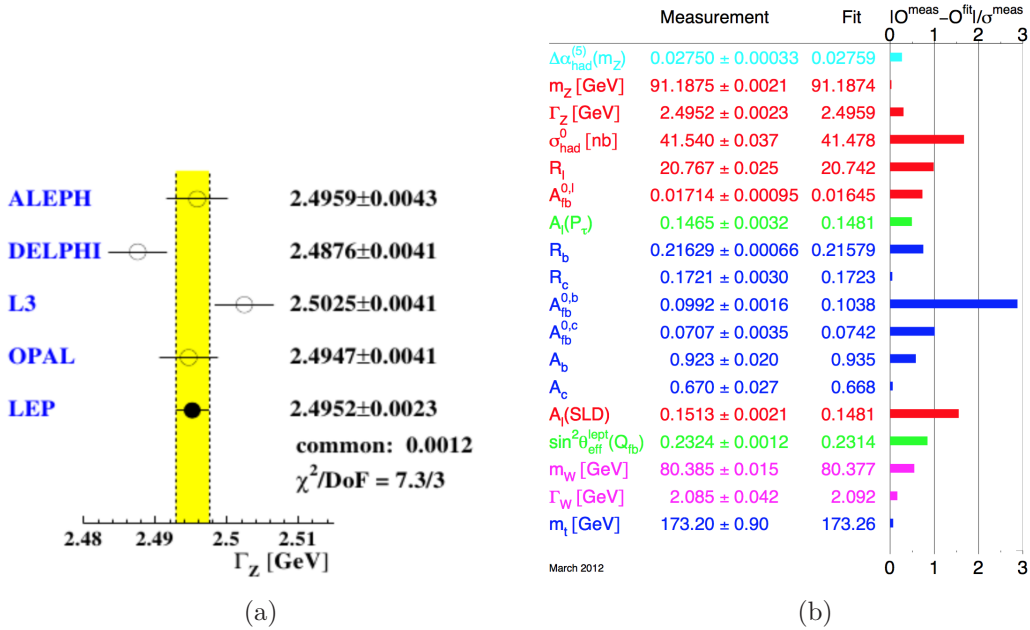


Fig. I.11: The example of combination of PO (Γ_Z) between experiments (a) and legacy list of POs combined between all experiments, representing the EWPD [110] (b).

Insofar as this procedure is an explicitly specified and mathematically meaningful transformation, the PO's possess the status of observability. The strategy is as follows: begin with the predicted amplitude, dressed by the weak loop corrections, and use the fact that in the SM there are several effects, such as

- a) the imaginary parts or
- b) the γ - Z interference or
- c) the pure QED background,

that have a usually negligible influence on the Z line shape. Therefore, PO's are determined by fitting FO's but we will have some ingredients that are still taken from the SM, making the final results dependent upon the SM. In this way the exact (de-convoluted) cross-section is successively reduced to a Z -resonance. It is a modification of a pure Breit-Wigner resonance because of the s -dependent width.

I.5.2 Key differences between LEP and LHC in context of POs

Before we start to consider a proposal for POs at LHC let us discuss what are the differences, not only in the collider properties but also in the theory status between LEP and LHC times. LEP was an electron-positron collider, well suited for precision measurements and, as we will discuss now, with much cleaner event productions. Already at LEP, the important quest was to separate the hard effects from the soft physics, which was then parametrised by the "radiator" function.

At LHC there are more sources of model dependency. As we will see below, the POs will be defined at the parton level, while in the detector we have stable particles and jets. Therefore, we need a bridge through parton distribution functions, parton showers, etc.

There is another difference to be taken into account: the status of the SM was also different. At LEP, the SM was still missing a key piece, the Higgs boson; therefore, the hypothesis was

the SM, the Higgs mass was the unknown and measurements were presented in a way to see bounds on m_H , as we can see in Fig. I.12.

Now the paradigm has changed: all particles of the SM have been observed and we do not really have a clear direction in which to look for NP. What is mostly missing, are precise measurements to be confronted with the SM or with a theory of SM deviations.

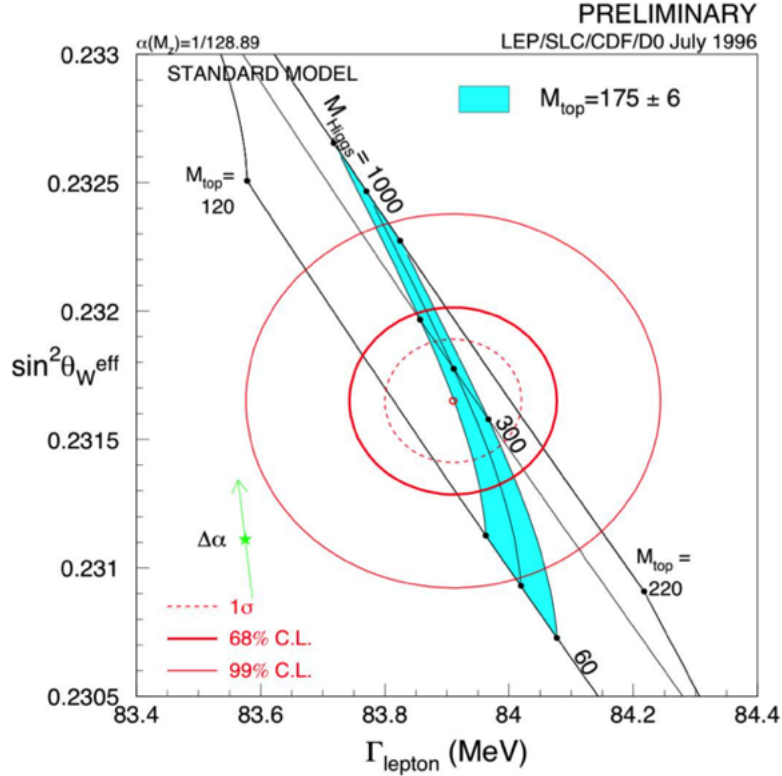


Fig. I.12: The plot presenting measured values of two LEP POs. On the plot also predictions for different Higgs and top quark masses are plotted. See Ref. [110]

I.5.3 Pseudoobservables for the LHC

POs proved to be a very successful tool for storing the LEP results, and allowed for better communication between experiments and theory; therefore, there is an ongoing discussion on reintroducing POs for LHC.

Although the experimental situation is quite different, the advantages of POs should be clear: a high degree of model independence and the possibility of reinterpreting experimental results when more precise theoretical calculations become available. In that regard, POs act as a bridge between the data collected in the experiment and the theory calculations. The POs can be obtained from the fiducial cross sections, by deconvoluting effects such as parton distribution functions and radiative corrections.

It is important to keep in mind that this procedure will be the source of an extra uncertainty, not necessarily small. It is of the highest importance to keep the uncertainties under control, requiring a careful cross-check of theoretical tools used in the analysis.

As it was described in detail in Section I.3, the fiducial or STXSs allow to store the experimental data, with a minimal dependence on the precision of the currently available calculations, and are the closest measurement to what is actually seen in the detectors. However, one of their

drawbacks, is that they cannot be used for the combinations and comparisons between the two experiments. For this reason, the proposal is to perform combination in terms of POs, as it was done at LEP.

Furthermore, theory upgrades can be applied at the level of fiducial quantities, rather than starting from raw data. POs, being well defined objects from the theoretical point of view, can be then interpreted in terms of more fundamental quantities such as Wilson coefficients or Lagrangian parameters of some UV complete theory.

In that regard, it would be much more handy for model builders to interpret the nature of NP and parameters of the specific models from POs, rather than trying to extract them directly from fiducial or template cross sections.

Also, some of the limitations of the κ -framework are reduced thanks to the flexibility of the POs. However, this goes with a cost: more parameters to fit and simulate. The set of POs used for parametrising Higgs properties was proposed both in the EW decays in Ref. [43] and in the EW production in Ref. [44]. From the theoretical point of view, the POs are inspired by the $\text{dim} = 6$ EFT Lagrangian (SMEFT), which we described in Section I.4.

In this case we end up with 20 real parameters for the Higgs decay observables, and additional 32 parameters in case of productions (corresponding to the interactions with the light quarks). The amount of the parameters can be significantly reduced when we consider some of the SM symmetries, such as flavour universality or CP conservation. The POs flexibility manifests in fact that we allow the modification not only in the Higgs couplings but also in coupling of the EW bosons with the final (initial) state fermions. Also the description of vertices is more detailed since it considers the different modifications for different tensor structures.

It is worth noting that we do not claim any theoretical supremacy of the POs with respect to the best SM or BSM calculations; the main reason of their use is that they represent an optimal way of keeping record of experimental data.

Let us now present how the LHC POs should be defined. In this review we will discuss the multi-pole expansion (MPE) of amplitudes and we will briefly mention in Section I.5.5 the factorization of a process into sub-processes, the details can be found in Ref. [46].

We start from the easiest case of the Higgs coupling to two fermions. At LHC this is directly measured by $H \rightarrow \tau^+ \tau^-$ and $H \rightarrow b\bar{b}$. In the most general form we can write this (tree level) amplitude decomposed in the CP conserving and violating part, although the latter is not present in the SM:

$$\mathcal{A}(H \rightarrow f\bar{f}) = -\frac{i}{\sqrt{2}}(y_S^f \bar{f}f + iy_P^f \bar{f}\gamma_5 f). \quad (\text{I.93})$$

The coefficients y_S^f and y_P^f are POs and need to be measured experimentally. We can also express them in the well known κ framework as:

$$\kappa_f = \frac{y_S^f}{y_{S,\text{SM}}^f}, \quad \delta_f^{\text{CP}} = \frac{y_P^f}{y_{S,\text{SM}}^f}. \quad (\text{I.94})$$

We need to note here, that the measurement of the total rate of Higgs BR to fermions, would not allow to differentiate between the two contributions, since it scales as:

$$\Gamma(H \rightarrow f\bar{f}) = \left[\kappa_f^2 + \left(\delta_f^{\text{CP}} \right)^2 \right] \Gamma(H \rightarrow f\bar{f})^{\text{SM}}. \quad (\text{I.95})$$

To access separately the information about the CP violating part of the above amplitude, the spins of the fermions need to be determined. It can be accessed, e.g. by the measurements of angular distributions of the τ s decay products. Note also that the CP violating part is not

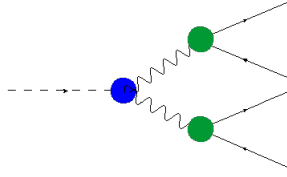


Fig. I.13: The Higgs decaying to 4 fermions via vector bosons.

present in the EFT formalism we presented in the previous chapter. It is so, because we assumed all the symmetries of the SM, including the CP one.

Obviously, POs must always match the best, available, calculations process by process. In the previous example we have considered $H \rightarrow b\bar{b}$ at LO in QCD; however, consider the EFT approach and analyse the decay at NLO in QCD. At this order, new real contributions enter at $\text{dim} = 6$ which either do not have a Born amplitude (chromomagnetic interaction) or are built starting from another amplitude. In these latter channels the same final state is reached through a completely different propagator structure.

For example, let us imagine a situation in which the Yukawa of the b -quark is SM-like and that other Wilson coefficients are greatly enhanced such that the resulting distribution in $m(b\bar{b})$ peaks towards lower masses in a way that cannot be described by simple QCD “radiation”. In this case, POs still represent the optimal way of separating $H \rightarrow b\bar{b}(g)$, $H \rightarrow gg$ (with one gluon converting into a $b\bar{b}$ pair) and $H \rightarrow b\bar{b}g$ (with a hard gluon).

The situation is more complicated when the Higgs boson decays into 4 fermions. In the SM the doubly-resonant part of the process goes via Higgs decaying into two vector bosons decaying then into fermions (detected or giving measured through their missing transverse energy in case of neutrinos).

A similar situation is also present in the SMEFT, although here a second decay channel is open: when the Higgs boson decays via the chromomagnetic operator into a pair of fermions and one vector boson.

We will construct the corresponding POs in the end of this Section, but here we start with introducing the doubly-resonant part of the process, $h \rightarrow VV \rightarrow f_1 f_2 \bar{f}_3 \bar{f}_4$: this is shown in Fig. I.13.

To ensure full flexibility we will proceed as follows:

- a) define couplings for Higgs decaying to vector bosons (as it is done in the κ -framework),
- b) define couplings for vector bosons decaying to fermions (blue and green blobs respectively).

If we want to study distributions and not only total rate modifiers, (as done in the κ -framework), different tensor structures of the amplitude need to be considered. Here we will present the case for the process of the Higgs effectively decaying into two Z bosons, which then decay into a pair of muons and a pair of electrons.

This reasoning can be easily repeated for the different decays in the second stage, and also while including the W bosons in the intermediate stage. For the general description we refer to the original paper, see Ref. [43].

The full description can be started with the definition of POs corresponding to $Z \rightarrow l^+ l^-$, the green blob from Fig. I.13. The Z -fermion interaction is governed by a term,

$$\Sigma_{f=f_L, f_R} Z_\mu c_Z^{\text{SM}} \bar{f} \gamma^\mu f, \quad c_Z^{\text{SM}}(f) = \frac{g}{c_W} (T_3(f) - Q(f) s_W^2) \quad (\text{I.96})$$

from which we can read out the generalised amplitude,

$$\mathcal{A}(Z \rightarrow f\bar{f}) = \sum_{f=f_L, f_R} \epsilon_\mu g_Z^{ff'} \bar{f}' \gamma^\mu f, \quad (\text{I.97})$$

where ϵ_μ is the polarisation of the Z boson and $g_Z^{ff'}$ is a generalised coefficient which takes the SM value $g_Z^{ff} = c_Z^{\text{SM}}(ff)$ (being zero for different flavours). Now, having two additional couplings in mind (note, that we do not include flavour violating neutral currents), i.e. g_Z^μ, g_Z^e , we need to define the coupling between H and two Z bosons. Let us decompose this amplitude as follows:

$$\mathcal{A}(h \rightarrow \mu^+(p_1)\mu^-(p_2)e^+(p_3)e^-(p_4)) = i \frac{2m_Z^2}{v} \sum_{\mu=\mu_L, \mu_R} \sum_{e=e_L, e_R} (\bar{\mu} \gamma_\mu \mu) (\bar{e} \gamma_\nu e) \mathcal{T}_{nc}^{\mu\nu}(q_1, q_2), \quad (\text{I.98})$$

where $q_1 = p_1 + p_2$ and $q_2 = p_3 + p_4$. Now we can decompose the tensor part of the amplitude $\mathcal{T}_{nc}^{\mu\nu}(q_1, q_2)$ into Lorentz-allowed tensor structures and their form factors:

$$\mathcal{T}_{nc}^{\mu\nu}(q_1, q_2) = g^{\mu\nu} F_L^{\mu e}(q_1, q_2) + \frac{g^{\mu\nu} q_1 \cdot q_2 + q_1^\nu q_2^\mu}{m_Z^2} F_T^{\mu e}(q_1, q_2) + \frac{\epsilon^{\mu\nu\rho\sigma} q_{1,\sigma} q_{2,\rho}}{m_Z^2} F_{\text{CP}}^{\mu e}(q_1, q_2). \quad (\text{I.99})$$

Now, the form factors can be expanded around the Z pole⁶. Let us note here that the transverse and CP-violating tensor structures, second and third one in Eq. (I.98), can also result from off-shell photons, mediated by the usual electromagnetic, charge dependent, coupling (eQ),

$$\begin{aligned} F_L^{\mu e}(q_1, q_2) &= \kappa_{ZZ} \frac{g_Z^\mu g_Z^e}{P_Z(q_1^2) P_Z(q_2^2)} + \frac{\epsilon_{Z\mu}}{m_Z^2} \frac{g_Z^e}{P_Z(q_2^2)} + \frac{\epsilon_{Ze}}{m_Z^2} \frac{g_Z^\mu}{P_Z(q_1^2)} + \Delta_L^{\text{SM}}(q_1^2, q_2^2) \\ F_T^{\mu e}(q_1, q_2) &= \epsilon_{ZZ} \frac{g_Z^\mu g_Z^e}{P_Z(q_1^2) P_Z(q_2^2)} + \epsilon_{Z\gamma} \left(\frac{eQ_\mu g_Z^e}{q_1^2 P_Z(q_2^2)} + \frac{eQ_e g_Z^\mu}{q_2^2 P_Z(q_1^2)} \right) + \epsilon_{\gamma\gamma} \frac{e^2 Q_\mu Q_e}{q_1^2 q_2^2} + \Delta_T^{\text{SM}}(q_1^2, q_2^2) \\ F_{\text{CP}}^{\mu e}(q_1, q_2) &= \epsilon_{ZZ}^{\text{CP}} \frac{g_Z^\mu g_Z^e}{P_Z(q_1^2) P_Z(q_2^2)} + \epsilon_{Z\gamma}^{\text{CP}} \left(\frac{eQ_\mu g_Z^e}{q_1^2 P_Z(q_2^2)} + \frac{eQ_e g_Z^\mu}{q_2^2 P_Z(q_1^2)} \right) + \epsilon_{\gamma\gamma}^{\text{CP}} \frac{e^2 Q_\mu Q_e}{q_1^2 q_2^2}. \end{aligned} \quad (\text{I.100})$$

The Δ s correspond to the SM sub-leading non-local contributions, which remain unaffected by $\text{dim} = 6$ operators. As we can see, on top of the Z coupling constants, g_Z^f , also new constants appeared: κ_{ZZ} and $\epsilon_{XX}^{(\text{CP})}$. In the longitudinal form factor we can see the momentum expansion around the pole, and it is pictorially represented in Fig. I.14.

These are additional POs, which describe the $H \rightarrow 2\mu 2e$ decays and would need to be determined in the experiments by measuring appropriate BRs. We can note here, that the Z POs, i.e. g_Z^f , were already determined by LEP with a good precision, and thus may be used as input parameters when we concentrate on determining the Higgs couplings.

We can also build the amplitudes for the Higgs decaying via charged vector bosons, e.g. $H \rightarrow \mu^+ e^- \nu_\mu \bar{\nu}_e$. Keeping the lepton flavour conservation as a valid symmetry in the vector boson decays we can see that these final states can only be mediated by the $W^+ W^-$ pair. However let us consider a slightly different final state: $H \rightarrow \mu^+ \mu^- \nu_\mu \bar{\nu}_\mu$. Although the final state looks pretty similar, here the situation is more complicated, since the decay can be mediated both by ZZ and $W^+ W^-$ pairs, and we need to take all the possibilities into account. To handle this

⁶We will not discuss here the fact that the Z on-shell mass should be replaced by the corresponding complex pole

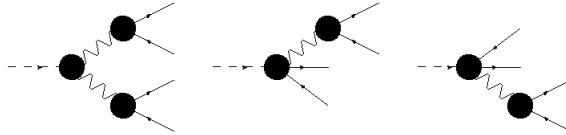


Fig. I.14: The pictorial representation of the expansion around physical poles for the longitudinal form factor for Higgs decaying in muon and electron pair.

situation we can perform a “top layer” decomposition into neutral currents (described above), and charged currents:

$$\begin{aligned} \mathcal{A}(H \rightarrow \mu^+ \mu^- \nu_\mu \bar{\nu}_\mu) &= \mathcal{A}_{nc}(H \rightarrow (Z \rightarrow \mu^+ \mu^-)(Z \rightarrow \nu_\mu \bar{\nu}_\mu)) \\ &\quad - \mathcal{A}_{cc}(H \rightarrow (W^+ \rightarrow \mu^+ \nu_\mu)(W^- \rightarrow \mu^- \bar{\nu}_\mu)). \end{aligned} \quad (\text{I.101})$$

The POs, as described by the different tensor structures, can be directly implemented into MC tools, which then enable the comparison with experiment. This condition is already satisfied with the POs that we have introduced and they have been implemented in the common Universal FeynRules Output (UFO) format, described in Ref. [111], allowing to use the model in many different MC tools. Extensive comparisons have also been performed with Prophecy4f and MadGraph5_aMC@NLO generators.

The POs we defined so far are thought of as a form of effective couplings; in Table I.10 we can see the relations between the partial widths of the Higgs boson and the POs at the amplitude level. For some of these widths, a measurement would not be enough to distinguish between two CP even and CP odd POs. It is important to keep in mind also that the quality of PO measurements will depend heavily on the uncertainty introduced by deconvoluting soft radiation and by the PDFs.

The numerical factors were obtained by calculating the full partial decay width into a given final state with only one PO *switched on* and by dividing by the BRs corresponding to vector boson decaying into two of final state particles. Therefore these coefficients depend on the accuracy of the theory of the presented calculations.

Using crossing symmetry we find that the same diagrams describing H decay into four fermions also govern the EW production modes of vector boson fusion and Higgsstrahlung. This means that, in principle, we can use the same set of POs. However, we are still missing dedicated POs for Higgs production via gluon fusion or associated with top quark pair. The authors of Ref. [37] advise to stick to κ_g and κ_t for these cases respectively. In the following we will consider the Higgs-gluon interactions in context of H decay into four quarks.

In the context of POs in production, addressed in Ref. [44], the momentum expansion around physical poles is valid only in limited kinematic regions. This is so because in the production it is not always the case that the Higgs boson is close to its threshold, and thus the standard definition of POs will not hold. In principle one should cut on the momentum transfer, something that is not directly available in the experiment.

Indeed, the cut can only be based on the p_T of (VBF) jets or Z boson in ZH production (which is correlated with the “theoretical” cut), however this correlation is becoming less and less clear for large values of the momentum transfer, and that could spoil the whole approach.

I.5.4 Extending the POs basis

Four-quark final states resulting from the effective coupling of the Higgs to gluons

The Higgs decaying into two quark-antiquark pairs via an effective gluon coupling is presented in Fig. I.15

| Physical PO | Connection with effective coupling PO | effective coupling PO |
|--|---|--|
| $\Gamma(H \rightarrow f\bar{f})$ | $\Gamma(H \rightarrow f\bar{f})^{\text{SM}}[(\kappa_f)^2 + (\delta_f^{\text{CP}})^2]$ | $\kappa_f, \delta_f^{\text{CP}}$ |
| $\Gamma(H \rightarrow \gamma\gamma)$ | $\Gamma(H \rightarrow \gamma\gamma)^{\text{SM}}[(\kappa_{\gamma\gamma})^2 + (\delta_{\gamma\gamma}^{\text{CP}})^2]$ | $\kappa_{\gamma\gamma}, \delta_{\gamma\gamma}^{\text{CP}}$ |
| $\Gamma(H \rightarrow Z\gamma)$ | $\Gamma(H \rightarrow Z\gamma)^{\text{SM}}[(\kappa_{Z\gamma})^2 + (\delta_{Z\gamma}^{\text{CP}})^2]$ | $\kappa_{Z\gamma}, \delta_{Z\gamma}^{\text{CP}}$ |
| $\Gamma(H \rightarrow Z_L Z_L)$ | $(0.209 \text{ MeV}) \times \kappa_{ZZ} ^2$ | κ_{ZZ} |
| $\Gamma(H \rightarrow Z_T Z_T)$ | $(1.9 \times 10^{-2} \text{ MeV}) \times \epsilon_{ZZ} ^2$ | ϵ_{ZZ} |
| $\Gamma^{\text{CPV}}(H \rightarrow Z_T Z_T)$ | $(8.0 \times 10^{-3} \text{ MeV}) \times \epsilon_{ZZ}^{\text{CP}} ^2$ | $\epsilon_{ZZ}^{\text{CP}}$ |
| $\Gamma(H \rightarrow Zf\bar{f})$ | $(3.7 \times 10^{-2} \text{ MeV}) \times N_c^f \epsilon_{Zf} ^2$ | ϵ_{Zf} |
| $\Gamma(H \rightarrow W_L W_L)$ | $(0.84 \text{ MeV}) \times \kappa_{WW} ^2$ | κ_{WW} |
| $\Gamma(H \rightarrow W_T W_T)$ | $(0.16 \text{ MeV}) \times \epsilon_{WW} ^2$ | ϵ_{WW} |
| $\Gamma^{\text{CPV}}(H \rightarrow W_T W_T)$ | $(6.8 \times 10^{-2} \text{ MeV}) \times \epsilon_{WW}^{\text{CP}} ^2$ | $\epsilon_{WW}^{\text{CP}}$ |
| $\Gamma(H \rightarrow Wf'\bar{f})$ | $(0.14 \text{ MeV}) \times N_c^f \epsilon_{Wf} ^2$ | ϵ_{Wf} |

Table I.10: The relation between the effective coupling POs and physical ones. N_c^f corresponds to the number of colours.

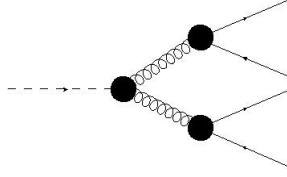


Fig. I.15: The Higgs decaying to 4 quarks via gluons.

First of all we shall define the POs corresponding to the gluon-quark sector. Based on the convention used in Eq. (I.97) we write:

$$\mathcal{A}(g \rightarrow q\bar{q}) = i \sum_q g_g^q \epsilon_\mu \bar{q} T^a \gamma^\mu q. \quad (\text{I.102})$$

Now we can rewrite the expression from Eq. (I.98), in this case

$$\mathcal{A}(h \rightarrow q(p_1)\bar{q}(p_2)q'(p_3)\bar{q}'(p_4)) = i\alpha_s^2 \sum_{q,q'} (\bar{q}\gamma^\mu q)(\bar{q}'\gamma^\nu q') \delta_{ab} \mathcal{T}^{\mu\nu}(q_1, q_2). \quad (\text{I.103})$$

where $q_1 = p_1 + p_2$ and $q_2 = p_3 + p_4$ correspond to the momenta of the gluons. The tensor can be expressed through the form factors,

$$\mathcal{T}^{\mu\nu}(q_1, q_2) = (g^{\mu\nu} q_1 \cdot q_2 - q_1^\nu q_2^\mu) F^g(q_1, q_2) + \epsilon^{\mu\nu\rho\sigma} q_{1,\rho} q_{2,\sigma} F_{\text{CP}}^g(q_1, q_2), \quad (\text{I.104})$$

which can be expressed in terms of the new POs,

$$F^g(q_1, q_2) = \kappa_{gg} \frac{g_g^q g_g^{q'}}{q_1^2 q_2^2} \quad (\text{I.105})$$

$$F_{\text{CP}}^g(q_1, q_2) = \kappa_{gg}^{\text{CP}} \frac{g_g^q g_g^{q'}}{q_1^2 q_2^2}.$$

It is important to note here that the above POs have been introduced for illustrative purposes and are as of today of no relevance in the framework of the LHC.

The QCD background makes it impossible to look for the 4 jets final state. Additionally, the huge uncertainties are connected with jet reconstructions and their assignment to quarks and gluons. It would probably make it also impossible to measure these POs even in an electron-positron collider, which would be able to see the 4 jet final state.

Helicity-violating amplitudes resulting from effective dipole interactions of the Higgs field to (light) fermions and weak gauge bosons

Let us now define the most general form of the amplitude for the 4 fermion final state of the Higgs decay.

$$\mathcal{A}(h \rightarrow f(p_1)\bar{f}(p_2)f'(p_3)\bar{f}'(p_4)) = i \sum_{f,f'} (\bar{f}'\Gamma_{\{\mu\}}^{(1)}f')(\bar{f}\Gamma_{\{\nu\}}^{(2)}f)\mathcal{T}^{(1,2)\{\mu\nu\}}. \quad (\text{I.106})$$

In the general case, each of the $\Gamma_{\{\mu\}}^{(i)}$ can be of the following form:

$$\Gamma = \left\{ \mathbf{1}, \gamma_5, \gamma_\mu, \gamma_\mu\gamma_5, \sigma_{\mu\nu} = [\gamma_\mu, \gamma_\nu] \right\}. \quad (\text{I.107})$$

So far we have adopted $\Gamma_{\{\mu\}}^{(i)} = \gamma_\mu$; now we will investigate the case with the magnetic operator (one of the operators of dim = 6 SMEFT). In that scenario, one of the $\Gamma_{\{\nu\}}^{(i)}$ will have a tensor structure $\sigma_{\mu\nu}$. The diagram for this interaction is presented in Fig. I.16.

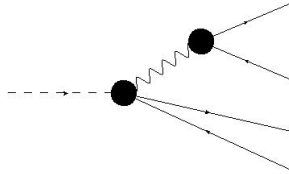


Fig. I.16: The Higgs dipole interaction, the vector can correspond to EW bosons or gluons.

We will use the usual POs for the vector bosons decaying into two fermions (see Eq. (I.97)), whereas the amplitude for the magnetic dipole interaction reads:

$$\mathcal{A}(h \rightarrow f(p_1)\bar{f}(p_2)f'(p_3)\bar{f}'(p_4)) = i \sum_{f,f'} (\bar{f}'\gamma^\mu f)(\bar{f}\sigma_{\mu\nu}f)\mathcal{T}^\nu(q), \quad (\text{I.108})$$

where $q = p_3 + p_4$ is the vector boson momentum transfer. Again we expand into form factors, however here we have just one tensor term:

$$\begin{aligned} \mathcal{T}^\nu(q) &= q^\nu F^{(\text{dip})}(q) \\ F^{(\text{dip})}(q) &= \kappa_{Zf}^{(\text{dip})} \frac{g_Z^f}{P_Z(q)} + \frac{\epsilon_{Zf}^{(\text{dip})}}{m_Z^2}. \end{aligned} \quad (\text{I.109})$$

Note that the lack of a CP odd tensor structure comes from the fact that the term $\sigma_{\mu\nu}\gamma_5$ can always be reduced into lower rank terms of basis Γ .

I.5.5 An alternative layer of POs

As we have seen, residues of resonant poles, κ -parameters and Wilson coefficients are different layers of POs. At LEP we had $g_{V\setminus A}^e$ but also $\Gamma(Z \rightarrow \bar{f}f)$ and $\sigma_{\text{peak}}^{\text{had}}$, therefore the question is: can

we define $\Gamma(H \rightarrow ZZ)$, $\sigma(\bar{t}tH)$ etc. at the PO level? Furthermore, can “physical” POs bypass ad-hoc constructions like “diagram removal” (not gauge invariant) or “diagram subtraction” (ad hoc prefactor and Breit-Wigner profile)?

It is clear that POs are conventionally defined but their definition should be consistent with first principles; here we concentrate on physical POs other than the ones defined in Table I.10 or defined with a different set of conventions. In particular, we are interested in going beyond fully extrapolated POs.

We have to consider several steps in constructing physical POs: multi-pole expansion, principal-value cuts, phase space factorization and helicity factorization. One should keep in mind the LEP example, the hadronic peak cross section extracted from $\sigma(e^+e^- \rightarrow \text{hadrons})$, even if LEP 1 was a “one resonance” problem while LHC is always a “multi-resonance” problem.

- **Multi Pole Expansion:** poles and their residues are intimately related to the gauge invariant splitting of the amplitude (Nielsen identities); residues of poles (after squaring the amplitude and after integration over residual variables) can be interpreted as physical POs, which requires factorization into sub-processes.
- **Phase Space Factorization:** gauge invariant splitting is not the same as factorization of the process into sub-processes, indeed phase space factorization requires the pole to be inside the physical region. It is the amplitude *squared* that matters.

Given an unstable particle we decompose the square of its propagator:

$$\Delta = \frac{1}{(s - M^2)^2 + \Gamma^2 M^2} = \frac{\pi}{M\Gamma} \delta(s - M^2) + \text{PV} \left[\frac{1}{(s - M^2)^2} \right] \quad (\text{I.110})$$

and use the n -body decay phase space

$$d\Phi_n(P, p_1 \dots p_n) = \frac{1}{2\pi} dQ^2 d\Phi_{n-j+1}(P, Q, p_{j+1} \dots p_n) d\Phi_j(Q, p_1 \dots p_j). \quad (\text{I.111})$$

To complete the decay ($d\Phi_j$) we need the δ -function. We can say that the δ -part of the resonant (squared) propagator opens the corresponding line allowing us to define physical POs (t -channel propagators cannot be cut).

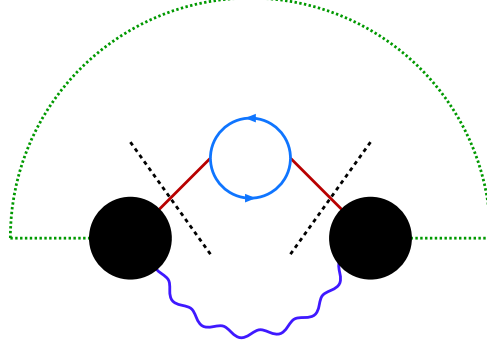
Principal-value cuts are better illustrated in terms of diagrams. First, we need the definition of K-diagrams.

K-diagrams Consider a diagram, and then consider the diagram obtained by joining the final states of the original diagram and its complex conjugate. We next consider a diagram in which the initial state lines are also connected together. The resulting diagram looks like a vacuum to vacuum Feynman diagram except that the initial legs connected together are really “cut” lines, i.e. we do not integrate over the momenta of the initial state lines but only average over their spins, as usual. Such a diagram is called a K diagram, as introduced in Ref. [112]. From a K diagram we can read the corresponding S -matrix.

The K diagram for the single (Z) resonant part of $H \rightarrow \bar{f}f\gamma$ is shown in Fig. I.17. The PO definition of $H \rightarrow Z\gamma$ is based on Fig. I.18, illustrating the PV cut (not to be confused with Cutkosky’s cutting rules).

Consider the process $qq \rightarrow \bar{f}_1 f_1 \bar{f}_2 f_2 jj$, according to the structure of the resonant poles we have different options in extracting physical POs, e.g.

$$\sigma(qq \rightarrow \bar{f}_1 f_1 \bar{f}_2 f_2 jj) \stackrel{PO}{\mapsto} \sigma(qq \rightarrow hjj) \text{Br}(H \rightarrow Z \bar{f}_1 f_1) \text{Br}(Z \rightarrow \bar{f}_2 f_2), \quad (\text{I.112})$$



K-diagram for SR

Fig. I.17: K diagram for the Z resonant part of the process H (dashed green line) $\rightarrow \bar{f}f\gamma$ (wavy blue line).

$$\sigma(qq \rightarrow \bar{f}_1 f_1 \bar{f}_2 f_2 jj) \stackrel{PO}{\longmapsto} \sigma(qq \rightarrow ZZjj) \text{Br}(Z \rightarrow \bar{f}_1 f_1) \text{Br}(Z \rightarrow \bar{f}_2 f_2). \quad (\text{I.113})$$

There are fine points when factorising a process into physical sub-processes (POs): extracting the δ from the (squared) propagator is not enough. Consider an amplitude that can be factorised as follows:

$$A = \mathcal{A}_\mu^{(1)} \Delta_{\mu\nu}(p) \mathcal{A}_\nu^{(2)}, \quad (\text{I.114})$$

where $\Delta_{\mu\nu}$ enters the propagator for a resonant, spin-1 particle. We would like to replace, using conserved currents,

$$\Delta_{\mu\nu} \rightarrow \frac{1}{s - s_c} \sum_\lambda \epsilon_\mu(p, \lambda) \epsilon_\nu^*(p, \lambda), \quad (\text{I.115})$$

where s_c is the complex pole and ϵ_μ are spin-1 polarization vectors. What we obtain is

$$|A|^2 = \frac{1}{|s - s_c|^2} \left| \sum_\lambda \left[A^{(1)} \cdot \epsilon(p, \lambda) \right] \left[A^{(2)} \cdot \epsilon^*(p, \lambda) \right] \right|^2, \quad (\text{I.116})$$

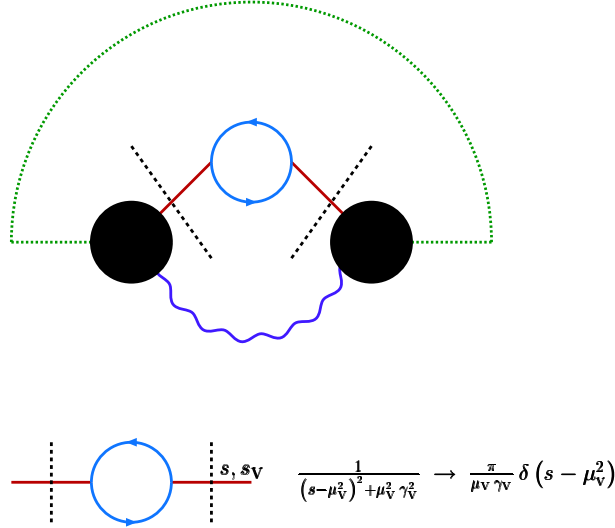
which means that we do not have what we need,

$$\sum_\lambda \left| A^{(1)} \cdot \epsilon(p, \lambda) \right|^2 \sum_\sigma \left| A^{(2)} \cdot \epsilon(p, \sigma) \right|^2. \quad (\text{I.117})$$

Is there a solution? If cuts are not introduced, the interference terms among different helicities oscillate over the phase space and drop out, i.e. we achieve factorisation, see Ref. [113]. In any case, the effects of cuts can be computed.

Another example will be the following:

$$\left. \begin{array}{l} \bar{t}t \\ t(\bar{t})W^-(W^+)\bar{b}(b) \end{array} \right\} \begin{array}{l} \text{DR part of} \\ \text{SR part of} \end{array} \left. \begin{array}{l} \\ \\ \end{array} \right\} WbWb \text{ production}$$



Proceed with Cutkosky's cutting rules

Fig. I.18: PV cuts defining the sub-processes $H \rightarrow Z\gamma$ and $Z \rightarrow \bar{f}f$; μ_V and γ_V parametrise the $V = Z$ complex pole.

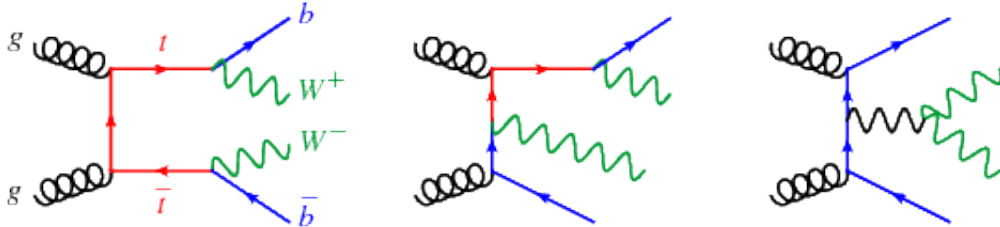


Fig. I.19: Sample of diagrams contributing to $gg \rightarrow WWbb$.

where DR stands for doubly-resonant and SR for single-resonant. Our proposal is: do not “kill” diagrams, write the K-diagrams corresponding to Fig. I.19 for $WbWb$ production and find the appropriate factorisation (i.e. the corresponding δ -parts). Of course, having few accessible discriminating kinematic variables, low statistics and high background is always a problem.

Summarising: the MPE should be understood as an “asymptotic expansion”, not as a NWA. The phase space decomposition is obtained by using the two parts in the propagator expansion: the δ -term is what we need to reconstruct POs, the PV-term (understood as a distribution) gives the remainder and POs are extracted without making any approximation. It is worth noting that, in extracting POs, analytic continuation (on-shell masses into complex poles) is performed only after integrating over residual variables, as done in Ref. [114].

Finally, let us stress again that the extraction of POs comes with a remnant of the under-

lying theory, e.g. at LEP there was a SM-remnant which, however, was shown to be negligible. At LHC this should be examined with great care, process-by-process and PO-by-PO.

I.6 Tools and phenomenological Lagrangian

In Section I.2 we discussed the need for an upgrade of the κ -framework to other frameworks with a more solid theoretical basis. However, for frameworks such as those discussed in Sections I.3 to I.5 to be usable in practice, it is fundamental that they are implemented in the software tools that are capable of interfacing theory and experiment.

Such tools should provide predictions for observables as a function of all relevant input parameters as well as some way of estimating the uncertainty from theory and from phase space effects, such as different acceptances/efficiencies compared to the SM-only predictions used in experimental analyses.

The goal of this section is to provide an overview of some of the available Monte Carlo event generators, and the theoretical basis that underpins automatic computations, highlighting some aspects related to the choice of phenomenological models and EFTs.

I.6.1 Theory: The quest for higher accuracy

With the growing precision of experimental analysis, there is a need to increase the accuracy of the corresponding theoretical predictions. So far, there has been a concerted effort to automate the NLO QCD corrections and this is the current standard that has been implemented in a number of MC generators, some of which are discussed below.

In addition, the NLO EW corrections are known for many processes, for example in Refs. [115, 116], while the QCD corrections for a range of $2 \rightarrow 2$ scattering processes are now known at NNLO and two Higgs production channels have reached N3LO precision, see Refs. [117–119]. Given the considerable effort that is required to reach this accuracy, and NNLO (even NLO EW) computations are far from being automatized.

When considering higher-order contributions, ultraviolet (UV) and infrared (IR) divergences, arising from virtual and real emission diagrams (see Fig. I.20) must be isolated and either removed through the renormalisation procedure (UV) or explicitly cancelled (IR). The UV divergences are cured by using divergent renormalisation counterterms so that the singularities are absorbed into the bare parameters. The counterterms are model-specific, and the renormalisation (especially when considering EW corrections) has to be implemented on a case-by-case basis.

The IR and collinear divergences typically cancel after performing the phase-space integration. In Quantum Electrodynamics (QED) and QCD, the Kinoshita-Lee-Nauenberg theorem [112, 120] ensures IR-finiteness of physical quantities. However, it has not yet been understood how this would work in full generality for an EFT (for example the computation of exclusive QCD jet observables at higher orders requires a method for the subtraction of IR singular configurations arising from multiple radiation of real partons).

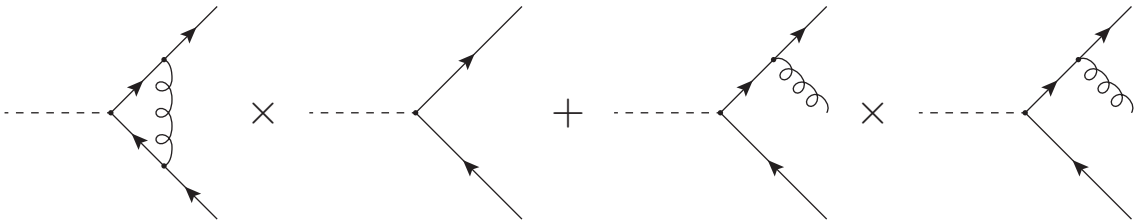


Fig. I.20: Virtual loop contribution and real emission diagrams included in a typical NLO QCD computation.

SMEFT in the IR

As an example, we derive the NLO partial width for the decay $Z \rightarrow \bar{l}l(\gamma)$, considering the QED-like operators of the Warsaw basis (i.e. involving photon fields), after the proper UV renormalisation, done for the SMEFT in Refs. [97, 98, 121–123], the LO amplitude for $Z \rightarrow ll$ reads as follows:

$$A_\mu = g A_\mu^{(4)} + gg_6 A_\mu^{(6)}, \quad (\text{I.118})$$

where the $\text{dim} = 6$ part can be written as

$$A_\mu^{(6)} = \frac{1}{4} \gamma_\mu (V_l + A_l \gamma^5), \quad (\text{I.119})$$

$$V_l = \frac{s_\theta^2}{c_\theta} (4s_\theta^2 - 7) a_{AA} + c_\theta (1 + 4s_\theta^2) a_{ZZ} + s_\theta (4s_\theta^2 - 3) a_{AZ} \\ + \frac{1}{4c_\theta} (7 - s_\theta^2) a_{\phi D} + \frac{2}{c_\theta} a_{\phi l V}, \quad (\text{I.120})$$

$$A_l = \frac{s_\theta^2}{c_\theta} a_{AA} + c_\theta a_{ZZ} + s_\theta a_{AZ} - \frac{1}{4c_\theta} a_{\phi D} + \frac{2}{c_\theta} a_{\phi l A}, \quad (\text{I.121})$$

with $a_{\phi l A} - a_{\phi l V} = 2a_{\phi l}$ and $a_{\phi l A} + a_{\phi l V} = 2(a_{\phi l}^{(3)} - a_{\phi l}^{(1)})$. The IR/collinear part of the one-loop virtual and real emission corrections take respectively the forms

$$\Gamma(Z \rightarrow \bar{l}l) \Big|_{\text{div}} = -\frac{g^4}{384\pi^3} M_Z s_\theta^2 \mathcal{F}^{\text{virt}} \left[\Gamma_0^{(4)} (1 + g_6 \Delta\Gamma) + g_6 \Gamma_0^{(6)} \right], \\ \Gamma(Z \rightarrow \bar{l}l\gamma) \Big|_{\text{div}} = \frac{g^4}{384\pi^3} M_Z s_\theta^2 \mathcal{F}^{\text{real}} \left[\Gamma_0^{(4)} (1 + g_6 \Delta\Gamma) + g_6 \Gamma_0^{(6)} \right], \quad (\text{I.122})$$

where IR/collinear divergences are contained in $\Gamma_0^{(4)}$ and $\Gamma_0^{(6)}$, $\mathcal{F}^{\text{virt}}$ and $\mathcal{F}^{\text{real}}$ are squared matrix elements and $\Delta\Gamma$ contains contributions from $\text{dim} = 6$ operators. Adding up these contributions and defining the linear combination of Wilson coefficients, the final result for the decay width is an IR/collinear-free quantity, given by

$$\Gamma_{\text{QED}}^1 = \frac{3\alpha}{4\pi} \frac{G_F M_Z^3}{24\sqrt{2}\pi} \left[(v_l^2 + 1) \left(1 + g_6 \delta_{\text{QED}}^{(6)} \right) + g_6 \Delta_{\text{QED}}^{(6)} \right], \quad (\text{I.123})$$

where $v_l = 1 - 4s_\theta^2$, $\delta_{\text{QED}}^{(6)}$, $\Delta_{\text{QED}}^{(6)}$ are driven by the presence of $\text{dim} = 6$ operators and can be cast in the following form:

$$\delta_{\text{QED}}^{(6)} = 2(2 - s_\theta^2) a_{AA} + 2s_\theta^2 a_{ZZ} + 2\frac{c_\theta^3}{s_\theta} a_{AZ} - \frac{1}{2} \frac{c_\theta^2}{s_\theta} a_{\phi D}, \\ \Delta_{\text{QED}}^{(6)} = (1 - 6v_l - v_l^2) \frac{1}{c_\theta} \left(s_\theta a_{AA} - \frac{1}{4} a_{\phi D} \right) + (1 + 2v_l - v_l^2) \left(a_{ZZ} + \frac{s_\theta}{c_\theta} a_{AZ} \right) \\ + \frac{512}{13} v_l a_{AZ} + \frac{2}{c_\theta} (a_{\phi l A} + v_l a_{\phi l V}). \quad (\text{I.124})$$

This result is important, not only for extending IR/collinear finiteness to the SMEFT but also because it shows that higher dimensional operators enter everywhere: signal, background and radiation. The latter is particularly relevant when one wants to include (SM-deconvoluted)

EW precision observable constraints in a fit to Higgs data. Since LEP POs are (mostly) SM-deconvoluted⁷, the effect of dim = 6 operators on the deconvolution procedure should be checked carefully.

In Eq. (I.123) $\Gamma_0 = G_F M_Z^3 / (24\sqrt{2}\pi) = 82.945(7)$ MeV is the standard partial width and the LEP definition is

$$\Gamma_l^0 = \frac{\Gamma_l}{1 + \frac{3}{4} \frac{\alpha(M_Z^2)}{\pi}}. \quad (\text{I.125})$$

Once again, fitting Γ_l^0 as reported at LEP with the SMEFT is not consistent; note that in Eq. (I.124) there are three PTG coefficients (i.e. not suppressed), $a_{\phi D}$ and $a_{\phi l V}, a_{\phi l A}$.

I.6.2 Phenomenological Lagrangians

Since we do not know the structure of the next SM, it is necessary to have a systematic way to look for deviations in the experimental data. Also, the moment we observe a deviation, it will be important to have the technology to interpret it properly.

There are two distinguished steps in this procedure: (a) the observation and (b) the interpretation of the deviation. In order to address (a), an approximate framework can be sufficient, but to move forward and interpret successfully the outcome of the experiments, a more solid and rigorous framework (for instance an EFT) is necessary.

We consider here *phenomenological models*, intended as models that are not completely rigorous from the theoretical point of view, but that can be used to guide searches. Indeed, fully consistent models like EFTs often require a large number of parameters, that makes them impractical. With *phenomenological Lagrangian* we refer here to the Lagrangian related to a *phenomenological model*. Because of their approximate nature, these Lagrangians are not adequate to provide NLO results.

In the literature it is possible to find many phenomenological models, but it is not always clear how to distinguish between these models (conceived to address point (a)), from theoretically motivated models (which are essential to address (b)). In order to look for deviations in a particular observable, phenomenological Lagrangians usually consist of the SM Lagrangian extended by some effective interactions selected from a basis of higher-dimensional operators. Depending on the procedure used to select such additional interactions, the obtained model will be also usable to address (b).

It is important to note that applying a certain field transformations to an EFT basis some operators might drop out, and the basis obtained in this way should give the same physics as before. It was shown in Refs. [124, 125] that this is in principle true, but only at the level of the (renormalised) S -matrix, and not at the Lagrangian level. Hence, a field can be transformed using linear or non-linear transformations (even non-local, at the price of introducing ghosts) and the S -matrix (hence the predictions for the physical quantities) will not change.

Nevertheless, as the physics is encoded in the S -matrix and not in the Lagrangian, it is not straightforward to get the same physics from the transformed Lagrangian. This problem was raised in Ref. [126] (see also Ref. [127]), where it is shown in an example that when a generic (non-gauge) transformation is applied to a field, it is necessary to adjust the external wavefunction renormalisation factors in order to recover the original S -matrix from the transformed Lagrangian.

⁷There are several levels of deconvolution and the most important are: single-deconvolution (SD), giving the kernel cross-sections without initial state QED radiation, but including all final-state correction factors; double-deconvolution (DD), giving the kernel cross-sections without initial- and final-state QED radiation and without any final-state QCD radiation

In other words, starting from an EFT Lagrangian \mathcal{L}_{EFT} , in general we cannot transform fields and pretend to use the transformed Lagrangian $\mathcal{L}'_{\text{EFT}}$ in a simple way as we would do with \mathcal{L}_{EFT} . If the fields are transformed with a non-gauge transformation, one would get different physical predictions from \mathcal{L}_{EFT} and $\mathcal{L}'_{\text{EFT}}$.

In conclusion, we should ask ourselves if it is worth applying non-linear field transformations to transform away unpleasant operators from a basis: if this is done consistently, the result for a physical quantity will not change (but its computation will be cumbersome); if this is not done with care, the risk is to downgrade a rigorous theory to a phenomenological model, not suitable to inspect the nature of deviations.

Examples of phenomenological models

To clarify the concept of phenomenological models, in the following we give some simple examples. In the first, we explain how to build a phenomenological Lagrangian that provides, at LO, rescaled SM production and decay amplitudes as in the κ -framework. The second example is provided by the Higgs Characterization framework as it was proposed in Ref. [128].

SM with rescaled Higgs couplings Let us consider the κ -framework which (as explained in Section I.2) was clearly proposed to address a type-(a) problem. A phenomenological Lagrangian for the framework can be obtained from the SM Lagrangian (supplemented by effective, SM-valued gluon-gluon-Higgs and photon-photon-Higgs couplings), with all the Higgs couplings modified by the introduction of multiplicative coefficients accordingly to Table I.11.

Indeed, using this Lagrangian to compute the LO production cross sections and Higgs partial decay widths, it is possible to obtain the defining relations for the coupling scale factors given in Table 2 of Ref. [9].

| SM coupling | Rescaling factor |
|-------------------|------------------|
| WWH | κ_W |
| ZZH | κ_Z |
| ttH | κ_t |
| bbH | κ_b |
| ggH (effective) | κ_g |
| AAH (effective) | κ_γ |
| $\tau\tau H$ | κ_τ |

Table I.11: Coupling factors in the κ -framework, as proposed in Ref. [9] (see Table 2).

Higgs Characterization framework The Higgs characterization framework from Ref. [128] can be thought of as the SM, with the Higgs boson replaced by a resonance X_J of mass 125 GeV, where for the sake of generality the spin can take the values $J = 0, 1$ or 2 , supplemented by interaction terms coming from $\text{dim} = 6$ operators. These terms come from hypothetical interactions of the Higgs-like resonance X_J with a new heavy sector, which resides at the scale Λ .

In the framework, all the $\text{dim} = 6$ operators which do not include the scalar field X_J are neglected. Moreover, all the interaction terms involving more than one X_J field, or more than three fields are neglected. This leads to a very compact phenomenological Lagrangian, but one has to keep in mind that the predictions worked out within the framework are applicable

consistently only when working at LO with production or decay processes involving one and only one X_J particle.

The phenomenological Lagrangian for the case $J = 0$ consists, as given in the main reference, in

$$\mathcal{L}_{\text{HC},0} = \mathcal{L}_{\text{SM}-H} + \mathcal{L}_0, \quad (\text{I.126})$$

where the fermionic interactions of the field X_0 , related to the mass eigenstates of the 125 GeV resonance, are given by the Lagrangian

$$\mathcal{L}_0^f = - \sum_{f=t,b,\tau} \bar{\psi}_f (c_\alpha \kappa_{Hff} g_{Hff} + i s_\alpha \kappa_{Aff} g_{Aff} \gamma_5) \psi_f X_0, \quad (\text{I.127})$$

and interaction terms with vector bosons are gathered in \mathcal{L}_0^V :

$$\begin{aligned} \mathcal{L}_0^V = & \left\{ c_\alpha \kappa_{\text{SM}} \left[\frac{1}{2} g_{HZZ} Z_\mu Z^\mu + g_{HWW} W_\mu^+ W^{-\mu} \right] \right. \\ & - \frac{1}{4} \left[c_\alpha \kappa_{H\gamma\gamma} g_{H\gamma\gamma} A_{\mu\nu} A^{\mu\nu} + s_\alpha \kappa_{A\gamma\gamma} g_{A\gamma\gamma} A_{\mu\nu} \tilde{A}^{\mu\nu} \right] \\ & - \frac{1}{2} \left[c_\alpha \kappa_{HZ\gamma} g_{HZ\gamma} Z_{\mu\nu} A^{\mu\nu} + s_\alpha \kappa_{AZ\gamma} g_{AZ\gamma} Z_{\mu\nu} \tilde{A}^{\mu\nu} \right] \\ & - \frac{1}{4} \left[c_\alpha \kappa_{Hgg} g_{Hgg} G_{\mu\nu}^a G^{a,\mu\nu} + s_\alpha \kappa_{Agg} g_{Agg} G_{\mu\nu}^a \tilde{G}^{a,\mu\nu} \right] \\ & - \frac{1}{4} \frac{1}{\Lambda} \left[c_\alpha \kappa_{HZZ} Z_{\mu\nu} Z^{\mu\nu} + s_\alpha \kappa_{AZZ} Z_{\mu\nu} \tilde{Z}^{\mu\nu} \right] \\ & - \frac{1}{2} \frac{1}{\Lambda} \left[c_\alpha \kappa_{HWW} W_{\mu\nu}^+ W^{-\mu\nu} + s_\alpha \kappa_{AWW} W_{\mu\nu}^+ \tilde{W}^{-\mu\nu} \right] \\ & \left. - \frac{1}{\Lambda} c_\alpha \left[\kappa_{H\partial\gamma} Z_\nu \partial_\mu A^{\mu\nu} + \kappa_{H\partial Z} Z_\nu \partial_\mu Z^{\mu\nu} + (\kappa_{H\partial W} W_\nu^+ \partial_\mu W^{-\mu\nu} + \text{h.c.}) \right] \right\} X_0. \end{aligned} \quad (\text{I.128})$$

Taking into account the fact that X_0 is the physical Higgs field, this phenomenological Lagrangian is very compact compared with a full EFT. This is due to the selection of terms explained above. For instance, consider the fermion-Higgs operators of the Warsaw basis given in Table 2 of Ref. [94]: among all the fermion-Higgs interactions, only terms coming from the operators reported in the upper-right sector of the table (labelled as $\psi^2 \varphi^3$) survive the selection. The terms labelled as $\psi^2 X \varphi$ give four-point Higgs interactions and are neglected. In the operators $\psi^2 \varphi^2 D$, in order to have only three-point interactions involving one Higgs field, one doublet is replaced by the Higgs VEV and the covariant derivative is replaced by the partial derivative, giving a vanishing contribution:

$$\begin{aligned} \left(\varphi^\dagger i \overleftrightarrow{D}_\mu \varphi \right) (\bar{\psi} \gamma^\mu \psi) & \longrightarrow i \left(v \overleftrightarrow{D}_\mu X_0 + X_0 \overleftrightarrow{D}_\mu v \right) (\bar{\psi} \gamma^\mu \psi), \\ & \longrightarrow i \left[v \left(\partial_\mu X_0 \right) - v \left(X_0 \overleftarrow{\partial}_\mu \right) \right] (\bar{\psi} \gamma^\mu \psi) = 0. \end{aligned} \quad (\text{I.129})$$

In a similar way also the operator $Q_{\varphi ud}$ is killed by the selection and there are no terms involving derivatives of X_0 in the Lagrangian \mathcal{L}_0^f reported in Eq. (I.127).

I.6.3 Tools

The aim of the first part of this review was to present and discuss some of the techniques that can be used to observe and interpret possible deviations that might show up at the LHC in the next years of data taking.

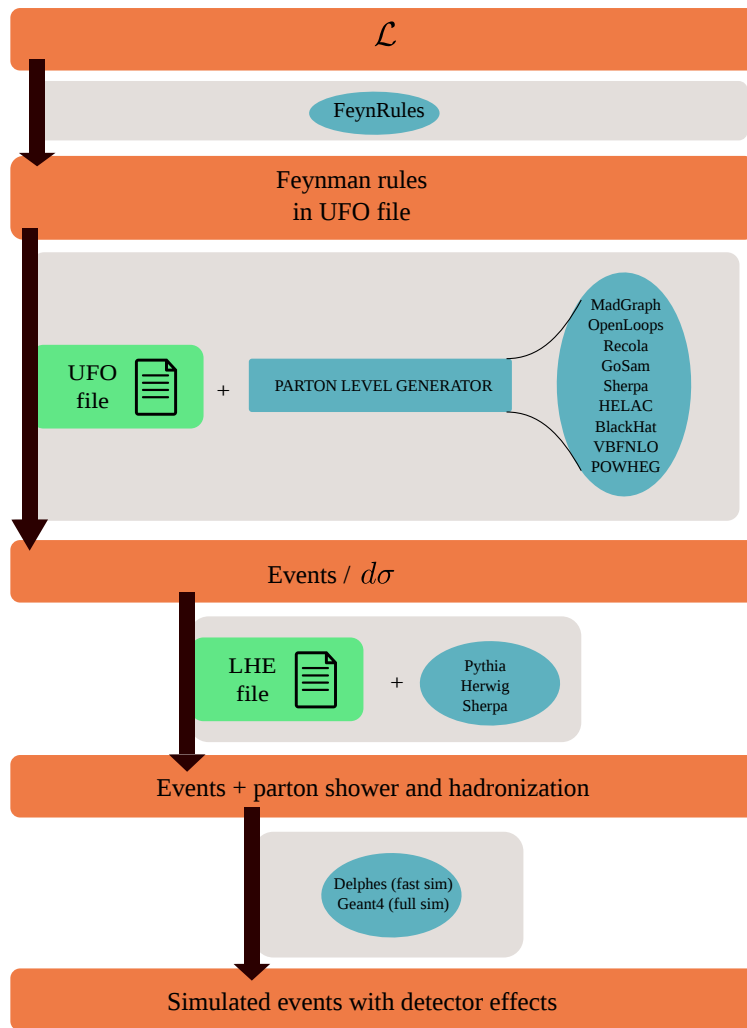


Fig. I.21: Work flow for the simulation of events using MC generators.

Regarding the EFTs and the phenomenological models, we addressed how Lagrangians, that are suitable to understand possible NP effects, can be built. Of course, as our practical way to observe elementary phenomena is through detector experiments, Lagrangians are not the full story.

To make a connection with the collected data it is necessary to have control of the hard scattering process, and also, we must be able to have a full simulation of the processes that we observe in the experiments. In Fig. I.21 we present schematically the steps that are necessary to have a full simulation, starting from the Lagrangian of the considered theory, and we report some of the available tools.

From the starting Lagrangian, the Mathematica package FeynRules, from Ref. [150] can be used to derive the Feynman rules for the theory. These can be exported in a UFO file, as defined in Ref. [111] which, together with a parton level generator (see Table I.12 for more details), can be used to generate events for the considered model.

The output of a parton level generator can be a differential distribution, but the generated

| Tool | LO | NLO QCD | Web page | References |
|-----------|------------------------|---------|---|----------------|
| MadGraph | ✓ | ✓ | http://madgraph.physics.illinois.edu/ | [129] |
| OpenLoops | | ✓ | https://openloops.hepforge.org/ | [130] |
| Recola | | ✓ | https://recola.hepforge.org/ | [131–136] |
| GoSam | | ✓ | https://gosam.hepforge.org/ | [137, 138] |
| Sherpa | ✓ | | https://sherpa.hepforge.org/trac/wiki | [139, 140] |
| HELAC | ✓ | ✓ | http://helac-phegas.web.cern.ch/helac-phegas/ | [141–143] |
| Tool | Process | | Web page | References |
| BlackHat | Multi-jet processes | | https://blackhat.hepforge.org/ | [144] |
| VBFNLO | Vector boson fusion | | https://www.itp.kit.edu/vbfnlo/wiki/doku.php | [145–147] |
| POWHEG | Various (see web page) | | http://powhegbox.mib.infn.it/ | [15, 148, 149] |

Table I.12: Web pages and references for some widely-used parton level generators available for automatic calculations.

events can also be stored in a Les Houches Event (LHE) file, a format that was introduced in Refs. [151, 152], which in turn can be used to simulate showers and hadronisation of the final states using a dedicate software like Pythia, from Refs. [20, 153], Herwig, from Refs. [154–161] or Sherpa, from Refs. [139, 140]).

Further, detector effects can be simulated using Delphes, described in Ref. [162] or more commonly, Geant4, from Refs. [21, 163, 164], which can be used respectively for fast (with simple smearing effects) or full (but time -consuming) simulations.

I.6.4 Connection between κ s, POs and Wilson coefficients

To finalise, in this section the connection between κ s, POs and Wilson coefficients is studied. An example is given showing how Wilson coefficients collapse into a smaller number of more general objects which we call physical POs, see Sect II.1.8 of Ref. [37]. Then we study the strategy to simultaneously extract the values of such parameters from data, via a likelihood minimisation. Technical issues arise at this point, given the high dimensionality of the theory parameters space. When going from SM to SMEFT the scattering amplitudes are modified as

$$\mathcal{A}_{\text{SMEFT}}^{\text{LO}} = \sum_{i=1,n} \mathcal{A}_{\text{SM}}^{(i)} + ig_6 \kappa_c \mathcal{A}_{\text{SMEFT}}^{\text{NLO}} = \sum_{i=1,n} \kappa_i \mathcal{A}_{\text{SM}}^{(i)} + ig_6 \kappa_c + g_6 \sum_{i=1,N} a_i \mathcal{A}_{\text{nf}}^{(i)}, \quad (\text{I.130})$$

with $g_6 = (\sqrt{2}G_F\Lambda^2)^{-1}$. The last term contains all the non-factorisable loop contributions. In there, we find the Wilson coefficients a_i , and the factors κ_i are linear combinations of the a_i .

Now, to understand how to connect POs with Wilson coefficients let us consider the process $h(P) \rightarrow \gamma_\mu(p_1)\gamma_\nu(p_2)$. The corresponding amplitude can be written as

$$\mathcal{A}_{\text{hAA}}^{\mu\nu} = i\mathcal{I}_{\text{hAA}} T^{\mu\nu} = -i \frac{2}{v_F M_h^2} \epsilon_{\gamma\gamma} T^{\mu\nu}, \quad (\text{I.131})$$

where $\epsilon_{\gamma\gamma}$ is a PO which is based on quantities that can be extracted from Green's functions. This can be conveniently rewritten as

$$\mathcal{I}_{\text{hAA}} = \frac{g_R^3 s_W^2}{8\pi^2} \sum_{I=W,t,b} \rho_I^{\text{hAA}} \mathcal{I}_{\text{hAA};\text{LO}}^I + g_F g_6 \frac{M_h^2}{M_W} a_{\text{AA}} + \frac{g_F^3 g_6}{\pi^2} \mathcal{I}_{\text{hAA}}^{\text{nf}}. \quad (\text{I.132})$$

Introducing $g_F^2 = 4\sqrt{2}G_F M_W^2$ and $c_W = M_W/M_Z$ and deriving

$$\kappa_I^{\text{hAA}} = \frac{g_F^3 s_W^2}{8\pi^2} \rho_I^{\text{hAA}}, \quad \kappa_c^{\text{hAA}} = g_F \frac{m_H^2}{M_W} a_{\text{AA}} \quad (\text{I.133})$$

and use Eq. (I.72) where a_{ij} are Wilson coefficients. The ρ factors are process dependent and are given by

$$\rho_1^{\text{proc}} = 1 + g_6 \Delta \rho_1^{\text{proc}}. \quad (\text{I.134})$$

In addition to this there are other non-factorizable contributions. This means that the κ factors can also be introduced at loop level, as combination of Wilson coefficients. But to do so it is needed to introduce process dependent and non-factorizable contributions, as described in Ref. [98]. Therefore at LO we can see the relation between the intermediate PO $\epsilon_{\gamma\gamma}$ and a Wilson coefficient a_{AA} :

$$\epsilon_{\gamma\gamma} = -\frac{1}{2} \frac{v_F}{m_h^2} \mathcal{I}_{\text{hAA}}, \quad \mathcal{I}_{\text{hAA}} = \mathcal{I}_{\text{hAA}}^{\text{SM}} + g_F g_6 \frac{m_h^2}{M_W} a_{\text{AA}}. \quad (\text{I.135})$$

Therefore with this formulation full consistency is achieved. We have some physical observable that is related to an EFT and does not have the inconsistencies of the interim framework (as highlighted in Section I.2). Then the question to answer is whether or not it is possible to extract these parameters from data in a global and simultaneous fit.

The main problem is the following: it is not clear if ATLAS/CMS can implement such a large number of independent parameters in the currently available fitting codes. They require speeds of recalculations with new input parameters of < 1 ms on average on a single CPU. However, they could pre-compute and transfer the results of these calculations into a generalized n -dimensional polynomial which could then enter the experimental fits.

Let us define for simplicity $P(X_1 = \mu_1, X_2 = \mu_2, \dots, X_m = \mu_m)$ the probability of measuring X_i with an μ_i expectation from the theoretical model (which can depend on some POs or Wilson coefficients of a $\text{dim} = 6$ EFT). The index m runs over all the performed measurements, such as STXS, as well as BRs and fiducial measurements.

For the sake of notation, let us call X_i each measurement, σ_i its error and ρ_{ij} its correlation factor with another measurement X_j . We also call μ_i the expected value of such a measurement. It depends on the Wilson coefficients of the underlying EFT or on POs, namely $\mu_i(k_1, \dots, k_p)$. Supposing each measurement follows a Gaussian distribution, which is justified by a generalized central limit theorem, the likelihood function becomes:

$$f_{X_1, \dots, X_m}(\mu_1, \dots, \mu_m) \propto \frac{1}{\Sigma} \exp \left[(X - \mu)^T \Sigma^{-1} (X - \mu) \right], \quad \text{with } \Sigma_{ij} = \sigma_i \sigma_j \rho_{ij}. \quad (\text{I.136})$$

All the errors and correlations between measurements are encoded in Σ . Taking into account all STXSs bins from all stages and all branching fraction measurements, the order of m is $\mathcal{O}(100)$.

The minimisation of such a function is challenging in many aspects. Firstly all the relations $\mu_i = \mu_i(k_1, \dots, k_p)$ are needed. These relations are most of the times not analytical and have to be computed through MC simulations. The available tools which can do it were listed in Table I.12.

Various MC simulations need to be generated with different sets of input values for the parameters of the theoretical model implemented. From there, a continuous parametrisation of the observables of interest can be extrapolated. The finer the grid of MC simulation is, the more accurate is the extrapolation. If p parameters are changed and each of them can take n different values, the total number of input simulations is n^p .

For example in $\dim = 6$ EFT, $p \approx 59$, and in general $p \approx 50$. If every parameter takes ~ 10 values (SM value, and some values around it), the number of simulations grows up to $\approx 10^{50}$ which is an unaffordable number.

Luckily, not all coefficients contribute to every observable, and, as explained in the example at the beginning of this section, often Wilson coefficients do combine into more general objects which are smaller in number. Typically less than 10 coefficients enter in the calculation of a BR or cross section.

On the other side, the number of values which parameters can take, can be minimised thanks to morphing techniques. Given an observable, polynomial function of parameters \vec{k} (this is true if there is a polynomial dependence of the scattering amplitude on the theory parameters), such techniques allow to obtain the value of the observable in a new point of the parameters space, as a function of a previous computed values of the observable. Labelling \vec{k}_i the point of the parameters phase space where the observable has been calculated, it means:

$$O_{\text{output}} = O(\vec{k}_{\text{new}}) = \sum_{j=0}^{N_{\text{input}}} w(\vec{k}_{\text{new}}, \vec{k}_j) \cdot O(\vec{k}_j), \quad (\text{I.137})$$

where $w(\vec{k}_{\text{new}}, \vec{k}_j)$ is a simple weight function, correlating the two parameters' phase space points \vec{k}_{new} and \vec{k}_j . This reduces the number of parameter variations to be simulated, making the number of MC samples to be produced to a reasonable number.

Once all the $\mu_i = \mu_i(k_1, \dots, k_p)$ relations have been obtained, the minimisation of the likelihood function has to be performed. Minimising a function requires multiple calls to it and if it is difficult to evaluate, the computing time to obtain the result can be large. For a multivariate Gaussian distribution as the one introduced in Eq. (I.136), the order of the problem depends on the number of points in the space of parameters which have to be evaluated ($G \approx n^p$), as well as with the dimension of vector of measurements, $\dim[\vec{X}] = \dim[\vec{\mu}] = m$. The order of the full calculation is found to be $G \cdot m!$ which in the case of $m = (100)$, makes it impossible to solve with the available tools, since $100! \approx 10^{150}$.

One possible solution to reduce the order of the problem could be to group observables which depend only on a subset of theory parameters, in order to factorise the problem into smaller dimension ones. If \vec{X}_a is a subset ($\dim[\vec{X}_a] = m_a < \dim[\vec{X}]$) of measurements for which only the subset \vec{k}_a ($\dim[\vec{k}_a] = p_a < \dim[\vec{k}]$) of all parameters enter its theoretical calculation, the order of the problem would be reduced to:

$$G \cdot m! \approx n^p \cdot m! \longrightarrow \prod_a G_a \cdot m_a! \approx \prod_a n_a^{p_a} \cdot m_a!, \quad \sum_a p_a = p \quad , \quad \sum_a m_a = m, \quad (\text{I.138})$$

by neglecting correlations between those observables. In the case of STXSs, this would mean grouping all STXS *bins* from different stages in terms of production modes. Strong correlations anyway cannot be neglected, since they change not only the error on the fitted parameters, but also their central value. Thus, if two bins from different production modes are found to be strongly correlated, factorisation is not possible. To give a numerical example, imagine it is possible to split the whole set of measurements in 10 subsets of dimension 10 each. To each of these subsets let us say that only 5 parameters of the initial 50 contribute. This translates into $m_a = 10, p_a = 5$ for each $a \in (1, 10)$. Let us also fix $n_a = 10$. The order of the problem decreases from 10^{160} to 10^{13} . The fit performed in this way is simultaneous for every subset of parameters, but not global.

Another way to reduce the order of the likelihood minimisation is to extract one parameter at a time, while profiling all the others, and repeating the procedure for all of them. The idea

of profiling has been introduced in Section I.2.2 and it is used in general in global fits up to now. This approximation makes the fit global, but not simultaneous, since every parameter is extracted separately.

In the case that no big deviation is found with respect to the SM, an expansion of the likelihood function around $X_i = \mu_i^{\text{SM}} = \mu_i(k_1^{\text{SM}}, \dots, k_1^{\text{SM}})$ is also possible. In the case of no discovery, the condition

$$X_i - \mu_i^{\text{SM}} < 5\sigma_i \quad (\text{I.139})$$

holds for every i .

Summarising, the minimisation of the full multivariate likelihood in a global and simultaneous way is a difficult problem which can not be solved exactly with the current available tools. A number of approximations can be applied to the problem to make it easier and thus solvable. The validity of such approximations have to be checked carefully, since neglecting strong correlations can also change central values of the parameters being fitted.

I.7 Summary

After the discovery of the Higgs boson at the LHC we still have a conventional vision: some very different physics occurs at Planck scale, and the SM is just an effective field theory. What about the next SM? A new weakly coupled renormalisable model? A tower of EFTs?

The SMEFT framework is useful because one can set limits on the effective coefficients in a model-independent way. This is why SMEFT in the bottom-up approach is so useful: we do not know what the tower of UV completions is (or if it exists at all) but we can formulate the SMEFT and perform calculations with it without needing to know what happens at arbitrarily high scales.

On the other hand interpreting such limits as bounds on UV models does require some assumption of the UV dynamics. Alternatively, is the SM close to a fundamental theory?

Understanding the Higgs boson properties is a pillar of the present paradigm. For a theory or hypothesis to count as scientific it ought to be falsifiable in principle. In that regard, the SM is a good falsifiable hypothesis. Nevertheless it is important to emphasise that the SM has withstood risky tests that it could have easily failed.

In this review we discussed the frameworks adopted during Run 1 at the LHC as well as some further improvements on the former. Understanding that the main accent should be put on observables (i.e. quantities related to an S -matrix) is important, and mapping those observables to a Lagrangian is a truly subtle affair, that we must understand and that cannot really be demoted.

In our view the problem is not how to imagine wild scenarios, but rather how to arrive at the correct scenario by making only small steps, without having to make unreasonable assumptions.

Finally, we want point out it is important to preserve the original data, not just our current interpretation of the results. The estimate of the missing higher order terms can change over time, modifying the lessons we have drawn from the data and projected into the parameters and implementation of the SMEFT.

Furthermore, considering projections for the precision to be reached in LHC Run 2 analyses, LO results for interpretations of the data in the SMEFT are challenged by consistency concerns and are not sufficient if the cut-off scale is in the few TeV range. The assignment of a theoretical error for SMEFT analyses is always important.

Chapter II

ϕ_η^* : A new variable for studying $H \rightarrow \gamma\gamma$ decays

II.1 Overview

After the landmark discovery of a Standard Model-like Higgs boson [1,2] in 2012 the main thrust of the LHC physics program has shifted to measuring its precise properties. The combination of experimental results from ATLAS and CMS using data taken in Run 1 at $\sqrt{s} = 7$ and 8 TeV [12] demonstrated that the properties are consistent with the predictions of the Standard Model (SM). At the same time, no convincing evidence for physics Beyond the Standard Model (BSM) was found.

Since 2015, the LHC has been operating at the higher centre of mass energy of 13 TeV. The cross sections for Higgs boson production are of course larger, but more importantly, the anticipated integrated luminosity for Run 2 is five times larger. This increased data set will enable a more precise determination of the Higgs boson properties. The current state of the art for predictions of production and decay of the Higgs bosons, and for the measurement of the Higgs boson properties is summarised in the Handbook of LHC Higgs cross sections: 4. Deciphering the nature of the Higgs sector (YR4) [37].

The main Higgs boson production mode takes place through gluon fusion, shown schematically in Fig. II.1 where the shaded blob represents all possible interactions between gluons and the Higgs boson. Because of the very narrow width of the Higgs boson, the invariant mass of the gluon pair is concentrated around m_H .

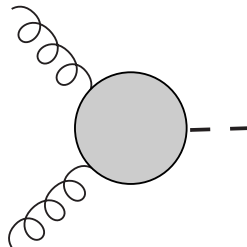


Fig. II.1: Schematic diagram showing the production of a Higgs boson via gluon fusion.

In the SM, the Higgs boson couples directly to the quarks,

$$\mathcal{L}_{\text{fermion}} = - \sum_q \kappa_q \frac{m_q}{v} \bar{q}qH, \quad (\text{II.1})$$

and the interaction is simply mediated through the quark loop shown in Fig. II.2(a) and $\kappa_q = 1$. The dominant contribution is from the top quark, but in certain kinematic regions the charm and bottom contributions are significant.

On the other hand, new physical effects not described by the SM, could also contribute to this process. For example, a new heavy particle, X , of mass m , that couples to both gluons and the Higgs boson will change the rate according to the mass, spin, colour and couplings [165]. The rate for colour octet particles is eight times higher than for colour singlets. As a concrete example, a massive colour triplet scalar particle, \tilde{q} , produces contributions as shown in Fig. II.2(b).

In the limit where the particles circulating in the loop are heavy, $m \gg m_H$, the interaction

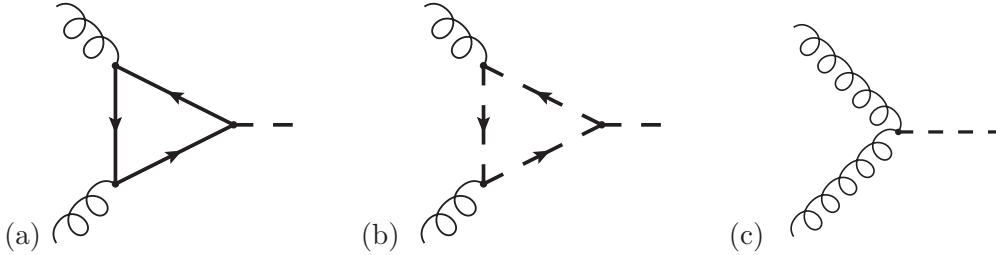


Fig. II.2: Representative Feynman diagrams showing the production of a Higgs boson via gluon fusion for (a) fermion loops (b) scalar loops and (c) the effective interaction.

is described by the effective interaction shown in Fig. II.2(c),

$$\mathcal{L}_{\text{eff}} = c_g \frac{\alpha_S}{12\pi} \frac{H}{v} G_{\mu\nu}^a G^{a\mu\nu}. \quad (\text{II.2})$$

When the mass of the particle is produced by the Higgs mechanism, the heavy particle does not decouple in the $m \gg m_H$ limit and this leads to a contribution to c_g .

Because the kinematics of the $2 \rightarrow 1$ process is so simple, different combinations of particles circulating in the loop simply affect the overall normalisation and measurements of the total cross section are not able to discriminate the mass scales of the various particles that mediate the ggH interaction. This is a consequence of the Higgs low energy theorem that entangles short- and long-distance effects [166, 167]. The normalisation is chosen such that (ignoring contributions from the light quarks and terms $\mathcal{O}(m_H^2/m_t^2)$) the total inclusive rate simply depends on the squares of the sum of two terms proportional to κ_t and c_g respectively [168],

$$\sigma_{\text{incl}}(\kappa_t, c_g) \sim (\kappa_t + c_g)^2 \sigma_{\text{incl}}^{\text{SM LO}(t)}. \quad (\text{II.3})$$

As a result, the measurement of the inclusive rate does not disentangle the effects of κ_t and c_g .

In the SM, $\kappa_q = 1$. However, in the case of the top loop where $m_t > m_H$ it is common to make predictions for the gluon fusion cross section using the effective interaction of Eq. (II.2), i.e. setting $\kappa_q = 0$ and $c_g = 1$. This is frequently called the Higgs Effective Field Theory (HEFT).

Since κ_t and c_g can be affected by new physics effects, it is clear that it is important to make measurements which allow an independent determination of c_g and κ_t . This requires a new energy scale much higher than the top-quark mass such that the low energy theorem no longer holds [169] and the degeneracy of κ_t and c_g breaks. This is done by recoiling the Higgs bosons against an additional jet as shown in Fig. II.3, and studying the process at high p_{TH} [95, 168, 170–175]. The QCD radiation acts as a probe to resolve the interaction, and at large p_{TH} there is sensitivity to particles with a mass $m \sim p_{TH}$. As a consequence, Higgs boson production at large transverse momentum has been widely studied.

In the SM, the Leading-Order (LO) heavy quark contribution occurs at $\mathcal{O}(\alpha_S^3)$ and arises through loop diagrams [176–179] such as Fig. II.4(a). The $\mathcal{O}(\alpha_S^4)$ Next-to-Leading Order (NLO) corrections including finite top-mass effects involve complicated two-loop graphs [180] and are not currently known exactly, although efforts have been made to estimate their size [181–183].

The hadronic radiation probes the internal structure of the hard scattering and the effective interaction also receives radiative corrections as shown in Fig. II.4(c). In this case, the NLO corrections [184–187] and $\mathcal{O}(\alpha_S^5)$ Next-to-Next-to-Leading Order (NNLO) corrections [188–193] are known.

Similarly, new heavy particles (X) will also receive different radiative corrections shown for example in Fig. II.4(b) that depend sensitively on the mass of the particle and on the transverse

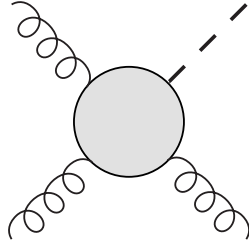


Fig. II.3: Schematic diagram showing the production of a Higgs boson with transverse momentum via gluon fusion.

momentum. When the transverse momentum is large compared to m , the new physics degrees of freedom are resolved and can in principle be isolated from the SM contributions.

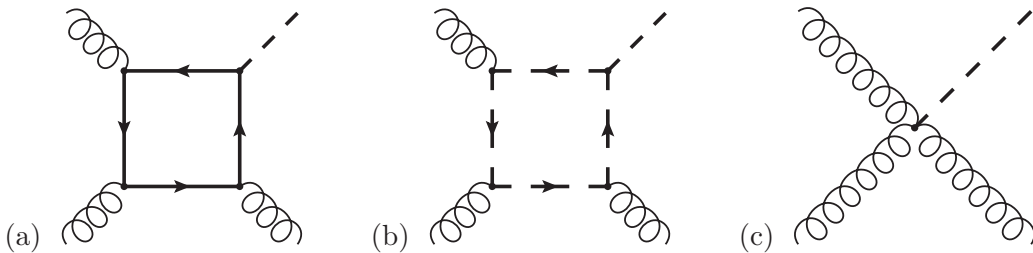


Fig. II.4: Representative Feynman diagrams for (a) fermion loops (b) scalar loops and (c) the effective interaction for the production of a Higgs boson via gluon fusion at large transverse momentum.

Of course, the Higgs boson decays, and the transverse momentum can only be constructed from the decay products. One of the cleanest decay channels is the rare $H \rightarrow \gamma\gamma$ decay which has a small branching ratio of $\sim 2.3 \cdot 10^{-3}$ so that current measurements are limited by statistics. This will improve with time with the continued operation of the LHC.

The purpose of this report is to propose a new and complementary observable for studying Higgs boson production at large transverse momentum in the case where the Higgs boson decays to two photons.

The ϕ_η^* observable was originally proposed for the study of Drell-Yan production of lepton pairs [194]. The p_{TZ} distribution is constructed from the transverse momentum of the leptons which relies on calorimetric measurements of the lepton energies. In contrast, the ϕ_η^* observable relies on measurements of the directions in ϕ and η of the two leptons rather than the energies. One can make use of both calorimeter and charged tracking information provided by the detector to determine the lepton directions. Ref. [194] demonstrated that the experimental resolution for ϕ_η^* is much better than p_{TZ} particularly when p_{TZ} is small. In the case at hand, we propose to extend the ϕ_η^* variable to describe a two photon system, even though there is no tracking information about the photons.

Our report is structured as follows. In section II.2, we recall the definition and properties of the ϕ_η^* variable itself. We show that although p_{TH} and ϕ_η^* both vanish in the Born limit, they are never directly related. We see that the fermion loop and effective interactions behave differently for the ϕ_η^* variable, and that this leads to clear differences between the leading order p_{TH} and ϕ_η^* distributions. In section II.3 we make a first study of the experimental resolution for the ϕ_η^* variable for photons. Even without the benefit of the charged track information, the experimental resolution for ϕ_η^* is improved compared to the transverse momentum of the photon pair, particularly at low transverse momentum. The effect of the parton shower on the p_{TH} and

ϕ_η^* variables is discussed in section II.4.

Once the viability of ϕ_η^* as an experimental observable has been established we turn to more theoretical considerations in section II.5, where we discuss the general structure of the $gggH$ vertex and how to compute the loop diagrams that can contribute to this process. We show how such calculations are structured, using the one-loop SM process as a pedagogic example. The notions of integral families, Integration-by-Parts identities, and master integrals are introduced and discussed, while the details of the calculation of the one-loop master integrals using differential equations are postponed to Appendix A. Details of the recently computed two-loop planar integrals [180] are discussed in Appendix B together with the more advanced techniques of integrand reduction, generalised polylogarithms, symbols and elliptic integrals.

Armed with the one-loop amplitude in the SM, section II.5.2.5 shows how to take the large mass limit of the one-loop integrals. This leads to a much simpler result that does not depend on m_t and we discuss for which values of p_{TH} this approximation breaks down. The equivalent, much simpler, calculation in the Higgs Effective Theory (HEFT) is briefly discussed in section II.5.3.

The uncertainties inherent in a perturbative calculation are discussed in section II.5.4. We discuss both the uncertainties that arise due to the truncation of the perturbative series, as well as the parametric uncertainties that arise from the choice of the values of the strong coupling, the heavy quark masses and the parton distribution functions (PDFs).

Higher order corrections are discussed in section II.5.5. Due to the complexity of the two-loop master integrals (and especially the non-planar graphs), the full NLO corrections in the SM are not yet available, and we only show results in the HEFT. Sections II.5.5.2 and II.5.5.3 make predictions for the p_{TH} and ϕ_η^* distributions at NLO and NNLO respectively. To simulate the anticipated effect of the heavy quark masses, we introduce two approximations - essentially retaining the exact LO mass dependence in a multiplicative and additive way - and compare and contrast the NLO and NNLO predictions for the ϕ_η^* and p_{TH} distributions. As is well known, at large p_{TH} , the HEFT breaks down leading to a large uncertainty in the NLO and NNLO predictions at large p_{TH} . However, the various approximations for the ϕ_η^* distribution are largely in agreement demonstrating that this is an observable that is much less sensitive to ultraviolet structure of the $gggH$ interaction and can be well described by the HEFT.

The potential of the ϕ_η^* distribution as a probe of BSM physics is discussed in section II.6. In section II.6.2 we study the effect of new physics effects on the ϕ_η^* distribution using a generic model in which a colour-triplet scalar particle is added to the SM. As expected from our analysis of the SM predictions, the p_{TH} distribution shows a clear effect, while the ϕ_η^* distribution does not. As a more concrete example, we focus on the light stop scenario within the MSSM proposed by the HXSWG [195] and study the feasibility of observing an effect in the ϕ_η^* distribution. Although the overall rate is affected by the presence of additional heavy fields, the shape of the ϕ_η^* distribution is relatively insensitive to heavy particle thresholds.

Our findings are briefly summarised in section II.7.

II.1.1 Default input parameters

Throughout our report, we fix the LHC centre-of-mass energy to be 13 TeV and, unless otherwise stated, use the following default input parameters: the Higgs boson mass, $m_H = 125$ GeV, the top quark mass, $m_t = 174$ GeV, the bottom quark mass, $m_b = 4.6$ GeV, the charm quark mass, $m_c = 1.42$ GeV. We use the PDF4LHC15_nnlo_30 PDF set [196] with $\alpha_S(M_Z) = 0.118$ and take the renormalisation and factorisation scales, μ_R and μ_F to be equal,

$$\mu = \mu_R = \mu_F.$$

For the Born process, $pp \rightarrow H$, we set $\mu = m_H/2$ while for Higgs bosons produced with finite transverse momentum, we set $\mu = M_{TH}/2$ where M_{TH} is the transverse mass of the Higgs boson,

$$M_{TH} = \sqrt{m_H^2 + p_{TH}^2}. \quad (\text{II.4})$$

The Higgs boson decays into two photons with a branching ratio of 0.00235. The photons are required to have rapidity, $|\eta| < 2.5$, and be isolated, such that the sum of the hadronic energy within a cone of $R = 0.4$ is less than 14 GeV. Jets are defined with the anti- k_T algorithm with $R = 0.4$.

II.2 Observables for probing Higgs boson recoil

In hadron collisions, the direction in which the two hadrons collide is extremely crowded and it is experimentally hard to distinguish what is a product of the collision itself and what is simply a remnant of the colliding hadrons.

In order to isolate the products of the interaction, it is convenient to study the component of the momentum of the particle which is transverse to the beam axis, the transverse momentum,

$$p_T = \sqrt{p_x^2 + p_y^2}, \quad (\text{II.5})$$

as well as the momentum parallel to the beam direction which is characterised by the rapidity,

$$\eta = \frac{1}{2} \log \left(\frac{E + p_z}{E - p_z} \right). \quad (\text{II.6})$$

For massless particles, $E = |p| = \sqrt{p_x^2 + p_y^2 + p_z^2} \equiv p_T \cosh \eta$, and the rapidity is also called the pseudorapidity.

In the laboratory frame, the four-momentum p_i^μ of a massless particle can be written in terms of the transverse momentum, p_{Ti} , the rapidity (or equivalently pseudorapidity), η_i and the azimuthal angle ϕ_i ,

$$p_i^\mu = (p_{Ti} \cosh \eta_i, \vec{p}_{Ti}, p_{Ti} \sinh \eta_i), \quad (\text{II.7})$$

where the vector transverse momentum is,

$$\vec{p}_{Ti} = (p_{Ti} \cos \phi_i, p_{Ti} \sin \phi_i). \quad (\text{II.8})$$

A measurement of p_T for a short-lived particle, is obtained by combining the p_T -measurements of its decay products. For small values of p_T , that procedure leads to a large experimental uncertainty on the reconstructed value. For a two particle system (such as Drell-Yan, or Higgs boson decay to photons), the transverse momentum of the pair is simply,

$$\vec{p}_T = \vec{p}_{T1} + \vec{p}_{T2}. \quad (\text{II.9})$$

As shown in Fig. II.5(a), in the transverse plane, $\Delta\phi$ is the azimuthal angle between p_{T1} and p_{T2} . When there are only two particles in the final state, $\Delta\phi = \pi$, and $\vec{p}_T = \vec{0}$ while in the general case $\Delta\phi < \pi$ and $\vec{p}_T \neq \vec{0}$. The individual transverse momenta are related to the magnitude of the transverse momentum of the pair by,

$$p_T^2 = p_{T1}^2 + p_{T2}^2 + 2p_{T1}p_{T2} \cos \Delta\phi. \quad (\text{II.10})$$

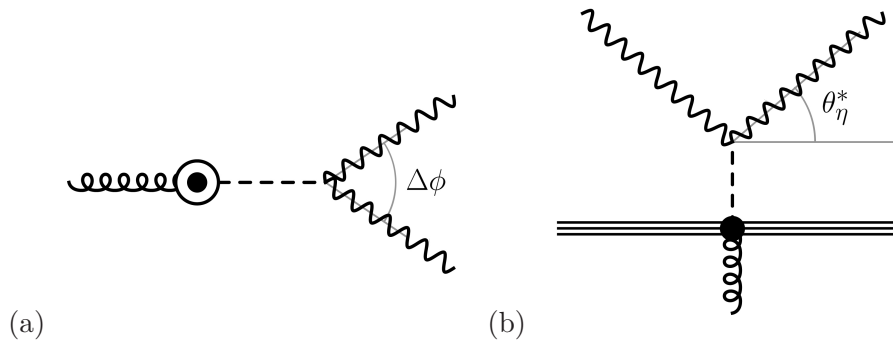


Fig. II.5: Illustration of the two angles that appear in the definition of ϕ_η^* : (a) shows $\Delta\phi$ in the plane perpendicular to the beam axis. (b) shows θ_η^* in the plane spanned by the beam axis and the Higgs boson, boosted along the beam axis so that the Higgs boson is purely transverse.

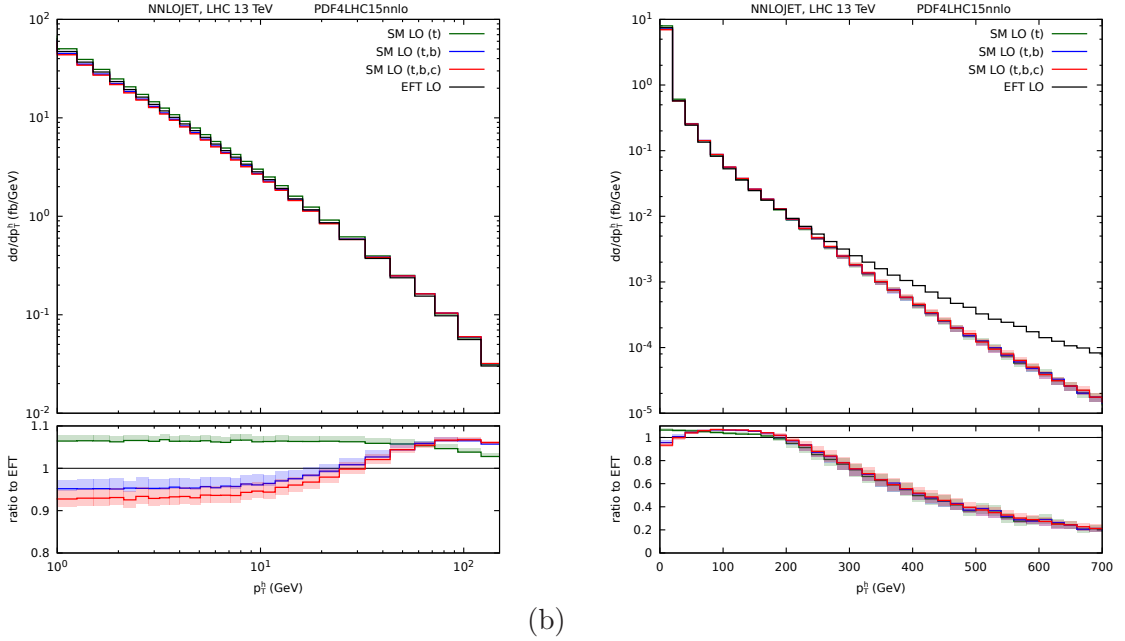


Fig. II.6: The Higgs boson transverse momentum distribution at $\sqrt{s} = 13$ TeV at leading order for the HEFT (black) and for the SM (a) at low p_{TH} and (b) at high p_{TH} . The SM predictions are shown for the top-quark alone (green), top and bottom quark loops (blue) and top, bottom and charm quark loops (red). The lower panels show the ratio normalised to the HEFT result.

In the small p_T region, $\cos \Delta\phi \sim -1$, and $p_{T1} \sim p_{T2}$, so that there are large cancellations between the terms on the RHS of Eq. (II.10), which ultimately leads to a poor experimental resolution.

As discussed in Sec. II.1, the main Higgs boson production mode is the gluon fusion process. Here we consider the rare but clean decay of the Higgs boson into two photons. The inclusive cross section for the two-photon decay of the Higgs boson produced via gluon fusion is dominated by low p_{TH} events and the inclusive cross sections for the HEFT and SM are similar. At leading order with the default parameters given in Section II.1.1 we find¹,

$$\sigma_{LO}^{SM}(t, b, c) = 24 \pm 3 \text{ fb} \quad (\text{II.11})$$

$$\sigma_{LO}^{HEFT} = 26 \pm 3 \text{ fb}. \quad (\text{II.12})$$

Fig. II.6 shows a comparison between the HEFT and the SM predictions for the p_{TH} distribution. As we can see Fig. II.6(a), for a Higgs boson with $p_{TH} < m_t$ the HEFT prediction almost perfectly reproduces the SM result with a deviation of less than a 10%. For $p_{TH} \approx m_t$ the distributions start to differ as we begin to resolve the structure of the loop. At larger p_{TH} , the two models lead to very different predictions demonstrating the potential of the p_{TH} distribution in resolving the details of the gluon-Higgs interaction.

II.2.1 A new observable: ϕ_η^*

To probe the low p_T region, an alternative angular variable, ϕ_η^* , has been proposed [194] which minimises the impact of these experimental uncertainties. This variable has been already studied

¹We note that the higher order corrections are significant and have been computed through to next-to-next-to-next-to-leading order (N3LO) [117, 118]

for the case of Z production decaying into two leptons [197, 198]. It is our goal to extend these studies to Higgs boson production decaying into two photons.

The variable ϕ_η^* is defined by:

$$\phi_\eta^* \equiv \tan\left(\frac{\phi_{\text{acop}}}{2}\right) \cdot \sin(\theta_\eta^*). \quad (\text{II.13})$$

In this definition, the acoplanarity angle is simply related to the angle between the particles in the transverse plane:

$$\phi_{\text{acop}} \equiv \pi - \Delta\phi. \quad (\text{II.14})$$

As depicted in Fig. II.5(b), θ_η^* is the scattering angle of the two particles with respect to the proton beam in the reference frame in which the two particles are back to back in the (r, θ) plane. In this frame, the parent particle is purely transverse. This frame is obtained by a longitudinal boost characterised by β such that the pseudorapidities in the new frame, η'_i are related to η_i by,

$$\eta'_i = \eta_i + \Delta\eta \quad (\text{II.15})$$

where

$$\Delta\eta = \frac{1}{2} \log\left(\frac{1-\beta}{1+\beta}\right) = -\left(\frac{\eta_1 + \eta_2}{2}\right). \quad (\text{II.16})$$

The transverse momenta are unaffected by the boost so that in this frame,

$$p_1'^\mu = \left(p_{T1} \cosh\left(\frac{\eta_1 - \eta_2}{2}\right), \vec{p}_{T1}, p_{T1} \sinh\left(\frac{\eta_1 - \eta_2}{2}\right)\right), \quad (\text{II.17})$$

$$p_2'^\mu = \left(p_{T2} \cosh\left(\frac{\eta_1 - \eta_2}{2}\right), \vec{p}_{T2}, -p_{T2} \sinh\left(\frac{\eta_1 - \eta_2}{2}\right)\right). \quad (\text{II.18})$$

From here we immediately see that,

$$\sin(\theta_\eta^*) = \frac{|p_T|}{E} = \text{sech}\left(\frac{\eta_1 - \eta_2}{2}\right), \quad (\text{II.19})$$

or equivalently,

$$\cos(\theta_\eta^*) = \frac{|p_z|}{E} = \tanh\left(\frac{\eta_1 - \eta_2}{2}\right). \quad (\text{II.20})$$

The ϕ_η^* variable measures the ‘‘deviation from back-to-backness’’ (acoplanarity) in the transverse plane and therefore vanishes at Born level where the azimuthal angle between the two leptons $\Delta\phi$ is exactly equal to π . Non-zero values of ϕ_η^* are produced by the same mechanism that generates non-zero p_{TH} , namely a recoil against hadronic emission from the partonic initial states. As a consequence, the ϕ_η^* distribution probes the same type of physics as the transverse momentum distribution. In the following we will investigate the relation between the two variables in further detail.

Fig. II.7 compares the HEFT and the SM predictions for the ϕ_η^* distribution for the Higgs boson decaying to two photons. As at low p_{TH} , Fig. II.7(a), shows that for a Higgs boson with $2m_H\phi_\eta^* < m_t$, the HEFT prediction lies within 10% of the SM result. However, unlike the p_{TH} distribution, at higher values of $2m_H\phi_\eta^* \approx m_t$ the agreement between the models persists. On the one hand, this implies that the ϕ_η^* distribution is less sensitive to the details of the gluon-Higgs interaction. On the other hand, it means that the ϕ_η^* distribution can be better predicted using the Higgs Effective Theory.

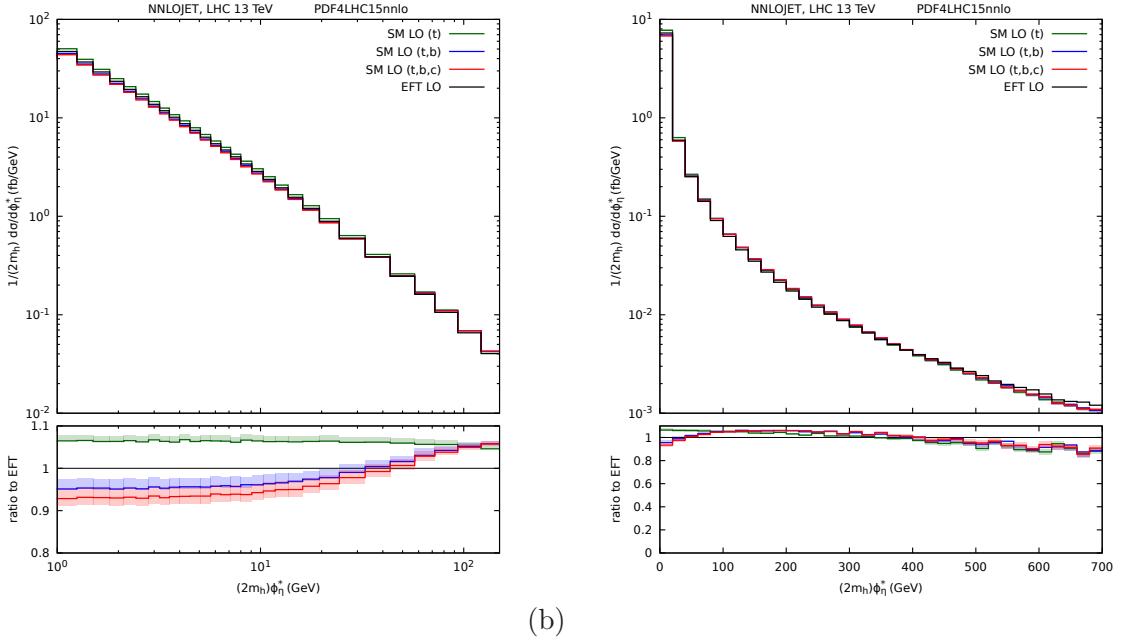


Fig. II.7: The Higgs boson ϕ_η^* distribution at $\sqrt{s} = 13$ TeV at leading order for the HEFT (black) and for the SM (a) at low ϕ_η^* and (b) at high ϕ_η^* . The SM predictions are shown for the top-quark alone (green), top and bottom quark loops (blue) and top, bottom and charm quark loops (red). The lower panels show the ratio normalised to the HEFT result.

II.2.1.1 ϕ_η^* in the low- p_{TH} regime

At very low p_{TH} (or ϕ_η^*) the cross section is dominated by large Sudakov-type logarithms of the vanishing observable. As discussed earlier, p_{TH} and ϕ_η^* vanish under the same circumstances. In the limit in which both variables vanish, we can find a relation between the two observables by looking at their dominant logarithmic behaviour [197, 199, 200]:

$$\frac{p_{TH}}{d\sigma_0} \frac{d\sigma}{dp_{TH}} = -8C_F \frac{\alpha_S}{\pi} \ln\left(\frac{p_{TH}}{m_H}\right) + \mathcal{O}(\alpha_S^2), \quad (\text{II.21})$$

$$\frac{\phi_\eta^*}{d\sigma_0} \frac{d\sigma}{d\phi_\eta^*} = -8C_F \frac{\alpha_S}{\pi} \ln\left(2\phi_\eta^*\right) + \mathcal{O}(\alpha_S^2), \quad (\text{II.22})$$

where $C_F = (N_c^2 - 1)/2N_c$. Although the two observables, p_{TH} and ϕ_η^* , are not directly related, by equating the arguments of the logarithms in Eqs. (II.21) and (II.22) we can derive an approximate relationship between the observables in the regions of the distributions that are dominated by Sudakov logarithms,

$$2m_H\phi_\eta^* \approx p_{TH}. \quad (\text{II.23})$$

We therefore systematically scale the ϕ_η^* distributions by a factor of $2m_H$ throughout this report.

Fig. II.8 shows the leading order SM predictions for the p_{TH} and ϕ_η^* distributions. We see that at low- p_{TH} , low- ϕ_η^* the two distributions are very similar. However, at larger values of p_{TH} and ϕ_η^* , the distributions are rather different. This difference becomes apparent around $p_{TH} \sim m_t$ and is because the p_{TH} distribution is able to resolve the top quark loop. In contrast, the ϕ_η^* distribution does not appear to resolve the top quark loop and from this point of view, behaves more like the inclusive cross section.

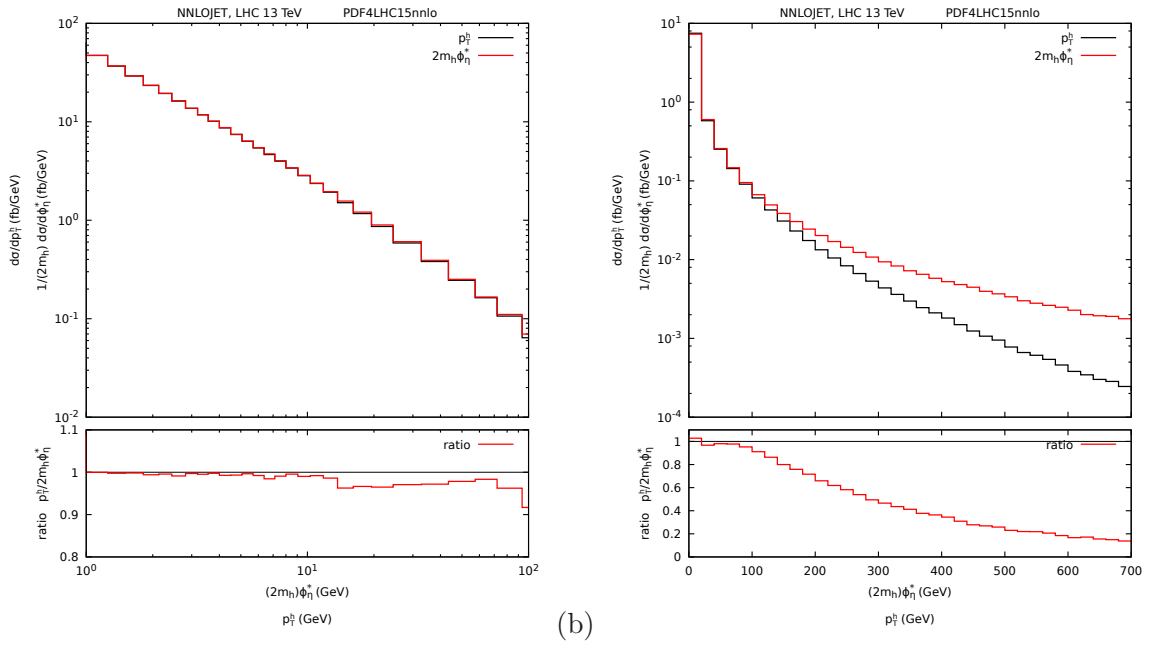


Fig. II.8: Comparison between the LO ϕ_η^* (red) and p_{TH} (black) distributions in the (a) low- p_{TH} , low- ϕ_η^* and (b) high- p_{TH} , high- ϕ_η^* regimes at 13 TeV.

II.3 Photons

In this section we will study the experimental resolution of the ϕ_η^* variable in two-photon events. We will concentrate on the reconstruction of photons and electrons with the CMS detector. Like ATLAS, this enormous and incredibly complex detector is composed of different sub-detectors assembled in an onion-like configuration and designed to reconstruct all the visible particles produced during a proton-proton collision. Each sub-detector interacts with the particles produced by the collisions and is designed to obtain a particular piece of information about each particle. The specific combination of information collected from many sub-detectors allows the reconstruction of different particles types.

II.3.1 Photon reconstruction and identification at the LHC detectors

Since we are concerned on the measurement of the Higgs boson when it decays into photons, we will focus only on the inner CMS sub-systems: the tracker and the electromagnetic calorimeter (ECAL). Within these sub-detectors, charged-particle trajectories are measured by the silicon pixel and strip tracker, with full azimuthal coverage within $|\eta| < 2.5$. A lead tungsten crystal ECAL and a scintillator hadron calorimeter (HCAL) surround the tracking volume and cover the region $|\eta| < 3$. The ECAL cells have widths of 0.0174 in both η and ϕ . A detailed description of the CMS detector can be found in Ref. [14]

The photons and electrons are usually reconstructed in the same way at the LHC detectors, mainly by combining information from the electromagnetic calorimeter and the inner tracking detectors. After being produced by a proton-proton collision, these particles travel through different sub-detectors before being stopped in the ECAL where they release all their energy as an electromagnetic shower. Photons and electrons are differentiated by the fact that electrons leave a charged track in the tracker that points towards the electromagnetic shower in the ECAL.

Unlike electrons, whose momentum can be measured precisely by the tracker, the photon energy measurement depends entirely on the intrinsic detector resolution of the ECAL. A precise measurement of the transverse momentum of Higgs boson that decays into a pair of photons is then limited by the ECAL performance.

As discussed in Sec. II.2, in order to probe the physics at low p_{TH} region ($p_{TH} \ll m_H$), we propose the use of new observable, ϕ_η^* , that could provide a precise measurement of the properties of $H \rightarrow \gamma\gamma$ events by avoiding the ECAL intrinsic resolution and using the angular information instead.

II.3.2 Event generation and detector simulation

Monte-Carlo $H \rightarrow \gamma\gamma$ events are generated using the `Madgraph5_aMC@NLO` [129] simulation framework with a centre-of-mass energy $\sqrt{s} = 13$ TeV and a Higgs boson mass set to $m_H = 125$ GeV. The events are generated at NLO accuracy including the matching and merging of parton multiplicities. The parton showering is taken care of by `Pythia8` [201] with the `CUETP8M1` [202] tune. A fast detector simulation is performed on those events using `DELPHES 3` [203] with the CMS detector configuration. This framework supplies the relevant sub-sensors resolutions and reconstruction efficiencies of the CMS detector described earlier².

In this study photon conversions into electron-positron pairs are neglected. The final photon and electron energy is obtained by applying the ECAL resolution function that depends on the intrinsic ECAL performances. True photons and electrons with no reconstructed track pointing to the ECAL are considered to be photons in the detector simulation `DELPHES 3`.

²Similarly a fast simulation with ATLAS can be performed.

II.3.3 Event selection

We use the same fiducial volume as used for the differential cross section measurements by CMS [204]. Events are accepted for further analysis if the diphoton invariant mass satisfies $|m_{\gamma\gamma} - 125| < 10$ GeV and the photons satisfy the following requirements:

- The leading and sub-leading photons satisfy $p_T^{\gamma_1}/m_{\gamma\gamma} > 1/3$ and $p_T^{\gamma_2}/m_{\gamma\gamma} > 1/4$;
- Each photon of the candidate pair entering the analysis is required to have $|\eta| < 2.5$, excluding the region $1.4442 < |\eta| < 1.566$ that corresponds to the gap in the ECAL between the barrel and end-cap;
- Each photon must be isolated with an isolation value of $I_{\text{iso}} < 0.1$ ³.

For each generated photon, the reconstructed photon candidate with the smallest

$$\Delta R = \sqrt{(\eta_{\text{rec}} - \eta_{\text{gen}})^2 + (\phi_{\text{rec}} - \phi_{\text{gen}})^2}$$

is computed. When $\Delta R < 0.2$ the generated photon is paired with a reconstructed photon.

The distributions of ϕ_η^* and $p_T^{\gamma\gamma}$ after the simulation of diphoton events are shown in Fig. II.9. We see that for both variables, there is a very good correlation between **truth** (the generated observable) and **reco** (the reconstructed observable) apart from very small values of the observables.

The relationship between ϕ_η^* and $p_T^{\gamma\gamma}$ for the diphoton pair in individual events is shown in Fig. II.10. In order to make a fair comparison between these two observables we scale ϕ_η^* by the factor of $2 \times m_H$ as discussed in the previous section.

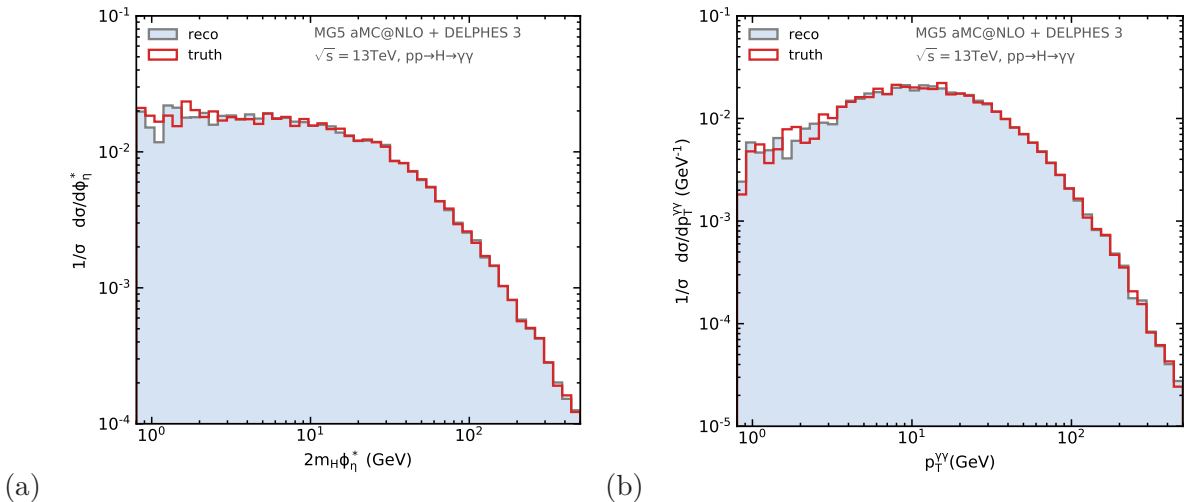


Fig. II.9: Distributions of (a) the transverse momentum $H \rightarrow \gamma\gamma$ and (b) ϕ_η^* at both generated (**truth**) and reconstructed (**reco**) levels.

II.3.4 Experimental resolution for diphoton scattering angle

Following the strategy as described in Ref. [194] in the context of the Z transverse momentum measurement, we start by measuring the relative resolution of ϕ_η^* and $p_T^{\gamma\gamma}$ in simulated diphoton

³The photon isolation is defined as the ratio between the transverse momentum of all the reconstructed objects within a radius of $\Delta R < 0.4$ and the photon candidate. This definition is slightly different from the usual definition used by the LHC experiments that use different types of isolation depending on the calorimeter and how the particles are reconstructed. More details can be found in Ref. [205].

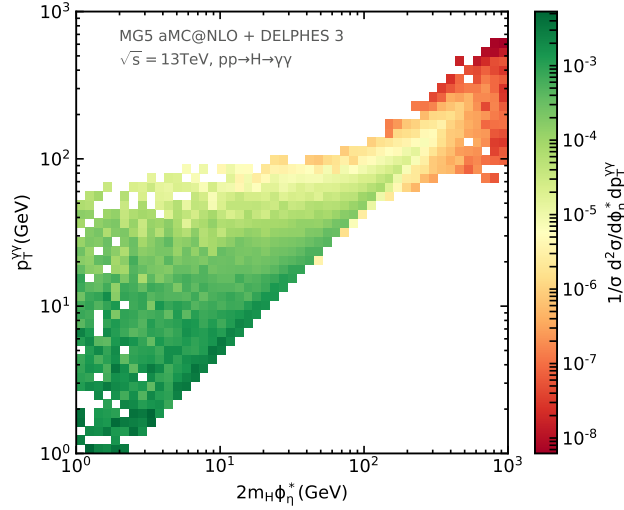


Fig. II.10: Relationship between $p_T^{\gamma\gamma}$ and ϕ_η^* for individual diphoton pairs.

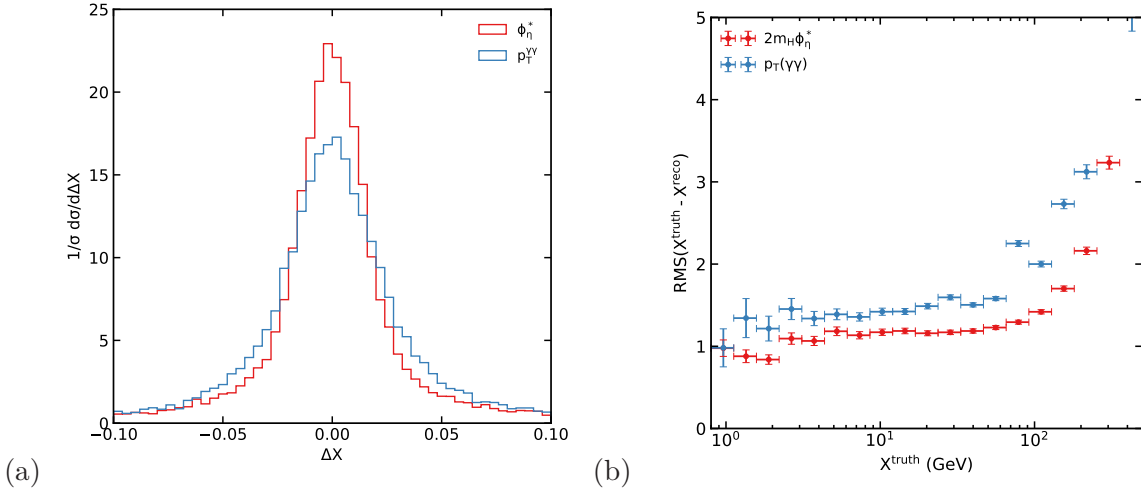


Fig. II.11: (a) Relative resolution of $X = 2m_H\phi_\eta^*$, $p_T^{\gamma\gamma}$. (b) Resolution of $X = 2m_H\phi_\eta^*$, $p_T^{\gamma\gamma}$.

events as shown in Figure II.11(a). Here we show the relative resolution for a given measured quantity X ($X = 2m_H\phi_\eta^*$, $p_T^{\gamma\gamma}$) as a function of the relative difference

$$\Delta X = (X^{\text{truth}} - X^{\text{reco}})/X^{\text{truth}}.$$

As expected the ϕ_η^* variable has a narrower relative resolution distribution than $p_T^{\gamma\gamma}$.

The resolution is defined as the RMS value of $X^{\text{truth}} - X^{\text{reco}}$ as a function of X^{truth} shown in Fig. II.11(b). We conclude that the angular variable $2m_H\phi_\eta^*$ has a better resolution in comparison with the simple calorimetric measurement of $p_T^{\gamma\gamma}$ in most of the range of X^{truth} . The improvement is roughly 30% in the range $1 \text{ GeV} < X^{\text{truth}} < 100 \text{ GeV}$.

Note that many systematic effects have been neglected in using the DELPHES simulation. One of the main sources of systematic uncertainties neglected is the determination of the hard scattering primary vertex in the presence of pile-up which could lead a mis-measurement of the scattering angles and thus the pseudo-rapidities of the two selected photons. The presence of

pile-up also introduces additional systematic uncertainties in the isolation criteria that might further bias the identification of the two photons.

II.4 Parton Showers

Let us now investigate the effect of the parton shower (PS) when simulating the two observables discussed so far. We concentrate on a very simple example, the production of a Higgs boson through gluon fusion. To make the discussion even clearer, we consider only the Higgs Effective Theory. Note that a complete description of how a parton shower works is beyond the scope of this report and we refer the reader to the useful references [206–209].

The differential partonic cross section, $d\hat{\sigma}$, for the Born (or leading order (LO)) hard scattering process, $gg \rightarrow H$, can be written as

$$d\hat{\sigma}_{gg \rightarrow H} = d\Phi_{2 \rightarrow 1} \frac{|\overline{\mathcal{M}}_{gg \rightarrow H}|^2}{F}, \quad (\text{II.24})$$

where the flux factor $F = 4p_1 \cdot p_2 = 2s_{12}$, $|\overline{\mathcal{M}}_{gg \rightarrow H}|^2$ is the spin and colour summed and averaged matrix element and $\Phi_{2 \rightarrow 1}$ represents the one-particle phase space. The explicit form for $d\Phi_{2 \rightarrow 1}$, requires that

$$d\hat{\sigma}_{gg \rightarrow H} \propto \delta^{(2)}(\vec{p}_{TH}), \quad (\text{II.25})$$

which follows from four-momentum conservation and implies that the value of p_{TH} is fixed to be identically zero.

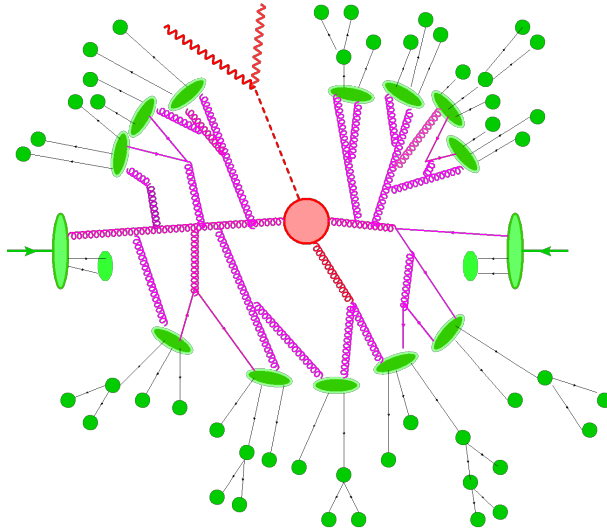


Fig. II.12: Pictorial representation of how a large p_{TH} Higgs boson event looks like from a Monte Carlo perspective. The hard interaction (big red blob) is followed by the decay of the Higgs boson to photons (red wavy lines). Additional hard QCD radiation is produced through final state (red) and initial state (magenta) before the final-state partons hadronise (dark green blobs) and hadrons decay (light green blobs).

In reality the two gluons in the initial state are very energetic and will emit other particles, gluons or quarks, which in turn will emit other particles and so on. A schematic representation of an event in which a Higgs boson is produced at large transverse momentum is shown in Fig. (II.12) showing emission from final state particles (red) and emission from the initial state (blue). The emissions will most likely be soft or collinear to the emitter, which allows us to make some approximations. The parton shower simply does the job of simulating emission after emission until the radiating particle runs out of energy, which is the point when partons hadronize (green lines and blobs in Fig. II.12).

To see how this works consider the splitting of a gluon into a pair of quarks where the splitting probability is given by

$$\mathcal{P}_{qq}(t, t') = \int_t^{t'} \frac{dt}{t} \left| \text{diagram} \right|^2 \propto \frac{\alpha_s}{2\pi} P_{qq}(z) \log \frac{t'}{t}. \quad (\text{II.26})$$

Repeated splittings gives rise to a series that behaves like

$$\frac{1}{m!} \left(\alpha_s \log \frac{t'}{t} \right)^m,$$

which can symbolically be summed and exponentiated to give

$$\Delta_i(t, t') = \exp \left(- \sum_{j \in (q, g)} \mathcal{P}_{ij}(t, t') \right). \quad (\text{II.27})$$

Δ is called the Sudakov form factor, which represents the unconditional branching probability for a parton not to undergo a branching process between the two energy scales t and t' [210–212]. Note that the Sudakov form factor accurately represents the *leading logarithmic* (LL) behaviour of the splittings. In practical implementations, the subleading logarithmic behaviour of parton showers is not yet well understood, and varies from code to code. Keeping in mind that the outcome of the parton shower has leading order and leading logarithmic accuracy, the main effect of showering a fixed order hard-process is to add more particles to the final state, each carrying a transverse momentum \vec{k}_{iT} which is weighted according to Δ . The primary effect of adding more particles in the final state follows from momentum conservation, and implies that

$$\delta^{(2)}(\vec{p}_{TH}) \rightarrow \delta^{(2)}(\vec{p}_{TH} + \sum_{i=1}^N \vec{k}_{iT}), \quad (\text{II.28})$$

which shifts the peak of the distribution from zero to some non-zero value. The energy that the shower can share among the additional final state particles is limited by the partonic centre of mass energy which in this case is of the order of m_H . Therefore, we should expect that applying the parton shower to the LO $2 \rightarrow 1$ process will lead to a p_{TH} distribution that exhibits a broad peak that suddenly falls off for $p_{TH} \approx m_H$. This is indeed the behaviour that is shown in Fig. (II.13)(a) by the $pp \rightarrow H$ PS prediction.

ϕ_η^* is of course a different variable, but it shares the key feature that at the Born level, it is required to vanish. The additional radiation in the parton shower produces a non-zero value for ϕ_η^* and the $pp \rightarrow H$ PS prediction shown Fig. (II.13)(a) has the same gross features as the p_{TH} distribution, namely a broad shoulder accompanied by a tailing off at larger values of ϕ_η^* .

Although the shower generates many emissions, each emission is roughly a factor of ten times less likely to happen than the previous one. The reason is that each emission comes at the cost of an additional power of α_S . Further, α_S is not constant but a monotonically decreasing function, and for most implementation of parton showers is evaluated at the k_T of the splitting. These two considerations together imply that the first few emissions have a larger weight than the later emissions, and splittings that exhibit a smaller k_T are more likely than those with a larger k_T . These two effects compete to determine the shape of the distribution and the position of the peak. Following these arguments, one could argue that a reasonable approximation would simply be to go one order higher in α_S and include exactly the emission of one extra particle in the hard scattering itself. In the case of $gg \rightarrow H$, this process introduces a variety of new channels, $gg \rightarrow Hg$, $q\bar{q} \rightarrow Hg$, $qg \rightarrow Hq$ that are discussed in detail in Sec. II.5. Here, we simply

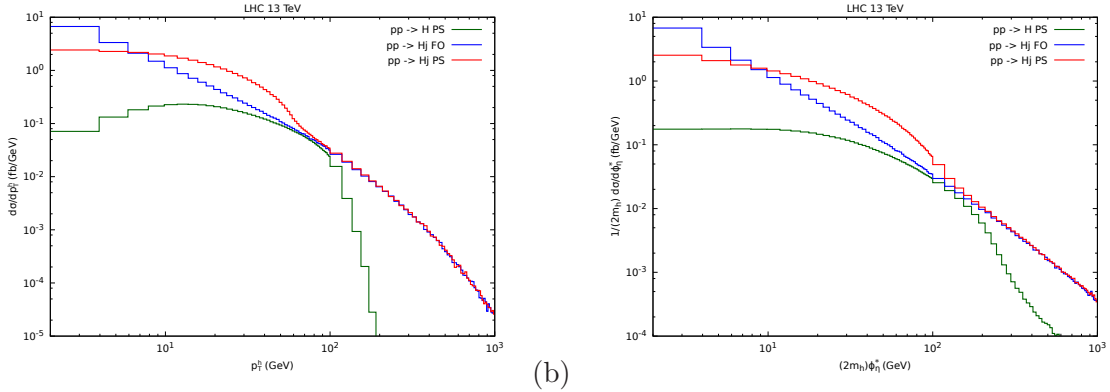


Fig. II.13: The effect of the parton shower on (a) the p_{TH} and (b) ϕ_η^* distributions. The curves show the effect of the parton shower on the $gg \rightarrow H$ process, $pp \rightarrow H$ PS (green), the fixed order $gg \rightarrow H j$ process FO (blue) and the parton shower applied to the FO process, $pp \rightarrow H j$ PS (red).

denote the sum of these contributions by $gg \rightarrow H j$ to reflect the fact that an additional parton j is present in the final state.

Let us first consider the case of $gg \rightarrow H j$ at fixed order (FO), *i.e.* with no parton shower. As for the Born contribution, we can write the differential cross section in terms of final state phase-space and matrix elements,

$$d\hat{\sigma}_{gg \rightarrow H j} = d\Phi_{2 \rightarrow 2} \frac{|\overline{\mathcal{M}}_{gg \rightarrow H j}|^2}{F} \propto \frac{d^2 \vec{p}_{TH}}{p_{TH}} \frac{d^2 \vec{k}_{jt}}{k_{jt}} \delta^{(2)}(\vec{p}_{TH} - \vec{k}_{jT}), \quad (\text{II.29})$$

where the δ function in this case simply forces the Higgs boson and the extra parton to be back-to-back and thus removes one of the two integration variables. In contrast to the $gg \rightarrow H$ case discussed earlier, we find the additional feature of the non trivial integration over p_{TH} . Although there is an extra particle recoiling against the Higgs boson, nothing prevents the extra parton to be very soft, or very collinear to the beam axis. In both cases this gives rise to a logarithmic divergence. What this means in practice is that events with $p_{TH} \sim 0$ GeV will have a larger weight (*i.e.* a larger probability to be produced). This feature can clearly be seen as the $pp \rightarrow H j$ FO prediction in Fig. (II.13)(a). In this case we indeed see a rise at low p_{TH} which diverges at $p_{TH} = 0$ GeV but is not included in the plot. We also see a rather hard distribution (compared to $pp \rightarrow H$ PS) because the single hard emission is precisely modelled. One can see the same effects in the FO ϕ_η^* distribution in Fig. (II.13)(b); a divergence at low ϕ_η^* accompanied by a hard tail at high ϕ_η^* .

Let us now investigate the effects of the parton shower on $gg \rightarrow H j$. As for the $2 \rightarrow 1$ case, the main effect of the shower is to shift and broaden the peak of the p_{TH} distribution. The main difference is that instead of having a sudden drop at $p_{TH} \sim m_H$, the p_{TH} distribution is harder because more energy is available to the shower through the emission of an extra particle in the hard process. We therefore expect a transition between the low p_{TH} region where the shower dominates and distorts the shape of the $pp \rightarrow H j$ FO distribution and the high p_{TH} region where impact of the shower is negligible. This phenomenon is displayed as $pp \rightarrow H j$ PS in Fig. (II.13)(a). As one might expect, the same effects are evident in the $pp \rightarrow H j$ PS prediction for the ϕ_η^* distribution in Fig. (II.13)(b); at low ϕ_η^* the parton shower produces a smooth shoulder that merges onto the hard FO tail at high ϕ_η^* .

II.5 Theoretical Predictions

In this section we describe the calculation of the fixed order matrix elements relevant to the production of Higgs bosons with non-zero transverse momentum and non-zero ϕ_η^* . We start by reviewing the general properties of the interaction shown in Fig. II.3. In the Standard Model, this blob is mediated by heavy quark loops. The one-loop matrix elements have been known for some time [176, 177] but the two-loop matrix elements are not yet known exactly [180]. We review the modern techniques that have been developed to tackle the complicated two-loop integrals that appear using the one-loop amplitude as an example. Finally, we show how the effective interaction can be recovered by taking the $m_t \rightarrow \infty$ limit.

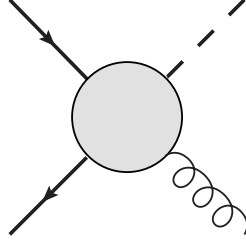


Fig. II.14: Schematic diagram showing the production of a Higgs boson with transverse momentum from quark-antiquark annihilation.

Note that in addition to the gluonic process shown in Fig. II.3, there is also a process involving a quark-antiquark pair shown in Fig. II.14 so that seven partonic channels contribute to the production of a Higgs boson plus a quark or gluon jet in proton-proton collisions:

$$\begin{aligned} qg \rightarrow qH, & \quad q\bar{q} \rightarrow qH, & \quad \bar{q}g \rightarrow \bar{q}H, & \quad g\bar{q} \rightarrow \bar{q}H, \\ q\bar{q} \rightarrow gH, & \quad \bar{q}q \rightarrow gH, & \quad gg \rightarrow gH. & \end{aligned} \quad (\text{II.30})$$

The calculational methodology is similar for all processes and in the following, we will mainly focus on the $gg \rightarrow gH$ process.

II.5.1 General Properties

II.5.1.1 Tensorial Structure of the Amplitude

The amplitude for the $gg \rightarrow gH$ process may be written in terms of the external polarisation vectors of the gluons and a third rank tensor $\mathcal{M}^{\mu\nu\tau}$ that describes the physics within the blob,

$$\mathcal{M}_{gg \rightarrow gH} = \mathcal{M}^{\mu\nu\tau} \varepsilon_\mu(p_1) \varepsilon_\nu(p_2) \varepsilon_\tau(p_3). \quad (\text{II.31})$$

If one wishes to exploit the helicities of the external particles, then Eq. (II.31) can be generalised,

$$A_{gg \rightarrow gH}^{h_1 h_2 h_3} = \mathcal{M}_{h_1 h_2 h_3}^{\mu\nu\tau} \varepsilon_\mu^{h_1}(p_1) \varepsilon_\nu^{h_2}(p_2) \varepsilon_\tau^{h_3}(p_3), \quad (\text{II.32})$$

where h_i denotes the helicities of the gluons. As we will see, all information required to evaluate $\mathcal{M}_{h_1 h_2 h_3}^{\mu\nu\tau}$ for any combination of the helicities of the external gluons can be directly obtained from the general tensor $\mathcal{M}^{\mu\nu\tau}$.

The most general tensorial structure of \mathcal{M} is formed by factors of the external momenta p_i^μ , the Lorentz invariant tensor $g^{\mu\nu}$ and the Lorentz invariant Levi-Civita tensor $\varepsilon^{\mu\nu\rho\sigma}$. The process $gg \rightarrow gH$ has four external particles, but due to momentum conservation we may express the momentum of the Higgs boson, p_4 , in terms of the momenta of the three gluons. We obtain

the general expression for the tensor decomposed amplitude

$$\mathcal{M}^{\mu\nu\tau} = \sum_{ijk=1}^3 F_{ijk} p_i^\mu p_j^\nu p_k^\tau + \sum_{i=1}^3 G_{i1} p_i^\mu g^{\nu\tau} + \sum_{i=1}^3 G_{i2} p_i^\nu g^{\mu\tau} + \sum_{i=1}^3 G_{i3} p_i^\tau g^{\mu\nu} + \sum_{i=1}^3 H_i p_i^\sigma \varepsilon^{\mu\nu\rho\sigma} \quad (\text{II.33})$$

where F_{ijk} , G_{ij} and H_i are scalar functions called formfactors. QCD is a parity invariant theory and therefore $H_i \equiv 0$. However, there may well be models in which this term is present. In this section, we are mainly concerned with the Standard Model and will neglect this parity violating term. Eq. (II.33) has 27 F_{ijk} terms and 9 G_{ij} terms. It is important to note that while the values of the formfactors depend on the specifics of the physical theory, the number of loops etc. but the tensorial decomposition given by Eq. (II.33) does not.

The terms in Eq. (II.33) are not physically independent. This can be seen from the Ward identities imposed by the gauge invariance of the theory, which say that any amplitude that may be written as $\mathcal{M}^\mu \varepsilon_\mu(p)$ for a massless vector boson with momentum p , must satisfy $\mathcal{M}^\mu p_\mu = 0$.

Imposing the Ward identity for each of the external gluons in turn and requiring that each of the (independent) second rank tensor coefficients vanish produces 30 relations between the coefficients of Eq. (II.33), of which 22 turn out to be independent. This leaves a gauge-invariant expression with 14 independent terms.

Of these 14 terms 10 turn out to be proportional to either p_1^μ , p_2^ν , or p_3^τ . As polarization vectors have the property that $\varepsilon(p) \cdot p = 0$, these terms will yield no contribution to the amplitude of Eq. (II.31). Thus only four physical terms are left,

$$\mathcal{M}_{\text{physical}}^{\mu\nu\tau} = F_{212} T_{212}^{\mu\nu\tau} + F_{332} T_{332}^{\mu\nu\tau} + F_{311} T_{311}^{\mu\nu\tau} + F_{312} T_{312}^{\mu\nu\tau}, \quad (\text{II.34})$$

where,

$$\begin{aligned} T_{212}^{\mu\nu\tau} &= (s_{12} g^{\mu\nu} - 2p_2^\mu p_1^\nu) (s_{23} p_1^\tau - s_{13} p_2^\tau) / (2s_{13}), \\ T_{332}^{\mu\nu\tau} &= (s_{23} g^{\nu\tau} - 2p_3^\nu p_2^\tau) (s_{13} p_2^\mu - s_{12} p_3^\mu) / (2s_{12}), \\ T_{311}^{\mu\nu\tau} &= (s_{13} g^{\tau\mu} - 2p_1^\tau p_3^\mu) (s_{12} p_3^\nu - s_{23} p_1^\nu) / (2s_{23}), \\ T_{312}^{\mu\nu\tau} &= \left(g^{\mu\nu} (s_{23} p_1^\tau - s_{13} p_2^\tau) + g^{\nu\tau} (s_{23} p_2^\mu - s_{12} p_3^\mu) + g^{\tau\mu} (s_{12} p_3^\nu - s_{23} p_1^\nu) \right. \\ &\quad \left. + 2p_3^\mu p_1^\nu p_2^\tau - 2p_2^\mu p_3^\nu p_1^\tau \right) / 2 \end{aligned} \quad (\text{II.35})$$

with $s_{ij} = (p_i + p_j)^2$.

We notice a symmetry between the first three terms of Eq. (II.34). This is due to the cyclic permutation invariance of \mathcal{M} , e.g. $\mathcal{M}(p_1^\mu, p_2^\nu, p_3^\rho) = \mathcal{M}(p_2^\nu, p_3^\rho, p_1^\mu)$, so we realize that only two of the terms of Eq. (II.34) are truly independent. These can be chosen as e.g. F_{311} and F_{312} , and are denoted the independent formfactors of the process.

The formfactors can be directly extracted from the tensor by introducing ‘‘projectors’’, $Q_{\mu\nu\tau}^{ijk}$ [213] with the property that

$$Q_{\mu\nu\tau}^{ijk} \mathcal{M}_{\text{physical}}^{\mu\nu\tau} = F_{ijk}. \quad (\text{II.36})$$

It is natural to construct the $Q_{\mu\nu\tau}^{ijk}$ as linear combinations of the $T_{ijk}^{\mu\nu\tau}$ appearing in Eq. (II.35) and to fix the coefficients such that Eq. (II.36) is satisfied. In general, these coefficients depend on the s_{ij} and the dimensionality of space-time d . Explicit calculation yields,

$$Q_{212}^{\mu\nu\tau} = \frac{1}{(d-3)s_{12}} \left(-\frac{ds_{13}}{2} T_{212}^{\mu\nu\tau} + \frac{d-4}{2} T_{332}^{\mu\nu\tau} + \frac{d-4}{s_{12}s_{13}} T_{311}^{\mu\nu\tau} + \frac{d-2}{s_{12}s_{23}} T_{312}^{\mu\nu\tau} \right), \quad (\text{II.37})$$

$$Q_{332}^{\mu\nu\tau} = \frac{1}{(d-3)s_{23}} \left(\frac{d-4}{s_{12}s_{23}} T_{212}^{\mu\nu\tau} - \frac{ds_{12}}{s_{13}s_{23}^2} T_{332}^{\mu\nu\tau} + \frac{d-4}{s_{13}^2} T_{311}^{\mu\nu\tau} + \frac{d-2}{s_{13}s_{23}} T_{312}^{\mu\nu\tau} \right), \quad (\text{II.38})$$

$$Q_{311}^{\mu\nu\tau} = \frac{1}{(d-3)s_{13}} \left(\frac{d-4}{s_{12}^2} T_{212}^{\mu\nu\tau} + \frac{d-4}{s_{13}s_{23}} T_{332}^{\mu\nu\tau} - \frac{ds_{23}}{s_{12}s_{13}^2} T_{311}^{\mu\nu\tau} + \frac{d-2}{s_{12}s_{13}} T_{312}^{\mu\nu\tau} \right), \quad (\text{II.39})$$

$$Q_{312}^{\mu\nu\tau} = \frac{(d-2)}{(d-3)s_{12}s_{23}s_{13}} \left(\frac{s_{13}}{s_{12}} T_{212}^{\mu\nu\tau} + \frac{s_{12}}{s_{23}} T_{332}^{\mu\nu\tau} + \frac{s_{23}}{s_{13}} T_{311}^{\mu\nu\tau} + \frac{d}{d-2} T_{312}^{\mu\nu\tau} \right), \quad (\text{II.40})$$

where the symmetry between the first three projectors remains apparent.

For the quark channels, rather than three free Lorenz indices, the tensorial amplitude will have one Lorentz index along with a spinor and an anti spinor index. For that case a similar projector technique may be used, see e.g. Ref. [213].

II.5.1.2 From the Amplitude to the Cross-section

The partonic cross-section is given in terms of the amplitude, $\mathcal{M}_{gg \rightarrow gH}$, by

$$\hat{\sigma}_{gg \rightarrow gH}(s_{12}) = \int d\Phi_{2 \rightarrow 2} \frac{|\overline{\mathcal{M}_{gg \rightarrow gH}}|^2}{F}. \quad (\text{II.41})$$

In four dimensions the 2-to-2 phase space for production of a Higgs boson plus jet is

$$\int d\Phi_{2 \rightarrow 2} = \int_{-1}^1 d \cos \theta \int_0^{2\pi} d\phi \frac{1}{32\pi^2} \left(1 - \frac{m_H^2}{s} \right). \quad (\text{II.42})$$

The gluon channel contribution to the hadronic cross-section is given by

$$\sigma_{pp \rightarrow hj}(s) = \int_0^1 dz_1 \int_0^1 dz_2 \int_{s_{12}^{\min}}^s ds_{12} \hat{\sigma}_{gg \rightarrow gh}(s_{12}) \delta(\hat{s} - z_1 z_2 s) f_g(z_1) f_g(z_2), \quad (\text{II.43})$$

where f_g is the gluon PDF and $s_{12}^{\min} = m_H^2$ is the minimum energy required to produce a Higgs boson on-shell. Introducing the parton luminosity,

$$\frac{d\mathcal{L}_{ij}}{d\tau} = \int_{\tau}^1 \frac{dx}{x} f_i(x) f_j\left(\frac{\tau}{x}\right) \quad (\text{II.44})$$

we may write the hadronic cross-section as

$$\sigma_{pp \rightarrow hj}(s) = \int_{\tau_0}^1 d\tau \frac{d\mathcal{L}_{gg}}{d\tau} \hat{\sigma}_{gg \rightarrow gh}(\tau s), \quad (\text{II.45})$$

where $\tau_0 = m_H^2/s$.

In conventional dimensional regularisation (CDR) the spin and colour averaged absolute square of the amplitude is given by

$$|\overline{\mathcal{M}_{gg \rightarrow gH}}|^2 = \frac{1}{(d-2)^2} \frac{1}{(N_c^2 - 1)^2} |\mathcal{M}_{gg \rightarrow gH}|^2, \quad (\text{II.46})$$

where we have divided by the number of polarisations, $(d-2)$, for each incoming gluons in order to average over their polarisations and by $N_c^2 - 1$ for each incoming gluon to average over their colours. The absolute square of the matrix element is given in terms of the form factors by

$$|\mathcal{M}_{gg \rightarrow gH}|^2 = \sum_{h_1, h_2, h_3} (\varepsilon_{\mu}^{h_1})^* \varepsilon_{\hat{\mu}}^{h_1} (\varepsilon_{\nu}^{h_2})^* \varepsilon_{\hat{\nu}}^{h_2} (\varepsilon_{\tau}^{h_3})^* \varepsilon_{\hat{\tau}}^{h_3} (\mathcal{M}^{\mu\nu\tau})^* \mathcal{M}^{\hat{\mu}\hat{\nu}\hat{\tau}} \quad (\text{II.47})$$

$$\begin{aligned}
&= \frac{1}{4} \left[\frac{(d-2)|F_{212}|^2 s_{12}^3 s_{23}}{s_{13}} + F_{212} F_{332}^* s_{12} s_{23}^2 + F_{212} F_{311}^* s_{12}^2 s_{13} + (d-2) F_{212} F_{312}^* s_{12}^2 s_{23} \right. \\
&+ F_{332} F_{212}^* s_{12} s_{23}^2 + \frac{(d-2)|F_{332}|^2 s_{13} s_{23}^3}{s_{12}} + F_{332} F_{311}^* s_{13}^2 s_{23} + (d-2) F_{332} F_{312}^* s_{13} s_{23}^2 \\
&+ F_{311} F_{212}^* s_{12}^2 s_{13} + F_{311} F_{332}^* s_{13}^2 s_{23} + \frac{(d-2)|F_{311}|^2 s_{12} s_{13}^3}{s_{23}} + (d-2) F_{311} F_{312}^* s_{12} s_{13}^2 \\
&\left. + (d-2) F_{312} F_{212}^* s_{12}^2 s_{23} + (d-2) F_{312} F_{332}^* s_{13} s_{23}^2 + (d-2) F_{312} F_{311}^* s_{12} s_{13}^2 \right. \\
&\left. + (3d-8)|F_{312}|^2 s_{12} s_{13} s_{23} \right], \tag{II.48}
\end{aligned}$$

where for the polarisation sums we have used the axial gauge expression

$$\sum_{pols} (\varepsilon_i^\mu(p_i))^* \varepsilon_i^\nu(p_i) = -g^{\mu\nu} + \frac{p_i^\mu n_i^\nu + p_i^\nu n_i^\mu}{p_i \cdot n_i}, \tag{II.49}$$

with n_i an arbitrary reference vector not collinear to p_i .

Eq. (II.48) looks rather cumbersome and a simpler expression for the absolute square of the matrix element can be written in terms of helicity amplitudes. We first fix the dimensionality of the space-time to four for all external particles, which corresponds to working in the 't Hooft-Veltman scheme (rather than CDR). In four dimensions we can then use the spinor helicity formalism to compute the helicity amplitudes, for a discussion of this topic see [214–218].

Each of the three gluons can have one of two helicities thus there are 2^3 helicity amplitudes, though they are not all independent. Firstly, the helicity amplitudes are related by parity,

$$\mathcal{M}_{gg \rightarrow gH}^{h_1 h_2 h_3} = -\mathcal{M}_{gg \rightarrow gH}^{-h_1 -h_2 -h_3}, \tag{II.50}$$

this reduces the number of potentially independent helicity amplitudes to 4. However, the remaining 4 are also related due to the permutation invariance of the amplitude

$$\mathcal{M}_{gg \rightarrow gH}^{++-}(s_{12}, s_{13}, s_{23}) = \mathcal{M}_{gg \rightarrow gH}^{+-+}(s_{13}, s_{23}, s_{12}) = \mathcal{M}_{gg \rightarrow gH}^{-++}(s_{23}, s_{12}, s_{13}). \tag{II.51}$$

In terms of the form factors the two independent helicity amplitudes are given by

$$\mathcal{M}_{gg \rightarrow gH}^{+++} = \frac{-s_{12} s_{23} s_{13}}{\sqrt{2} \langle 12 \rangle \langle 23 \rangle \langle 31 \rangle} \left(\frac{s_{12}}{2s_{13}} F_{212} + \frac{s_{23}}{2s_{12}} F_{332} + \frac{s_{13}}{2s_{23}} F_{311} + F_{312} \right), \tag{II.52}$$

$$\mathcal{M}_{gg \rightarrow gH}^{++-} = \frac{F_{212} s_{12} \langle 23 \rangle [21]^2}{2\sqrt{2} \langle 12 \rangle [31]}. \tag{II.53}$$

We may write now the absolute square of the matrix element as a sum of absolute squares of the 8 helicity amplitudes

$$|\mathcal{M}_{gg \rightarrow gH}|^2 = \sum_{h_1, h_2, h_3 = \pm} |\mathcal{M}_{gg \rightarrow gH}^{h_1 h_2 h_3}|^2. \tag{II.54}$$

When using this expression care should be taken to average over the correct number of transverse polarisations of the gluon, now 2 rather than $d-2$.

Unlike the formfactors themselves, Eqs. (II.47) and (II.54) are quite general and do not depend on the details of the interaction.

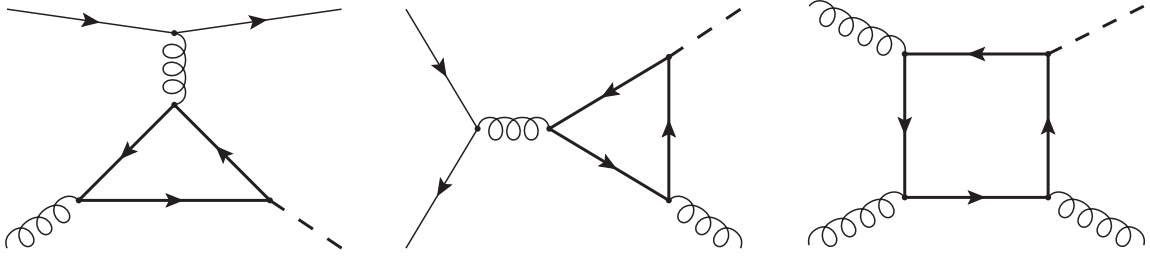


Fig. II.15: Example Feynman diagrams for the channels $q\bar{q} \rightarrow qH$, $q\bar{q} \rightarrow gH$ and $gg \rightarrow gH$ at leading order in the Standard Model.

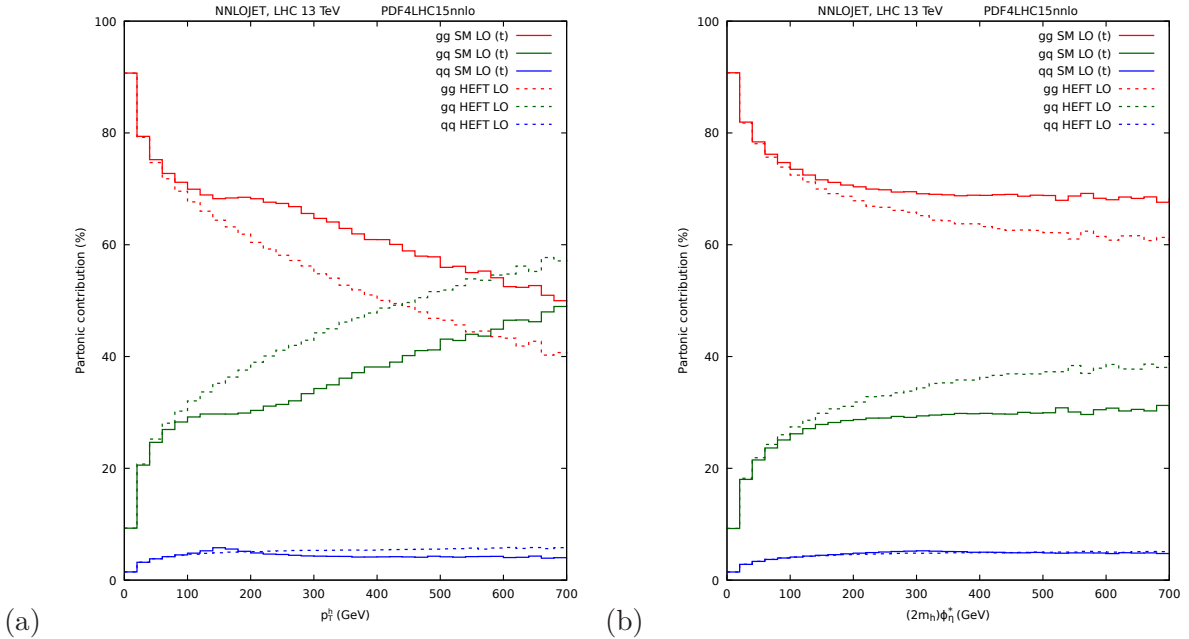


Fig. II.16: The percentage contributions from the gluon-gluon (red), gluon-quark (green) and quark-quark (blue) channels to the (a) p_{TH} and (b) ϕ_n^* distributions at $\sqrt{s} = 13$ TeV in the Standard Model with a top quark loop. The breakdown using the Higgs Effective Theory is shown dashed.

II.5.2 The Standard Model at one-loop

The LO contribution to Higgs boson plus jet production contains Feynman diagrams with one loop. Examples of the Feynman diagrams in the $q\bar{q} \rightarrow qH$, $q\bar{q} \rightarrow gH$ and $gg \rightarrow gH$ channels are shown in Fig. II.15. The channels involving a quark in the initial or final state are all related by crossing symmetries and so it is sufficient to calculate the matrix element for any one of these channels and obtain the others by crossing. The result for all partonic channels was first calculated in 1988 [176] and later analysed in detail for Higgs boson plus jet production, including expansions in the limit of large top-quark mass [177].

Fig II.16 shows the percentage contribution of the gg , $q\bar{q} \equiv q\bar{q} + \bar{q}q + gq + g\bar{q}$ and $qq \equiv q\bar{q} + \bar{q}q + qq + \bar{q}\bar{q}$ partonic channels for the p_{TH} and ϕ_n^* distributions. We see that for the LHC the gluon-gluon channel is dominant due to the high gluon luminosity, but that the quark-gluon channel is also important. We clearly see the effect of the $gg \rightarrow t\bar{t}$ threshold that enhances the $q\bar{q}$ channel around $p_{TH} \sim m_t$. We note that dominance of the gluon-gluon channel persists to

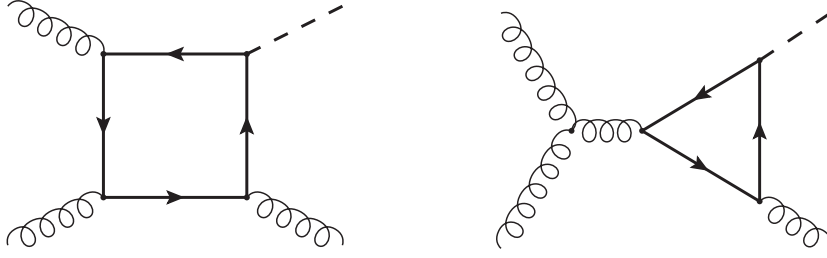


Fig. II.17: Feynman diagrams (2 out of 12) for the process $gg \rightarrow gH$ at leading order in the Standard Model.

higher values of $2m_H \phi_\eta^*$.

We will recompute this channel using techniques that are also applicable to multi-loop calculations. For this channel, there are 12 diagrams contributing at leading order: the two diagrams shown in Fig. II.17 plus the $3!$ permutations of the gluons.

In general we can write an L -loop amplitude as

$$A_{L\text{-loop}} = \sum_{i \in \text{diagrams}} \int \prod_{l=1}^L \frac{d^d k_l}{i\pi^{d/2}} \frac{N_i(\{k\})}{\prod_{j \in i} D_j(\{k\})} \quad (\text{II.55})$$

Here D_j denote the denominators stemming from the propagators of the Feynman diagrams, i.e. terms of the form $(k+p)^2 - m^2$, while N_i contains the rest of the terms in the Feynman diagram, i.e. all gamma matrices, colour factors, polarization vectors, spinors, and all other factors provided by the Feynman rules. Most importantly, N_i is a scalar. This means that after performing the traces, all of the loop momenta appear either contracted with one of the physical momenta, $k_i \cdot p_j$, or one of the external polarisations, $k_i \cdot \varepsilon_j$, or with another loop momentum $k_i \cdot k_j$. Here we will adopt the strategy of projectors described in Sec. II.5.1.1 so that the polarisation vectors are removed and the loop momentum only appears in terms like $k_i \cdot p_j$ and $k_i \cdot k_j$.

There are several public codes available for generating expressions for Eq. (II.55), see for example, Refs. [219–222]. These programs typically generate algebraic expressions for the Feynman diagrams (according to some model) without performing any algebra. This means that the numerators of the diagrams in general will contain long strings and traces of (Dirac) gamma matrices, from external fermions and fermions in loops respectively, along with products of the colour factors T_{ij}^a and f_{abc} from vertices containing coloured particles. Several algebraic manipulation programs enabling the reduction of such factors exist, see for example, Refs. [220, 223].

II.5.2.1 Integral Families

Finding a systematic and homogeneous way of expressing Feynman integrals, is crucial in order to identify relations between them. For a process with P external particles in (integer) D dimensions, only $E = \min(P-1, D)$ of these external momenta will be independent. P is reduced by one due to momentum conservation relating the momenta, while in a D -dimensional space, any vector can be expressed as a linear combination of D basis vectors. For an P -point process with L loops, it is not hard to realize that the number of inherently different scalar products of the type $k_i \cdot p_j$ or $k_i \cdot k_j$ is given by

$$N = L(L+1)/2 + LE \quad (\text{II.56})$$

where the first term comes from contracting the loop momenta with themselves, and the second from contraction the loop momenta with the external ones.

For $H + j$ production $E = 3$ so that at one-loop $N = 4$. This is exactly the number of propagators in the box-diagram (seen as g_9 on Fig. II.18) and reflects the fact that all propagators of integrals contributing to the one-loop process can be written as a subset of those of the box. We choose the propagators of the box diagram to be

$$\begin{aligned} D_1 &= k_1^2 - m_t^2, \\ D_2 &= (k_1 - p_1)^2 - m_t^2, \\ D_3 &= (k_1 - p_1 - p_2)^2 - m_t^2, \\ D_4 &= (k_1 - p_1 - p_2 - p_3)^2 - m_t^2, \end{aligned} \tag{II.57}$$

and we introduce the *integral family*

$$I_{\alpha_1, \alpha_2, \alpha_3, \alpha_4} = \int \frac{d^d k_1}{i\pi^{d/2}} \frac{1}{D_1^{\alpha_1} D_2^{\alpha_2} D_3^{\alpha_3} D_4^{\alpha_4}}. \tag{II.58}$$

Here the indices $\alpha_1, \dots, \alpha_4 \in \mathbb{Z}$ encode the power of the propagators appearing in a particular integral. As we will see, there are nine master integrals, which can be obtained by setting one or more of the α_i equal to zero.

In this case, the four independent scalar products are related to the propagator factors through,

$$\begin{aligned} k_1 \cdot k_1 &= D_1 + m_t^2, \\ 2k_1 \cdot p_1 &= D_1 - D_2 + p_1^2, \\ 2k_1 \cdot p_2 &= D_2 - D_3 + (p_1 + p_2)^2 - p_1^2, \\ 2k_1 \cdot p_3 &= D_3 - D_4 + (p_1 + p_2 + p_3)^2 - (p_1 + p_2)^2. \end{aligned} \tag{II.59}$$

The general strategy is to rewrite scalar products involving loop momentum appearing in the numerator as propagator factors. Sometimes these propagator factors will cancel against one of the propagators of the Feynman diagram, reducing the corresponding α_i by one. Any propagator factors remaining in the numerator simply have a negative value for the corresponding α_i .

To express all integrals appearing in the problem we will also need ‘‘crossed’’ integral families, these are related to the above integral family by permuting the external momenta.

For the two-loop process $N = 9$, but as we will see later, the most complicated Feynman integrals have at most seven propagators, so only seven of the nine scalar products can be expressed in terms of the propagators actually present in the problem. The remaining two are denoted irreducible scalar products (or ISPs) and they are inherently present in the problem. To identify and apply such relations systematically, goes under the name of integrand reductions, and is described in further detail in Appendix B.2.

II.5.2.2 Integration-By-Parts identities

One way of obtaining relations between Feynman integrals within a particular integral family is through the application of Integration-By-Parts (IBP) relations. The general form of the IBP relation states that

$$\int \frac{d^d k}{i\pi^{d/2}} \frac{\partial}{\partial k^\mu} v^\mu F(k) = 0, \tag{II.60}$$

where v can be any Lorentz vector and where $F(k)$ contains the Feynman integrand along with the remaining integrations for a multi-loop integral [224].

Eq. (II.60) works by letting the differential operator work on $F(k)$, where it will yield a sum of different terms, and thus expose a relationship between the corresponding Feynman integrals. We illustrate this with the example of the one-loop massless ($p_1^2 = p_2^2 = 0$) triangle. We define

$$J_{a_1, a_2, a_3} = \int \frac{d^d k}{i\pi^{d/2}} \frac{1}{((k - p_1)^2)^{a_1} (k^2)^{a_2} ((k + p_2)^2)^{a_3}}, \quad (\text{II.61})$$

where the normal triangle integral of course corresponds to $J_{1,1,1}$. Applying Eq. (II.60) to $J_{1,1,1}$ with $v = k$ (and using the fact that $\partial k^\mu / \partial k^\mu = d$), immediately yields the relation

$$(d - 4)J_{1,1,1} - J_{2,0,1} - J_{1,0,2} = 0, \quad (\text{II.62})$$

showing that the triangle integral $J_{1,1,1}$ may be re-expressed solely in terms bubble-type integrals (i.e. integrals with only two propagators), and the use of a second IBP will show that the triangle $J_{1,1,1}$ may be reduced solely to the plain bubble integral $J_{1,0,1}$, the relation being

$$J_{1,1,1} = \frac{-2(d - 3)}{s_{12}(d - 4)} J_{1,0,1}. \quad (\text{II.63})$$

Choosing different values for v , built from either internal or external momentum, and using different starting (or seed) integrals produces different IBP relations. The complete set of linearly independent IBP relations is finite, but nevertheless, it is conjectured that these IBP relations are sufficient to deduce all relations between Feynman integrals [225]⁴.

The integrals that cannot be eliminated by the IBP reduction are known as *master integrals*. While the number of master integrals is fixed by the full set of IBP relations, there is a lot of freedom in choosing which set of integrals to use. In general it is convenient to pick a set as *simple* as possible, which may be defined firstly as integrals with a minimal set of propagators (so choosing the bubble over the triangle), and then as integrals with as few propagators with powers higher than one, or alternatively with the smallest number of numerator factors.

An algorithm which systematizes the IBP relations according to such a criterion of simplicity, exists and is known as the Laporta algorithm [226], and several implementations of that algorithm are publicly available [227–232].

Even with the implementations mentioned above, the integral reductions are a bottleneck in current multi-loop Feynman integral calculations. Therefore several attempts have been made at finding alternative methods to achieve the reduction to master integrals. Examples of this include attempts at simplifying the IBPs in order to avoid integrals with squared propagators in the intermediate results [233–235], or at reducing directly to master integrals by identifying characteristic “master contours” in complex phase space [236, 237]. None of these developments will be described further here.

The number of master integrals for a given multi-loop process is highly dependent on the number of loops and mass-scales and can range from a few to a number in the hundreds. For the two-loop planar $gg \rightarrow gH$ there are 125 master integrals - too many for them to be listed here, see Ref. [180] for the full list and an accompanying figure.

Beyond one-loop, more than one integral family is needed when it is not possible to write all the integrals as having propagators which are a subset of the propagators of one diagram.

⁴Except relations imposed by symmetries of the diagrams, and relations imposed by the finite dimensionality of the space spanned by the external momenta.

For the planar contribution to $gg \rightarrow gH$ two families are needed (one corresponding to diagrams where the massive quark goes all the way around the diagram, and one where it stays on one side), but for the practical calculation four different families were used [180].

II.5.2.3 One-Loop Master Integrals

Use of the IBP identities shows that there are 9 master integrals (other integrals related to these by crossing symmetries also appear in the amplitude) defined by

$$\begin{aligned}
g_1(m_t^2) &= I_{2,0,0,0}, \\
g_2(s_{12}, m_t^2) &= I_{2,0,1,0}, & g_3(s_{23}, m_t^2) &= I_{0,2,0,1}, & g_4(m_H^2, m_t^2) &= I_{2,0,0,1}, \\
g_5(s_{12}, m_t^2) &= I_{1,1,1,0}, & g_6(s_{23}, m_t^2) &= I_{0,1,1,1}, \\
g_7(s_{12}, m_H^2, m_t^2) &= I_{1,0,1,1}, & g_8(s_{23}, m_H^2, m_t^2) &= I_{1,1,0,1}, \\
g_9(s_{12}, s_{23}, m_H^2, m_t^2) &= I_{1,1,1,1},
\end{aligned} \tag{II.64}$$

and shown in Fig. II.18. For practical calculations, these integrals need to be evaluated, either analytically or numerically (see for example Ref. [238] and references therein). The most common method for analytic evaluation of integrals is by identifying the differential equations (in terms of the external parameters, s_{ij}) and solving them [239–242]. In Appendix A we show how this can be done.

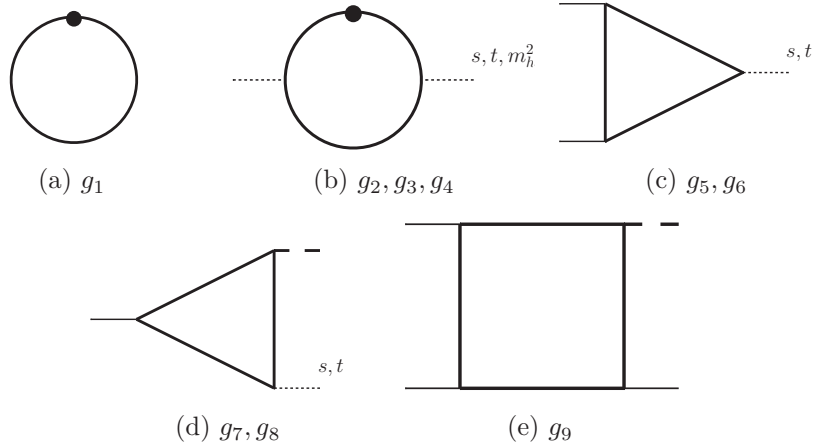


Fig. II.18: The nine one-loop master integrals for the $gg \rightarrow gH$ process.

II.5.2.4 The One-Loop Formfactors

By applying the projectors, as described in Sec. II.5.1.1, each diagram's contribution to each form factor can be computed. For example, the contribution of the triangle diagram shown in II.17 to F_{312} is:

$$F_{312} \supset f^{abc} C_\epsilon \frac{e g_{ht} g_s^3}{(d-3)} \left[(d-4) \frac{2m_t}{s_{12} s_{23}} I_{1,-1,0,1}^{(132)} + d \frac{4m_t}{s_{12} s_{23}} I_{1,1,-1,0}^{(132)} + (d-4) \frac{-4m_t}{s_{12} s_{23}} I_{1,0,-1,1}^{(132)} + \dots \right],$$

where $C_\epsilon = \pi^{d/2} / (2\pi)^d \Gamma(1-\epsilon)^2 \Gamma(1+\epsilon) / \Gamma(1-2\epsilon) = 1/(16\pi^2) + \mathcal{O}(\epsilon)$ and the ellipsis denotes a further 50 terms.

Using the IBP identities we can relate each integral appearing in the amplitude to our selected master integrals. Inserting these relations into the expression for our amplitude we

obtain:

$$\begin{aligned}
F_{212}(s_{12}, s_{13}, s_{23}) = & f^{abc} C_\epsilon \frac{2m_t e g_{ht} g_s^3}{(d-3)(d-2)} \left[\frac{8(d-4)(s_{12}^2 - s_{13}s_{23})}{s_{12}s_{23}(s_{12} + s_{13})(s_{12} + s_{23})} A(m_H^2, m_t^2) \right. \\
& - \frac{4(d-4)}{s_{12}s_{23}} B(s_{12}, m_H^2, m_t^2) \\
& - \frac{4s_{13} \left((d-4)s_{12}^2 + 2ds_{12}s_{23} + ds_{23}^2 \right)}{s_{12}^2 s_{23} (s_{12} + s_{23})^2} B(s_{13}, m_H^2, m_t^2) \\
& - \frac{4 \left((d-4)s_{12}^2 + 2ds_{12}s_{13} + ds_{13}^2 \right)}{s_{12}^2 (s_{12} + s_{13})^2} B(s_{23}, m_H^2, m_t^2) \\
& - \frac{(d-4) \left(s_{13}^2 + s_{23}^2 \right)}{s_{13}^2 s_{23}^2} C(s_{12}, s_{13}, s_{23}, m_t^2) \\
& - \frac{s_{13}^2 \left((d-4)s_{12}^2 + ds_{23}^2 \right)}{s_{12}^3 s_{23}^2} C(s_{13}, s_{23}, s_{12}, m_t^2) \\
& - \frac{s_{23} \left((d-4)s_{12}^2 + ds_{13}^2 \right)}{s_{12}^3 s_{13}} C(s_{23}, s_{12}, s_{13}, m_t^2) \\
& + \frac{2(d-3)(s_{13} + s_{23}) \left((d-2)s_{12} - 8m_t^2 \right)}{s_{12}^2 s_{23}} g_7(s_{12}, m_H^2, m_t^2) \\
& + \frac{2(d-3) \left((d-2)s_{12} \left(s_{12}^2 - s_{23}^2 \right) - 8m_t^2 \left(s_{12}^2 - 2s_{12}s_{23} - s_{23}^2 \right) \right)}{s_{12}^2 s_{23} (s_{12} + s_{23})} g_7(s_{13}, m_H^2, m_t^2) \\
& + \frac{2(d-3) \left((d-2)s_{12} \left(s_{12}^2 - s_{13}^2 \right) - 8m_t^2 \left(s_{12}^2 - 2s_{12}s_{13} - s_{13}^2 \right) \right)}{s_{12}^2 s_{23} (s_{12} + s_{13})} g_8(s_{23}, m_H^2, m_t^2) \\
& + \frac{(d-2) \left((d-4)s_{12}s_{23} + (d-3)s_{12}s_{13} - 4m_t^2 s_{13} \right)}{s_{12}s_{13}} g_9(s_{12}, s_{23}, m_H^2, m_t^2) \\
& + \frac{(d-2)s_{13} \left((d-4)s_{12}s_{13} + (d-3)s_{12}s_{23} - 4m_t^2 s_{23} \right)}{s_{12}^2 s_{23}^2} g_9(s_{12}, s_{13}, m_H^2, m_t^2) \\
& \left. + \frac{(d-2)s_{13} \left(-(d-3)s_{12}^2 + ds_{13}s_{23} + 12m_t^2 s_{12} \right)}{s_{12}^3} g_9(s_{23}, s_{13}, m_H^2, m_t^2) \right],
\end{aligned}$$

$$F_{311}(s_{23}, s_{12}, s_{13}) = F_{332}(s_{13}, s_{23}, s_{12}) = F_{212}(s_{12}, s_{13}, s_{23}),$$

$$\begin{aligned}
F_{312}(s_{12}, s_{13}, s_{23}) = & f^{abc} C_\epsilon \frac{2m_t e g_{ht} g_s^3}{(d-3)(d-2)} \left[\left(\frac{8(d-4)}{s_{12}s_{13} + s_{13}s_{23}} \right) A(m_H^2) \right. \\
& + \frac{4 \left((d-2)s_{13}^2 + 2ds_{13}s_{23} + (d-2)s_{23}^2 \right)}{s_{13}s_{23}(s_{13} + s_{23})^2} B(s_{12}, m_H^2, m_t^2) \\
& + \frac{(d-2)s_{12} \left(s_{13}^2 + s_{23}^2 \right)}{s_{13}^2 s_{23}^2} C(s_{12}, s_{13}, s_{23}, m_t^2) \\
& \left. + \frac{4(d-3) \left((d-2)(s_{13} + s_{23}) - 8m_t^2 \right)}{s_{12}(s_{13} + s_{23})} g_7(s_{12}, m_H^2, m_t^2) \right],
\end{aligned}$$

$$\begin{aligned}
& \left. + \frac{(d-2) \left(-(d-2)s_{12}s_{23} + (d-3)s_{13}^2 - 4m_t^2 s_{13} \right)}{s_{13}^2} g_9(s_{12}, s_{23}, m_H^2, m_t^2) \right] \\
& + (s_{12} \rightarrow s_{13}, s_{13} \rightarrow s_{23}, s_{23} \rightarrow s_{12}) + (s_{12} \rightarrow s_{23}, s_{13} \rightarrow s_{12}, s_{23} \rightarrow s_{13}).
\end{aligned}$$

The abbreviations A, B, C are

$$\begin{aligned}
A(m_H^2, m_t^2) &= g_1(m_t^2) + (4m_t^2 - m_H^2)g_4(m_H^2, m_t^2), \\
B(x, m_H^2, m_t^2) &= (4m_t^2 - x)g_{2,3}(x, m_t^2) - (4m_t^2 - m_H^2)g_4(m_H^2, m_t^2), \\
C(x, y, z, m_t^2) &= (d-2)g_{5,6}(x, m_t^2) - (d-2)\frac{y+z}{x}g_{7,8}(x, m_H^2, m_t^2),
\end{aligned}$$

here $g_{i,j}$ means either g_i or g_j depending on the argument x . Note that some integrals which are related to the master integrals by crossing, e.g., $g_7(s_{13}, m_H^2, m_t^2)$ also appear in the formfactors.

II.5.2.5 Heavy Top-Quark Limit

One interesting limit is obtained by considering that the top-quark mass is very much larger than the Higgs boson mass and the other scales present in the integral (s_{12}, s_{13}, s_{23}) .

Starting from the form factors presented in Sec. II.5.2.4 we can straightforwardly expand the coefficient of each master integral in inverse powers of m_t^2 . The expansion of the master integrals is straightforward given the analytic results (see Appendix A),

$$g_1(m_t^2) = (-1)^2 \Gamma(2 - d/2) \left(\frac{1}{m_t^2} \right)^{2-d/2}, \quad (\text{II.65})$$

$$g_2(s_{12}, m_t^2) = (-1)^3 \Gamma(3 - d/2) \left(\frac{1}{m_t^2} \right)^{3-d/2} \left(\frac{1}{2} + \frac{s_{12}}{m_t^2} \frac{(3-d/2)}{12} + \mathcal{O}\left(\frac{1}{m_t^4}\right) \right), \quad (\text{II.66})$$

$$g_5(s_{12}, m_t^2) = (-1)^3 \Gamma(3 - d/2) \left(\frac{1}{m_t^2} \right)^{3-d/2} \left(\frac{1}{2} + \frac{s_{12}}{m_t^2} \frac{(3-d/2)}{24} + \mathcal{O}\left(\frac{1}{m_t^4}\right) \right), \quad (\text{II.67})$$

$$g_7(s_{12}, m_H^2, m_t^2) = (-1)^3 \Gamma(3 - d/2) \left(\frac{1}{m_t^2} \right)^{3-d/2} \left(\frac{1}{2} + \frac{(s_{12} + m_H^2)}{m_t^2} \frac{(3-d/2)}{24} + \mathcal{O}\left(\frac{1}{m_t^4}\right) \right), \quad (\text{II.68})$$

$$g_9(s_{12}, s_{23}, m_H^2, m_t^2) = (-1)^4 \Gamma(4 - d/2) \left(\frac{1}{m_t^2} \right)^{4-d/2} \left(\frac{1}{6} + \mathcal{O}\left(\frac{1}{m_t^2}\right) \right). \quad (\text{II.69})$$

The series expansion in some kinematic invariant or mass of the master integrals can also be obtained without knowing the result of the integral using the technique of *expansion by regions* [243–245]. Let us demonstrate the procedure by applying it to one of the multi-scale triangle integrals $g_7(s, m_H^2, m_t^2)$. In the case at hand we wish to expand in inverse powers of the top-quark mass. All propagators are top-quark propagators and therefore there is only one *region*, which is equivalent to the one-loop integral itself. We begin by Feynman parametrising the integral,

$$g_7(s_{12}, m_H^2, m_t^2) = (-1)^3 \Gamma(3 - d/2) \int_0^\infty \left(\prod_{i=1}^3 dx_i \right) \delta(1 - \sum_{i=1}^3 x_i) \frac{\mathcal{U}^{3-d}}{\mathcal{F}^{3-d/2}},$$

$$\mathcal{U} = x_1 + x_2 + x_3,$$

$$\mathcal{F} = -s_{12}x_2x_3 - m_H^2x_1x_3 + m_t^2(x_1 + x_2 + x_3)^2.$$

Introducing a scaling parameter ρ via the substitution $m_t^2 = \bar{m}_t^2/\rho$, $s_{12} = \bar{s}_{12}$, $m_H^2 = \bar{m}_H^2$ and factoring out the overall dependence on ρ we obtain

$$g_7(s_{12}, m_H^2, m_t^2) = (-1)^3 \Gamma(3 - d/2) \int_0^\infty \left(\prod_{i=1}^3 dx_i \right) \delta(1 - \sum_{i=1}^3 x_i) \rho^{3-d/2} \frac{\mathcal{U}^{3-d}}{\mathcal{F}^{3-d/2}},$$

$$\mathcal{U} = x_1 + x_2 + x_3,$$

$$\mathcal{F} = \rho(-\bar{s}_{12}x_2x_3 - \bar{m}_H^2x_1x_3) + \bar{m}_t^2(x_1 + x_2 + x_3)^2.$$

Series expanding in ρ gives

$$g_7(s_{12}, m_H^2, m_t^2) = (-1)^3 \Gamma(3 - d/2) \int_0^\infty \left(\prod_{i=1}^3 dx_i \right) \delta(1 - \sum_{i=1}^3 x_i) \rho^{3-d/2}$$

$$\left[\frac{(x_1 + x_2 + x_3)^{3-d}}{(\bar{m}_t^2(x_1 + x_2 + x_3)^2)^{3-d/2}} \right.$$

$$\left. - \rho(3 - d/2)(-\bar{s}_{12}x_2x_3 - \bar{m}_H^2x_1x_3) \frac{(x_1 + x_2 + x_3)^{3-d}}{(\bar{m}_t^2(x_1 + x_2 + x_3)^2)^{4-d/2}} + \mathcal{O}(\rho^2) \right].$$

All scales can be factored out of each integral and this greatly simplifies their evaluation,

$$\int_0^\infty \left(\prod_{i=1}^3 dx_i \right) \delta(1 - \sum_{i=1}^3 x_i) \frac{1}{(x_1 + x_2 + x_3)^3} = \frac{1}{2},$$

$$\int_0^\infty \left(\prod_{i=1}^3 dx_i \right) \delta(1 - \sum_{i=1}^3 x_i) \frac{x_2x_3}{(x_1 + x_2 + x_3)^4} = \frac{1}{24},$$

$$\int_0^\infty \left(\prod_{i=1}^3 dx_i \right) \delta(1 - \sum_{i=1}^3 x_i) \frac{x_1x_3}{(x_1 + x_2 + x_3)^4} = \frac{1}{24}.$$

Inserting the results for these integrals into the expansion of $g_7(s_{12}, m_H^2, m_t^2)$ and rewriting \bar{m}_t^2 , \bar{s}_{12} , \bar{m}_H^2 in terms of the original variables, the dependence on ρ cancels and we obtain the result of Eq. (II.68).

Expanding each of the form factors in the $m_t \rightarrow \infty$ limit we obtain:

$$F_{212} = N \frac{1}{s_{23}}, \quad F_{332} = N \frac{1}{s_{13}}, \quad F_{311} = N \frac{1}{s_{12}}, \quad F_{312} = N \left(\frac{1}{s_{23}} + \frac{1}{s_{13}} + \frac{1}{s_{12}} \right), \quad (\text{II.70})$$

where

$$N = f^{abc} C_\epsilon \frac{8}{3} \frac{e g_{ht} g_s^3}{m_t} = f^{abc} C_\epsilon \frac{8}{3} \frac{g_s^3}{v}. \quad (\text{II.71})$$

Inserting the result for each of the form factors into Eq. (II.48) we obtain the result for the squared amplitude in the limit $d \rightarrow 4 - 2\epsilon$,

$$|\mathcal{M}_{gg \rightarrow gH}|^2 = 4N_c \left(N_c^2 - 1 \right) \frac{\alpha_S^3}{\pi v^2} \frac{(m_H^8 + s_{12}^4 + s_{13}^4 + s_{23}^4)(1 - 2\epsilon) + \epsilon/2(m_H^4 + s_{12}^2 + s_{13}^2 + s_{23}^2)^2}{9s_{12}s_{13}s_{23}}.$$

We must now assess in what range of the kinematic invariants s_{12} and s_{13} this expansion is valid. To gain some intuition, let us first consider a single integral $g_5(s_{12}, m_t^2)$ appearing in the amplitude. The integral has two massless on-shell legs and one leg off-shell with mass s_{12} ,

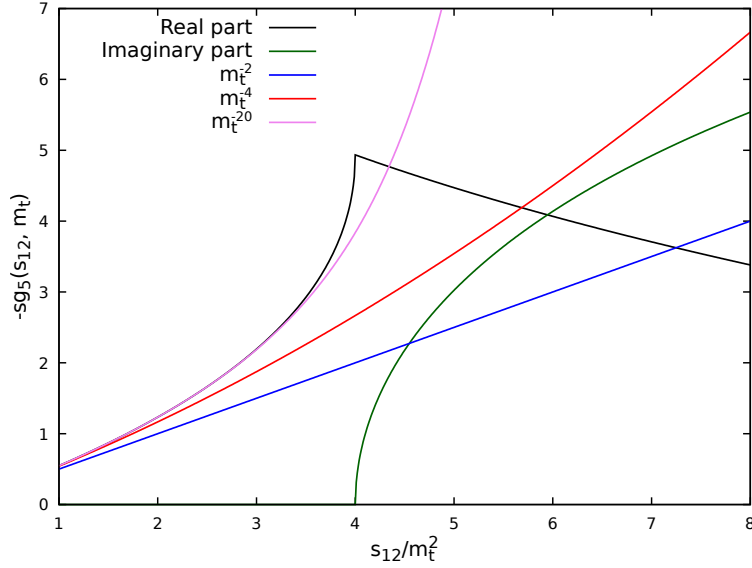


Fig. II.19: The real and imaginary part of the triangle integral $g_5(s_{12}, m_t^2)$ together with the result obtained in the large top-mass expansion keeping up to the 1st, 2nd and 10th terms in the series.

the internal propagators are all massive with mass m_t . In a compact notation the result for this integral is

$$-s_{12} g_5(s_{12}, m_t^2) = -\frac{1}{2} \ln^2 \left(\frac{1-\beta}{1+\beta} \right), \quad \beta = \sqrt{1 - \frac{4m_t^2}{s_{12}}}.$$

The integral has a branch point at $s_{12} = 4m_t^2$ which corresponds to the top-quark propagators going on-shell. We can see in Fig. II.19 that for $s_{12} \geq 4m_t^2$ the integral develops an imaginary part. Since the integral depends only on s_{12} and m_t^2 the heavy top-quark mass expansion for this integral corresponds to an expansion in $s_{12}/4m_t^2$ centred at 0 with a radius of convergence equal to 1. The first few terms are given by

$$-s_{12} g_5(s_{12}, m_t^2) = \frac{s_{12}}{2m_t^2} + \frac{s_{12}^2}{24m_t^4} + \mathcal{O}\left(\frac{s_{12}^3}{m_t^6}\right). \quad (\text{II.72})$$

Fig. II.19 also shows the large mass expansion result keeping the n terms of the series in (s_{12}/m_t^2) with $n = 1, 2, 10$. We can see that above the top-quark threshold the series expansion does not converge to the true result.

Given the break down of the heavy-top quark expansion of the loop integrals for $s_{12} \geq 4m_t^2$, upon which the amplitude and cross-section depend, we expect that the discrepancy between the heavy top-quark limit and the full calculation grows above this threshold. Fig. II.20 shows that for $\sqrt{s_{12}} < 2m_t$ the ratio of the SM prediction retaining the full top mass dependence to the HEFT prediction is roughly constant. Since s_{12} is greater than m_H^2 this implies that at the lowest values of s_{12} the expansion parameter is,

$$\frac{s_{12}}{4m_t^2} \sim \frac{m_H^2}{4m_t^2} \sim 0.13.$$

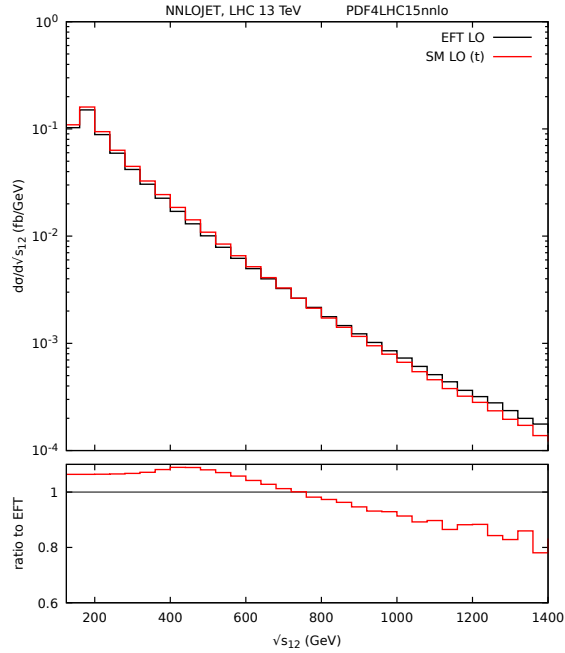


Fig. II.20: The partonic invariant mass distribution for the Standard Model with a single top quark compared with the Higgs Effective Theory for the gluon induced partonic channel. The lower panel shows the ratio.

Relative to the leading term, we have neglected terms of this order, and indeed, we see that the SM and HEFT predictions differ by $\mathcal{O}(10\%)$. Somewhat above $\sqrt{s_{12}} \sim 2m_t$ the SM prediction is further enhanced relative to the HEFT prediction as the top-quark can become on shell. When the partonic invariant mass $\sqrt{s_{12}}$ is much greater than $2m_t$ the SM begins to fall relative to the HEFT prediction leading to a larger discrepancy far above the threshold.

In the $gg \rightarrow gH$ process, the energy E_H of the Higgs boson in the partonic centre of mass frame is given by,

$$E_H^2 = \frac{(s_{12} - m_H^2)^2}{4s_{12}}. \quad (\text{II.73})$$

The Higgs boson transverse momentum is

$$p_{TH} = E_H \sin \theta, \quad (\text{II.74})$$

where θ is the angle between the Higgs boson and the beam axis in this frame. It is further related to the Mandelstam variables by,

$$p_{TH}^2 = \frac{s_{13}s_{23}}{s_{12}}. \quad (\text{II.75})$$

Since $E_H \geq p_{TH}$, solving Eq. (II.73) for s_{12} yields a lower bound in terms of p_{TH} ,

$$s_{12} = \left(E_H + \sqrt{E_H^2 + m_H^2} \right)^2 \geq \left(p_{TH} + \sqrt{p_{TH}^2 + m_H^2} \right)^2. \quad (\text{II.76})$$

For a fixed s_{12} , the largest p_{TH} is obtained when the bound in Eq. (II.76) is saturated. Setting $s_{12} = 4m_t^2$ therefore tells us for which values of p_{TH} the threshold starts to open,

$$p_{TH} > \frac{4m_t^2 - m_H^2}{4m_t}. \quad (\text{II.77})$$

For example, with $m_H = 125$ GeV, $m_t = 174$ GeV we obtain $p_{TH} > 152$ GeV. Above this value of p_{TH} all contributions to the differential cross-section come from above the top-quark threshold where we can not reliably trust the heavy top-quark expansion. The p_{TH} distribution for the heavy-top quark limit and for the Standard Model is shown in Fig. II.6 and, as expected, at large p_{TH} we can see a very large deviation between the exact and approximate results.

At lower values of p_{TH} there may be a contribution to the differential cross-section from above the top-quark threshold (since $E_H \geq p_{TH}$). However, the parton luminosity strongly prefers smaller invariant masses so that the majority of the cross section comes from within the radius of convergence of the heavy top-quark expansion and the approximate results are reliable. This can be also seen in Fig. II.6 where the exact and approximate results are in good agreement at low to medium p_{TH} .

The discrepancy is less marked for the ϕ_η^* distribution shown in Fig. II.7 since a particular value of ϕ_η^* gets contributions from a range of p_{TH} . Again, since the p_{TH} distribution is peaked at lower p_{TH} , this means that most of the ϕ_η^* distribution is dominated by the low p_{TH} region.

Another approach to studying the high p_{TH} behaviour of Higgs boson plus (multi) jet production is the use of leading-log high energy resummation techniques. It has been shown shown that for large p_{TH} the differential partonic cross section scales as $1/p_{TH}^2$ in the SM, whilst in the large top-quark mass limit it scales only as $1/p_{TH}$ [246, 247].

II.5.3 Heavy Top-Quark Effective Theory

The one-loop amplitude in the limit of large top-quark mass is extremely simple in comparison to the result retaining the full top mass dependence. From its simplicity, one might guess that there is a much simpler way of obtaining the amplitude directly in the large quark mass limit. Indeed, this turns out to be the case. Rather than computing the full amplitude and then taking the limit $m_t \rightarrow \infty$, it is much simpler to first take the limit at the level of the Lagrangian. This can be done by integrating out the top-quark field. The result is that the Lagrangian now contains an effective coupling between the Higgs and two or more gluons:

$$\mathcal{L}_{eff} \supset c_g \frac{\alpha_S}{12\pi} \frac{H}{v} G_{\mu\nu}^a G^{a\ \mu\nu}$$

where the effective coupling c_g is computed by matching the effective theory to the full theory. This involves computing some quantity that depends on the effective coupling in the effective theory and in the full theory and then demanding that the two quantities are equivalent. Thus, we could in principle compute the matching using our full result for Higgs plus jet or by computing a simpler quantity, for example the top-quark contribution to the gluon self energy [248]. The effective coupling c_g is known to four-loops [248, 249] and, to $\mathcal{O}(\alpha_S^2)$ is given by the perturbative expansion,

$$c_g = 1 + \frac{11}{4} \frac{\alpha_S}{\pi} + \mathcal{O}(\alpha_S^2).$$

The interactions in the effective theory are schematically related to those in the full theory, as illustrated in Fig. II.21.

The effective Lagrangian generates vertices involving the Higgs boson and two or more gluons. From the Lagrangian we can derive the Feynman rules shown in Fig. II.22, where

$$\begin{aligned} H^{\mu\nu}(p_1, p_2) &= g^{\mu\nu} p_1 \cdot p_2 - p_1^\nu p_2^\mu, \\ V_{abc}^{\mu\nu\rho}(p_1, p_2, p_3) &= g_s f^{abc} (g^{\mu\nu}(p_1^\rho - p_2^\rho) + g^{\nu\rho}(p_2^\mu - p_3^\mu) + g^{\rho\mu}(p_3^\nu - p_1^\nu)), \\ X_{abcd}^{\mu\nu\rho\sigma} &= -ig_s^2 \left(f^{abe} f^{cde} (g^{\mu\rho} g^{\nu\sigma} - g^{\mu\sigma} g^{\nu\rho}) \right. \\ &\quad \left. + f^{ace} f^{bde} (g^{\mu\nu} g^{\rho\sigma} - g^{\mu\sigma} g^{\nu\rho}) \right) \end{aligned}$$

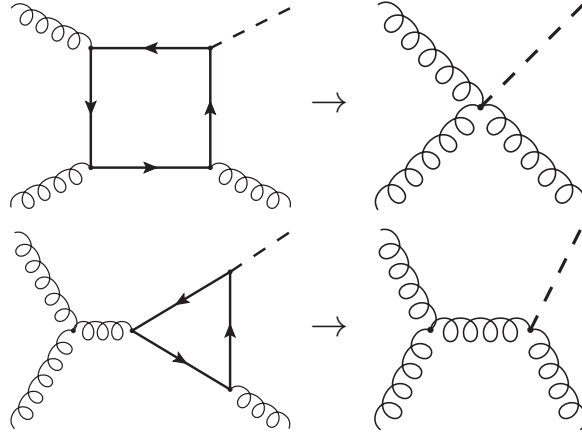


Fig. II.21: Schematic picture of the relation between the SM Feynman Diagrams and those of the HEFT, where the Higgs boson has an effective coupling to gluons.

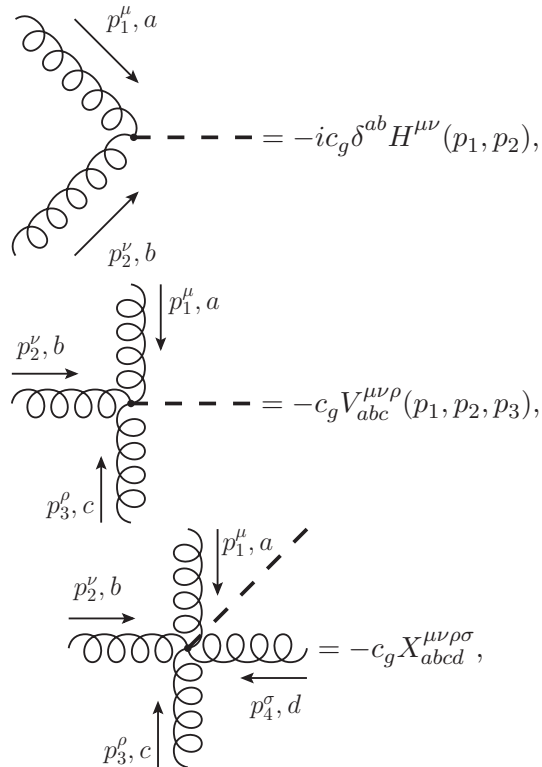


Fig. II.22: The HEFT Feynman rules involving the effective coupling of the Higgs boson to gluons.

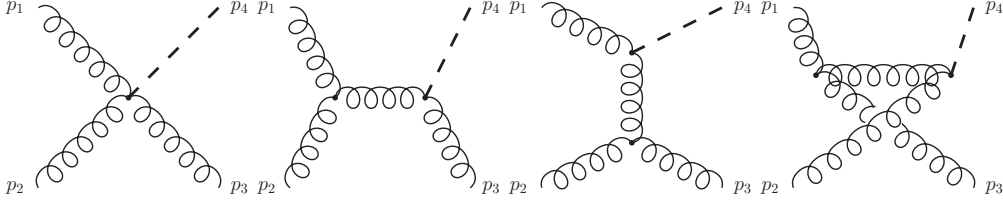


Fig. II.23: The Feynman diagrams for the process $gg \rightarrow gH$ at leading order in the HEFT.

$$+f^{ade}f^{bce}(g^{\mu\nu}g^{\sigma\rho} - g^{\mu\rho}g^{\nu\sigma}).$$

In the effective theory, four diagrams contribute to the $gg \rightarrow gH$ partonic channel at leading order, shown in Fig. II.23. We can compute these diagrams by decomposing the amplitude as described in II.5.1.1 and using projectors to extract the formfactors, or (since they are tree level diagrams) simply by squaring them. The result for the squared amplitude in the limit $d \rightarrow 4 - 2\epsilon$ is

$$|\mathcal{M}_{gg \rightarrow gH}|^2 = 4N_c(N_c^2 - 1) \frac{\alpha_S^3}{\pi v^2} \frac{(m_H^8 + s_{12}^4 + s_{13}^4 + s_{23}^4)(1 - 2\epsilon) + \epsilon/2(m_H^4 + s_{12}^2 + s_{13}^2 + s_{23}^2)^2}{9s_{12}s_{13}s_{23}}.$$

in agreement with the first term of the expansion of the full theory result in the limit of large top mass.

Note that in contrast to the full theory, the Feynman rules of the effective theory allow for Higgs plus jet production at tree-level. Concretely, the $\mathcal{O}(\alpha_S^3)$ calculation was one-loop in the full theory but tree-level in the effective theory, the $\mathcal{O}(\alpha_S^4)$ calculation is two-loop in the full theory but only one-loop in the effective theory and so on. This fact makes computing a given perturbative order vastly simpler in the effective theory than in the full theory. However, the effective theory is yet simpler still, since the top-quark has been integrated out of this theory the integrals in the effective theory contain no top-quark propagators, this means that there are no integrals with massive internal lines at any order in QCD in the effective theory.

II.5.4 Theory Uncertainties

In order to fully assess the potential of ϕ_η^* as an observable, we must determine whether it leads to smaller theoretical uncertainties than p_{TH} and find out whether the overall conclusions regarding its usefulness may be affected by arbitrary choices in the theory settings.

The theoretical uncertainties can be loosely classified as:

- Missing higher order uncertainties (MHOU): Observables in high energy quantum field theory can only be calculated as a perturbative expansion in the coupling constants, of which only the first few terms are known exactly. Usually the terms which have not been computed are estimated though *scale variations*.
- Parametric uncertainties: These arise from the fact that some theoretical parameters parameters cannot be calculated from the theory. These include, for example, the PDF uncertainties, the value of the strong coupling constant and the treatment of the heavy quark masses.

A particular difficulty with MHOUs is that there currently isn't a well established procedure to interpret them in a statistically consistent way, because nothing is known a priori about the distribution of the higher order coefficients. Some refinements can be made if we make some assumptions about the coefficients of the perturbative expansion. For example, that they are

bounded from above and distributed uniformly in a given range [250], or that they exhibit a similar behaviour to that of known perturbative series [251].

On the other hand the parametric uncertainties are obtained by procedures that involve propagating statistical uncertainties from the experimental data and simulations, where the statistical distribution of the parameters are under control. However, the parameters themselves are typically affected by MHOUs, and therefore the distinction above is only indicative.

We now discuss the various sources of theory uncertainty in the Leading Order computation described in Section II.5 and the approach we have taken to estimate their impact, while making connections to the results in Sections II.4 and II.5.5 where appropriate.

II.5.4.1 Scale uncertainties

MHOUs are typically estimated by varying the renormalisation and factorization scales that enter the calculation. This procedure (commonly called *scale variations*) can capture some of the effect of the missing higher orders by exploiting the fact that the dependency on the scales is formally a higher order effect that cancels at all orders (see e.g. Chapter 12 of Ref. [252]).

Conventionally, the following procedure is followed:

- Select a *central scale*. Typically one chooses a scale that minimizes the scale dependence (see e.g. [253]), since this choice is likely to also minimize the logarithmic contributions in the higher order terms.
- A *scale uncertainty* is assigned by varying the factorization and renormalisation scales following some prescription and repeating the calculation. A common choice is to use the same value for μ_R and μ_F , $\mu = \mu_R = \mu_F$, and call the “scale uncertainty” the range $\frac{1}{2}(\sigma_{2\mu} - \sigma_{\frac{1}{2}\mu})$, where $\sigma_{2\mu}$ and $\sigma_{\frac{1}{2}\mu}$ are the values of the observable calculate setting both the renormalisation and factorization scale to 2 and $\frac{1}{2}$ times the central scale respectively. The Higgs Cross Section Working group recommends a more involved 7 point variation procedure [37].

We note that while finding a sensible value for the central scale is simple for single scale problems, it is a known fact that for more complicated process selecting an *optimal* scale is non-trivial and can lead to important phenomenological differences, bigger than the scale variations discussed above. For example in, Ref. [254] various choice of scales for the jet cross sections are discussed and it is shown that the scale choice can have an effect on the description of the data that is more significant than the error band estimated by scale variations. Consequently, while currently there doesn’t exist an agreed upon procedure among the community, it is recommended that several scale choices are considered, possibly also assigning an uncertainty associated to the choice of central scale.

To estimate the scale uncertainties, we have obtained the p_{TH} and ϕ_η^* distributions for our central scale choice,

$$\mu_R = \mu_F = \frac{1}{2}M_{TH}$$

and for both scales multiplied simultaneously by either $\frac{1}{2}$ or 2. Additionally, we have considered a fixed scale $\mu_R = \mu_F = m_H$. While this is not a good choice at large p_{TH} [255], it allows us to set limits on the effect of a particularly unfortunate choice, and furthermore it is interesting to observe the different behaviour of ϕ_η^* and p_{TH} . The results are presented in Fig. II.24. By fluctuating about the central scale by a factor two we obtain a scale uncertainty of approximately $\pm 30\%$, which contains the NLO prediction [255]. Because high values of ϕ_η^* are affected by the contributions coming from low p_{TH} , they change less when the scale is set to m_H .

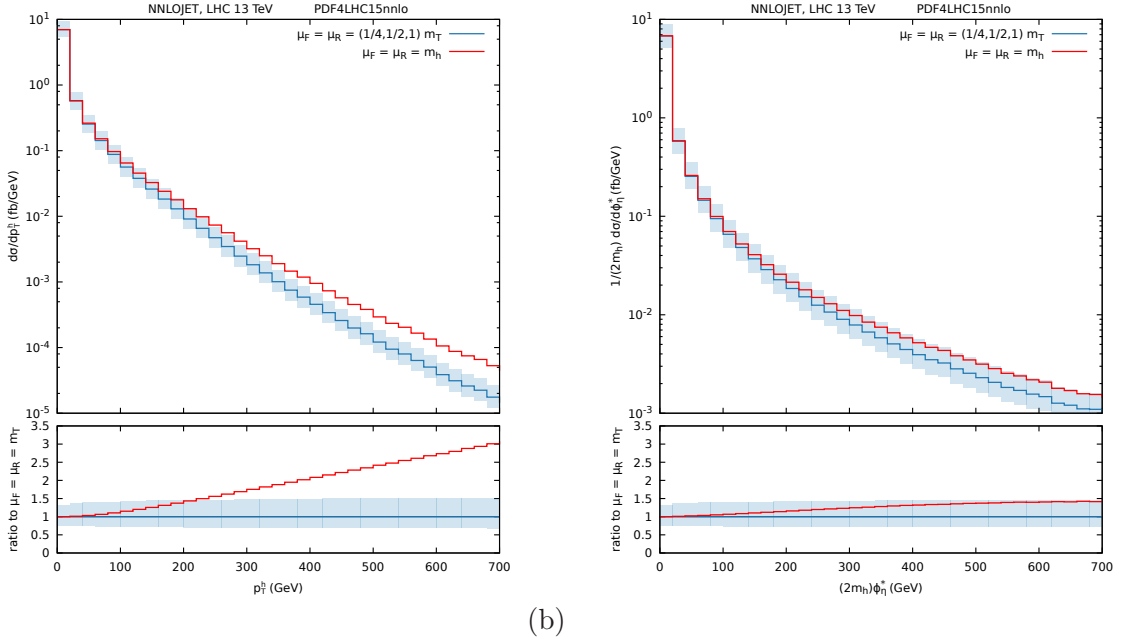


Fig. II.24: (a) p_{TH} and (b) ϕ_η^* distributions with scale variations. The band shows the scale uncertainty estimation obtained by multiplying the central choice of scales ($\mu_R = \mu_F = m_T/2$) by 0.5 and 2. The red line shows the effect of fixing both scales to m_H .

II.5.4.2 α_S uncertainties

The value of the strong coupling constant, α_S , is not a fundamental input of the theory and needs to be estimated from data. Several methods exist for determining α_S at various scales (including Lattice calculations, determinations from parton densities and structure functions, global electroweak fits, and τ decays [256]). These are related though the running of the coupling constant to yield a value of $\alpha_S(M_Z)$ in the $\overline{\text{MS}}$ scheme. Note that it is only possible to relate the value of the coupling constant obtained at some arbitrary scale to $\alpha_S(M_Z)$ through QCD running up to some finite perturbative order. Similarly, the dependence on α_S in the high energy processes that are used for the coupling constant determinations is only known in perturbation theory. Consequently it is affected by MHOUs, which need to be estimated for each measurement.

One would typically repeat the calculation with a matching PDF set for the two values corresponding to the upper and lower fluctuations around the global average. Currently, the recommended values are [37].

$$\alpha_S(M_Z) = 0.118 \pm 0.001 \quad (\text{II.78})$$

with the prescription of using $\alpha_S(M_Z) = 0.118$ as the central value and $\alpha_S(M_Z) = 0.117$ and $\alpha_S(M_Z) = 0.119$ as upper and lower variations respectively.

The PDF4LHC PDF set we are using comes with the slightly more conservative choice of

$$\alpha_S(M_Z) = 0.118 \pm 0.0015 \quad (\text{II.79})$$

and we have computed the p_{TH} and ϕ_η^* distributions using the PDF4LHC15_nnlo_asvar PDF sets [196]. The results are presented in Fig. II.25. For both distributions, we obtain uncertainties of less than $\pm 5\%$ across the whole range of the observable.

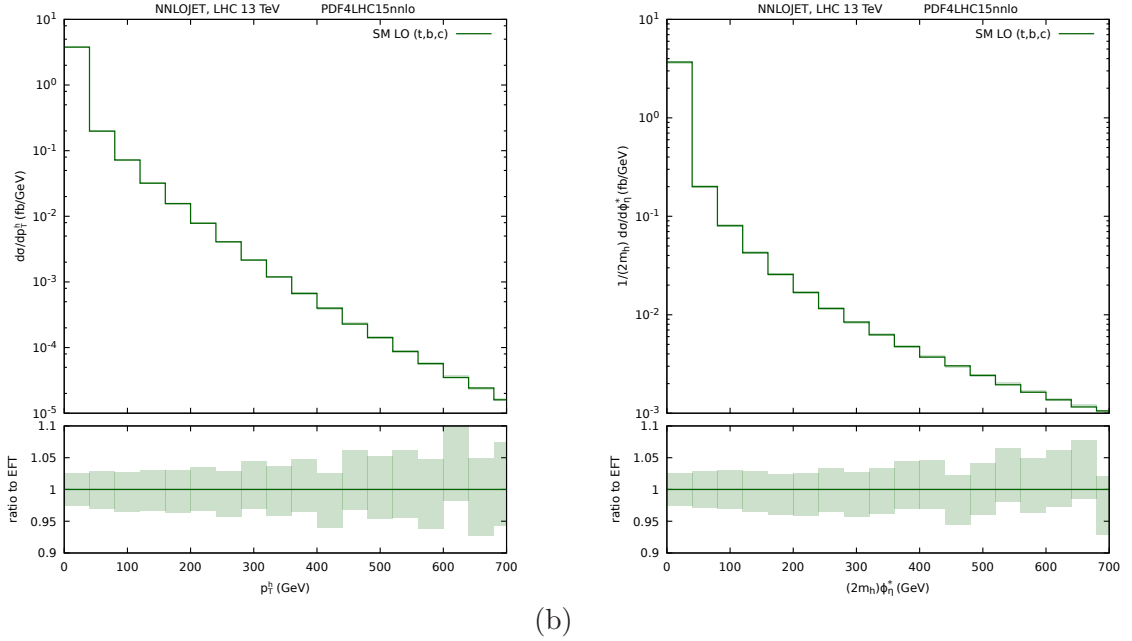


Fig. II.25: (a) p_{TH} and (b) ϕ_{η}^* distributions with α_S variations. As described in the main text, we have used the $\alpha_S(M_Z) = 0.118$ as central reference (solid line) and the predictions with $\alpha_S(M_Z) = 0.1165$ and $\alpha_S(M_Z) = 0.1195$ to compute the uncertainty band.

II.5.4.3 Heavy quark mass uncertainties

The precise formulation of the renormalisation scheme used to define the masses of the heavy quarks can have an important impact on the numerical results. At leading order, the different schemes simply reduce to different numerical values of the quark masses. Consequently, we estimate the associated uncertainty as coming from the difference between the results for these different schemes. These differences (of $\sim 15\%$) are considerably larger than the uncertainties associated with the determination of the masses within each of the schemes (of $\sim 3\%$), which we therefore neglect.

At higher orders, this uncertainty is significantly reduced notably due to the appearance of the renormalisation scheme dependent counterterms which compensate the mass differences (see Ref. [257] and references therein).

In order to assess the uncertainty related to the definition of the heavy quark masses, we have computed the p_{TH} and ϕ_{η}^* distributions with three variations of the top and bottom masses, but otherwise using the default setup described in Sec. II.1.1. We have selected ranges consistent with the differences arising from renormalisation schemes quoted in the PDG 2016 report [256]: For the top quark we have used 160, 174 and 188 GeV, and for the bottom quark we have used 4.2, 4.6 and 5 GeV. For the top mass, this range contains the pole and $\overline{\text{MS}}$ masses as well as the results from the direct measurement of the $t\bar{t}$ cross section. For the bottom mass, the range contains the results from the renormalon subtracted and $\overline{\text{MS}}$ determinations. We display the results in Fig. II.26. In the low p_{TH} and ϕ_{η}^* regions, the impact of varying the quark masses is negligible compared to impact of the parton shower (see Sec. II.4).

In fact, the effects of changes in the bottom mass are at the percent level over the whole range of p_{TH} and ϕ_{η}^* , and are therefore negligible at the level of precision of this calculation. The value of the top mass becomes a relevant sources of uncertainty at large p_{TH} as it leads to a $\sim 10\%$ increased uncertainty. On the other hand, the predictions for large values of ϕ_{η}^* are affected much less by the changes in m_t , with changes below 3%.

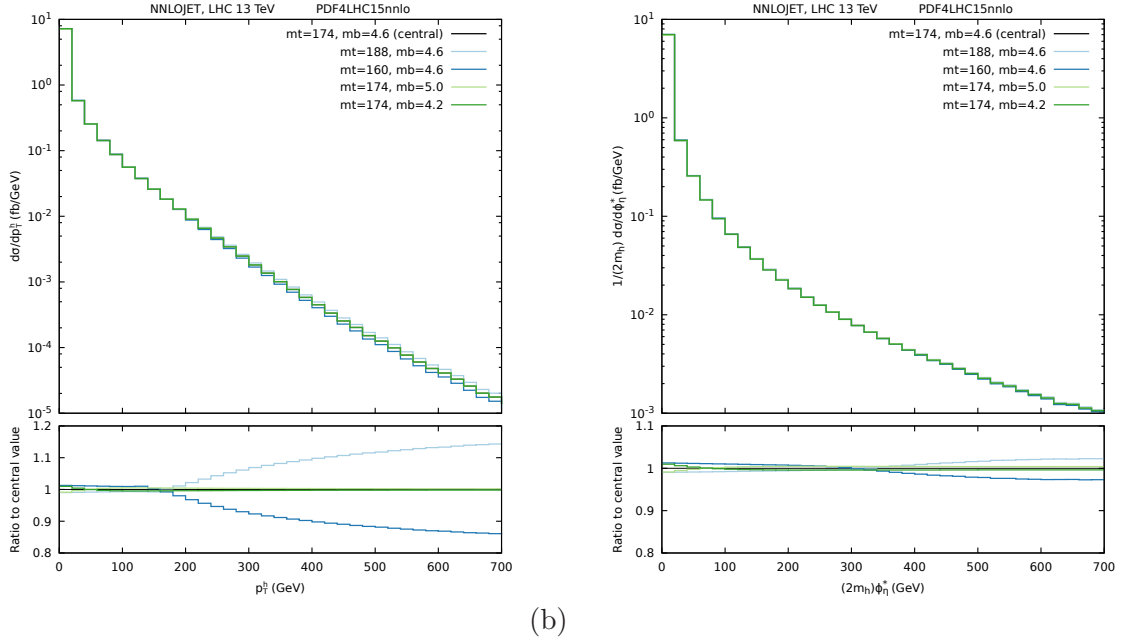


Fig. II.26: (a) p_{TH} and (b) ϕ_{η}^* distributions with variations in the heavy quark masses. The lines show upwards (dark) and downwards (light) variations of m_t at fixed m_b (blue) and variations of m_b at fixed m_t (green).

II.5.4.4 PDF uncertainties

The structure of the proton cannot be calculated in perturbation theory and must be estimated by matching the theoretical knowledge of the short range interaction partonic interaction to the experimental results. The proton structure is characterized by the so called *Parton Distribution Functions* (PDFs). See Ref. [258] and references therein for a more detailed discussion.

Several groups produce global PDF fits, which differ in the way the PDFs are parametrized, the fitting algorithm, the dataset that is used to produce the fit, theoretical choices such as the treatment of the perturbative evolution of the heavy quarks.

PDF uncertainties are computed by first convolving the partonic matrix element with variations of the central PDF determination, and then following a specific prescription defined for each PDF set to obtain the final value of the uncertainty. Ref. [196] contains a recent review of the recommended settings and usages.

Note that PDFs themselves depend heavily on the strong coupling constant. Normally PDF fits are provided for different values α_S , which must be used consistently with the α_S variations discussed above. The usual prescription is to compute only the central PDF value for the two variations of the strong coupling, without also estimating the PDF errors.

Additionally the PDFs are affected by MHOU and parametric uncertainties such as the value of the heavy quark masses (although the dependence is moderate and in the case of the charm mass can be reduced by explicitly fitting the charm PDF [259]). These are currently not included in the definition of ‘‘PDF uncertainty’’.

We have used the PDF4LHC15_nnlo_30 set to estimate the PDF uncertainty for the p_{TH} and ϕ_{η}^* distributions shown in Fig. II.27. Because these observables probe slightly different parton-parton luminosities, see Fig. II.16, the detailed behaviour is different for the two observables. For the p_{TH} distribution, we obtain uncertainties that are typically $\pm(2-3)\%$ but growing at larger p_{TH} . The ϕ_{η}^* distribution is dominated by the regions where the PDF’s are

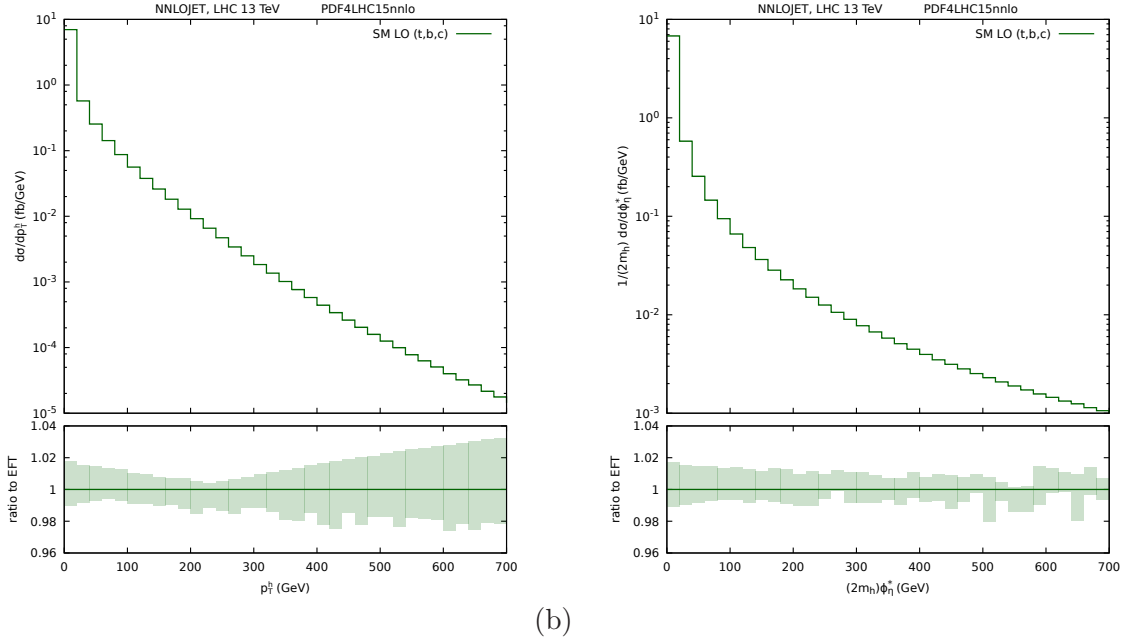


Fig. II.27: (a) p_{TH} and (b) ϕ_{η}^* distributions with the associated PDF uncertainty.

better known with a correspondingly smaller uncertainty of $\pm(1-2)\%$.

We conclude that the main sources of theoretical uncertainties in this process are those due to missing higher orders, which motivates the effort of improving the accuracy of the calculation as we discuss next.

II.5.5 Higher Orders

In order to make precise predictions in perturbative quantum field theories, one has to go beyond the leading order. In QCD, the perturbation is done around small values of the strong coupling constant, or rather small values of α_S which is proportional to the square thereof. At the energy scale of the LHC, the value of α_S is slightly smaller than 0.1 which means that a first estimate of the uncertainty introduced by leaving out the next-to leading order (NLO) contribution is approximately 10%, that of leaving out the NNLO will be 1% and so on.

Another related source of uncertainty is that fixed-order calculations introduce a “characteristic energy scale” μ in the problem, and the predicted cross section depends on the value assigned to that parameter. Introducing higher order terms makes the dependence of the result on that parameter smaller, and thus decreases the uncertainty from that source as described in Sec. II.5.4.1.

II.5.5.1 NLO corrections in the Standard Model

At NLO there are two conceptually different contributions, denoted virtual corrections and real corrections respectively. The former comes from diagrams with one loop more than the leading order diagrams, and the latter from diagrams with one additional radiated parton integrated over the enlarged phase-space:

$$\sigma_{gg \rightarrow gH}^{\text{NLO}} = \left[\text{diagram 1} \right] \times \left[\text{diagram 2} \right]^* + \text{cc.} + \int d\Phi \left[\text{diagram 3} \right]^2 \quad (\text{II.80})$$

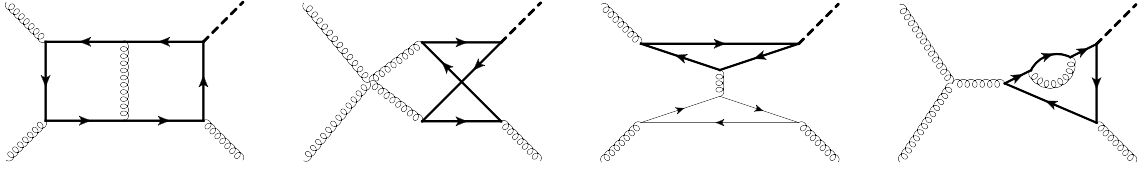


Fig. II.28: Four of the 286 Feynman diagrams contributing to the two-loop QCD correction to $gg \rightarrow gH$.

The terms combine in such a way that divergences from the additional particle in the real radiation becoming “soft” (e.g. having small values of the momentum), cancel with some of the divergences (the so-called IR divergences) coming from the loop in the virtual correction.

At the next order in the perturbative expansion (NNLO) there will be three kinds of terms, one with two extra loops (the virtual-virtual corrections), one with an extra loop and an extra particle (the real-virtual corrections), and one with two extra radiated particles (the real-real corrections). The cancellations between the associated divergences take place in a way that is conceptually similar to the NLO case but in practice much more complicated both in terms of calculation the loop corrections, performing the phase-space integrals, and deriving the cancellation of the divergences.

This growth in the number of terms, continues at each order in the perturbative expansion. In the following we will focus on the virtual corrections, but have in mind that all the terms have to be included in order to obtain a finite contribution.

For Higgs boson + jet production where the leading order term was given by Feynman diagrams with one loop, the next-to leading order virtual correction is given by two-loop diagrams, and that computation is at the very edge of what is possible with the current computational technology [180, 260, 261].

$gg \rightarrow gH$ contains 286 Feynman diagrams, and $q\bar{q} \rightarrow gH$ and $qg \rightarrow qH$ each an additional 61. The numerator of each diagram will initially contain between 100 and 1000 terms, but this number will grow immensely in the intermediate steps of the gamma matrix algebra and the colour factor algebra. But while these numbers are large, this part of the calculation is no challenge for a computer. The real challenge is in computing the two-loop Feynman integrals.

(Semi)analytical expressions for the planar subset of the integrals, were recently computed in Ref. [180]. A more thorough discussion of the techniques used for that computation will be described in Appendix B. The final result of that computation takes up about 500 MB, and this fact alone should motivate the search for simpler methods to approximate the NLO and the higher contributions.

II.5.5.2 NLO corrections in the Higgs Effective Theory

For a fully consistent description of the mass effects at high transverse momentum, one would like to have the NLO (and ultimately also NNLO) predictions with exact mass dependence. However, as discussed in the previous section, owing to the complexity of the two-loop virtual amplitudes, these are not available at present.

The NLO corrections have been computed in the HEFT [184, 185, 187]. There are 60 one-loop diagrams, of which the most complicated is the box integral shown in Fig. II.29. As noted earlier, these one-loop integrals are simpler than those in the SM at LO- the external particles are the same, but the particles circulating in the loop are massless gluons.

As also discussed earlier, at large values of p_{TH} , the HEFT approach is guaranteed to fail. We therefore introduce two approximate approaches to estimating the effect of a finite top

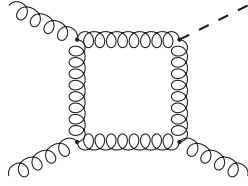


Fig. II.29: One of the Feynman diagrams contributing to $gg \rightarrow gH$ at one-loop in the HEFT.

quark mass. For the inclusive Higgs boson production cross section, it has been observed that the top quark mass corrections at NLO [179, 262–264] can be well-approximated by re-weighting the NLO HEFT cross section by the ratio of SM and HEFT predictions at leading order:

$$R = \sigma_{\text{LO}}^{\text{SM}} / \sigma_{\text{LO}}^{\text{HEFT}} \quad (\text{II.81})$$

where $\sigma_{\text{LO}}^{\text{SM}}$ includes the exact mass dependence of top quark loops. The numerically smaller contributions from charm and bottom quarks to the inclusive Higgs boson cross section can be accounted for in the same form by including the relevant quark loops in the numerator. In the following, the re-weighting factor R will always include charm, bottom and top loops in $\sigma_{\text{LO}}^{\text{SM}}$, while normalising to $\sigma_{\text{LO}}^{\text{HEFT}}$ with infinite top quark mass. In the HEFT, all other quarks are treated massless, and their Yukawa couplings are set to zero.

This inclusive re-weighting factor can be generalised to the transverse momentum distribution (which is also inclusive in all hadronic radiation) as

$$R(p_{TH}) = \left(\frac{d\sigma_{\text{LO}}^{\text{SM}}}{dp_{TH}} \right) / \left(\frac{d\sigma_{\text{LO}}^{\text{HEFT}}}{dp_{TH}} \right). \quad (\text{II.82})$$

Multiplying the higher order HEFT predictions bin-by-bin with this factor, yields the HEFT \otimes M approximation

$$\frac{d\sigma_{\text{NLO}}^{\text{HEFT}\otimes\text{M}}}{dp_{TH}} \equiv R(p_{TH}) \left(\frac{d\sigma_{\text{NLO}}^{\text{HEFT}}}{dp_{TH}} \right) \quad (\text{II.83})$$

which correctly captures the leading logarithms in the quark mass corrections [246, 247] at all orders, while failing in general to describe subleading logarithms and non-logarithmic terms. The computation of subleading mass corrections at NLO [172, 181, 265] also suggests the applicability of the HEFT \otimes M procedure. To quantify the uncertainty associated with this re-weighting procedure, we consider also the additive HEFT \oplus M prediction obtained by substituting only the LO HEFT contribution by the full LO mass-dependence,

$$\frac{d\sigma_{\text{NLO}}^{\text{HEFT}\oplus\text{M}}}{dp_{TH}} \equiv \left(\frac{d\sigma_{\text{NLO}}^{\text{HEFT}}}{dp_{TH}} \right) + (R(p_{TH}) - 1) \left(\frac{d\sigma_{\text{LO}}^{\text{HEFT}}}{dp_{TH}} \right). \quad (\text{II.84})$$

The inclusion of quark mass effects at LO damps the p_{TH} spectrum. Consequently, in the HEFT \oplus M prediction at large p_{TH} , the harder higher order HEFT corrections dominate over the softer LO contribution with exact mass dependence. Even if the yet unknown NLO corrections to the exact mass dependence turn out to be numerically large, there is no reason for them to increase substantially with transverse momentum. The HEFT \oplus M approximation is therefore an overestimate of the hardness of the mass-corrected transverse momentum spectrum, and can be considered to be an upper bound on the actual exact mass dependence.

The HEFT \otimes M prediction reweights the full spectrum with the softness of the LO mass dependence of the $(H + 1)$ -parton process. A recent study [266] demonstrated that the mass-dependent suppression (with respect to the HEFT prediction) of large transverse momentum

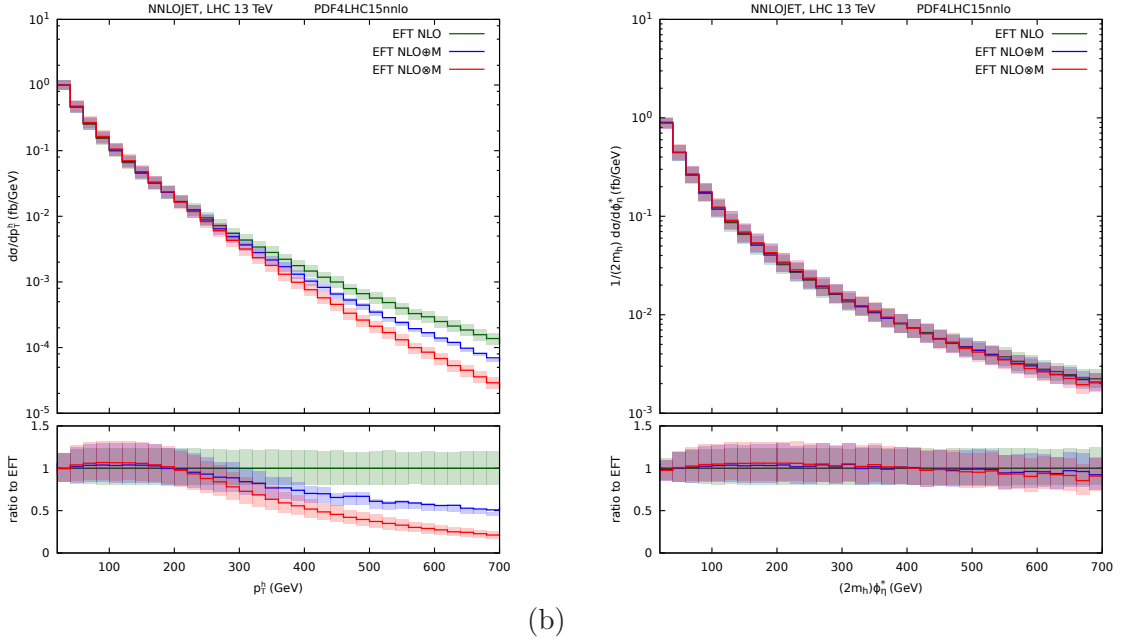


Fig. II.30: The Higgs boson (a) p_{TH} and (b) ϕ_η^* distributions at $\sqrt{s} = 13$ TeV for the NLO HEFT (green), NLO HEFT \oplus M (blue) and NLO HEFT \otimes M (red) approximations discussed in the text. The lower panels show the ratio normalised to the NLO Higgs Effective Theory result.

configurations is less strong for the $(H + 2)$ -parton and $(H + 3)$ -parton processes than it is for the $(H + 1)$ -parton process. Consequently, HEFT \otimes M could be considered as a lower bound on the exact mass dependence.

Fig. II.30 shows the NLO predictions for the p_{TH} and ϕ_η^* distributions in the three approximations, HEFT, HEFT \oplus M and HEFT \otimes M. We see that below $p_{TH} \sim 200$ GeV, all three approximations lead to a similar prediction for the p_{TH} distribution. Above $p_{TH} \sim 200$ GeV, the three are clearly different with the HEFT \otimes M prediction being softer than the HEFT \oplus M distribution. As discussed above, the SM NLO result is likely to lie between the HEFT \oplus M and HEFT \otimes M distributions and the uncertainty on the p_{TH} distribution is thus much larger than the scale uncertainty for any individual prediction.

On the other hand, each bin in the ϕ_η^* distribution samples a wide range of p_{TH} leading to rather similar predictions for all three approximations with at most a $\pm 5\%$ difference, while the scale uncertainty of $O(\pm 20\%)$ is much larger. If the SM NLO result does actually lie between the HEFT \oplus M and HEFT \otimes M distributions, then this implies that the NLO HEFT is good estimator of the ϕ_η^* distribution.

II.5.5.3 NNLO corrections in the Higgs Effective Theory

The NNLO $\mathcal{O}(\alpha_S^5)$ corrections have also been computed in the HEFT [188–193]. There are 1305 two-loop $gg \rightarrow gH$ and 328 two-loop $q\bar{q} \rightarrow gH$ diagrams, and a representative diagram is shown in Fig. II.31.

The two-loop matrix elements were computed in Ref. [213] using the projector method discussed in Sec. II.5. The two-loop master integrals are the same as those for $\gamma^* \rightarrow q\bar{q}g$ [267, 268] continued into the relevant phase space region [269] and were computed using the differential equation method [241]. These expressions are in terms of generalised harmonic polylogarithms which can be evaluated numerically [270, 271]. The one-loop $gg \rightarrow ggH$, $q\bar{q} \rightarrow ggH$ and $q\bar{q} \rightarrow Q\bar{Q}H$ helicity amplitudes have been computed analytically using unitarity meth-

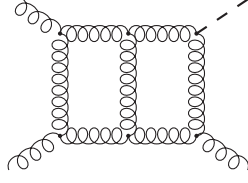


Fig. II.31: One of the Feynman diagrams contributing to $gg \rightarrow gH$ at two-loops in the HEFT.

ods [272–274]. The implementation of the NNLO corrections within NNLOJET employs the antenna subtraction method to isolate the infrared singularities [275–285]. The H +jet and p_{TH} distributions have been computed within the NNLOJET framework [189,193].

The NNLO predictions in the Higgs Effective Theory are shown in Fig. II.32. We see that for both p_{TH} and ϕ_η^* spectra, the NLO effects are sizeable compared to LO (typically 80-100%), but that for p_{TH} , $2m_H\phi_\eta^* > 100$ GeV, the NNLO effects are small compared to NLO. For both distributions, the scale uncertainty is reduced from O(30%) at LO to O(20%) at NLO, and reduced further to O(10%) at NNLO.

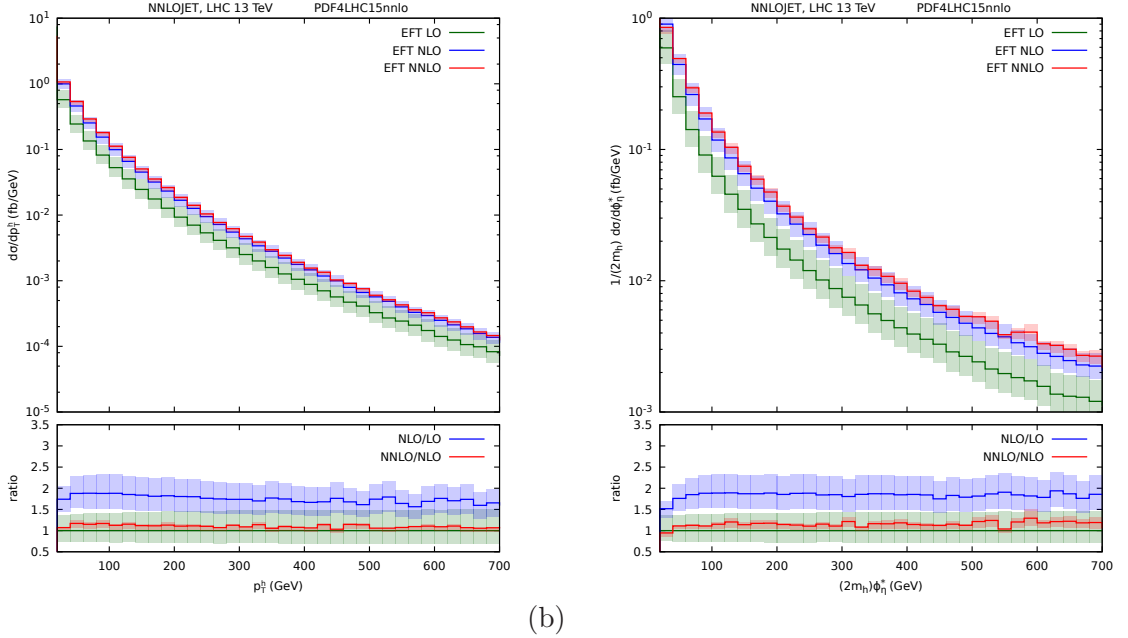


Fig. II.32: The Higgs boson (a) p_{TH} and (b) ϕ_η^* distributions at $\sqrt{s} = 13$ TeV for the HEFT at LO (green), NLO (blue) and NNLO (red). The lower panels show the ratio of NLO/LO (blue) and NNLO/NLO (red).

Following the discussion at NLO, we modify the HEFT prediction either by scaling the differential cross section by the SM LO result,

$$\frac{d\sigma_{\text{NNLO}}^{\text{HEFT}\otimes\text{M}}}{dp_{TH}} \equiv R(p_{TH}) \left(\frac{d\sigma_{\text{NNLO}}^{\text{HEFT}}}{dp_{TH}} \right), \quad (\text{II.85})$$

or by simply replacing the LO HEFT contribution by the LO result with the exact mass dependence,

$$\frac{d\sigma_{\text{NNLO}}^{\text{HEFT}\otimes\text{M}}}{dp_{TH}} \equiv \left(\frac{d\sigma_{\text{NNLO}}^{\text{HEFT}}}{dp_{TH}} \right) + (R(p_{TH}) - 1) \left(\frac{d\sigma_{\text{LO}}^{\text{HEFT}}}{dp_{TH}} \right). \quad (\text{II.86})$$

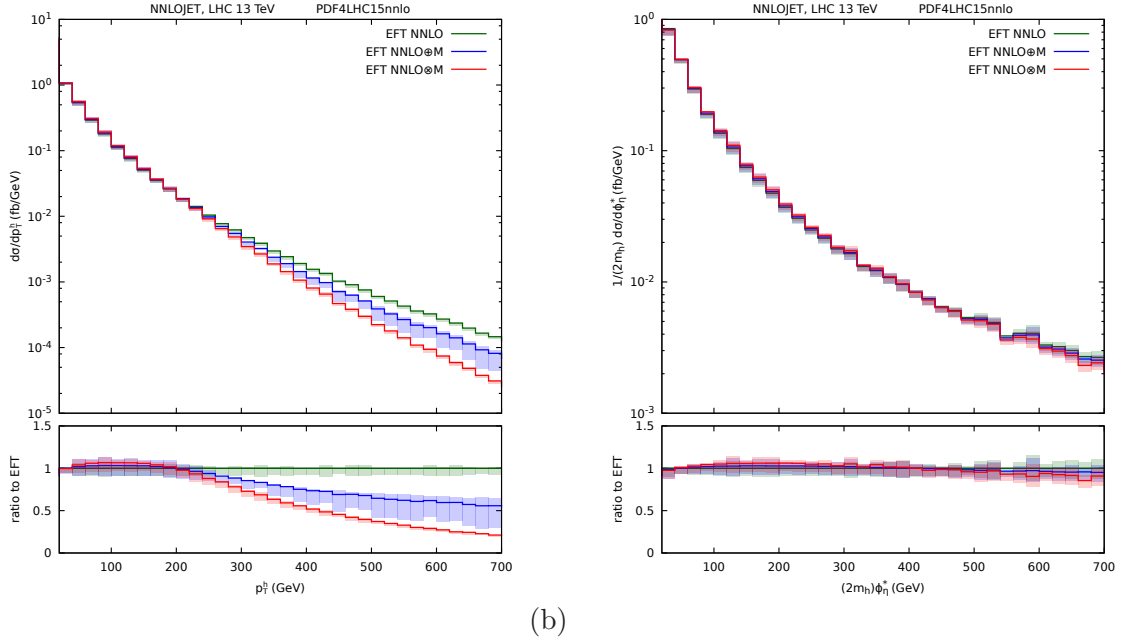


Fig. II.33: The Higgs boson (a) p_{TH} and (b) ϕ_η^* distributions at $\sqrt{s} = 13$ TeV for the NNLO HEFT (green), NNLO HEFT \oplus M (blue) and NNLO HEFT \otimes M (red) approximations discussed in the text. The lower panels show the ratio normalised to the NNLO Higgs Effective Theory result.

The NNLO predictions for the p_{TH} and ϕ_η^* distributions are shown in Fig. II.30. At small p_{TH} , the HEFT \otimes M and HEFT \oplus M approximations are very similar and lead to a small enhancement compared to the pure HEFT. However, as at LO and NLO, with increasing p_{TH} , the non-pointlike nature of the heavy quark loop becomes resolved leading to a softening of the p_{TH} spectrum as compared to the HEFT prediction. This suppression is more severe for the HEFT \otimes M approximation than for the HEFT \oplus M approximation. We observe that at large p_{TH} the scale uncertainty for the HEFT \oplus M approximation is much larger than that for the HEFT \otimes M prediction [193]. Even so, the difference between the two predictions is larger than the scale uncertainty of either and could reasonably be considered as an estimate of the current theoretical uncertainty at large p_{TH} .

As at NLO, the ϕ_η^* distribution exhibits a rather different behaviour and the three approximations again lie within a few percent of each other. Employing the same logic as for the p_{TH} distribution, i.e., that the HEFT \oplus M and HEFT \otimes M distributions span the likely range of the prediction including top mass effects, we deduce that the ϕ_η^* distribution can be reliably estimated by the HEFT prediction with a residual scale uncertainty of about 10%.

II.6 Beyond the Standard Model

The Standard Model has been extremely compatible with almost all the measurements made in particle physics experiments over the last few decades with no convincing hints of additional physics. However, despite its success so far, the Standard Model suffers a number of theoretical shortcomings and also falls short of explaining several experimental observations. This suggests that it cannot be the complete theory of nature, but rather serves as an effective theory of the energy regime we are currently able to probe. One of the theoretical failings of the SM concerns the stability of the Higgs mass, which requires large cancellations between its bare mass and the quantum corrections from the particles that couple to it. New Physics models that address this issue predict new particles whose contributions to the loops can soften the unnatural fine tuning. These new particles are typically heavy resonances that couple strongly to the Higgs and can either be scalars, as in the case of supersymmetric models, or fermionic top partners, predicted by many composite Higgs models.

II.6.1 Searches for BSM Physics

The new particle spectrum can affect the production and decay rates of SM particles, in particular the Higgs boson. New massive coloured particles can participate in the loop induced gluon fusion process and alter the Higgs boson production cross section. Heavy top partners may also mix with the top quark and induce a modified Yukawa coupling, which would also affect the gluon fusion cross section⁵. It is therefore important to resolve the details of the gluon-Higgs interaction. Precise measurements of this vertex can reveal the dynamics of the particles in the loop, and quantify possible deviations from the SM predictions.

We can parametrise the missing information about the exact nature of the gluon-Higgs interaction in terms of effective operators. If the new particles in the loop are much heavier than the Higgs, they will modify the coefficient c_g of the effective interaction of Eq. (II.2). If there are no new particles participating in the loop as in the Standard Model then $c_g = 0$. Similarly, modifications to the Yukawa coupling arising from, for instance, heavy top partners that mix with the top quark can adjust the top Yukawa interaction (II.1) by a factor κ_t (compared to the SM value of $\kappa_t = 1$).

As discussed earlier, to a good approximation, the gluon fusion cross section is dominated by contributions from top-quark loops and from the effective interaction and is proportional to $(\kappa_t + c_g)^2$ (see Eq. (II.3)). As a result, the measurement of the inclusive rate does not disentangle the effects of κ_t and c_g . In a large class of BSM models such as Composite Higgs or Little Higgs models, the change in the top-quark Yukawa coupling may also compensate for the effects of the new particles such that the inclusive cross section is SM-like and there are no traces of the new particle spectrum observed at the LHC. Cancellations of this nature may also happen in SUSY models such as the MSSM, where the deviations of the inclusive cross section from the observed SM-like values vanish for certain values of the trilinear coupling of the Higgs boson and a pair of scalar top quarks (stops), A_t [286].

In order to independently determine c_g and κ_t a new energy scale much higher than the top-quark mass is necessary such that the low energy theorem no longer holds [169]. In this case, the degeneracy of κ_t and c_g can be lifted. This is achieved by recoiling the Higgs bosons against an additional jet, and studying the process at high p_{TH} [95, 168, 170–175].

As a concrete example, in BSM models such as the MSSM, heavy squark loops will also contribute to the production of boosted Higgs bosons as shown in Fig. II.34. Lets assume that the mass of the squark $m \gg m_H$. In this case, one could use the effective interaction to compute the contribution to the inclusive Higgs boson cross section. At low p_{TH} , this would

⁵This would also change the experimentally difficult high-multiplicity $t\bar{t}h$ final state.

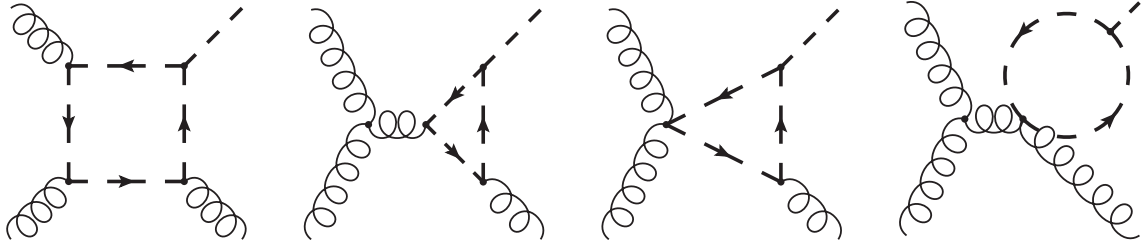


Fig. II.34: Feynman diagrams for the process $gg \rightarrow gh$ mediated by scalar particles at leading order.

also be a good description. However, because the effective interaction is a dimension-5 operator, the amplitude grows with energy, E/m , and the cross section will grow like $E^2/m^2 \sim p_{TH}^2/m^2$. Eventually this growth will violate unitarity. Long before that happens, the approximation $m \rightarrow \infty$ loses validity, and the differential cross section becomes sensitive to the masses in the loop, thereby revealing possible new physics which was otherwise invisible in both the inclusive cross section and in the low p_{TH} region. One can now understand why it is important to study the p_{TH} spectrum of the Higgs to find deviations from SM predictions.

II.6.2 A Simple Model

To see more explicitly how BSM effects can be disentangled we construct a simple but generic BSM model that might contain either heavy fermions or heavy scalars or both. We consider a model where boosted Higgs boson production cross section receives contributions from a complex colour triplet scalar loop with mass m_s as well as contributions involving the top-quark and some heavy unknown particles whose interaction with the Higgs boson is described by the effective vertex of Eq. (II.2). The scalar-scalar-higgs interaction is given by,

$$\mathcal{L}_{\text{scalar}} = \kappa_s \frac{2m_s^2}{v} S^\dagger S H, \quad (\text{II.87})$$

while the interactions of the scalar with the gluons are determined by gauge invariance and the covariant derivative. We can write the full matrix element for the Higgs boson coupling to gluons as

$$\mathcal{M}(\kappa_t, \kappa_s, c_g) = \kappa_t \mathcal{M}_F + \kappa_s \mathcal{M}_S + c_g \mathcal{M}_{UV}, \quad (\text{II.88})$$

where \mathcal{M}_F is the one-loop amplitude taking into account the full top-quark mass dependence, \mathcal{M}_S is the amplitude with the full scalar mass dependence and \mathcal{M}_{UV} is the amplitude arising from the effective interaction. The coefficients κ_t and κ_s scale any effects that the new heavy particles may have on the couplings of the top-quark and the scalar to the Higgs boson. This simple model can be straightforwardly generalised to contain contributions from the charm and bottom quarks and multiple scalar particles (as in SUSY models), however for simplicity we will only consider the top-quark and a single generic scalar colour triplet.

The amplitude for the gluon fusion production of a Higgs boson is,

$$\mathcal{M}^{gg} = \kappa_t \mathcal{M}_F^{gg} + \kappa_s \mathcal{M}_S^{gg} + c_g \mathcal{M}_{UV}^{gg}, \quad (\text{II.89})$$

where the individual contributions can be summarised as,

$$\mathcal{M}_F^{gg} = \frac{1}{v} A_{1/2}(\tau_t), \quad (\text{II.90})$$

$$\mathcal{M}_S^{gg} = \frac{1}{v} A_0(\tau_s), \quad (\text{II.91})$$

$$\mathcal{M}_{UV}^{gg} = \frac{1}{v} A_\infty, \quad (\text{II.92})$$

where $\tau_i = 4m_i^2/m_H^2$. The well known loop functions are (see for example Ref. [165]),

$$A_0(\tau) = -\tau[1 - \tau f(\tau)], \quad (\text{II.93})$$

$$A_{1/2}(\tau) = 2\tau[1 + (1 - \tau)f(\tau)], \quad (\text{II.94})$$

with

$$f(\tau) = \begin{cases} \arcsin^2 \frac{1}{\sqrt{\tau}}, & \tau \geq 1 \\ -\frac{1}{4} \left(\log \frac{1+\sqrt{1-\tau}}{1-\sqrt{1-\tau}} - i\pi \right)^2, & \tau < 1 \end{cases}, \quad (\text{II.95})$$

and

$$A_\infty = \frac{4}{3}. \quad (\text{II.96})$$

If the mass of m_{X_i} is large enough, we can simplify the loop functions by taking $\tau \rightarrow \infty$ such that

$$A_0(\tau) \rightarrow \frac{1}{4} A_\infty \quad (\text{II.97})$$

$$A_{1/2}(\tau) \rightarrow A_\infty. \quad (\text{II.98})$$

This UV behaviour means that we can simplify Eq. (II.89) when the scalar mass is much bigger than m_H by the replacements,

$$\kappa_s \rightarrow 0, \quad c_g \rightarrow c_g + \frac{\kappa_s}{4}. \quad (\text{II.99})$$

Similarly, the HEFT is obtained by taking the limit where the top-quark mass is much larger than m_H , and amounts to the replacements,

$$\kappa_t \rightarrow 0, \quad c_g \rightarrow c_g + \kappa_t. \quad (\text{II.100})$$

This model therefore includes both the top-quark contribution to the SM ($\kappa_t = 1$, $\kappa_s = 0$ and $c_g = 0$) and the HEFT ($\kappa_t = 0$, $\kappa_s = 0$ and $c_g = 1$). If both top-quark and scalar masses are large compared to the Higgs boson mass, then we can set,

$$\kappa_t \rightarrow 0, \quad \kappa_s \rightarrow 0, \quad c_g \rightarrow c_g + \kappa_t + \frac{\kappa_s}{4}. \quad (\text{II.101})$$

In this model, because $m_t > m_H$ and we assume that $m_s > m_t$, the lowest order gluon fusion cross section is sensitive to the combination of couplings,

$$\sigma_{\text{LO}} \sim \left(\kappa_t + \frac{1}{4} \kappa_s + c_g \right)^2 \sigma_{\text{LO}}^{\text{SM}}, \quad (\text{II.102})$$

and measurements of the total cross section cannot discriminate between models that have different values of κ_t , κ_s and c_g .

As discussed earlier, QCD radiation probes the internal structure of the effective interaction and the effects of various new physics contributions can be disentangled by studying boosted Higgs bosons. The amplitudes due to fermion loops and/or the effective interaction have been discussed earlier. The scalar contribution was computed in Refs. [178, 262] and the

matrix elements implemented in the numerical code `SusHi` [287]. We have ported the routines directly from `SusHi` to `NNLOJET`.

Following Ref. [288,289], we write the contribution to the cross section of the simple model above p_{TH}^{cut} and normalised to the top-quark contribution as

$$\begin{aligned} \frac{\sigma(p_{TH}^{\text{cut}})}{\sigma^{SM}(p_{TH}^{\text{cut}})} &= \frac{\int_{p_{TH}^{\text{cut}}}^{\infty} dp_{TH} d\Omega |\kappa_t \mathcal{M}_F + \kappa_s \mathcal{M}_S + c_g \mathcal{M}_{UV}|^2}{\int_{p_{TH}^{\text{cut}}}^{\infty} dp_{TH} d\Omega |\mathcal{M}_F|^2} \\ &= \left(\kappa_t + \frac{1}{4} \kappa_s + c_g \right)^2 \\ &\quad + \delta_{ts}(p_{TH}^{\text{cut}}) \kappa_t \kappa_s + \delta_{tg}(p_{TH}^{\text{cut}}) \kappa_t c_g + \delta_{sg}(p_{TH}^{\text{cut}}) \kappa_s c_g \\ &\quad + \epsilon_s(p_{TH}^{\text{cut}}) \kappa_s^2 + \epsilon_g(p_{TH}^{\text{cut}}) c_g^2 \end{aligned} \quad (\text{II.103})$$

where

$$\delta_{tg}(p_{TH}^{\text{cut}}) = \frac{2 \int_{p_{TH}^{\text{cut}}}^{\infty} dp_{TH} d\Omega \text{Re}(\mathcal{M}_F \mathcal{M}_{UV}^*)}{\int_{p_{TH}^{\text{cut}}}^{\infty} dp_{TH} d\Omega |\mathcal{M}_F|^2} - 2, \quad (\text{II.104})$$

$$\delta_{ts}(p_{TH}^{\text{cut}}) = \frac{2 \int_{p_{TH}^{\text{cut}}}^{\infty} dp_{TH} d\Omega \text{Re}(\mathcal{M}_F \mathcal{M}_S^*)}{\int_{p_{TH}^{\text{cut}}}^{\infty} dp_{TH} d\Omega |\mathcal{M}_F|^2} - \frac{1}{2}, \quad (\text{II.105})$$

$$\delta_{sg}(p_{TH}^{\text{cut}}) = \frac{2 \int_{p_{TH}^{\text{cut}}}^{\infty} dp_{TH} d\Omega \text{Re}(\mathcal{M}_S \mathcal{M}_{UV}^*)}{\int_{p_{TH}^{\text{cut}}}^{\infty} dp_{TH} d\Omega |\mathcal{M}_F|^2} - \frac{1}{2}, \quad (\text{II.106})$$

$$\epsilon_g(p_{TH}^{\text{cut}}) = \frac{\int_{p_{TH}^{\text{cut}}}^{\infty} dp_{TH} d\Omega |\mathcal{M}_{UV}|^2}{\int_{p_{TH}^{\text{cut}}}^{\infty} dp_{TH} d\Omega |\mathcal{M}_F|^2} - 1, \quad (\text{II.107})$$

$$\epsilon_s(p_{TH}^{\text{cut}}) = \frac{\int_{p_{TH}^{\text{cut}}}^{\infty} dp_{TH} d\Omega |\mathcal{M}_S|^2}{\int_{p_{TH}^{\text{cut}}}^{\infty} dp_{TH} d\Omega |\mathcal{M}_F|^2} - \frac{1}{16}. \quad (\text{II.108})$$

Analogous expressions can be derived for the normalised cross sections above $\phi_\eta^{*,\text{cut}}$.

For small values of p_{TH}^{cut} or $\phi_\eta^{*,\text{cut}}$, the coefficients ϵ_i , δ_{ij} are all small. In this limit, we are simply probing the gross effect of the ggH coupling and we recover the total cross section which is proportional to $\left(\kappa_t + \frac{1}{4}\kappa_s + c_g\right)^2$. However, at larger values of p_{TH}^{cut} , the top-quark and scalar loops become resolved and the ϵ_i and δ_{ij} grow. This is demonstrated in Fig. II.35(a) where the various coefficients are shown as a function of p_{TH}^{cut} for $m_s = 250$ GeV, $m_s = 500$ GeV and $m_s = 2500$ GeV. In all cases, the value of the coefficient increases with p_{TH}^{cut} . As a consistency check, we observe that for a very large scalar quark mass, $m_s = 2500$ GeV, the hierarchy predicted by absorbing the effect of the scalar into the effective interaction,

$$\delta_{sg} \sim \frac{1}{2} \epsilon_g, \quad \delta_{ts} \sim \frac{1}{4} \delta_{tg}, \quad \epsilon_s \sim \frac{1}{16} \epsilon_g, \quad (\text{II.109})$$

is satisfied. We also see that for smaller values of m_s , and particularly when p_{TH}^{cut} is large enough to resolve the mass of the particle circulating the loop, the effects are smaller.

In contrast, as shown in Fig. II.35(b), the corresponding coefficients as a function of $\phi_\eta^{*,\text{cut}}$ are much smaller and are less sensitive to the masses of the new scalars or the contribution of the effective vertices. In particular, increasing the value of $\phi_\eta^{*,\text{cut}}$ does not lead to larger values of these parameters.

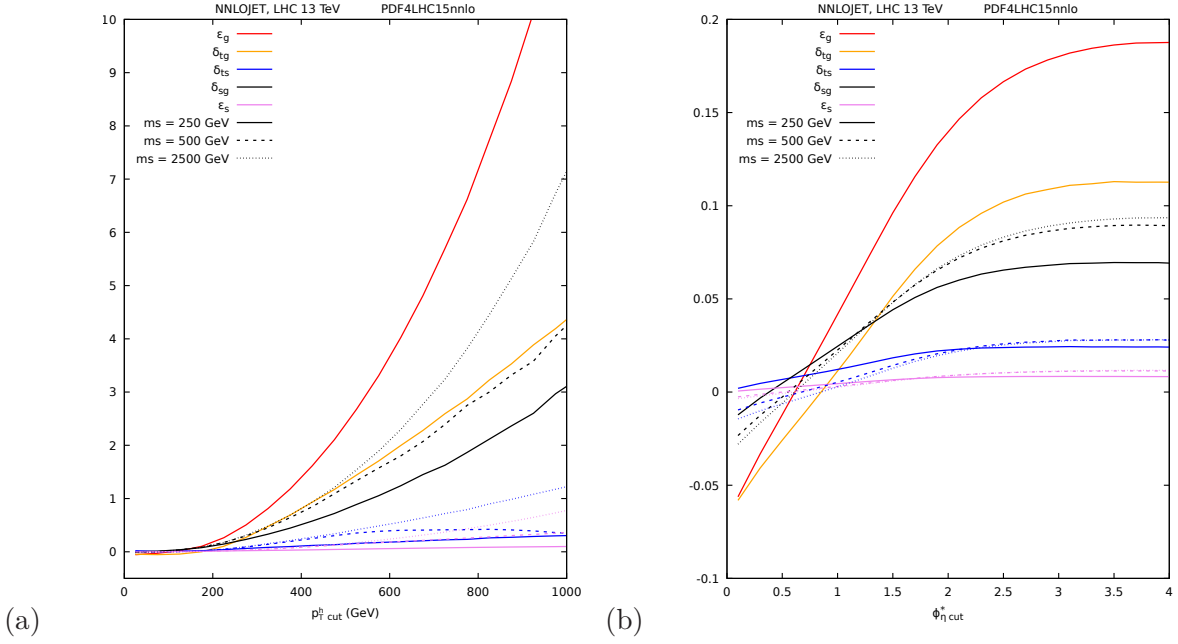


Fig. II.35: Coefficients ϵ_i and δ_{ij} as a function of (a) p_{TH}^{cut} and (b) $\phi_{\eta}^{*,cut}$ for $m_s = 250$ GeV (solid), $m_s = 500$ GeV (dashed) and $m_s = 2500$ GeV (dotted).

This comparison demonstrates that the variable ϕ_{η}^* , which we have shown to have various theoretical and experimental merits over the more traditional variable p_{TH} , fails to be a better variable for discriminating between new physics models.

II.6.3 MSSM: light stop scenario

In supersymmetric models, stops contribute to the gluon fusion process through loop diagrams and their effect depends mainly on their masses and mixing [290, 291]. It has been shown that even within the current limits on squark masses, the total cross section could be suppressed by a factor $\sim 15\%$ (citation here) in the context of the Minimal Supersymmetric Standard Model (MSSM). In this section we therefore carry out a numerical study of the impact of the new states predicted in the MSSM on the Higgs boson p_{TH} and ϕ_{η}^* distributions.

To illustrate the size of the possible effects, we consider the *light stop* MSSM benchmark point proposed by the HXSWG [195]. This benchmark point features relatively light stops. However, the couplings of the squarks to the lightest higgs boson have opposite signs so that if both squarks have the same mass, they destructively interfere and give a null effect. Therefore, the stop masses $m_{\tilde{t}_1}$ and $m_{\tilde{t}_2}$ should be somewhat different to give rise to a sizeable effect. The parameters for the HXSWG light stop scenario are:

$$\mu = 350 \text{ GeV}, \quad \tan \beta = 20, \quad M_3 = 1500 \text{ GeV}, \quad (\text{II.110})$$

$$M_A = 600 \text{ GeV}, \quad M_2 = 500 \text{ GeV}, \quad M_{\tilde{t}_3} = 1000 \text{ GeV} \quad (\text{II.111})$$

$$A_t = X_t + \mu / \tan \beta; \quad X_t = 2M_{SUSY}, \quad (\text{II.112})$$

where M_{SUSY} is the SUSY scale, given by the mass terms of the third generation squarks;

$$M_{\tilde{t}_L} = M_{\tilde{t}_R} = M_{\tilde{b}_L} = M_{\tilde{b}_R} = M_{SUSY}. \quad (\text{II.113})$$

The stop masses are obtained by diagonalising the stop mixing matrix,

$$M_{\tilde{t}}^2 = \begin{pmatrix} M_L^2 & m_t X_t \\ m_t X_t & M_R^2 \end{pmatrix} \quad (\text{II.114})$$

where,

$$M_L^2 = M_{\tilde{t}_L}^2 + m_t^2 + \left(\frac{1}{2} - \frac{2}{3} \sin^2 \theta_W\right) \cos(2\beta) M_Z^2 \quad (\text{II.115})$$

$$M_R^2 = M_{\tilde{t}_R}^2 + m_t^2 + \frac{2}{3} \sin^2 \theta_W \cos(2\beta) M_Z^2 \quad (\text{II.116})$$

and $\sin^2 \theta_W = 1 - M_W^2/M_Z^2$. The physical stop masses are given by,

$$\begin{pmatrix} m_{\tilde{t}_1}^2 & 0 \\ 0 & m_{\tilde{t}_2}^2 \end{pmatrix} = \begin{pmatrix} \cos \theta_t & \sin \theta_t \\ -\sin \theta_t & \cos \theta_t \end{pmatrix} M_{\tilde{t}}^2 \begin{pmatrix} \cos \theta_t - \sin \theta_t \\ \sin \theta_t & \cos \theta_t \end{pmatrix}$$

where

$$\tan 2\theta_t = \frac{2m_t X_t}{M_L^2 - M_R^2}, \quad (\text{II.117})$$

so that,

$$m_{\tilde{t}_1}^2 = \frac{M_L^2 + M_R^2}{2} - \frac{1}{2} \left((M_L^2 - M_R^2)^2 + 4m_t^2 X_t^2 \right)^{1/2}, \quad (\text{II.118})$$

$$m_{\tilde{t}_2}^2 = \frac{M_L^2 + M_R^2}{2} + \frac{1}{2} \left((M_L^2 - M_R^2)^2 + 4m_t^2 X_t^2 \right)^{1/2}. \quad (\text{II.119})$$

The couplings of the lightest Higgs boson to stops are given by,

$$\begin{aligned} g_{h\tilde{t}_1\tilde{t}_1} &= \frac{\cos(\alpha)}{\sin(\beta)} - \sin(\alpha + \beta) \left[\frac{1}{2} \cos(\theta_t)^2 - \frac{2}{3} \sin^2 \theta_W \cos(2\theta_t) \right] \frac{M_Z^2}{m_t^2} \\ &\quad - \frac{1}{2m_t} \sin(2\theta_t) \left[\frac{\cos(\alpha)}{\sin(\beta)} A_t + \frac{\sin(\alpha)}{\sin(\beta)} \mu \right], \end{aligned} \quad (\text{II.120})$$

$$\begin{aligned} g_{h\tilde{t}_2\tilde{t}_2} &= \frac{\cos(\alpha)}{\sin(\beta)} - \frac{1}{2} \sin(\alpha + \beta) \left[\frac{1}{2} \sin(\theta_t)^2 + \frac{2}{3} \sin^2 \theta_W \cos(2\theta_t) \right] \frac{M_Z^2}{m_t^2} \\ &\quad + \frac{1}{2m_t} \sin(2\theta_t) \left[\frac{\cos(\alpha)}{\sin(\beta)} A_t + \frac{\sin(\alpha)}{\sin(\beta)} \mu \right]. \end{aligned} \quad (\text{II.121})$$

In the specific MSSM benchmark points considered here, we are in the *decoupling limit* where the lightest CP-even state h has SM couplings to the SM particles [292–294] and the mixing angle α is related to β by,

$$\sin(\beta - \alpha) = 1. \quad (\text{II.122})$$

This produces a much simpler expression for the couplings,

$$g_{h\tilde{t}_1\tilde{t}_1} = 1 + \cos(2\beta) \left(\frac{1}{2} \cos(\theta_t)^2 - \frac{2}{3} \sin^2 \theta_W \cos(2\theta_t) \right) \frac{M_Z^2}{m_t^2} - \frac{1}{2} \sin(2\theta_t) \frac{X_t}{m_t}, \quad (\text{II.123})$$

$$g_{h\tilde{t}_2\tilde{t}_2} = 1 + \cos(2\beta) \left(\frac{1}{2} \sin(\theta_t)^2 + \frac{2}{3} \sin^2 \theta_W \cos(2\theta_t) \right) \frac{M_Z^2}{m_t^2} + \frac{1}{2} \sin(2\theta_t) \frac{X_t}{m_t}. \quad (\text{II.124})$$

These couplings are normalised to the Lagrangian interaction,

$$\mathcal{L}_{\text{int}} = i \frac{2m_t^2}{v} g_{h\tilde{t}_i\tilde{t}_i}$$

so that the relationship between the $g_{h\tilde{t}_i\tilde{t}_i}$ and $\kappa_{\tilde{t}_i}$ for $i = 1, 2$ is

$$\kappa_{\tilde{t}_i} = \frac{m_t^2}{m_{\tilde{t}_i}^2} g_{h\tilde{t}_i\tilde{t}_i}. \quad (\text{II.125})$$

For the benchmark points, inserting the values for M_{SUSY} and the default parameters of Section II.1.1 into Eqs. (II.118)–(II.124), we find the input parameters relevant for Higgs production shown in Table II.1.

| BP | M_{SUSY} (GeV) | $m_{\tilde{t}_1}$ (GeV) | $m_{\tilde{t}_2}$ (GeV) | $g_{h\tilde{t}_1\tilde{t}_1}$ | $g_{h\tilde{t}_2\tilde{t}_2}$ |
|----|------------------|-------------------------|-------------------------|-------------------------------|-------------------------------|
| 1 | 500 | 323 | 672 | -1.94 | 3.80 |
| 2 | 600 | 423 | 773 | -2.52 | 4.38 |
| 3 | 800 | 624 | 972 | -3.67 | 5.53 |

Table II.1: Input parameters for the three light stop MSSM benchmark points, BP1, BP2 and BP3.

For these SUSY parameters, Eqs. (II.115)–(II.124) simplify considerably, and lead to;

$$\theta_t \sim \frac{\pi}{4}, \quad (\text{II.126})$$

$$m_{\tilde{t}_1} \sim M_{SUSY} - m_t, \quad (\text{II.127})$$

$$m_{\tilde{t}_2} \sim M_{SUSY} + m_t, \quad (\text{II.128})$$

$$g_{h\tilde{t}_1\tilde{t}_1} \sim 1 - \frac{M_{SUSY}}{m_t}, \quad (\text{II.129})$$

$$g_{h\tilde{t}_2\tilde{t}_2} \sim 1 + \frac{M_{SUSY}}{m_t}. \quad (\text{II.130})$$

Essentially this amounts to ignoring terms proportional to $M_Z^2/m_t/M_{SUSY}$.

Using the results of the previous section, we can also estimate the size of the stop contribution to the gluon fusion cross section. Both stops make a contribution to the gluon fusion amplitude, δM^{gg} , where

$$\begin{aligned} \delta M^{gg}/M_{\text{SM}}^{gg} &= \frac{\kappa_{\tilde{t}_1}}{4} + \frac{\kappa_{\tilde{t}_2}}{4} \\ &= \frac{m_t^2}{4m_{\tilde{t}_1}^2} g_{h\tilde{t}_1\tilde{t}_1} + \frac{m_t^2}{4m_{\tilde{t}_2}^2} g_{h\tilde{t}_2\tilde{t}_2} \end{aligned} \quad (\text{II.131})$$

$$\sim -\frac{m_t^2}{2(M_{SUSY}^2 - m_t^2)}. \quad (\text{II.132})$$

For the benchmark points BP1, BP2 and BP3, the gluon fusion cross section is changed by -14.9% (-13.3%), -9.9% (-9.0%) and -5.3% (-4.9%) respectively. The numbers in brackets are those obtained through use of the approximate formula (II.132).

The sbottom masses are given by a similar equation to (II.114), but because $m_b \ll M_{SUSY}$, the two sbottom masses are both close to M_{SUSY} and their contributions largely cancel.

The p_{TH} and ϕ_η^* distributions for the three benchmark points characterised by different values of M_{SUSY} are shown in Fig. II.36. These distributions are obtained with the NNLOJET code and the default input parameters as specified in Sec. II.1.1 and are normalised to the LO SM distribution with the exact mass dependence of the top-, bottom- and charm-quark loops as

shown in Figs. II.6 and II.7. The dominant gluon fusion contribution is shown as dashed lines. As expected from the earlier discussion, the stop quarks suppress the total cross section, by around 15%, 10%, and 5% in BP1, BP2 and BP3 respectively. This is evident in the low p_{TH} and low ϕ_η^* where most of the cross section is concentrated.⁶

Figure II.36(a) shows that the p_{TH} distribution is sensitive to the masses of the stop quarks. As discussed in Section II.5.2.5, for a heavy particle of mass M , the thresholds start to open when

$$p_{TH} \sim M \left(1 - \frac{m_H^2}{4M^2} \right).$$

The first peak for each of these plots occurs when p_{TH} is close to the top mass. Even though the cross section is normalised to the SM value, the effects of the top quark threshold is not completely washed away because of the interference between the top and squark loops. There is dip at around $m_{\tilde{t}_1} \sim M_{SUSY} - m_t$ where the first stop quark threshold starts to open, and a smaller peak at around $m_{\tilde{t}_2} \sim M_{SUSY} + m_t$ where the second stop quark threshold opens. These effects are much more evident in the gluon-gluon initiated channel than in the quark-gluon contribution.

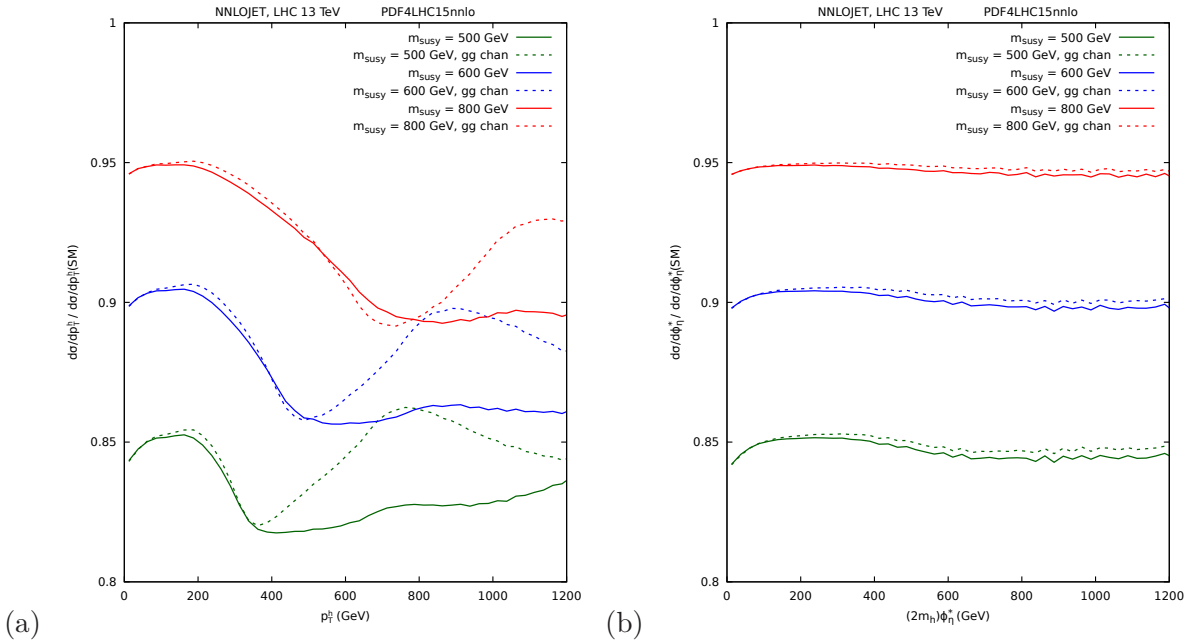


Fig. II.36: The ratio of the Higgs boson (a) p_{TH} and (b) ϕ_η^* distributions at $\sqrt{s} = 13$ TeV for the three benchmark points, $M_{SUSY} = 500$ GeV (green), $M_{SUSY} = 600$ GeV (blue) and $M_{SUSY} = 800$ GeV (red) relative to the LO SM prediction computed with top, bottom and charm quark loops. The dotted lines show the contributions coming from the gluon-gluon initial state.

In complete contrast, and as expected from the discussion in the section II.6.2, the ϕ_η^* distribution shown in Figure II.36(b) is essentially insensitive to the heavy particle thresholds.

Even though Figure II.36 is a naive leading order estimate which ignores higher order contribution that could significantly affect the cross sections, we expect that the sensitivity of the p_{TH} distribution, and the corresponding insensitivity of the ϕ_η^* distribution will be preserved. Therefore our recommendation is that:

⁶The small additional suppression is due to the charm and bottom quark loops.

- a) the p_{TH} distribution is exploited for new physics searches
- b) the ϕ_η^* distribution is used for precise measurements of the Higgs boson parameters.

II.7 Summary

In this part of the report, we proposed a new observable for the study of Higgs bosons that decay into two photons, ϕ_η^* . This variable is complementary to the transverse momentum of the Higgs, since it relies on the measurement of the directions in ϕ and η of the two photons rather than the energies.

When the Higgs boson is produced at rest in the transverse plane, i.e. $p_{TH} = 0$, then ϕ_η^* also vanishes. However, for finite values of p_{TH} and ϕ_η^* , the two variables are unrelated.

We made a rudimentary study of the experimental resolution for photon pairs coming from Higgs boson decays using a fast detector simulation of the CMS detector. While a number of systematic effects, notably pileup, were ignored, our study showed that $2m_H\phi_\eta^*$ has a better resolution compared to the simple calorimetric measurement of $p_T^{\gamma\gamma}$. This means that although there is no tracking information about the photons, ϕ_η^* is nevertheless a viable observable and has the potential to give additional information on the production of boosted Higgs bosons.

The ϕ_η^* distribution behaves very differently to the (well-studied) p_{TH} distribution. In particular, as ϕ_η^* grows, it does not appear to resolve the short distance properties of the interaction producing the Higgs. This is in complete contrast to the p_{TH} distribution in which finite mass effects start to become important (typically for $p_{TH} > m_t$ in the SM, and for $p_{TH} > M$ for new particles of mass M).

The normalisation of the ϕ_η^* distribution is sensitive to the combination of particles that are involved in the $gg \rightarrow H$ interaction (just as for the inclusive Higgs boson cross section), but the shape of the ϕ_η^* distribution is less sensitive to new physics effects.

On the other hand, this has the positive feature that the ϕ_η^* distribution can be more reliably calculated, even in the Higgs Effective Theory. We showed explicitly that different ways of estimating the top-quark mass dependence of the spectrum beyond Leading-Order (the HEFT \oplus M and HEFT \otimes M approximations) produced essentially identical results to the HEFT at NLO and at NNLO. We also found that relative to NLO, the NNLO corrections are small, and that the scale uncertainty is significantly reduced. We take this as a strong indication that the NNLO HEFT prediction for the ϕ_η^* distribution is close to what might be found if the full top mass dependence would be available. The ϕ_η^* distribution is therefore an ideal observable for extracting detailed information about the Higgs boson.

Armed with a new and precisely measurable observable, we anticipate that measurements of boosted Higgs bosons in the two photon decay channel could provide useful additional information about the interactions of the Higgs boson.

Appendices

A Calculation of the One-Loop Master Integrals

In this Appendix, we will demonstrate how to compute the one-loop master integrals that appeared in Sec. II.5.2.3.

A.1 The canonical basis

As discussed in Sec. II.5.2.3, the integral family defined by the four propagators of Eq. (II.57),

$$\begin{aligned} D_1 &= k_1^2 - m_t^2, \\ D_2 &= (k_1 - p_1)^2 - m_t^2, \\ D_3 &= (k_1 - p_1 - p_2)^2 - m_t^2, \\ D_4 &= (k_1 - p_1 - p_2 - p_3)^2 - m_t^2, \end{aligned}$$

can be written in terms of the 9 master integrals $g_1 \dots g_9$ described in Eq. (II.64). However, we are free to choose a convenient basis of master integrals, and the best choice depends on the method to be used to solve the integrals. Here we will use the method of differential equations since that is a powerful method for computing more complicated two-loop integrals. This method works by identifying the differential equations that each integral satisfies [239–242] and solving the equations iteratively.

In this case, a good choice of basis for this method is the so-called *canonical* basis where the differential equations for each integral is in a very particular form discussed below. The question then is how to identify the canonical basis. The set of integrals given in Eq. (II.64) is *not* the canonical basis. However, it is a suitable starting point for finding the canonical basis and is known as a *pre-canonical* basis.

Several methods are known for finding the canonical basis, see for example [295–299]. Here we will use a method inspired by Magnus and Dyson series as described in [297]. The 9 pre-canonical integrals obey a set of 4 partial differential equations in $s \in \{s_{12}, s_{23}, p_4^2, m_t^2\}$,

$$\partial_s \vec{g} = B_s \vec{g}, \quad (\text{A.1})$$

where each of the B_s are 9×9 matrices. Additionally, the integrals obey a so-called *scaling* equation,

$$\partial_\varphi \vec{g} = B_\varphi \vec{g}, \quad (\text{A.2})$$

where

$$\partial_\varphi = \left[-\frac{\alpha}{2} + s_{12} \partial_{s_{12}} + s_{23} \partial_{s_{23}} + p_4^2 \partial_{p_4^2} \right]. \quad (\text{A.3})$$

Here, B_φ is another 9×9 matrix and $\alpha = md + 2s - 2r$ is the mass dimension of an m -loop integral with r propagators in the denominators and s propagators in the numerator. The “scaling” equation can be used as a consistency check of the partial differential equations in the other variables.

A differential equation is said to be in canonical form if it can be written as

$$d\vec{f} = \epsilon(d\tilde{A})\vec{f}. \quad (\text{A.4})$$

The matrix $(d\tilde{A})$ should be in so-called “d log form”, this means that it should be possible to write each of its elements as a sum of derivatives of logarithms with rational number coefficients.

To obtain the canonical form for our differential equation, our goal will be to find a matrix T with entries consisting of algebraic functions of the invariants, masses and d such that $\vec{f} = T\vec{g}$

obeys (A.4). In order to achieve this it is useful to understand how the differential equation transforms under a basis change. Inserting $\vec{f} = T\vec{g}$ into (A.1) and using the product rule, we obtain the basis change formula,

$$\partial\vec{f} = T^{-1} (BT - \partial(T)) \vec{f}. \quad (\text{A.5})$$

A.2 Solving the differential equations

It is often useful to write the differential equations in terms of dimensionless variables. To do this we can factor a dimensionful parameter, which we choose as m_t^2 , from each integral in order to make it dimensionless. The integrals are then functions only of three dimensionless invariants, which we choose as

$$x_1 = \frac{s_{12}}{m_t^2}, \quad x_2 = \frac{p_4^2}{m_t^2}, \quad x_3 = \frac{s_{23}}{m_t^2}. \quad (\text{A.6})$$

The 3 partial derivatives with respect to the dimensionful variables s_{12}, s_{23}, p_4^2 are related to 3 partial derivatives with respect to the dimensionless invariants x_1, x_2, x_3 via a Jacobian matrix,

$$\begin{pmatrix} \partial_{x_1} \\ \partial_{x_2} \\ \partial_{x_3} \end{pmatrix} = \begin{pmatrix} \frac{\partial x_1}{\partial s_{12}} & \frac{\partial x_2}{\partial s_{12}} & \frac{\partial x_3}{\partial s_{12}} \\ \frac{\partial x_1}{\partial p_4^2} & \frac{\partial x_2}{\partial p_4^2} & \frac{\partial x_3}{\partial p_4^2} \\ \frac{\partial x_1}{\partial s_{23}} & \frac{\partial x_2}{\partial s_{23}} & \frac{\partial x_3}{\partial s_{23}} \end{pmatrix}^{-1} \begin{pmatrix} \partial_{s_{12}} \\ \partial_{p_4^2} \\ \partial_{s_{23}} \end{pmatrix}. \quad (\text{A.7})$$

Using this we first exchange our partial differential equations with respect to dimensionful variables for those in terms of dimensionless variables. The scaling equations provide only information on the mass dimension of the integrals and can be used to determine the power of m_t^2 to be factored from each integral. The 9 pre-canonical integrals now obey 3 partial differential equations in $x \in \{x_1, x_2, x_3\}$,

$$\partial_x \vec{g} = B_x \vec{g}, \quad (\text{A.8})$$

with B_x a 9×9 matrix for each variable, their entries consist of rational functions of the dimensionless invariants, the mass m_t^2 and d .

We first try to rescale each of our integrals by ϵ^{a_i} with $a_i \in \mathbb{Z}$ such that the off-diagonal terms of our matrix have leading term ϵ . The differential equation in terms of the new integrals can be obtained by using the basis change formula (A.5) with

$$T = \text{diag}(\epsilon^{a_1}, \dots, \epsilon^{a_9}). \quad (\text{A.9})$$

In the case at hand we find that choosing $a_1, a_2, a_3, a_4 = 0$ and $a_5, a_6, a_7, a_8, a_9 = 1$ allows us to obtain a differential equation in the desired form.

Next, we note that each of our B_x matrices depend linearly on ϵ ,

$$B_x(\vec{x}, \epsilon) = B_x^{(0)}(\vec{x}) + \epsilon B_x^{(1)}(\vec{x}). \quad (\text{A.10})$$

This simplifies finding the canonical basis. Cases without this property are also discussed in [297]. We change the basis of integrals via Magnus series $\Omega[B_x^{(0)}]$ obtained using $B_x^{(0)}$ as kernel,

$$\vec{f}(\vec{x}, \epsilon) = e^{\Omega[B_x^{(0)}]} \vec{g}(\vec{x}, \epsilon). \quad (\text{A.11})$$

Due to rescaling the integrals by ϵ in (A.9) the matrices $B_x^{(0)}$ are diagonal and the Magnus series is truncated at first order,

$$\Omega_1[B_x^{(0)}] = \int_{x_0}^x d\tau_1 B_x^{(0)}(\tau_1). \quad (\text{A.12})$$

Repeating this basis change for each variable we finally obtain an ϵ factorised form for each of the partial derivative matrices B_x . The canonical form of the differential equation can be constructed from these transformed matrices.

The relation between the canonical master integrals, \vec{f} , and the pre-canonical master integrals, \vec{g} , is given by taking the product of all basis change matrices, the result is

$$f_1 = g_1, \quad (\text{A.13})$$

$$f_2 = m_t^2 \sqrt{4 - x_1} \sqrt{x_1} g_2, \quad (\text{A.14})$$

$$f_3 = m_t^2 \sqrt{4 - x_3} \sqrt{x_3} g_3, \quad (\text{A.15})$$

$$f_4 = m_t^2 \sqrt{4 - x_2} \sqrt{x_2} g_4, \quad (\text{A.16})$$

$$f_5 = \epsilon m_t^2 x_1 g_5, \quad (\text{A.17})$$

$$f_6 = \epsilon m_t^2 x_3 g_6, \quad (\text{A.18})$$

$$f_7 = \epsilon m_t^2 (x_2 - x_1) g_7, \quad (\text{A.19})$$

$$f_8 = \epsilon m_t^2 (x_2 - x_3) g_8 \quad (\text{A.20})$$

$$f_9 = \epsilon m_t^4 \sqrt{4x_2 - 4x_1 - 4x_3 + x_1 x_3} \sqrt{x_1} \sqrt{x_3} g_9. \quad (\text{A.21})$$

In the canonical form, the differential equation system may be written as

$$d\vec{f} = (d\tilde{A})\vec{f}, \quad (\text{A.22})$$

where the coupling matrix \tilde{A} is

$$\tilde{A} = \epsilon \begin{bmatrix} 0 & 0 & 0 & 0 & 0 & 0 & 0 & 0 & 0 \\ E_2(x_1) & E_1(x_1) & 0 & 0 & 0 & 0 & 0 & 0 & 0 \\ E_2(x_3) & 0 & E_1(x_3) & 0 & 0 & 0 & 0 & 0 & 0 \\ E_2(x_2) & 0 & 0 & E_1(x_2) & 0 & 0 & 0 & 0 & 0 \\ 0 & E_2(x_1) & 0 & 0 & 0 & 0 & 0 & 0 & 0 \\ 0 & 0 & E_2(x_3) & 0 & 0 & 0 & 0 & 0 & 0 \\ 0 & E_2(x_1) & 0 & -E_2(x_2) & 0 & 0 & 0 & 0 & 0 \\ 0 & 0 & E_2(x_3) & -E_2(x_2) & 0 & 0 & 0 & 0 & 0 \\ 0 & E_3(x_1, x_3) & E_3(x_3, x_1) & E_4 & E_5 & E_5 & E_5 & E_5 & E_6 \end{bmatrix} \quad (\text{A.23})$$

and where the entries of the matrix are given as

$$\begin{aligned} E_1(x_i) &= -\log(4 - x_i) \\ E_2(x_i) &= -2 \log \left(\sqrt{4 - x_i} + \sqrt{-x_i} \right) \\ E_3(x_i, x_j) &= 2 \log(x_2 - x_1) + 2 \log(x_2 - x_3) \\ &\quad - 4 \log \left(\sqrt{4 - x_i} \sqrt{-x_j} + \sqrt{4(x_2 - x_1 - x_3) + x_1 x_3} \right) \\ E_4 &= -2 \log(x_2 - x_1) - 2 \log(x_2 - x_3) \\ &\quad + 4 \log \left(\sqrt{4 - x_2} \sqrt{-x_1} \sqrt{-x_3} + \sqrt{-x_2} \sqrt{4(x_2 - x_1 - x_3) + x_1 x_3} \right) \\ E_5 &= -\log(x_2 - x_1 - x_3) + 2 \log \left(\sqrt{-x_1} \sqrt{-x_3} + \sqrt{4(x_2 - x_1 - x_3) + x_1 x_3} \right) \\ E_6 &= \log(x_2 - x_1 - x_3) - \log(4(x_2 - x_1 - x_3) + x_1 x_3) \end{aligned} \quad (\text{A.24})$$

In order to integrate the system of differential equations, we have to decide on a boundary condition. In the phase-space point $x_1 = x_2 = x_3 = 0$ (corresponding to $s_{12} = s_{23} = m_H^2 = 0, m_t^2 = 1$), the Feynman integrals themselves are finite⁷ and as all the members of the canonical basis except f_1 have prefactors that are zero in that point, they all vanish with the exception of f_1 - the tadpole integral - which is given as

$$f_1|_{x_1=x_2=x_3=0} = 1 + \frac{\pi^2}{12}\epsilon^2 + \mathcal{O}(\epsilon^3) \quad (\text{A.25})$$

As all the members of the canonical basis have uniform weight⁸ we know that the ϵ^0 term is purely numerical, and thus we deduce from the boundary point that all the members of the canonical basis are 0 at the ϵ^0 order, with the exception of f_1 . To find the expressions at the next order in ϵ we will use the differential equation. In order to simplify the solution procedure we will make a change of variables from x_i to the new dimensionless variables z_i , known as Landau variables, defined as

$$x_i = -\frac{(z_i - 1)^2}{z_i}. \quad (\text{A.26})$$

These variables have the property of making some of the square-roots present in Eq. (A.24) factorize, as⁹

$$-2 \log(\sqrt{4 - x_i} + \sqrt{-x_i}) = -2 \log(2) - \log(z_i). \quad (\text{A.27})$$

Inserting these variables and doing the derivative with respect to z_1 , we get the differential equation

$$\frac{df_2^{(1)}}{dz_1} = -\frac{1}{z_1}, \quad (\text{A.28})$$

while the derivative of the first-order terms of the remaining canonical master integrals with respect to z_1 is zero. Integrating the system up, gives $f_2^{(1)} = -\log(z_1) + c(z_2, z_3)$, and as the derivative with respect to the remaining variables vanishes along with the value at the boundary point, we conclude that $c(z_2, z_3) = 0$, so after substituting back, we get the result

$$f_2^{(1)} = -2 \log(\sqrt{4 - x_1} + \sqrt{-x_1}) + 2 \log(2). \quad (\text{A.29})$$

Following the same procedure with z_2 and z_3 , gives the expressions

$$\begin{aligned} f_3^{(1)} &= -2 \log(\sqrt{4 - x_3} + \sqrt{-x_3}) + 2 \log(2), \\ f_4^{(1)} &= -2 \log(\sqrt{4 - x_2} + \sqrt{-x_2}) + 2 \log(2), \end{aligned} \quad (\text{A.30})$$

while the remaining canonical masters give zero, also at the first order in ϵ .

⁷this can be seen e.g. from the Schwinger parametrization.

⁸Uniform weight means that the n th term in the ϵ expansion consists solely of functions with weight n , as explained in appendix B.4, and additionally that the prefactors of these functions have to given solely in terms of rational numbers, so without any kinematical dependence.

⁹One might worry about whether the right hand side of Eq. (A.27) contains a factor of $i\pi$ from the branch cut of the logarithm. But any such constants can be discarded as the matrix \tilde{A} only contributes through its derivative.

Continuing to the second order in ϵ , the derivatives with respect to z_1 become

$$\begin{aligned}\frac{df_2^{(2)}}{dz_1} &= -\left(\frac{1}{z_1} - \frac{2}{z_1 + 1}\right) \log(z_1), \\ \frac{df_5^{(2)}}{dz_1} &= \frac{1}{z_1} \log(z_1), \\ \frac{df_7^{(2)}}{dz_1} &= \frac{1}{z_1} \log(z_1),\end{aligned}\tag{A.31}$$

with all the remaining z_1 derivatives except the last, that of the box, being zero.

Integrating up gives

$$\begin{aligned}f_2^{(2)} &= \text{Li}_2(-z_1) - \frac{1}{2} \log^2(z_1) + \log(z_1) \log(1 + z_1) + c_2(z_2, z_3), \\ f_5^{(2)} &= \frac{1}{2} \log^2(z_1) + c_5(z_2, z_3), \\ f_7^{(2)} &= \frac{1}{2} \log^2(z_1) + c_7(z_2, z_3),\end{aligned}\tag{A.32}$$

in terms of z_1 and the remaining integration constant.

It may at this point be worth mentioning that while in this specific case the integrals could be performed rather easily, in general that is not the case. The function class known as generalized polylogarithms (with is discussed in further detail in Appendix B.4) can be of great help with this, as the way it is defined identifies it as a natural way of expressing such integrals. It is however not needed for this case, and will not be mentioned any further.

As the derivatives of $f_2^{(2)}$ and $f_5^{(2)}$ with respect to the remaining variables are zero, we deduce that c_2 and c_5 are genuine constants, and then the boundary point allow us identify $c_2 = -\text{Li}_2(-1) = \pi^2/12$ and $c_5 = 0$. For c_7 on the other hand, we get that

$$\begin{aligned}\frac{dc_7}{dz_2} &= \frac{df_7^{(2)}}{dz_2} = -\frac{1}{z_2} \log(z_2) \Leftrightarrow \\ c_7 &= -\frac{1}{2} \log^2(z_2) + b(z_3)\end{aligned}\tag{A.33}$$

and following the same procedure once again, we conclude that $b(z_3) = 0$.

Going through the same procedure with the remaining canonical master integrals in the remaining variables, and substituting the original dimensionless variables, the x_i , back, we get in total

$$f_1 = 1 + \frac{\pi^2}{12} \epsilon^2 + \mathcal{O}(\epsilon^3),\tag{A.34}$$

$$f_2 = H_1(x_1) \epsilon + H_2(x_1) \epsilon^2 + \mathcal{O}(\epsilon^3),\tag{A.35}$$

$$f_3 = H_1(x_3) \epsilon + H_2(x_3) \epsilon^2 + \mathcal{O}(\epsilon^3),\tag{A.36}$$

$$f_4 = H_1(x_2) \epsilon + H_2(x_2) \epsilon^2 + \mathcal{O}(\epsilon^3),\tag{A.37}$$

$$f_5 = H_3(x_1) \epsilon^2 + \mathcal{O}(\epsilon^3),\tag{A.38}$$

$$f_6 = H_3(x_3) \epsilon^2 + \mathcal{O}(\epsilon^3),\tag{A.39}$$

$$f_7 = H_4(x_1, x_2) \epsilon^2 + \mathcal{O}(\epsilon^3),\tag{A.40}$$

$$f_8 = H_4(x_3, x_2) \epsilon^2 + \mathcal{O}(\epsilon^3),\tag{A.41}$$

with

$$H_1(x_i) = 2\left(\log(2) - \log(\sqrt{4 - x_i} + \sqrt{-x_i})\right),$$

$$\begin{aligned}
H_2(x_i) &= 2\left(\log(4-x_i) + \log(\sqrt{4-x_i} - \sqrt{-x_i}) - \log(2)\right), \\
&\quad \times \left(\log(\sqrt{4-x_i} - \sqrt{-x_i}) - \log(2)\right) + 2\operatorname{Li}_2\left(\frac{(\sqrt{4-x_i} - \sqrt{-x_i})^2}{-4}\right) + \frac{\pi^2}{6}, \\
H_3(x_i) &= \frac{1}{2}H_1(x_i)^2, \\
H_4(x_i, x_2) &= H_3(x_i) - H_3(x_2).
\end{aligned} \tag{A.42}$$

Only the box integral f_9 remains to be calculated. The transformation to Landau variables does not factorize the remaining square root, the $\sqrt{4(x_2 - x_1 - x_3) + x_1x_3}$. This makes this case a good illustration of an alternative method of solving a canonical system of differential equations - that of “symbols”. For introductions to *symbols*, see Refs. [300, 301] or Appendix B.5 where the subject is introduced more thoroughly than it will be here. The main idea is to associate a certain algebraic object - the symbol - to the various functions (logarithms and polylogarithms) that may appear in the result. Additionally such a *symbol* may be associated with the differential equation, and the procedure then consists of making a linear fit of the set of possible functions, to the differential equation. The result of such a fit, will be very close to the desired solution, and the difference can, in this case, be found solely from the differential equation along with a numerical fits.

Following this method, the result for the box f_9 may be expressed as

$$\begin{aligned}
\frac{f_9}{\epsilon^2} &= -4\log(\alpha_{1,1})^2 + 4\log(\alpha_{1,2})^2 + \log(-\alpha_u)^2 - 4\log(\alpha_2)\log(x_2 - x_1) \\
&\quad - 4\log(\alpha_2)\log(x_2 - x_3) - 2\log(x_1)\log(x_2 - x_3) + \log(x_2 - x_3)^2 \\
&\quad + 4\log(\alpha_{1,2})(-2\log(\alpha_4) + \log(x_2 - x_1) + \log(x_2 - x_3)) \\
&\quad + \log(\alpha_{1,1})(8\log(\alpha_{3,1}) - 4\log(-x_3)) + 4\log(\alpha_2)\log(-x_3) + \log(-x_3)^2 \\
&\quad + 2\log(-\alpha_u)(-\log(x_1) + \log(x_2 - x_1) + \log(x_2 - x_3) - 2\log(-x_3)) \\
&\quad + 2\left[\pi^2 + 4i\pi\log(2) + 2\log(2)^2 - 8\log(2)\log(\alpha_{1,3}) + 4\log(\alpha_{1,3})^2\right. \\
&\quad + 4\log(2)\log(\alpha_{3,3}) - 2\log(\alpha_{3,3})^2 + 4\log(2)\log(\alpha_4) - 4\log(2)\log(x_1) \\
&\quad + 2\log(\alpha_2)\log(x_1) + 2\log(\alpha_{3,3})\log(x_1) - 4\log(2)\log(\alpha_{3,1}) \\
&\quad \left. + i\pi(-2\log(\alpha_2) - 2\log(\alpha_{3,3}) + \log(x_1) - \log(x_2 - x_1) + 2\log(-x_3))\right] \\
&\quad - 2\operatorname{Li}_2\left(\frac{-4}{\alpha_{1,1}^2}\right) + 2\operatorname{Li}_2\left(\frac{-4}{\alpha_{1,3}^2}\right) - 2\operatorname{Li}_2\left(\frac{4\alpha_u}{\alpha_2}\right) + \operatorname{Li}_2\left(\frac{16\alpha_u}{\alpha_{1,2}\alpha_2}\right) + \operatorname{Li}_2\left(\frac{\alpha_{1,2}^2\alpha_u}{\alpha_2}\right) \\
&\quad - 4\operatorname{Li}_2\left(\frac{\alpha_{1,3}\sqrt{-x_1}}{\alpha_{3,3}}\right) - 2\operatorname{Li}_2\left(\frac{\alpha_{1,1}^2(x_1 - x_2)}{\alpha_{3,1}^2}\right) + \operatorname{Li}_2\left(\frac{x_2 - x_1}{\alpha_u}\right) + 2\operatorname{Li}_2\left(\frac{4(x_2 - x_1)}{\alpha_{3,1}^2}\right) \\
&\quad \left. + \operatorname{Li}_2\left(\frac{x_1}{x_2 - x_3}\right) - 2\operatorname{Li}_2\left(\frac{4(x_2 - x_3)}{\alpha_{3,3}^2}\right) + 4\operatorname{Li}_2\left(\frac{\alpha_{1,1}(x_1 - x_2)}{\alpha_{3,1}\sqrt{-x_3}}\right) + 2\operatorname{Li}_2\left(\frac{\alpha_{1,3}^2(x_3 - x_2)}{\alpha_{3,3}^2}\right)\right],
\end{aligned} \tag{A.43}$$

where we have used the abbreviations

$$\begin{aligned}
\alpha_u &\equiv x_2 - x_1 - x_3, \\
\alpha_{1,i} &\equiv \sqrt{4-x_i} + \sqrt{-x_i}, \\
\alpha_2 &\equiv \sqrt{-x_1}\sqrt{-x_3} + \sqrt{4(x_2 - x_1 - x_3) + x_1x_3}, \\
\alpha_{3,1} &\equiv \sqrt{4-x_1}\sqrt{-x_3} + \sqrt{4(x_2 - x_1 - x_3) + x_1x_3},
\end{aligned}$$

$$\begin{aligned}
\alpha_{3,3} &\equiv \sqrt{-x_1}\sqrt{4-x_3} + \sqrt{4(x_2-x_1-x_3)+x_1x_3}, \\
\alpha_4 &\equiv \sqrt{-x_1}\sqrt{-x_3}\sqrt{4-x_2} + \sqrt{-x_2}\sqrt{4(x_2-x_1-x_3)+x_1x_3}.
\end{aligned}
\tag{A.44}$$

B Two-loop Feynman Integrals

In this appendix we will lay out the steps needed to compute the two-loop contributions to Higgs boson + jet production. We will follow closely the approach used in Ref. [180].

We begin with a description of how to get expressions for the Feynman diagrams or the numerators thereof. Then follows a discussion of the reduction of the Feynman integrals to a minimal set - the master integrals. Next we discuss how to evaluate those integrals using the differential equation method enhanced by the use of canonical bases and symbols, in order to obtain an expression in terms of generalized polylogarithms, which at the two-loop level are reducible to Li_n and $\text{Li}_{2,2}$. We conclude with a discussion of cases where these approaches are insufficient and bigger classes of functions, such as elliptic integrals, are needed.

B.1 Extracting the numerator

In general we can write any loop-level amplitude as

$$A_{L\text{-loop}} = \sum_{i \in \text{diagrams}} \int \frac{\prod_l^L d^d k_l}{(i\pi^{d/2})^L} \frac{N_i(\{k\})}{\prod_{j \in i} D_j(\{k\})} \quad (\text{B.1})$$

where as usual D_j denotes the denominators stemming from the propagators of the Feynman diagrams, i.e. terms of the form $(k+p)^2 - m^2$, while N_i contains the rest of the terms in the Feynman diagram, i.e all gamma matrices, colour factors, polarization vectors, spinors, and all other factors provided by the Feynman rules.

As discussed earlier, the Feynman rules from which to generate Eq. (B.1) have been implemented in several codes [219–222]. In general, the numerators of the diagrams will contain long strings and traces of (Dirac) gamma matrices, from external fermions and fermions in loops respectively, along with products of the colour factors T_{ij}^a and f_{abc} from vertices containing coloured particles.

Several computer implementations of the algebra enabling the reduction of such factors exist [220, 223], the authors of ref. [180] used a private implementation in FORM. The bottleneck for such reductions are the gamma Matrix identities, the trace of a product of $2n$ gamma matrices has in general $(2n - 1)!!$ terms, so finding ways to minimize that number can save significant computational time.

There are other methods which may be used to minimize the work which has to be done in order to extract the numerator of Eq. (B.1), though such methods were not found necessary for the calculations in ref. [180]. Without going into detail, the numerators of diagrams consisting purely of three-point vertices will be identical to products of three-point tree-level amplitudes, except that the propagating particles are off shell. So, by mathematically putting these particles on shell with a procedure known as *generalized unitarity cuts* [302, 303], the coefficients of those diagrams can be extracted solely from tree-level diagrams without the need for performing any kind of gamma algebra. The coefficients of the remaining diagrams may be extracted by similar methods using the knowledge of the three-point vertex diagrams as *subtraction terms*. This method, known as the *OPP method* [304] [305–307], have been used for the complete automation of one-loop-calculations [137, 138, 144, 308–312], and similar method may be extended to higher loops [236, 237, 313–322].

B.2 Integrand reduction

After applying projectors (as described in section II.5.1.1), we can express the matrix element as $M \equiv M^{\mu\nu\tau} \mathcal{P}_{\mu\nu\tau}$, where

$$M = \sum_{i \in \text{diagrams}} \int \frac{\prod_l^L d^d k_l}{(i\pi^{d/2})^L} \frac{N_i(\{k\})}{\prod_{j \in i} D_j(\{k\})}, \quad (\text{B.2})$$

as in Eq. (B.1). After performing all gamma- and colour algebra, the k dependence of the numerators N_i will be solely true scalar products of the form $k_i \cdot k_j$, $k_i \cdot p_j$, or $k \cdot \omega$ where the vector ω is defined to be perpendicular to all the physical momenta $\omega^\mu \propto \varepsilon^{\nu_1 \nu_2 \nu_3 \mu} p_{1\nu_1} p_{2\nu_2} p_{3\nu_3}$.

The renormalizability of the theory imposes that maximally four powers of each loop-momentum is allowed to appear in the numerators. That constraint limits the number of different Feynman integrals which have to be performed to a large but finite number, but it is still clearly desirable to find a way to minimize that number.

One way of doing so is called *Integrand Reduction*. This first consist of re-expressing the amplitude as a sum over *topologies* defined as distinct sets of propagators

$$M = \sum_{i \in \text{topologies}} \int \frac{\prod_l^L d^d k_l}{(i\pi^{d/2})^L} \frac{\Delta_i(\{k\})}{\prod_{j \in i} D_j(\{k\})}, \quad (\text{B.3})$$

where Δ denotes the irreducible numerator, which means that all terms in N which are proportional to some of the propagators D have been ‘‘cancelled out’’ leaving only the irreducible part Δ . A simple example would be a term in the denominator of Eq. (B.2) which contains the factor $k_i \cdot p_j$ while the denominator contains e.g. the propagators k_i^2 and $(k_i - p_j)^2 - m^2$. We might then perform a form of partial fractioning

$$C \frac{k \cdot p}{(k^2) ((k - p)^2 - m^2)} = \frac{C}{2} \left(\frac{p^2 - m^2}{(k^2) ((k - p)^2 - m^2)} - \frac{1}{k^2} + \frac{1}{(k - p)^2 - m^2} \right) \quad (\text{B.4})$$

showing how that term is reducible to an integral with a constant numerator plus terms in lower topologies. For multi-loop integrals performing the integrand reduction solely using ‘‘partial fractioning’’ is not always practical, one will miss relations unless one is very careful. There are ways to systematize this reduction which ensure that all relations are captured. These methods utilize insights from the mathematical field of algebraic geometry, and this is not the place to describe these developments. See for instance Refs. [317, 319, 323].

Integrand reduction is able to significantly reduce the number of integrals needed to evaluate an amplitude. Yet the number remains uncomfortably large, for the propagator structure corresponding to the first diagram of Fig. II.28, 84 non-zero terms remain after the reduction. To reduce the number further, we will need to go beyond integrand-level relations to relations that hold only at the integral-level - the so-called IBP identities which are described in section II.5.2.2 in the main text.

B.3 The differential equation method

After reducing the set of Feynman integrals that needs to be solved to a minimal set, we can no longer postpone discussing methods for solving them. Traditional text-book methods such as Feynman parametrization are rarely sufficient beyond one-loop as they themselves yield multi-dimensional integrals that are hard or impossible to solve. The method that will be described here is that of differential equations [239–242, 324] which is one of the main methods being used for current Feynman integral computations.

In its traditional version, the differential equation method consists of relating the derivative (with respect to a kinematic variable) of the Feynman integral which one wants to solve, with the Feynman integral itself along with Feynman integrals of similar or lower complexity. Doing so allows one to integrate the differential equation using traditional methods for first-order differential equations, usually giving in a result in terms of gamma functions, hyper-geometric functions, or some generalization there-of.

Yet for more involved Feynman integrals, there may be more than one master integral with a given topology. That is the case for the double-box calculated in ref. [242]. For that case the differential equations for the two double-box topologies will couple, giving a second order differential equation for each of the master integrals which can not be solved in general. An approach for solving this problem is to pick the two master integrals in a way such that the derivatives of the two master integrals is proportional to the $\epsilon = (4 - d)/2$ from dimensional regularization, as it was done in ref. [242].

This allows for an solution of the differential equation system at each order in ϵ , which after all is all that is needed, as only terms up to a fixed order in ϵ can contain physical information. So writing each of the master integrals $f(\epsilon, d)$ (with x denoting all the kinematic variables) as

$$f(\epsilon, x) = \sum_{j=j_{\min}}^{\infty} \epsilon^j f^{(j)}(x), \quad (\text{B.5})$$

allows us to compute $f^{(i)}$ in terms of $f^{(i-1)}$ along with the boundary condition which can be calculated in some convenient point, such as the point where all kinematic variables equal one.

A recently developed systematic approach to this decoupling is denoted the canonical form [296]. A differential equation system in the canonical form is given as

$$d\bar{f}(\epsilon, x) = \epsilon \left(\sum_k A_k d \log(y_k(x)) \right) \bar{f}(\epsilon, x). \quad (\text{B.6})$$

Here \bar{f} is a vector made of all the master integrals, $y_j(x)$ are algebraic functions of the kinematic variables x , and the matrices A_j consist of rational numbers only. Specifically this corresponds to a differential equation in each variable

$$\frac{\partial}{\partial x_i} f_a^{(j)}(x) = \sum_k A_{kab} \frac{\partial \log(y_k)}{\partial x_i} f_b^{(j-1)}(x), \quad (\text{B.7})$$

which can be solved using general methods described in the next sections.

How does one get a differential equation system into canonical form? There is no general method which works in all cases. One method described in [325], consist of imposing that the leading singularity of the Feynman-integrals are constant. All canonical integrals have this property [326], so reducing the search space to such integrals simplifies the problem of finding the canonical basis significantly. Other approaches include the application of Magnus series [297] which is the method used in the example in the main text and App. A, and many other approaches are available as well [295, 298, 299], none of which will be described here. For further recent developments, see [327–330].

For the mass-less double box of the example in the previous chapter the canonical form is given in ref. [296]. For that case the only modifications that are needed are the addition of certain kinematical prefactors and the raising of the power of some of the propagators from one to two. For more involved cases, such as the $gg \rightarrow gH$ integrals computed in [180], the same is true for the canonical form of many of the master integrals, yet for some the canonical master integrals have to be expressed as sums of integrals.

B.4 Generalized Polylogarithms

In general the solutions of differential equation systems in canonical form, may be expressed in terms of a function-class denoted generalized polylogarithms (GPLs) [331]. Generalized polylogarithms (also known as Goncharov polylogarithms or hyperlogarithms) are defined recursively as

$$G(a_1, \dots, a_n; x) = \int_0^x \frac{dz}{z - a_1} G(a_2, \dots, a_n; z), \quad (\text{B.8})$$

where the integration path is a straight line, and where $G(; x) \equiv 1$. The exception is the case where all the a -indices equal zero, in which case

$$G(\bar{0}_n; x) = \frac{1}{n!} \log^n(x). \quad (\text{B.9})$$

A piece of terminology that we will need later is the concept of *weight* which is defined as the number of a -indices or correspondingly as the number of recursive integrals.

Many functions often encountered in the (ϵ -expanded) results for Feynman integrals, are special cases of generalized polylogarithms

$$\log(x) = G(0, x) \quad \text{Li}_n(x) = -G(\bar{0}_{n-1}, 1, x), \quad (\text{B.10})$$

where the latter function is the classical (or Euler) polylogarithm, defined recursively as

$$\text{Li}_n(x) = \int_0^x \frac{dz}{z} \text{Li}_{n-1}(z), \quad (\text{B.11})$$

with $\text{Li}_1(x) = -\log(1 - x)$.

At the one-loop level all Feynman integrals may be expressed (up to the ϵ^0 part) in terms of the functions \log and Li_2 and thus they are always given in terms of generalized polylogarithms. At higher weights this is true not for all, but for a large class of functions, since whenever the differential equation system for a Feynman integral can be expressed in canonical form, the result may be expressed in terms of GPLs.

For the case where the algebraic functions $y(x)$ of Eqs. (B.6) and (B.7) may be expressed as polynomials, this is easy to see. In that case the logarithms of Eqs. (B.6) and (B.7) factorize, and Eq. (B.7) may be expressed as

$$\frac{\partial}{\partial x_i} f_a^{(j)}(x) = \sum_k A_{kab} \frac{1}{x_i - a_k} f_b^{(j-1)}(x), \quad (\text{B.12})$$

which we see has the exact form of Eq. (B.8), allowing for a result given directly in terms of generalized polylogarithms. Whether or not this property is present for all algebraic forms of $y(x)$ including cases where no variables change can be found that allows for a rationalization, must be considered an open question.

GPLs fulfill a large number of relations between themselves. They go under names such as the re-scaling relation, and the shuffle and stuffle relations. We shall not summarize those here, see for instance refs. [301, 332–334]. We will however mention one property - namely the fact that all GPL can be reduced to a certain minimal set of functions, of lower complexity than the general GPL [301]. In general this statement is a conjecture, but for GPLs of weight ≤ 4 which is all that is needed for Feynman integrals with two loops, this has been shown explicitly [335] and the minimal set for that case is the functions \log , Li_n with $n \leq 4$, and the special function $\text{Li}_{2,2}$, which in the language of GPLs is given as

$$\text{Li}_{2,2}(x, y) = G(0, 1, 0, \frac{1}{y}; x). \quad (\text{B.13})$$

Evaluating a GPL numerically, may be done by reexpressing is as an infinite sum, which may be truncated once the desired numerical precision has been obtained. A `GiNaC` implementation which can be used to evaluate any GPL using such techniques, is presented in ref. [333]. Another option is to first reduce the GPLs to a minimal set of functions, and then use specialized tools to evaluate those, such as those presented in refs. [335, 336].

B.5 Symbols

The large number of relations between the GPLs make the task of reducing them to a minimal set quite challenging. One mathematical tool which simplifies the application of these relations very significantly is that of *symbols* [300, 301]. Symbols are short for *Chen symbols*, as they utilize the iterated structure of the polylogarithmic functions, which are of the form of *Chen iterated integrals* [337]. Popularly expressed, the algebra of these symbols captures the algebraic parts of the relations between the polylogarithmic functions but leaves out the analytical parts. This is shown by the fact that the rules of symbol calculus explicitly set to zero factors such as π , which arise from the analyticity, as the branch-cut of the logarithm is given as $2\pi i$ and those of the poly-logarithms contain similar factors.

Explicitly, the symbol \mathcal{S} of a GPL is defined recursively, and given as [338]

$$\mathcal{S}(G(a_1, \dots, a_n; x)) = \sum_1^n \left(\mathcal{S}(G(a_1, \dots, \hat{a}_i, \dots, a_n; x)) \otimes (a_i - a_{i-1}) - \mathcal{S}(G(a_1, \dots, \hat{a}_i, \dots, a_n; x)) \otimes (a_i - a_{i+1}) \right), \quad (\text{B.14})$$

where $a_{n+1} \equiv 0$ and $a_0 \equiv x$, and where \hat{a}_i denotes that the a_i entry is left out. The recursions ends as $\mathcal{S}(\log(x)) = x$. In simple cases this reduces to

$$\begin{aligned} \mathcal{S}(\log^n(x)) &= n! (x \otimes \dots \otimes x) \\ \mathcal{S}(\text{Li}_n(x)) &= -((1-x) \otimes x \otimes \dots \otimes x), \end{aligned} \quad (\text{B.15})$$

both with n entries in the symbol.

The individual terms in the symbol, are thus tensorial factors of the general form $\alpha_1 \otimes \dots \otimes \alpha_n$, where n is the weight of the original polylogarithmic function. These terms fulfil algebraic rules such as

$$a \otimes bc \otimes d = a \otimes b \otimes d + a \otimes c \otimes d, \quad (\text{B.16})$$

which reflect the corresponding property of the logarithm. From this we get that $a \otimes 1 \otimes b = 0$ and likewise for any root of unity. From the mathematical properties, it is guaranteed that expressions which have the same symbol, are identical up to factors for which the symbol vanish, such as factors¹⁰ containing π and other of what is known as transcendental constants.

To show a simple example

$$\begin{aligned} \mathcal{S}(\text{Li}_2(x)) &= -((1-x) \otimes x), \\ \mathcal{S}(\text{Li}_2(1/x)) &= ((1-x) \otimes x) - (x \otimes x), \\ \mathcal{S}(\log^2(-x)) &= 2(x \otimes x), \end{aligned} \quad (\text{B.17})$$

from which we may deduce the relation

$$\text{Li}_2\left(\frac{1}{x}\right) = -\text{Li}_2(x) - \frac{1}{2} \log^2(-x) + c, \quad (\text{B.18})$$

¹⁰The fact that the symbol of π vanishes, can be seen from the fact that $\mathcal{S}(\text{Li}_2(1)) = -(0 \otimes 1) = 0$, and $\text{Li}_2(1) = \pi^2/6$.

where c is a term containing factors for which the symbol vanishes. Such factors can usually be found numerically, and for this case it turns out that $c = -\pi^2/6$.

The minimal set of objects which may appear inside the symbol is called the alphabet and the set of possible terms in the symbol which contain the letters of that alphabet are called words. In the example above the alphabet consists of two letters x and $1-x$, but in the general case the set may be much larger, the alphabet of the largest of the integral families of Ref. [180] contained 49 letters.

The general strategy [300,301] for using symbols to simplify expressions containing GPLs (often denoted the DGR algorithm after the authors of Ref. [301]) is as follows:

1. Find the symbol S of the expressions that needs reducing.
2. Find a “basis” of functions containing all the words present in S .
3. Invert the system to get an expression with matching symbol.
4. Find remaining factors not captured by the symbol.

Point 2 on that list is the difficult part. For a logarithm of a specific argument, we see that a criterion for that logarithm to be present in the basis is that its argument can be written as a product of alphabet letters. For the classical polylogarithm $\text{Li}_n(x)$ the criterion is that both x and $1-x$ has that property, and for $\text{Li}_{2,2}$ there is a similar but stricter criterion. However, there is an infinite number of functions fulfilling these criteria, and to find a set that is complete and not over-complete is a significant (computer-)algebraic challenge.

Point 4 on the list is also far from easy, as the set of functions containing factors for which the symbol vanishes is rather large in general. There is a development of the symbol framework, utilizing the mathematical concept of coproducts [339], which may be used to capture most of these terms with a similar algorithm, but these developments will not be described here.

Yet the symbol is not only for simplification, but may be used in general to extract the result from a differential equation in canonical form without going through the step of GPLs. Whenever we have a differential equation on the form of Eq. (B.6), the symbol may be found as

$$\begin{aligned} df_i^{(n)}(x) &= \sum_{j,k} A_{kij} d \log(y_k(x)) f_j^{(n-1)}(x) \Leftrightarrow \\ \mathcal{S}(f_i^{(n)}(x)) &= \sum_{j,k} A_{kij} \mathcal{S}(f_j^{(n-1)}(x)) \otimes y_k(x) \end{aligned} \quad (\text{B.19})$$

This replaces point 1 in the above procedure, which then may be used to solve the differential equation at each order in ϵ . The remaining factors in point 4 are fixed at each order by the boundary conditions of the differential equation, making that step much simpler than it is in the general case.

No assumption was made in Eq. (B.19) that the letters $y(x)$ had to be polynomial, as it was assumed in for instance Eq. (B.12). And thus we see that an expression in terms of GPLs may be obtained for any differential equation in canonical form, as long as a suitable basis of functions to which to fit can be found.

It is this procedure which was used to solve the canonical integrals in Ref. [180], with one exception: The size of the alphabet made it too impractical to find a basis of genuine polylogarithms to span the result. Only up to weight two was this possible, so at weights three and four a one-fold integral was used to express the result.

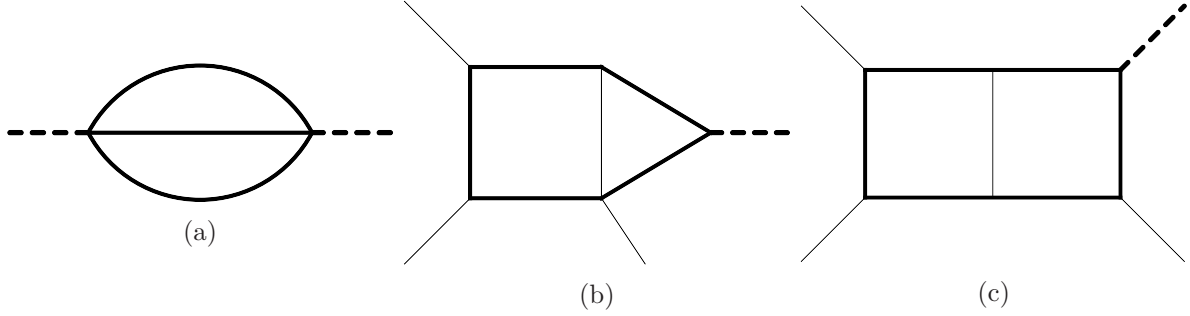


Fig. B.1: (a) is the well-known elliptic massive sunrise diagram. (b) and (c) are the elliptic topologies arising in the context of planar $gg \rightarrow gH$ at two-loop: the box-triangle I_{bt}^A and the double-box I_{db}^A

B.6 Elliptic integrals

It is not all Feynman integrals which can be expressed in terms of GPLs, once we move beyond the one-loop case. The best known example is the so-called massive sunrise diagram [340–342] shown in Fig. B.1(a)

$$I_{\text{massive sunrise}} = \iint \frac{d^d k_1 d^d k_2}{(i\pi^{d/2})^2} \frac{1}{(k_1^2 - m^2)((k_2 + p)^2 - m^2)((k_1 - k_2)^2 - m^2)}, \quad (\text{B.20})$$

where $p^2 = s$, for which the result contains the functions

$$K(k) \equiv \int_0^1 \frac{dx}{\sqrt{(1-x^2)(1-k^2x^2)}}, \quad (\text{B.21})$$

$$E(k) \equiv \int_0^1 \sqrt{\frac{1-k^2x^2}{(1-x^2)}} dx, \quad (\text{B.22})$$

which are denoted the complete elliptic integral of the first and second kind respectively, and which are independent functions not expressible in terms of generalized polylogarithms.

There have been a lot of studies in the previous years of this class of functions [236, 325, 343–347] particularly attempting to generalize polylogarithmic functions to this larger class. But so far no mathematical tool-set exist which is anywhere nearly as powerful as that of canonical basis and symbols for GPLs.

Elliptic integrals also show up in the results for eight of the planar $gg \rightarrow gH$ integrals of Ref. [180]. This is not in the form of the massive sunset graph, but rather in the form of the two topologies I_{bt}^A and I_{db}^A shown on Fig. B.1, which contain four master integrals each. For the six-propagator box-triangle topology I_{bt}^A , the ellipticity reveals itself when getting the topology to canonical form turns out to be impossible, and the best that can be done is to obtain a differential equation of the form

$$\frac{\partial}{\partial x} \bar{f}_{\text{bt}}(\epsilon, x) = A(x) \bar{f}_{\text{bt}}(\epsilon, x) + \epsilon B(x) \bar{f}_{\text{bt}}(\epsilon, x) + \epsilon \sum \bar{C}(x) f_{\text{lower } i}(\epsilon, x). \quad (\text{B.23})$$

A basis can be found where the matrix A can be expressed as

$$A(x) = \begin{bmatrix} a_{11}(x) & a_{12}(x) & 0 & 0 \\ a_{21}(x) & a_{22}(x) & 0 & 0 \\ a_{31}(x) & a_{32}(x) & a_{33}(x) & 0 \\ a_{41}(x) & a_{42}(x) & 0 & a_{44}(x) \end{bmatrix} \quad (\text{B.24})$$

where we see that at the level of the homogeneous term, the first two entries of \bar{f}_{bt} decouple and form their own two-by-two sub-system. This property may be used to write a second-order differential equation for the homogeneous part of the equation, which may be solved with the result given in terms of elliptic integrals. Using the “method of the variation of constants”, the general solution may then be expressed as a one-fold integral over the homogeneous solution multiplied with the lower order terms as well as with various other factors, yielding the full result for the two first entries of \bar{f}_{bt} as integrals over elliptic integrals. The remaining two entries may then, from the differential equation, be written as integrals over those solutions, though it turns out to be possible to reduce the number of recursive integrals for this case by one, using methods that will not be described here.

For the seven-propagator topology I_{db}^A , the ellipticity enters only through the elliptic sub-topology. It is thus possible to describe the differential equation as

$$\frac{\partial}{\partial x} \bar{f}_{\text{db}}(\epsilon, x) = \epsilon D(x) \bar{f}_{\text{db}}(\epsilon, x) + E(x) \bar{f}_{\text{bt}}(\epsilon, x) + \epsilon \sum \bar{F}(x) f_{\text{lower } i}(\epsilon, x), \quad (\text{B.25})$$

where the “lower” in the last term includes contributions from the I_{bt} topology. It is possible to remove the $E(x) \bar{f}_{\text{bt}}(\epsilon, x)$ term and get the equation to an ϵ -factorized form [295], but as the I_{bt} -topology itself involve elliptic integrals, doing so does not remove any elliptic integrals from the result, it merely ensures that no new ones appear. For further considerations of the elliptic functions appearing in these topologies, see Refs. [328–330, 348, 349].

Final remarks

The result of the calculation of the planar Feynman integrals contributing to the process $gg \rightarrow gH$ as described in Ref. [180] takes up around 500 MB and to evaluate the expression in one phase-space point with eight digits of accuracy, takes about 20 minutes on one CPU core. This is primarily due to the fact that the result is expressed as an integral (or for the elliptic cases, as double or triple iterated integrals) which has to be performed numerically.

Needless to say, such a timing is not suitable for inclusion in for instance a Monte Carlo event generator, and this fact should motivate the search for methods to approximate the result, such as those described in Refs. [260, 261] as well as in sections II.5.5.2 and II.5.5.3.

References

- [1] ATLAS Collaboration, G. Aad et al., *Observation of a new particle in the search for the Standard Model Higgs boson with the ATLAS detector at the LHC*, Phys. Lett. **B716** (2012) 1–29, [arXiv:1207.7214 \[hep-ex\]](#).
- [2] CMS Collaboration, S. Chatrchyan et al., *Observation of a new boson at a mass of 125 GeV with the CMS experiment at the LHC*, Phys. Lett. **B716** (2012) 30–61, [arXiv:1207.7235 \[hep-ex\]](#).
- [3] P. W. Higgs, *Broken symmetries, massless particles and gauge fields*, Phys. Lett. **12** (1964) 132–133.
- [4] P. W. Higgs, *Broken Symmetries and the Masses of Gauge Bosons*, Phys. Rev. Lett. **13** (1964) 508–509.
- [5] F. Englert and R. Brout, *Broken Symmetry and the Mass of Gauge Vector Mesons*, Phys. Rev. Lett. **13** (1964) 321–323.
- [6] G. S. Guralnik, C. R. Hagen, and T. W. B. Kibble, *Global Conservation Laws and Massless Particles*, Phys. Rev. Lett. **13** (1964) 585–587.
- [7] P. W. Higgs, *Spontaneous Symmetry Breakdown without Massless Bosons*, Phys. Rev. **145** (1966) 1156–1163.
- [8] T. W. B. Kibble, *Symmetry breaking in nonAbelian gauge theories*, Phys. Rev. **155** (1967) 1554–1561.
- [9] LHC Higgs Cross Section Working Group Collaboration, A. David, A. Denner, M. Duehrssen, M. Grazzini, C. Grojean, G. Passarino, M. Schumacher, M. Spira, G. Weiglein, and M. Zanetti, *LHC HXSWG interim recommendations to explore the coupling structure of a Higgs-like particle*, [arXiv:1209.0040 \[hep-ph\]](#).
- [10] C. Mariotti and G. Passarino, *Higgs boson couplings: measurements and theoretical interpretation*, Int. J. Mod. Phys. **A32** (2017) 1730003, [arXiv:1612.00269 \[hep-ph\]](#).
- [11] R. Gauld, B. D. Pecjak, and D. J. Scott, *QCD radiative corrections for $h \rightarrow b\bar{b}$ in the Standard Model Dimension-6 EFT*, Phys. Rev. **D94** (2016) 074045, [arXiv:1607.06354 \[hep-ph\]](#).
- [12] ATLAS, CMS Collaboration, G. Aad et al., *Measurements of the Higgs boson production and decay rates and constraints on its couplings from a combined ATLAS and CMS analysis of the LHC pp collision data at $\sqrt{s} = 7$ and 8 TeV*, JHEP **08** (2016) 045, [arXiv:1606.02266 \[hep-ex\]](#).
- [13] ATLAS Collaboration, G. Aad et al., *The ATLAS Experiment at the CERN Large Hadron Collider*, JINST **3** (2008) S08003.
- [14] CMS Collaboration, S. Chatrchyan et al., *The CMS Experiment at the CERN LHC*, JINST **3** (2008) S08004.
- [15] S. Alioli, P. Nason, C. Oleari, and E. Re, *A general framework for implementing NLO calculations in shower Monte Carlo programs: the POWHEG BOX*, JHEP **06** (2010) 043, [arXiv:1002.2581 \[hep-ph\]](#).
- [16] Y. Gao, A. V. Gritsan, Z. Guo, K. Melnikov, M. Schulze, and N. V. Tran, *Spin determination of single-produced resonances at hadron colliders*, Phys. Rev. **D81** (2010) 075022, [arXiv:1001.3396 \[hep-ph\]](#).
- [17] S. Bolognesi, Y. Gao, A. V. Gritsan, K. Melnikov, M. Schulze, N. V. Tran, and A. Whitbeck, *On the spin and parity of a single-produced resonance at the LHC*, Phys. Rev. **D86** (2012) 095031, [arXiv:1208.4018 \[hep-ph\]](#).
- [18] I. Anderson et al., *Constraining anomalous HVV interactions at proton and lepton colliders*, Phys. Rev. **D89** (2014) 035007, [arXiv:1309.4819 \[hep-ph\]](#).

- [19] A. V. Gritsan, R. Röntsch, M. Schulze, and M. Xiao, *Constraining anomalous Higgs boson couplings to the heavy flavor fermions using matrix element techniques*, Phys. Rev. **D94** (2016) 055023, arXiv:1606.03107 [hep-ph].
- [20] T. Sjöstrand, S. Ask, J. R. Christiansen, R. Corke, N. Desai, P. Ilten, S. Mrenna, S. Prestel, C. O. Rasmussen, and P. Z. Skands, *An Introduction to PYTHIA 8.2*, Comput. Phys. Commun. **191** (2015) 159–177, arXiv:1410.3012 [hep-ph].
- [21] GEANT4 Collaboration, S. Agostinelli et al., *GEANT4: A Simulation toolkit*, Nucl. Instrum. Meth. **A506** (2003) 250–303.
- [22] A. Bredenstein, A. Denner, S. Dittmaier, and M. M. Weber, *Precise predictions for the Higgs-boson decay $H \rightarrow WW/ZZ \rightarrow 4$ leptons*, Phys. Rev. **D74** (2006) 013004, arXiv:hep-ph/0604011 [hep-ph].
- [23] A. Bredenstein, A. Denner, S. Dittmaier, and M. M. Weber, *Precision calculations for the Higgs decays $H \rightarrow ZZ/WW \rightarrow 4$ leptons*, Nucl. Phys. Proc. Suppl. **160** (2006) 131–135, arXiv:hep-ph/0607060 [hep-ph].
- [24] A. Bredenstein, A. Denner, S. Dittmaier, and M. M. Weber, *Radiative corrections to the semileptonic and hadronic Higgs-boson decays $H \rightarrow W W / Z Z \rightarrow 4$ fermions*, JHEP **02** (2007) 080, arXiv:hep-ph/0611234 [hep-ph].
- [25] G. Cowan, K. Cranmer, E. Gross, and O. Vitells, *Asymptotic formulae for likelihood-based tests of new physics*, Eur. Phys. J. **C71** (2011) 1554, arXiv:1007.1727 [physics.data-an]. [Erratum: Eur. Phys. J. **C73**,2501(2013)].
- [26] M. Bohm, A. Denner, and H. Joos, *Gauge theories of the strong and electroweak interaction*. B. G. Teubner, Stuttgart, 2001.
- [27] B. A. Kniehl, *Radiative corrections for $H \rightarrow f$ anti- f (γ) in the standard model*, Nucl. Phys. **B376** (1992) 3–28.
- [28] A. Denner, *Techniques for calculation of electroweak radiative corrections at the one loop level and results for W physics at LEP-200*, Fortsch. Phys. **41** (1993) 307–420, arXiv:0709.1075 [hep-ph].
- [29] A. Biekötter, J. Brehmer, and T. Plehn, *Extending the limits of Higgs effective theory*, Phys. Rev. **D94** (2016) 055032, arXiv:1602.05202 [hep-ph].
- [30] N. Kauer and G. Passarino, *Inadequacy of zero-width approximation for a light Higgs boson signal*, JHEP **08** (2012) 116, arXiv:1206.4803 [hep-ph].
- [31] F. Caola and K. Melnikov, *Constraining the Higgs boson width with ZZ production at the LHC*, Phys. Rev. **D88** (2013) 054024, arXiv:1307.4935 [hep-ph].
- [32] M. Ghezzi, G. Passarino, and S. Uccirati, *Bounding the Higgs Width Using Effective Field Theory*, PoS **LL2014** (2014) 072, arXiv:1405.1925 [hep-ph].
- [33] C. Englert, M. McCullough, and M. Spannowsky, *Combining LEP and LHC to bound the Higgs Width*, Nucl. Phys. **B902** (2016) 440–457, arXiv:1504.02458 [hep-ph].
- [34] F. Boudjema et al., *On the presentation of the LHC Higgs Results*, in *Workshop on Likelihoods for the LHC Searches Geneva, Switzerland, January 21-23, 2013*. 2013. arXiv:1307.5865 [hep-ph].
- [35] ATLAS Collaboration, G. Aad et al., *Fiducial and differential cross sections of Higgs boson production measured in the four-lepton decay channel in pp collisions at $\sqrt{s}=8$ TeV with the ATLAS detector*, Phys. Lett. **B738** (2014) 234–253, arXiv:1408.3226 [hep-ex].
- [36] CMS Collaboration, *Measurement of inclusive and differential fiducial cross sections for Higgs boson production in the H -to- $4l$ decay channel in p - p collisions at 7 TeV and 8 TeV*, Tech. Rep. CMS-PAS-HIG-14-028, CERN, Geneva, 2015.

- <https://cds.cern.ch/record/2040210>.
- [37] LHC Higgs Cross Section Working Group Collaboration, D. de Florian et al., *Handbook of LHC Higgs Cross Sections: 4. Deciphering the Nature of the Higgs Sector*, arXiv:1610.07922 [hep-ph].
 - [38] ATLAS Collaboration Collaboration, *Combined measurements of the Higgs boson production and decay rates in $H \rightarrow ZZ^* \rightarrow 4\ell$ and $H \rightarrow \gamma\gamma$ final states using pp collision data at $\sqrt{s} = 13$ TeV in the ATLAS experiment*, Tech. Rep. ATLAS-CONF-2016-081, CERN, Geneva, Aug, 2016. <https://cds.cern.ch/record/2206272>.
 - [39] T. Plehn, G. P. Salam, and M. Spannowsky, *Fat Jets for a Light Higgs*, Phys. Rev. Lett. **104** (2010) 111801, arXiv:0910.5472 [hep-ph].
 - [40] F. Demartin, F. Maltoni, K. Mawatari, B. Page, and M. Zaro, *Higgs characterisation at NLO in QCD: CP properties of the top-quark Yukawa interaction*, Eur. Phys. J. **C74** (2014) 3065, arXiv:1407.5089 [hep-ph].
 - [41] J. A. Aguilar-Saavedra, *A Minimal set of top-Higgs anomalous couplings*, Nucl. Phys. **B821** (2009) 215–227, arXiv:0904.2387 [hep-ph].
 - [42] ATLAS Collaboration, G. Aad et al., *Differential top-antitop cross-section measurements as a function of observables constructed from final-state particles using pp collisions at $\sqrt{s} = 7$ TeV in the ATLAS detector*, JHEP **06** (2015) 100, arXiv:1502.05923 [hep-ex].
 - [43] M. Gonzalez-Alonso, A. Greljo, G. Isidori, and D. Marzocca, *Pseudo-observables in Higgs decays*, Eur. Phys. J. **C75** (2015) 128, arXiv:1412.6038 [hep-ph].
 - [44] A. Greljo, G. Isidori, J. M. Lindert, and D. Marzocca, *Pseudo-observables in electroweak Higgs production*, Eur. Phys. J. **C76** (2016) 158, arXiv:1512.06135 [hep-ph].
 - [45] M. J. G. Veltman, *Perturbation theory of massive Yang-Mills fields*, Nucl. Phys. **B7** (1968) 637–650.
 - [46] A. David and G. Passarino, *Through precision straits to next standard model heights*, Rev. Phys. **1** (2016) 13–28, arXiv:1510.00414 [hep-ph].
 - [47] S. Weinberg, *Effective Gauge Theories*, Phys. Lett. **B91** (1980) 51–55.
 - [48] V. Silveira and A. Zee, *SCALAR PHANTOMS*, Phys. Lett. **161B** (1985) 136–140.
 - [49] R. M. Schabinger and J. D. Wells, *A Minimal spontaneously broken hidden sector and its impact on Higgs boson physics at the large hadron collider*, Phys. Rev. **D72** (2005) 093007, arXiv:hep-ph/0509209 [hep-ph].
 - [50] G. M. Pruna and T. Robens, *Higgs singlet extension parameter space in the light of the LHC discovery*, Phys. Rev. **D88** (2013) no. 11, 115012, arXiv:1303.1150 [hep-ph].
 - [51] T. Robens and T. Stefaniak, *Status of the Higgs Singlet Extension of the Standard Model after LHC Run 1*, Eur. Phys. J. **C75** (2015) 104, arXiv:1501.02234 [hep-ph].
 - [52] T. Robens and T. Stefaniak, *LHC Benchmark Scenarios for the Real Higgs Singlet Extension of the Standard Model*, Eur. Phys. J. **C76** (2016) no. 5, 268, arXiv:1601.07880 [hep-ph].
 - [53] M. Gorbahn, J. M. No, and V. Sanz, *Benchmarks for Higgs Effective Theory: Extended Higgs Sectors*, JHEP **10** (2015) 036, arXiv:1502.07352 [hep-ph].
 - [54] J. Elias-Miro, J. R. Espinosa, G. F. Giudice, H. M. Lee, and A. Strumia, *Stabilization of the Electroweak Vacuum by a Scalar Threshold Effect*, JHEP **06** (2012) 031, arXiv:1203.0237 [hep-ph].
 - [55] G. W. Anderson and L. J. Hall, *The Electroweak phase transition and baryogenesis*, Phys. Rev. **D45** (1992) 2685–2698.
 - [56] J. R. Espinosa and M. Quiros, *The Electroweak phase transition with a singlet*, Phys.

- Lett. **B305** (1993) 98–105, [arXiv:hep-ph/9301285](#) [hep-ph].
- [57] S. Dittmaier and C. Grosse-Knetter, *Deriving nondecoupling effects of heavy fields from the path integral: A Heavy Higgs field in an $SU(2)$ gauge theory*, Phys. Rev. **D52** (1995) 7276–7293, [arXiv:hep-ph/9501285](#) [hep-ph].
- [58] S. Dittmaier and C. Grosse-Knetter, *Integrating out the standard Higgs field in the path integral*, Nucl. Phys. **B459** (1996) 497–536, [arXiv:hep-ph/9505266](#) [hep-ph].
- [59] T. Appelquist and J. Carazzone, *Infrared Singularities and Massive Fields*, Phys. Rev. **D11** (1975) 2856.
- [60] C. Becchi, A. Rouet, and R. Stora, *Renormalizable theories with symmetry breaking*, in *Field Theory, quantization and statistical physics. In memory of Bernard Jowet*, E. Tirapegui, ed., pp. 3–32. 1981.
- [61] B. S. DeWitt, *Quantum Theory of Gravity. 2. The Manifestly Covariant Theory*, Phys. Rev. **162** (1967) 1195–1239.
- [62] G. 't Hooft, *An algorithm for the poles at dimension four in the dimensional regularization procedure*, Nucl. Phys. **B62** (1973) 444–460.
- [63] L. F. Abbott, *The Background Field Method Beyond One Loop*, Nucl. Phys. **B185** (1981) 189–203.
- [64] L. F. Abbott, *Introduction to the Background Field Method*, Acta Phys. Polon. **B13** (1982) 33.
- [65] A. Denner, G. Weiglein, and S. Dittmaier, *Gauge invariance of green functions: Background field method versus pinch technique*, Phys. Lett. **B333** (1994) 420–426, [arXiv:hep-ph/9406204](#) [hep-ph].
- [66] A. Denner, G. Weiglein, and S. Dittmaier, *Application of the background field method to the electroweak standard model*, Nucl. Phys. **B440** (1995) 95–128, [arXiv:hep-ph/9410338](#) [hep-ph].
- [67] M. K. Gaillard, *The Effective One Loop Lagrangian With Derivative Couplings*, Nucl. Phys. **B268** (1986) 669–692.
- [68] B. Henning, X. Lu, and H. Murayama, *How to use the Standard Model effective field theory*, JHEP **01** (2016) 023, [arXiv:1412.1837](#) [hep-ph].
- [69] F. del Aguila, Z. Kunszt, and J. Santiago, *One-loop effective lagrangians after matching*, Eur. Phys. J. **C76** (2016) 244, [arXiv:1602.00126](#) [hep-ph].
- [70] M. Boggia, R. Gomez-Ambrosio, and G. Passarino, *Low energy behaviour of standard model extensions*, JHEP **05** (2016) 162, [arXiv:1603.03660](#) [hep-ph].
- [71] B. Henning, X. Lu, and H. Murayama, *One-loop Matching and Running with Covariant Derivative Expansion*, [arXiv:1604.01019](#) [hep-ph].
- [72] R. Alonso, E. E. Jenkins, A. V. Manohar, and M. Trott, *Renormalization Group Evolution of the Standard Model Dimension Six Operators III: Gauge Coupling Dependence and Phenomenology*, JHEP **04** (2014) 159, [arXiv:1312.2014](#) [hep-ph].
- [73] A. Freitas, D. Lopez-Val, and T. Plehn, *When matching matters: Loop effects in Higgs effective theory*, Phys. Rev. **D94** (2016) 095007, [arXiv:1607.08251](#) [hep-ph].
- [74] H. Georgi, *Thoughts on effective field theory*, Nucl. Phys. Proc. Suppl. **29BC** (1992) 1–10.
- [75] H. Georgi, *Effective field theory*, Ann. Rev. Nucl. Part. Sci. **43** (1993) 209–252.
- [76] J. Bain, *Emergence in effective field theories*, Eur. J. Phil. Sci. **3** (2013) 257–273.
- [77] C. G. Callan, Jr., S. R. Coleman, J. Wess, and B. Zumino, *Structure of phenomenological Lagrangians. 2.*, Phys. Rev. **177** (1969) 2247–2250.
- [78] A. Manohar and H. Georgi, *Chiral Quarks and the Nonrelativistic Quark Model*, Nucl.

- Phys. **B234** (1984) 189.
- [79] D. B. Kaplan, *Effective field theories*, in *Beyond the standard model 5. Proceedings, 5th Conference, Balholm, Norway, April 29-May 4, 1997*. 1995. [arXiv:nucl-th/9506035 \[nucl-th\]](#).
 - [80] A. V. Manohar, *Effective field theories*, Lect. Notes Phys. **479** (1997) 311–362, [arXiv:hep-ph/9606222 \[hep-ph\]](#).
 - [81] A. G. Cohen, D. B. Kaplan, and A. E. Nelson, *Counting 4 pis in strongly coupled supersymmetry*, Phys. Lett. **B412** (1997) 301–308, [arXiv:hep-ph/9706275 \[hep-ph\]](#).
 - [82] M. A. Luty, *Naive dimensional analysis and supersymmetry*, Phys. Rev. **D57** (1998) 1531–1538, [arXiv:hep-ph/9706235 \[hep-ph\]](#).
 - [83] J. Polchinski, *Effective field theory and the Fermi surface*, in *Theoretical Advanced Study Institute (TASI 92): From Black Holes and Strings to Particles Boulder, Colorado, June 3-28, 1992*. 1992. [arXiv:hep-th/9210046 \[hep-th\]](#).
 - [84] I. Z. Rothstein, *TASI lectures on effective field theories*, [arXiv:hep-ph/0308266 \[hep-ph\]](#).
 - [85] W. Skiba, *Effective Field Theory and Precision Electroweak Measurements*, in *Physics of the large and the small, TASI 09, proceedings of the Theoretical Advanced Study Institute in Elementary Particle Physics, Boulder, Colorado, USA, 1-26 June 2009*, pp. 5–70. 2011. [arXiv:1006.2142 \[hep-ph\]](#).
 - [86] C. P. Burgess, *Introduction to Effective Field Theory*, Ann. Rev. Nucl. Part. Sci. **57** (2007) 329–362, [arXiv:hep-th/0701053 \[hep-th\]](#).
 - [87] E. E. Jenkins, A. V. Manohar, and M. Trott, *On Gauge Invariance and Minimal Coupling*, JHEP **09** (2013) 063, [arXiv:1305.0017 \[hep-ph\]](#).
 - [88] E. E. Jenkins, A. V. Manohar, and M. Trott, *Naive Dimensional Analysis Counting of Gauge Theory Amplitudes and Anomalous Dimensions*, Phys. Lett. **B726** (2013) 697–702, [arXiv:1309.0819 \[hep-ph\]](#).
 - [89] G. Buchalla, O. Cata, and C. Krause, *A Systematic Approach to the SILH Lagrangian*, Nucl. Phys. **B894** (2015) 602–620, [arXiv:1412.6356 \[hep-ph\]](#).
 - [90] G. Buchalla, O. Catá, and C. Krause, *On the Power Counting in Effective Field Theories*, Phys. Lett. **B731** (2014) 80–86, [arXiv:1312.5624 \[hep-ph\]](#).
 - [91] B. M. Gavela, E. E. Jenkins, A. V. Manohar, and L. Merlo, *Analysis of General Power Counting Rules in Effective Field Theory*, Eur. Phys. J. **C76** (2016) 485, [arXiv:1601.07551 \[hep-ph\]](#).
 - [92] I. Brivio and M. Trott, *The Standard Model as an Effective Field Theory*, [arXiv:1706.08945 \[hep-ph\]](#).
 - [93] S. Weinberg, *Baryon and Lepton Nonconserving Processes*, Phys. Rev. Lett. **43** (1979) 1566–1570.
 - [94] B. Grzadkowski, M. Iskrzynski, M. Misiak, and J. Rosiek, *Dimension-Six Terms in the Standard Model Lagrangian*, JHEP **10** (2010) 085, [arXiv:1008.4884 \[hep-ph\]](#).
 - [95] F. Maltoni, E. Vryonidou, and C. Zhang, *Higgs production in association with a top-antitop pair in the Standard Model Effective Field Theory at NLO in QCD*, JHEP **10** (2016) 123, [arXiv:1607.05330 \[hep-ph\]](#).
 - [96] O. Bessidskaia Bylund, F. Maltoni, I. Tsinikos, E. Vryonidou, and C. Zhang, *Probing top quark neutral couplings in the Standard Model Effective Field Theory at NLO in QCD*, JHEP **05** (2016) 052, [arXiv:1601.08193 \[hep-ph\]](#).
 - [97] G. Passarino and M. Trott, *The Standard Model Effective Field Theory and Next to Leading Order*, [arXiv:1610.08356 \[hep-ph\]](#).

- [98] M. Ghezzi, R. Gomez-Ambrosio, G. Passarino, and S. Uccirati, *NLO Higgs effective field theory and κ -framework*, JHEP **07** (2015) 175, arXiv:1505.03706 [hep-ph].
- [99] M. B. Einhorn and J. Wudka, *The Bases of Effective Field Theories*, Nucl. Phys. **B876** (2013) 556–574, arXiv:1307.0478 [hep-ph].
- [100] L. Lehman, *Extending the Standard Model Effective Field Theory with the Complete Set of Dimension-7 Operators*, Phys. Rev. **D90** (2014) 125023, arXiv:1410.4193 [hep-ph].
- [101] A. Kobach, *Baryon Number, Lepton Number, and Operator Dimension in the Standard Model*, Phys. Lett. **B758** (2016) 455–457, arXiv:1604.05726 [hep-ph].
- [102] L. Lehman and A. Martin, *Hilbert Series for Constructing Lagrangians: expanding the phenomenologist’s toolbox*, Phys. Rev. **D91** (2015) 105014, arXiv:1503.07537 [hep-ph].
- [103] Y. Liao and X.-D. Ma, *Operators up to Dimension Seven in Standard Model Effective Field Theory Extended with Sterile Neutrinos*, Phys. Rev. **D96** (2017) 015012, arXiv:1612.04527 [hep-ph].
- [104] C. Hartmann, W. Shepherd, and M. Trott, *The Z decay width in the SMEFT: y_t and λ corrections at one loop*, JHEP **03** (2017) 060, arXiv:1611.09879 [hep-ph].
- [105] J. Brehmer, A. Freitas, D. Lopez-Val, and T. Plehn, *Pushing Higgs Effective Theory to its Limits*, Phys. Rev. **D93** (2016) 075014, arXiv:1510.03443 [hep-ph].
- [106] M. Sekulla, W. Kilian, T. Ohl, and J. Reuter, *Effective Field Theory and Unitarity in Vector Boson Scattering*, PoS **LHCP2016** (2016) 052, arXiv:1610.04131 [hep-ph].
- [107] U. Aydemir, M. M. Anber, and J. F. Donoghue, *Self-healing of unitarity in effective field theories and the onset of new physics*, Phys. Rev. **D86** (2012) 014025, arXiv:1203.5153 [hep-ph].
- [108] D. Yu. Bardin and G. Passarino, *The standard model in the making: Precision study of the electroweak interactions*. 1999.
- [109] The ALEPH, DELPHI, L3, OPAL, SLD Collaborations, the LEP Electroweak Working Group, the SLD Electroweak and Heavy Flavour Groups, *Precision Electroweak Measurements on the Z Resonance*, Phys. Rept. **427** (2006) 257, hep-ex/0509008.
- [110] The ALEPH, DELPHI, L3, OPAL Collaborations, the LEP Electroweak Working Group, *Electroweak Measurements in Electron-Positron Collisions at W-Boson-Pair Energies at LEP*, Phys. Rept. **532** (2013) 119, arXiv:1302.3415 [hep-ex].
- [111] C. Degrande, C. Duhr, B. Fuks, D. Grellscheid, O. Mattelaer, and T. Reiter, *UFO - The Universal FeynRules Output*, Comput. Phys. Commun. **183** (2012) 1201–1214, arXiv:1108.2040 [hep-ph].
- [112] T. Kinoshita, *Mass singularities of Feynman amplitudes*, J. Math. Phys. **3** (1962) 650–677.
- [113] C. F. Uhlemann and N. Kauer, *Narrow-width approximation accuracy*, Nucl. Phys. **B814** (2009) 195–211, arXiv:0807.4112 [hep-ph].
- [114] S. Goria, G. Passarino, and D. Rosco, *The Higgs Boson Lineshape*, Nucl. Phys. **B864** (2012) 530–579, arXiv:1112.5517 [hep-ph].
- [115] B. Biedermann, A. Denner, S. Dittmaier, L. Hofer, and B. Jäger, *Next-to-leading-order electroweak corrections to the production of four charged leptons at the LHC*, JHEP **01** (2017) 033, arXiv:1611.05338 [hep-ph].
- [116] S. Dittmaier, A. Huss, and G. Knippen, *Next-to-leading-order QCD and electroweak corrections to WWW production at proton-proton colliders*, JHEP **09** (2017) 034, arXiv:1705.03722 [hep-ph].
- [117] C. Anastasiou, C. Duhr, F. Dulat, F. Herzog, and B. Mistlberger, *Higgs Boson*

- Gluon-Fusion Production in QCD at Three Loops*, Phys. Rev. Lett. **114** (2015) 212001, arXiv:1503.06056 [hep-ph].
- [118] C. Anastasiou, C. Duhr, F. Dulat, E. Furlan, T. Gehrmann, F. Herzog, A. Lazopoulos, and B. Mistlberger, *High precision determination of the gluon fusion Higgs boson cross-section at the LHC*, JHEP **05** (2016) 058, arXiv:1602.00695 [hep-ph].
- [119] F. A. Dreyer and A. Karlberg, *Vector-Boson Fusion Higgs Production at Three Loops in QCD*, Phys. Rev. Lett. **117** (2016) 072001, arXiv:1606.00840 [hep-ph].
- [120] T. D. Lee and M. Nauenberg, *Degenerate Systems and Mass Singularities*, Phys. Rev. **133** (1964) B1549–B1562.
- [121] C. Hartmann and M. Trott, *On one-loop corrections in the standard model effective field theory; the $\Gamma(H \rightarrow \gamma\gamma)$ case*, JHEP **07** (2015) 151, arXiv:1505.02646 [hep-ph].
- [122] C. Hartmann and M. Trott, *Higgs Decay to Two Photons at One Loop in the Standard Model Effective Field Theory*, Phys. Rev. Lett. **115** (2015) 191801, arXiv:1507.03568 [hep-ph].
- [123] G. Passarino, *NLO Standard model effective field theory for Higgs and EW precision data*, PoS **LL2016** (2016) 003, arXiv:1607.01236 [hep-ph].
- [124] J. S. R. Chisholm, *Change of variables in quantum field theories*, Nucl. Phys. **26** (1961) 469–479.
- [125] R. E. Kallosh and I. V. Tyutin, *The Equivalence theorem and gauge invariance in renormalizable theories*, Yad. Fiz. **17** (1973) 190–209. [Sov. J. Nucl. Phys.17,98(1973)].
- [126] G. Passarino, *Field reparametrization in effective field theories*, Eur. Phys. J. Plus **132** (2017) 16, arXiv:1610.09618 [hep-ph].
- [127] I. Brivio and M. Trott, *Scheming in the SMEFT... and a reparameterization invariance!*, JHEP **07** (2017) 148, arXiv:1701.06424 [hep-ph].
- [128] P. Artoisenet et al., *A framework for Higgs characterisation*, JHEP **11** (2013) 043, arXiv:1306.6464 [hep-ph].
- [129] J. Alwall, R. Frederix, S. Frixione, V. Hirschi, F. Maltoni, O. Mattelaer, H. S. Shao, T. Stelzer, P. Torrielli, and M. Zaro, *The automated computation of tree-level and next-to-leading order differential cross sections, and their matching to parton shower simulations*, JHEP **07** (2014) 079, arXiv:1405.0301 [hep-ph].
- [130] F. Cascioli, P. Maierhofer, and S. Pozzorini, *Scattering Amplitudes with Open Loops*, Phys. Rev. Lett. **108** (2012) 111601, arXiv:1111.5206 [hep-ph].
- [131] S. Actis, A. Denner, L. Hofer, A. Scharf, and S. Uccirati, *Recursive generation of one-loop amplitudes in the Standard Model*, JHEP **04** (2013) 037, arXiv:1211.6316 [hep-ph].
- [132] S. Actis, A. Denner, L. Hofer, J.-N. Lang, A. Scharf, and S. Uccirati, *RECOLA: REcursive Computation of One-Loop Amplitudes*, Comput. Phys. Commun. **214** (2017) 140–173, arXiv:1605.01090 [hep-ph].
- [133] A. Denner, S. Dittmaier, and L. Hofer, *COLLIER - A fortran-library for one-loop integrals*, PoS **LL2014** (2014) 071, arXiv:1407.0087 [hep-ph].
- [134] A. Denner and S. Dittmaier, *Scalar one-loop 4-point integrals*, Nucl. Phys. **B844** (2011) 199–242, arXiv:1005.2076 [hep-ph].
- [135] A. Denner and S. Dittmaier, *Reduction schemes for one-loop tensor integrals*, Nucl. Phys. **B734** (2006) 62–115, arXiv:hep-ph/0509141 [hep-ph].
- [136] A. Denner and S. Dittmaier, *Reduction of one loop tensor five point integrals*, Nucl. Phys. **B658** (2003) 175–202, arXiv:hep-ph/0212259 [hep-ph].
- [137] G. Cullen, N. Greiner, G. Heinrich, G. Luisoni, P. Mastrolia, et al., *Automated One-Loop Calculations with GoSam*, Eur.Phys.J. **C72** (2012) 1889, arXiv:1111.2034 [hep-ph].

- [138] G. Cullen, H. van Deurzen, N. Greiner, G. Heinrich, G. Luisoni, et al., *GoSam-2.0: a tool for automated one-loop calculations within the Standard Model and beyond*, Eur. Phys. J. **C74** (2014) 3001, [arXiv:1404.7096 \[hep-ph\]](#).
- [139] T. Gleisberg, S. Hoeche, F. Krauss, A. Schalicke, S. Schumann, and J.-C. Winter, *SHERPA 1. alpha: A Proof of concept version*, JHEP **02** (2004) 056, [arXiv:hep-ph/0311263 \[hep-ph\]](#).
- [140] T. Gleisberg, S. Hoeche, F. Krauss, M. Schonherr, S. Schumann, F. Siegert, and J. Winter, *Event generation with SHERPA 1.1*, JHEP **02** (2009) 007, [arXiv:0811.4622 \[hep-ph\]](#).
- [141] A. Kanaki and C. G. Papadopoulos, *HELAC: A Package to compute electroweak helicity amplitudes*, Comput. Phys. Commun. **132** (2000) 306–315, [arXiv:hep-ph/0002082 \[hep-ph\]](#).
- [142] C. G. Papadopoulos, *PHEGAS: A Phase space generator for automatic cross-section computation*, Comput. Phys. Commun. **137** (2001) 247–254, [arXiv:hep-ph/0007335 \[hep-ph\]](#).
- [143] A. Cafarella, C. G. Papadopoulos, and M. Worek, *Helac-Phegas: A Generator for all parton level processes*, Comput. Phys. Commun. **180** (2009) 1941–1955, [arXiv:0710.2427 \[hep-ph\]](#).
- [144] C. Berger, Z. Bern, L. Dixon, F. Febres Cordero, D. Forde, et al., *An Automated Implementation of On-Shell Methods for One-Loop Amplitudes*, Phys.Rev. **D78** (2008) 036003, [arXiv:0803.4180 \[hep-ph\]](#).
- [145] K. Arnold et al., *VBFNLO: A Parton level Monte Carlo for processes with electroweak bosons*, Comput. Phys. Commun. **180** (2009) 1661–1670, [arXiv:0811.4559 \[hep-ph\]](#).
- [146] K. Arnold et al., *VBFNLO: A Parton Level Monte Carlo for Processes with Electroweak Bosons – Manual for Version 2.5.0*, [arXiv:1107.4038 \[hep-ph\]](#).
- [147] J. Baglio et al., *Release Note - VBFNLO 2.7.0*, [arXiv:1404.3940 \[hep-ph\]](#).
- [148] P. Nason, *A New method for combining NLO QCD with shower Monte Carlo algorithms*, JHEP **11** (2004) 040, [arXiv:hep-ph/0409146 \[hep-ph\]](#).
- [149] S. Frixione, P. Nason, and C. Oleari, *Matching NLO QCD computations with Parton Shower simulations: the POWHEG method*, JHEP **11** (2007) 070, [arXiv:0709.2092 \[hep-ph\]](#).
- [150] A. Alloul, N. D. Christensen, C. Degrande, C. Duhr, and B. Fuks, *FeynRules 2.0 - A complete toolbox for tree-level phenomenology*, Comput. Phys. Commun. **185** (2014) 2250–2300, [arXiv:1310.1921 \[hep-ph\]](#).
- [151] J. Alwall et al., *A Standard format for Les Houches event files*, Comput. Phys. Commun. **176** (2007) 300–304, [arXiv:hep-ph/0609017 \[hep-ph\]](#).
- [152] J. M. Butterworth et al., *THE TOOLS AND MONTE CARLO WORKING GROUP Summary Report from the Les Houches 2009 Workshop on TeV Colliders*, in *Physics at TeV colliders. Proceedings, 6th Workshop, dedicated to Thomas Binoth, Les Houches, France, June 8-26, 2009*. 2010. [arXiv:1003.1643 \[hep-ph\]](#).
- [153] T. Sjostrand, S. Mrenna, and P. Z. Skands, *PYTHIA 6.4 Physics and Manual*, JHEP **05** (2006) 026, [arXiv:hep-ph/0603175 \[hep-ph\]](#).
- [154] M. Bahr et al., *Herwig++ Physics and Manual*, Eur. Phys. J. **C58** (2008) 639–707, [arXiv:0803.0883 \[hep-ph\]](#).
- [155] M. Bahr, S. Gieseke, M. Gigg, D. Grellscheid, K. Hamilton, S. Platzer, P. Richardson, M. H. Seymour, and J. Tully, *Herwig++ 2.3 Release Note*, [arXiv:0812.0529 \[hep-ph\]](#).
- [156] M. Bahr et al., *Herwig++ 2.2 Release Note*, [arXiv:0804.3053 \[hep-ph\]](#).

- [157] J. Bellm et al., *Herwig 7.0/Herwig++ 3.0 Release Note*, Eur. Phys. J. **C76** (2016) 196, arXiv:1512.01178 [hep-ph].
- [158] J. Bellm et al., *Herwig 7.1 Release Note*, arXiv:1705.06919 [hep-ph].
- [159] S. Gieseke et al., *Herwig++ 2.5 Release Note*, arXiv:1102.1672 [hep-ph].
- [160] K. Arnold et al., *Herwig++ 2.6 Release Note*, arXiv:1205.4902 [hep-ph].
- [161] J. Bellm et al., *Herwig++ 2.7 Release Note*, arXiv:1310.6877 [hep-ph].
- [162] DELPHES 3 Collaboration, J. de Favereau, C. Delaere, P. Demin, A. Giammanco, V. Lemaitre, A. Mertens, and M. Selvaggi, *DELPHES 3, A modular framework for fast simulation of a generic collider experiment*, JHEP **02** (2014) 057, arXiv:1307.6346 [hep-ex].
- [163] J. Allison et al., *Geant4 developments and applications*, IEEE Trans. Nucl. Sci. **53** (2006) 270.
- [164] J. Allison et al., *Recent developments in GEANT4*, Nucl. Instrum. Meth. **A835** (2016) 186–225.
- [165] C. Englert, A. Freitas, M. M. Mühlleitner, T. Plehn, M. Rauch, M. Spira, and K. Walz, *Precision Measurements of Higgs Couplings: Implications for New Physics Scales*, J. Phys. **G41** (2014) 113001, arXiv:1403.7191 [hep-ph].
- [166] J. R. Ellis, M. K. Gaillard, and D. V. Nanopoulos, *A Phenomenological Profile of the Higgs Boson*, Nucl. Phys. **B106** (1976) 292.
- [167] M. A. Shifman, A. I. Vainshtein, M. B. Voloshin, and V. I. Zakharov, *Low-Energy Theorems for Higgs Boson Couplings to Photons*, Sov. J. Nucl. Phys. **30** (1979) 711–716. [Yad. Fiz.30,1368(1979)].
- [168] C. Grojean, E. Salvioni, M. Schlaffer, and A. Weiler, *Very boosted Higgs in gluon fusion*, JHEP **05** (2014) 022, arXiv:1312.3317 [hep-ph].
- [169] A. Banfi, A. Martin, and V. Sanz, *Probing top-partners in Higgs+jets*, JHEP **08** (2014) 053, arXiv:1308.4771 [hep-ph].
- [170] R. V. Harlander and T. Neumann, *Probing the nature of the Higgs-gluon coupling*, Phys. Rev. **D88** (2013) 074015, arXiv:1308.2225 [hep-ph].
- [171] A. Azatov and A. Paul, *Probing Higgs couplings with high p_T Higgs production*, JHEP **01** (2014) 014, arXiv:1309.5273 [hep-ph].
- [172] S. Dawson, I. M. Lewis, and M. Zeng, *Effective field theory for Higgs boson plus jet production*, Phys. Rev. **D90** (2014) 093007, arXiv:1409.6299 [hep-ph].
- [173] U. Langenegger, M. Spira, and I. Strebel, *Testing the Higgs Boson Coupling to Gluons*, arXiv:1507.01373 [hep-ph].
- [174] M. Grazzini, A. Ilnicka, M. Spira, and M. Wiesemann, *Modeling BSM effects on the Higgs transverse-momentum spectrum in an EFT approach*, JHEP **03** (2017) 115, arXiv:1612.00283 [hep-ph].
- [175] N. Deutschmann, C. Duhr, F. Maltoni, and E. Vryonidou, *Gluon-fusion Higgs production in the Standard Model Effective Field Theory*, arXiv:1708.00460 [hep-ph].
- [176] R. K. Ellis, I. Hinchliffe, M. Soldate, and J. J. van der Bij, *Higgs Decay to $\tau^+ \tau^-$: A Possible Signature of Intermediate Mass Higgs Bosons at the SSC*, Nucl. Phys. **B297** (1988) 221–243.
- [177] U. Baur and E. W. N. Glover, *Higgs Boson Production at Large Transverse Momentum in Hadronic Collisions*, Nucl. Phys. **B339** (1990) 38–66.
- [178] D. Graudenz, M. Spira, and P. M. Zerwas, *QCD corrections to Higgs boson production at proton proton colliders*, Phys. Rev. Lett. **70** (1993) 1372–1375.
- [179] R. Harlander and P. Kant, *Higgs production and decay: Analytic results at*

- next-to-leading order QCD*, JHEP **12** (2005) 015, arXiv:hep-ph/0509189 [hep-ph].
- [180] R. Bonciani, V. Del Duca, H. Frellesvig, J. M. Henn, F. Moriello, and V. A. Smirnov, *Two-loop planar master integrals for Higgs \rightarrow 3 partons with full heavy-quark mass dependence*, JHEP **12** (2016) 096, arXiv:1609.06685 [hep-ph].
- [181] R. V. Harlander, T. Neumann, K. J. Ozeren, and M. Wiesemann, *Top-mass effects in differential Higgs production through gluon fusion at order α_s^4* , JHEP **08** (2012) 139, arXiv:1206.0157 [hep-ph].
- [182] T. Neumann and M. Wiesemann, *Finite top-mass effects in gluon-induced Higgs production with a jet-veto at NNLO*, JHEP **11** (2014) 150, arXiv:1408.6836 [hep-ph].
- [183] T. Neumann and C. Williams, *The Higgs boson at high p_T* , Phys. Rev. **D95** (2017) 014004, arXiv:1609.00367 [hep-ph].
- [184] C. R. Schmidt, *$H \rightarrow g g g$ ($g q$ anti- q) at two loops in the large M_t limit*, Phys. Lett. **B413** (1997) 391–395, arXiv:hep-ph/9707448 [hep-ph].
- [185] D. de Florian, M. Grazzini, and Z. Kunszt, *Higgs production with large transverse momentum in hadronic collisions at next-to-leading order*, Phys. Rev. Lett. **82** (1999) 5209–5212, arXiv:hep-ph/9902483 [hep-ph].
- [186] C. J. Glosser and C. R. Schmidt, *Next-to-leading corrections to the Higgs boson transverse momentum spectrum in gluon fusion*, JHEP **12** (2002) 016, arXiv:hep-ph/0209248 [hep-ph].
- [187] V. Ravindran, J. Smith, and W. L. Van Neerven, *Next-to-leading order QCD corrections to differential distributions of Higgs boson production in hadron hadron collisions*, Nucl. Phys. **B634** (2002) 247–290, arXiv:hep-ph/0201114 [hep-ph].
- [188] R. Boughezal, F. Caola, K. Melnikov, F. Petriello, and M. Schulze, *Higgs boson production in association with a jet at next-to-next-to-leading order in perturbative QCD*, JHEP **06** (2013) 072, arXiv:1302.6216 [hep-ph].
- [189] X. Chen, T. Gehrmann, E. W. N. Glover, and M. Jaquier, *Precise QCD predictions for the production of Higgs + jet final states*, Phys. Lett. **B740** (2015) 147–150, arXiv:1408.5325 [hep-ph].
- [190] R. Boughezal, F. Caola, K. Melnikov, F. Petriello, and M. Schulze, *Higgs boson production in association with a jet at next-to-next-to-leading order*, Phys. Rev. Lett. **115** (2015) 082003, arXiv:1504.07922 [hep-ph].
- [191] R. Boughezal, C. Focke, W. Giele, X. Liu, and F. Petriello, *Higgs boson production in association with a jet at NNLO using jetiness subtraction*, Phys. Lett. **B748** (2015) 5–8, arXiv:1505.03893 [hep-ph].
- [192] F. Caola, K. Melnikov, and M. Schulze, *Fiducial cross sections for Higgs boson production in association with a jet at next-to-next-to-leading order in QCD*, Phys. Rev. **D92** (2015) 074032, arXiv:1508.02684 [hep-ph].
- [193] X. Chen, J. Cruz-Martinez, T. Gehrmann, E. W. N. Glover, and M. Jaquier, *NNLO QCD corrections to Higgs boson production at large transverse momentum*, JHEP **10** (2016) 066, arXiv:1607.08817 [hep-ph].
- [194] A. Banfi, S. Redford, M. Vesterinen, P. Waller, and T. R. Wyatt, *Optimisation of variables for studying dilepton transverse momentum distributions at hadron colliders*, Eur. Phys. J. **C71** (2011) 1600, arXiv:1009.1580 [hep-ex].
- [195] M. Carena, S. Heinemeyer, O. Stål, C. E. M. Wagner, and G. Weiglein, *MSSM Higgs Boson Searches at the LHC: Benchmark Scenarios after the Discovery of a Higgs-like Particle*, Eur. Phys. J. **C73** (2013) 2552, arXiv:1302.7033 [hep-ph].
- [196] J. Butterworth et al., *PDF4LHC recommendations for LHC Run II*, J. Phys. **G43**

- (2016) 023001, [arXiv:1510.03865](#) [hep-ph].
- [197] A. Gehrmann-De Ridder, T. Gehrmann, E. W. N. Glover, A. Huss, and T. A. Morgan, *NNLO QCD corrections for Drell-Yan p_T^Z and ϕ^* observables at the LHC*, JHEP **11** (2016) 094, [arXiv:1610.01843](#) [hep-ph].
- [198] ATLAS Collaboration, G. Aad et al., *Measurement of the transverse momentum and ϕ_η^* distributions of Drell-Yan lepton pairs in proton-proton collisions at $\sqrt{s} = 8$ TeV with the ATLAS detector*, Eur. Phys. J. **C76** (2016) 291, [arXiv:1512.02192](#) [hep-ex].
- [199] G. Bozzi, S. Catani, D. de Florian, and M. Grazzini, *Transverse-momentum resummation and the spectrum of the Higgs boson at the LHC*, Nucl. Phys. **B737** (2006) 73–120, [arXiv:hep-ph/0508068](#) [hep-ph].
- [200] A. Banfi, M. Dasgupta, and R. M. Duran Delgado, *The $a(T)$ distribution of the Z boson at hadron colliders*, JHEP **12** (2009) 022, [arXiv:0909.5327](#) [hep-ph].
- [201] T. Sjostrand, S. Mrenna, and P. Z. Skands, *A Brief Introduction to PYTHIA 8.1*, Comput. Phys. Commun. **178** (2008) 852–867, [arXiv:0710.3820](#) [hep-ph].
- [202] P. Skands, S. Carrazza, and J. Rojo, *Tuning PYTHIA 8.1: the Monash 2013 Tune*, Eur. Phys. J. **C74** (2014) 3024, [arXiv:1404.5630](#) [hep-ph].
- [203] M. Selvaggi, *DELPHES 3: A modular framework for fast-simulation of generic collider experiments*, J. Phys. Conf. Ser. **523** (2014) 012033.
- [204] CMS Collaboration, *Measurement of differential fiducial cross sections for Higgs boson production in the diphoton decay channel in pp collisions at $\sqrt{s} = 13$ TeV*, Tech. Rep. CMS-PAS-HIG-17-015, CERN, Geneva, 2017. <https://cds.cern.ch/record/2257530>.
- [205] CMS Collaboration, *Particle-Flow Event Reconstruction in CMS and Performance for Jets, Taus, and MET*, Tech. Rep. CMS-PAS-PFT-09-001, CERN, Geneva, 2009. <https://cds.cern.ch/record/1194487>.
- [206] S. Höche, *Introduction to parton-shower event generators*, in *Theoretical Advanced Study Institute in Elementary Particle Physics: Journeys Through the Precision Frontier: Amplitudes for Colliders (TASI 2014) Boulder, Colorado, June 2-27, 2014*. 2014. [arXiv:1411.4085](#) [hep-ph].
- [207] B. R. Webber, *Monte Carlo Simulation of Hard Hadronic Processes*, Ann. Rev. Nucl. Part. Sci. **36** (1986) 253–286.
- [208] S. Schumann and F. Krauss, *A Parton shower algorithm based on Catani-Seymour dipole factorisation*, JHEP **03** (2008) 038, [arXiv:0709.1027](#) [hep-ph].
- [209] S. Catani, F. Krauss, R. Kuhn, and B. R. Webber, *QCD matrix elements + parton showers*, JHEP **11** (2001) 063, [arXiv:hep-ph/0109231](#) [hep-ph].
- [210] S. Catani, B. R. Webber, and G. Marchesini, *QCD coherent branching and semiinclusive processes at large x* , Nucl. Phys. **B349** (1991) 635–654.
- [211] R. K. Ellis, H. Georgi, M. Machacek, H. D. Politzer, and G. G. Ross, *Factorization and the Parton Model in QCD*, Phys. Lett. **B78** (1978) 281–284.
- [212] D. Amati, R. Petronzio, and G. Veneziano, *Relating Hard QCD Processes Through Universality of Mass Singularities. 2.*, Nucl. Phys. **B146** (1978) 29–49.
- [213] T. Gehrmann, M. Jaquier, E. W. N. Glover, and A. Koukoutsakis, *Two-Loop QCD Corrections to the Helicity Amplitudes for $H \rightarrow 3$ partons*, JHEP **02** (2012) 056, [arXiv:1112.3554](#) [hep-ph].
- [214] Z. Xu, D.-H. Zhang, and L. Chang, *Helicity Amplitudes for Multiple Bremsstrahlung in Massless Nonabelian Gauge Theories*, Nucl. Phys. **B291** (1987) 392–428.
- [215] F. A. Berends, R. Kleiss, and S. Jadach, *Radiative Corrections to Muon Pair and Quark Pair Production in electron-Positron Collisions in the $Z(0)$ Region*, Nucl. Phys. **B202**

- (1982) 63–88.
- [216] CALKUL Collaboration, F. A. Berends, R. Kleiss, P. de Causmaecker, R. Gastmans, W. Troost, and T. T. Wu, *Multiple Bremsstrahlung in Gauge Theories at High-energies. 3. Finite Mass Effects in Collinear Photon Bremsstrahlung*, Nucl. Phys. **B239** (1984) 382–394.
 - [217] CALKUL Collaboration, F. A. Berends, R. Kleiss, P. de Causmaecker, R. Gastmans, W. Troost, and T. T. Wu, *Multiple Bremsstrahlung in Gauge Theories at High-Energies. 4. The Process $e^+e^- \rightarrow \gamma\gamma\gamma\gamma$* , Nucl. Phys. **B239** (1984) 395–409.
 - [218] L. J. Dixon, *Calculating scattering amplitudes efficiently, in QCD and beyond. Proceedings, Theoretical Advanced Study Institute in Elementary Particle Physics, TASI-95, Boulder, USA, June 4-30, 1995*. 1996. arXiv:hep-ph/9601359 [hep-ph].
 - [219] P. Nogueira, *Automatic Feynman graph generation*, J. Comput. Phys. **105** (1993) 279–289.
 - [220] T. Hahn and M. Perez-Victoria, *Automatized one loop calculations in four-dimensions and D-dimensions*, Comput. Phys. Commun. **118** (1999) 153–165, arXiv:hep-ph/9807565 [hep-ph].
 - [221] T. Hahn, *Generating Feynman diagrams and amplitudes with FeynArts 3*, Comput. Phys. Commun. **140** (2001) 418–431, arXiv:hep-ph/0012260 [hep-ph].
 - [222] V. Shtabovenko, R. Mertig, and F. Orellana, *New Developments in FeynCalc 9.0*, Comput. Phys. Commun. **207** (2016) 432–444, arXiv:1601.01167 [hep-ph].
 - [223] J. A. M. Vermaseren, *New features of FORM*, arXiv:math-ph/0010025 [math-ph].
 - [224] A. G. Grozin, *Integration by parts: An Introduction*, Int. J. Mod. Phys. **A26** (2011) 2807–2854, arXiv:1104.3993 [hep-ph].
 - [225] R. N. Lee, *Group structure of the integration-by-part identities and its application to the reduction of multiloop integrals*, JHEP **07** (2008) 031, arXiv:0804.3008 [hep-ph].
 - [226] S. Laporta, *High precision calculation of multiloop Feynman integrals by difference equations*, Int. J. Mod. Phys. **A15** (2000) 5087–5159, arXiv:hep-ph/0102033 [hep-ph].
 - [227] C. Anastasiou and A. Lazopoulos, *Automatic integral reduction for higher order perturbative calculations*, JHEP **07** (2004) 046, arXiv:hep-ph/0404258 [hep-ph].
 - [228] A. Smirnov, *Algorithm FIRE – Feynman Integral REduction*, JHEP **0810** (2008) 107, arXiv:0807.3243 [hep-ph].
 - [229] A. von Manteuffel and C. Studerus, *Reduze 2 - Distributed Feynman Integral Reduction*, arXiv:1201.4330 [hep-ph].
 - [230] R. N. Lee, *Presenting LiteRed: a tool for the Loop InTEgrals REDuction*, arXiv:1212.2685 [hep-ph].
 - [231] A. V. Smirnov, *FIRE5: a C++ implementation of Feynman Integral REDuction*, Comput. Phys. Commun. **189** (2015) 182–191, arXiv:1408.2372 [hep-ph].
 - [232] P. Maierhoefer, J. Usovitsch, and P. Uwer, *Kira - A Feynman Integral Reduction Program*, arXiv:1705.05610 [hep-ph].
 - [233] J. Gluza, K. Kajda, and D. A. Kosower, *Towards a Basis for Planar Two-Loop Integrals*, Phys. Rev. **D83** (2011) 045012, arXiv:1009.0472 [hep-th].
 - [234] H. Ita, *Two-loop Integrand Decomposition into Master Integrals and Surface Terms*, Phys. Rev. **D94** (2016) 116015, arXiv:1510.05626 [hep-th].
 - [235] K. J. Larsen and Y. Zhang, *Integration-by-parts reductions from unitarity cuts and algebraic geometry*, Phys. Rev. **D93** (2016) 041701, arXiv:1511.01071 [hep-th].
 - [236] S. Caron-Huot and K. J. Larsen, *Uniqueness of two-loop master contours*, JHEP **1210** (2012) 026, arXiv:1205.0801 [hep-ph].

- [237] M. Søgaard and Y. Zhang, *Multivariate Residues and Maximal Unitarity*, JHEP **1312** (2013) 008, [arXiv:1310.6006 \[hep-th\]](#).
- [238] S. Borowka, G. Heinrich, S. P. Jones, M. Kerner, J. Schlenk, and T. Zirke, *SecDec-3.0: numerical evaluation of multi-scale integrals beyond one loop*, Comput. Phys. Commun. **196** (2015) 470–491, [arXiv:1502.06595 \[hep-ph\]](#).
- [239] A. Kotikov, *Differential equations method. New technique for massive Feynman diagram calculation*, Physics Letters B **254** (1991) 158 – 164.
<http://www.sciencedirect.com/science/article/pii/037026939190413K>.
- [240] E. Remiddi, *Differential equations for Feynman graph amplitudes*, Nuovo Cim. **A110** (1997) 1435–1452, [arXiv:hep-th/9711188 \[hep-th\]](#).
- [241] T. Gehrmann and E. Remiddi, *Differential equations for two loop four point functions*, Nucl.Phys. **B580** (2000) 485–518, [arXiv:hep-ph/9912329 \[hep-ph\]](#).
- [242] T. Gehrmann and E. Remiddi, *Using differential equations to compute two loop box integrals*, Nucl. Phys. Proc. Suppl. **89** (2000) 251–255, [arXiv:hep-ph/0005232 \[hep-ph\]](#).
- [243] M. Beneke and V. A. Smirnov, *Asymptotic expansion of Feynman integrals near threshold*, Nucl. Phys. **B522** (1998) 321–344, [arXiv:hep-ph/9711391 \[hep-ph\]](#).
- [244] V. A. Smirnov and E. R. Rakhmetov, *The Strategy of regions for asymptotic expansion of two loop vertex Feynman diagrams*, Theor. Math. Phys. **120** (1999) 870–875, [arXiv:hep-ph/9812529 \[hep-ph\]](#). [Teor. Mat. Fiz.120,64(1999)].
- [245] V. A. Smirnov, *Problems of the strategy of regions*, Phys. Lett. **B465** (1999) 226–234, [arXiv:hep-ph/9907471 \[hep-ph\]](#).
- [246] E. Bagnaschi and A. Vicini, *The Higgs transverse momentum distribution in gluon fusion as a multiscale problem*, JHEP **01** (2016) 056, [arXiv:1505.00735 \[hep-ph\]](#).
- [247] F. Caola, S. Forte, S. Marzani, C. Muselli, and G. Vita, *The Higgs transverse momentum spectrum with finite quark masses beyond leading order*, JHEP **08** (2016) 150, [arXiv:1606.04100 \[hep-ph\]](#).
- [248] K. G. Chetyrkin, J. H. Kuhn, and C. Sturm, *QCD decoupling at four loops*, Nucl. Phys. **B744** (2006) 121–135, [arXiv:hep-ph/0512060 \[hep-ph\]](#).
- [249] K. Chetyrkin, P. Baikov, and J. Kühn, *The β -function of Quantum Chromodynamics and the effective Higgs-gluon-gluon coupling in five-loop order*, PoS **LL2016** (2016) 010.
- [250] M. Cacciari and N. Houdeau, *Meaningful characterisation of perturbative theoretical uncertainties*, JHEP **09** (2011) 039, [arXiv:1105.5152 \[hep-ph\]](#).
- [251] A. David and G. Passarino, *How well can we guess theoretical uncertainties?*, Phys. Lett. **B726** (2013) 266–272, [arXiv:1307.1843 \[hep-ph\]](#).
- [252] M. Peskin and D. Schroeder, *An Introduction To Quantum Field Theory*. Frontiers in Physics. Avalon Publishing, 1995.
- [253] S. Buehler and A. Lazopoulos, *Scale dependence and collinear subtraction terms for Higgs production in gluon fusion at N³LO*, JHEP **10** (2013) 096, [arXiv:1306.2223 \[hep-ph\]](#).
- [254] J. Currie, E. W. N. Glover, A. Gehrmann-De Ridder, T. Gehrmann, A. Huss, and J. Pires, *Single jet inclusive production for the individual jet p_T scale choice at the LHC*, in *23rd Cracow Epiphany Conference on Particle Theory Meets the First Data from LHC Run 2 Cracow, Poland, January 9-12, 2017*. 2017. [arXiv:1704.00923 \[hep-ph\]](#).
- [255] N. Greiner, S. Hoeche, G. Luisoni, M. Schonherr, J.-C. Winter, and V. Yundin, *Higgs + Multi-jets in Gluon Fusion*, in *Proceedings, 12th International Symposium on Radiative Corrections (Radcor 2015) and LoopFest XIV (Radiative Corrections for the LHC and Future Colliders): Los Angeles, CA, USA, June 15-19, 2015*, vol. RADCOR2015, p. 009.

2016. [arXiv:1601.03722](#) [[hep-ph](#)].
- [256] Particle Data Group Collaboration, C. Patrignani et al., *Review of Particle Physics*, *Chin. Phys.* **C40** (2016) 100001.
- [257] T. Schmidt and M. Spira, *Higgs Boson Production via Gluon Fusion: Soft-Gluon Resummation including Mass Effects*, *Phys. Rev.* **D93** (2016) 014022, [arXiv:1509.00195](#) [[hep-ph](#)].
- [258] S. Forte, *Parton distributions at the dawn of the LHC*, *Acta Phys. Polon.* **B41** (2010) 2859–2920, [arXiv:1011.5247](#) [[hep-ph](#)].
- [259] NNPDF Collaboration, R. D. Ball, V. Bertone, M. Bonvini, S. Carrazza, S. Forte, A. Guffanti, N. P. Hartland, J. Rojo, and L. Rottoli, *A Determination of the Charm Content of the Proton*, *Eur. Phys. J.* **C76** (2016) 647, [arXiv:1605.06515](#) [[hep-ph](#)].
- [260] T. Neumann and C. Williams, *The Higgs boson at high p_T* , *Phys. Rev.* **D95** (2017) 014004, [arXiv:1609.00367](#) [[hep-ph](#)].
- [261] K. Melnikov, L. Tancredi, and C. Wever, *Two-loop $gg \rightarrow Hg$ amplitude mediated by a nearly massless quark*, *JHEP* **11** (2016) 104, [arXiv:1610.03747](#) [[hep-ph](#)].
- [262] M. Spira, A. Djouadi, D. Graudenz, and P. M. Zerwas, *Higgs boson production at the LHC*, *Nucl. Phys.* **B453** (1995) 17–82, [arXiv:hep-ph/9504378](#) [[hep-ph](#)].
- [263] U. Aglietti, R. Bonciani, G. Degrossi, and A. Vicini, *Analytic Results for Virtual QCD Corrections to Higgs Production and Decay*, *JHEP* **01** (2007) 021, [arXiv:hep-ph/0611266](#) [[hep-ph](#)].
- [264] C. Anastasiou, S. Bucherer, and Z. Kunszt, *HPro: A NLO Monte-Carlo for Higgs production via gluon fusion with finite heavy quark masses*, *JHEP* **10** (2009) 068, [arXiv:0907.2362](#) [[hep-ph](#)].
- [265] S. Dawson, I. M. Lewis, and M. Zeng, *Usefulness of effective field theory for boosted Higgs production*, *Phys. Rev.* **D91** (2015) 074012, [arXiv:1501.04103](#) [[hep-ph](#)].
- [266] N. Greiner, S. Höche, G. Luisoni, M. Schönherr, and J.-C. Winter, *Full mass dependence in Higgs boson production in association with jets at the LHC and FCC*, *JHEP* **01** (2017) 091, [arXiv:1608.01195](#) [[hep-ph](#)].
- [267] T. Gehrmann and E. Remiddi, *Two loop master integrals for $\gamma^* \rightarrow 3$ jets: The Planar topologies*, *Nucl. Phys.* **B601** (2001) 248–286, [arXiv:hep-ph/0008287](#) [[hep-ph](#)].
- [268] T. Gehrmann and E. Remiddi, *Two loop master integrals for $\gamma^* \rightarrow 3$ jets: The Nonplanar topologies*, *Nucl. Phys.* **B601** (2001) 287–317, [arXiv:hep-ph/0101124](#) [[hep-ph](#)].
- [269] T. Gehrmann and E. Remiddi, *Analytic continuation of massless two loop four point functions*, *Nucl. Phys.* **B640** (2002) 379–411, [arXiv:hep-ph/0207020](#) [[hep-ph](#)].
- [270] T. Gehrmann and E. Remiddi, *Numerical evaluation of harmonic polylogarithms*, *Comput. Phys. Commun.* **141** (2001) 296–312, [arXiv:hep-ph/0107173](#) [[hep-ph](#)].
- [271] T. Gehrmann and E. Remiddi, *Numerical evaluation of two-dimensional harmonic polylogarithms*, *Comput. Phys. Commun.* **144** (2002) 200–223, [arXiv:hep-ph/0111255](#) [[hep-ph](#)].
- [272] E. W. N. Glover, P. Mastrolia, and C. Williams, *One-loop ϕ -MHV amplitudes using the unitarity bootstrap: The General helicity case*, *JHEP* **08** (2008) 017, [arXiv:0804.4149](#) [[hep-ph](#)].
- [273] S. Badger, E. W. Nigel Glover, P. Mastrolia, and C. Williams, *One-loop Higgs plus four gluon amplitudes: Full analytic results*, *JHEP* **01** (2010) 036, [arXiv:0909.4475](#) [[hep-ph](#)].
- [274] S. Badger, J. M. Campbell, R. K. Ellis, and C. Williams, *Analytic results for the*

- one-loop NMHV Hqgg amplitude*, JHEP **12** (2009) 035, arXiv:0910.4481 [hep-ph].
- [275] A. Gehrmann-De Ridder, T. Gehrmann, and E. W. N. Glover, *Antenna subtraction at NNLO*, JHEP **09** (2005) 056, arXiv:hep-ph/0505111 [hep-ph].
- [276] A. Gehrmann-De Ridder, T. Gehrmann, and E. W. N. Glover, *Infrared structure of $e^+e^- \rightarrow 2$ jets at NNLO*, Nucl. Phys. **B691** (2004) 195–222, arXiv:hep-ph/0403057 [hep-ph].
- [277] A. Gehrmann-De Ridder, T. Gehrmann, and E. W. N. Glover, *Gluon-gluon antenna functions from Higgs boson decay*, Phys. Lett. **B612** (2005) 49–60, arXiv:hep-ph/0502110 [hep-ph].
- [278] A. Gehrmann-De Ridder, T. Gehrmann, and E. W. N. Glover, *Quark-gluon antenna functions from neutralino decay*, Phys. Lett. **B612** (2005) 36–48, arXiv:hep-ph/0501291 [hep-ph].
- [279] A. Gehrmann-De Ridder, T. Gehrmann, E. W. N. Glover, and G. Heinrich, *Infrared structure of $e^+e^- \rightarrow 3$ jets at NNLO*, JHEP **11** (2007) 058, arXiv:0710.0346 [hep-ph].
- [280] A. Daleo, T. Gehrmann, and D. Maitre, *Antenna subtraction with hadronic initial states*, JHEP **04** (2007) 016, arXiv:hep-ph/0612257 [hep-ph].
- [281] A. Daleo, A. Gehrmann-De Ridder, T. Gehrmann, and G. Luisoni, *Antenna subtraction at NNLO with hadronic initial states: initial-final configurations*, JHEP **01** (2010) 118, arXiv:0912.0374 [hep-ph].
- [282] T. Gehrmann and P. F. Monni, *Antenna subtraction at NNLO with hadronic initial states: real-virtual initial-initial configurations*, JHEP **12** (2011) 049, arXiv:1107.4037 [hep-ph].
- [283] R. Boughezal, A. Gehrmann-De Ridder, and M. Ritzmann, *Antenna subtraction at NNLO with hadronic initial states: double real radiation for initial-initial configurations with two quark flavours*, JHEP **02** (2011) 098, arXiv:1011.6631 [hep-ph].
- [284] A. Gehrmann-De Ridder, T. Gehrmann, and M. Ritzmann, *Antenna subtraction at NNLO with hadronic initial states: double real initial-initial configurations*, JHEP **10** (2012) 047, arXiv:1207.5779 [hep-ph].
- [285] J. Currie, E. W. N. Glover, and S. Wells, *Infrared Structure at NNLO Using Antenna Subtraction*, JHEP **04** (2013) 066, arXiv:1301.4693 [hep-ph].
- [286] H. E. Haber and G. L. Kane, *Implications of a Higgs Interpretation of the Zeta (8.3)*, Nucl. Phys. **B250** (1985) 716–728.
- [287] R. V. Harlander, S. Liebler, and H. Mantler, *SusHi: A program for the calculation of Higgs production in gluon fusion and bottom-quark annihilation in the Standard Model and the MSSM*, Comput. Phys. Commun. **184** (2013) 1605–1617, arXiv:1212.3249 [hep-ph].
- [288] M. Schlaffer, M. Spannowsky, M. Takeuchi, A. Weiler, and C. Wymant, *Boosted Higgs Shapes*, Eur. Phys. J. **C74** (2014) 3120, arXiv:1405.4295 [hep-ph].
- [289] R. V. Harlander, S. Liebler, and H. Mantler, *SusHi Bento: Beyond NNLO and the heavy-top limit*, Comput. Phys. Commun. **212** (2017) 239–257, arXiv:1605.03190 [hep-ph].
- [290] S. Dawson, A. Djouadi, and M. Spira, *QCD corrections to SUSY Higgs production: The Role of squark loops*, Phys. Rev. Lett. **77** (1996) 16–19, arXiv:hep-ph/9603423 [hep-ph].
- [291] R. Dermisek and I. Low, *Probing the Stop Sector and the Sanity of the MSSM with the Higgs Boson at the LHC*, Phys. Rev. **D77** (2008) 035012, arXiv:hep-ph/0701235 [HEP-PH].

- [292] H. E. Haber, *Challenges for nonminimal Higgs searches at future colliders*, in *Perspectives for electroweak interactions in e^+e^- collisions. Proceedings, Ringberg Workshop, Tegernsee, Germany, February 5-8, 1995*, pp. 219–232. 1995. [arXiv:hep-ph/9505240](#) [hep-ph].
- [293] A. Djouadi, V. Driesen, W. Hollik, and J. I. Illana, *The Coupling of the lightest SUSY Higgs boson to two photons in the decoupling regime*, *Eur. Phys. J.* **C1** (1998) 149–162, [arXiv:hep-ph/9612362](#) [hep-ph].
- [294] A. Djouadi, *The Anatomy of electro-weak symmetry breaking. II. The Higgs bosons in the minimal supersymmetric model*, *Phys. Rept.* **459** (2008) 1–241, [arXiv:hep-ph/0503173](#) [hep-ph].
- [295] T. Gehrmann, A. von Manteuffel, L. Tancredi, and E. Weihs, *The two-loop master integrals for $q\bar{q} \rightarrow VV$* , *JHEP* **06** (2014) 032, [arXiv:1404.4853](#) [hep-ph].
- [296] J. M. Henn, *Multiloop integrals in dimensional regularization made simple*, *Phys.Rev.Lett.* **110** (2013) 251601, [arXiv:1304.1806](#) [hep-th].
- [297] M. Argeri, S. Di Vita, P. Mastrolia, E. Mirabella, J. Schlenk, U. Schubert, and L. Tancredi, *Magnus and Dyson Series for Master Integrals*, *JHEP* **03** (2014) 082, [arXiv:1401.2979](#) [hep-ph].
- [298] R. N. Lee, *Reducing differential equations for multiloop master integrals*, *JHEP* **04** (2015) 108, [arXiv:1411.0911](#) [hep-ph].
- [299] C. Meyer, *Transforming differential equations of multi-loop Feynman integrals into canonical form*, *JHEP* **04** (2017) 006, [arXiv:1611.01087](#) [hep-ph].
- [300] A. B. Goncharov, M. Spradlin, C. Vergu, and A. Volovich, *Classical Polylogarithms for Amplitudes and Wilson Loops*, *Phys. Rev. Lett.* **105** (2010) 151605, [arXiv:1006.5703](#) [hep-th].
- [301] C. Duhr, H. Gangl, and J. R. Rhodes, *From polygons and symbols to polylogarithmic functions*, *JHEP* **10** (2012) 075, [arXiv:1110.0458](#) [math-ph].
- [302] R. E. Cutkosky, *Singularities and discontinuities of Feynman amplitudes*, *J. Math. Phys.* **1** (1960) 249.
- [303] R. Britto, F. Cachazo, and B. Feng, *Generalized unitarity and one-loop amplitudes in $N=4$ super-Yang-Mills*, *Nucl. Phys.* **B725** (2005) 275–305, [arXiv:hep-th/0412103](#) [hep-th].
- [304] G. Ossola, C. G. Papadopoulos, and R. Pittau, *Reducing full one-loop amplitudes to scalar integrals at the integrand level*, *Nucl.Phys.* **B763** (2007) 147–169, [arXiv:hep-ph/0609007](#) [hep-ph].
- [305] D. Forde, *Direct extraction of one-loop integral coefficients*, *Phys.Rev.* **D75** (2007) 125019, [arXiv:0704.1835](#) [hep-ph].
- [306] S. Badger, *Direct Extraction Of One Loop Rational Terms*, *JHEP* **0901** (2009) 049, [arXiv:0806.4600](#) [hep-ph].
- [307] W. T. Giele, Z. Kunszt, and K. Melnikov, *Full one-loop amplitudes from tree amplitudes*, *JHEP* **0804** (2008) 049, [arXiv:0801.2237](#) [hep-ph].
- [308] G. Ossola, C. G. Papadopoulos, and R. Pittau, *CutTools: A Program implementing the OPP reduction method to compute one-loop amplitudes*, *JHEP* **0803** (2008) 042, [arXiv:0711.3596](#) [hep-ph].
- [309] R. K. Ellis, W. Giele, Z. Kunszt, K. Melnikov, and G. Zanderighi, *One-loop amplitudes for W^+ 3 jet production in hadron collisions*, *JHEP* **0901** (2009) 012, [arXiv:0810.2762](#) [hep-ph].
- [310] P. Mastrolia, G. Ossola, T. Reiter, and F. Tramontano, *Scattering AMplitudes from*

- Unitarity-based Reduction Algorithm at the Integrand-level*, JHEP **1008** (2010) 080, arXiv:1006.0710 [hep-ph].
- [311] G. Bevilacqua, M. Czakon, M. Garzelli, A. van Hameren, A. Kardos, et al., *HELAC-NLO*, Comput.Phys.Commun. **184** (2013) 986–997, arXiv:1110.1499 [hep-ph].
- [312] S. Badger, B. Biedermann, P. Uwer, and V. Yundin, *Numerical evaluation of virtual corrections to multi-jet production in massless QCD*, Comput. Phys. Commun. **184** (2013) 1981–1998, arXiv:1209.0100 [hep-ph].
- [313] P. Mastrolia and G. Ossola, *On the Integrand-Reduction Method for Two-Loop Scattering Amplitudes*, JHEP **1111** (2011) 014, arXiv:1107.6041 [hep-ph].
- [314] D. A. Kosower and K. J. Larsen, *Maximal Unitarity at Two Loops*, Phys.Rev. **D85** (2012) 045017, arXiv:1108.1180 [hep-th].
- [315] S. Badger, H. Frellesvig, and Y. Zhang, *Hepta-Cuts of Two-Loop Scattering Amplitudes*, JHEP **1204** (2012) 055, arXiv:1202.2019 [hep-ph].
- [316] S. Badger, H. Frellesvig, and Y. Zhang, *An Integrand Reconstruction Method for Three-Loop Amplitudes*, JHEP **1208** (2012) 065, arXiv:1207.2976 [hep-ph].
- [317] Y. Zhang, *Integrand-Level Reduction of Loop Amplitudes by Computational Algebraic Geometry Methods*, JHEP **1209** (2012) 042, arXiv:1205.5707 [hep-ph].
- [318] R. H. Kleiss, I. Malamos, C. G. Papadopoulos, and R. Verheyen, *Counting to One: Reducibility of One- and Two-Loop Amplitudes at the Integrand Level*, JHEP **1212** (2012) 038, arXiv:1206.4180 [hep-ph].
- [319] S. Badger, H. Frellesvig, and Y. Zhang, *A Two-Loop Five-Gluon Helicity Amplitude in QCD*, JHEP **1312** (2013) 045, arXiv:1310.1051 [hep-ph].
- [320] S. Badger, G. Mogull, A. Ochirov, and D. O’Connell, *A Complete Two-Loop, Five-Gluon Helicity Amplitude in Yang-Mills Theory*, JHEP **10** (2015) 064, arXiv:1507.08797 [hep-ph].
- [321] D. C. Dunbar and W. B. Perkins, *Two-loop five-point all plus helicity Yang-Mills amplitude*, Phys. Rev. **D93** (2016) 085029, arXiv:1603.07514 [hep-th].
- [322] S. Badger, G. Mogull, and T. Peraro, *Local integrands for two-loop all-plus Yang-Mills amplitudes*, JHEP **08** (2016) 063, arXiv:1606.02244 [hep-ph].
- [323] P. Mastrolia, E. Mirabella, G. Ossola, and T. Peraro, *Scattering Amplitudes from Multivariate Polynomial Division*, Phys.Lett. **B718** (2012) 173–177, arXiv:1205.7087 [hep-ph].
- [324] C. G. Papadopoulos, *Simplified differential equations approach for Master Integrals*, JHEP **07** (2014) 088, arXiv:1401.6057 [hep-ph].
- [325] J. M. Henn, *Lectures on differential equations for Feynman integrals*, J. Phys. **A48** (2015) 153001, arXiv:1412.2296 [hep-ph].
- [326] N. Arkani-Hamed, J. L. Bourjaily, F. Cachazo, and J. Trnka, *Local Integrals for Planar Scattering Amplitudes*, JHEP **06** (2012) 125, arXiv:1012.6032 [hep-th].
- [327] C. Meyer, *Algorithmic transformation of multi-loop master integrals to a canonical basis with CANONICA*, arXiv:1705.06252 [hep-ph].
- [328] A. Primo and L. Tancredi, *On the maximal cut of Feynman integrals and the solution of their differential equations*, Nucl. Phys. **B916** (2017) 94–116, arXiv:1610.08397 [hep-ph].
- [329] H. Frellesvig and C. G. Papadopoulos, *Cuts of Feynman Integrals in Baikov representation*, JHEP **04** (2017) 083, arXiv:1701.07356 [hep-ph].
- [330] A. Primo and L. Tancredi, *Maximal cuts and differential equations for Feynman*

- integrals. An application to the three-loop massive banana graph*, Nucl. Phys. **B921** (2017) 316–356, [arXiv:1704.05465 \[hep-ph\]](#).
- [331] A. B. Goncharov, *Multiple polylogarithms, cyclotomy and modular complexes*, Math. Res. Lett. **5** (1998) 497–516, [arXiv:1105.2076 \[math.AG\]](#).
- [332] D. J. B. Jonathan M. Borwein, David M. Bradley and P. Lisonek, *Special Values of Multiple Polylogarithms*, Trans. of the Am. Math. Soc. **353** (2001) 907–941.
- [333] J. Vollinga and S. Weinzierl, *Numerical evaluation of multiple polylogarithms*, Comput. Phys. Commun. **167** (2005) 177, [arXiv:hep-ph/0410259 \[hep-ph\]](#).
- [334] E. Panzer, *Algorithms for the symbolic integration of hyperlogarithms with applications to Feynman integrals*, Comput. Phys. Commun. **188** (2014) 148–166, [arXiv:1403.3385 \[hep-th\]](#).
- [335] H. Frellesvig, D. Tommasini, and C. Wever, *On the reduction of generalized polylogarithms to Li_n and $Li_{2,2}$ and on the evaluation thereof*, JHEP **03** (2016) 189, [arXiv:1601.02649 \[hep-ph\]](#).
- [336] S. Kirchner, *LiSK - A C++ Library for Evaluating Classical Polylogarithms and $Li_{2,2}$* , [arXiv:1605.09571 \[hep-ph\]](#).
- [337] K.-T. Chen, *Iterated path integrals*, Bull. Am. Math. Soc. **83** (1977) 831–879.
- [338] L. J. Dixon, J. M. Drummond, M. von Hippel, and J. Pennington, *Hexagon functions and the three-loop remainder function*, JHEP **12** (2013) 049, [arXiv:1308.2276 \[hep-th\]](#).
- [339] C. Duhr, *Hopf algebras, coproducts and symbols: an application to Higgs boson amplitudes*, JHEP **08** (2012) 043, [arXiv:1203.0454 \[hep-ph\]](#).
- [340] M. Caffo, H. Czyz, S. Laporta, and E. Remiddi, *The Master differential equations for the two loop sunrise selfmass amplitudes*, Nuovo Cim. **A111** (1998) 365–389, [arXiv:hep-th/9805118 \[hep-th\]](#).
- [341] S. Laporta and E. Remiddi, *Analytic treatment of the two loop equal mass sunrise graph*, Nucl.Phys. **B704** (2005) 349–386, [arXiv:hep-ph/0406160 \[hep-ph\]](#).
- [342] L. Adams, C. Bogner, and S. Weinzierl, *The two-loop sunrise graph with arbitrary masses*, J. Math. Phys. **54** (2013) 052303, [arXiv:1302.7004 \[hep-ph\]](#).
- [343] S. Bloch and P. Vanhove, *The elliptic dilogarithm for the sunset graph*, J. Number Theor. **148** (2015) 328–364, [arXiv:1309.5865 \[hep-th\]](#). [arXiv:1309.5865](#).
- [344] M. Sogaard and Y. Zhang, *Elliptic Functions and Maximal Unitarity*, Phys. Rev. **D91** (2015) 081701, [arXiv:1412.5577 \[hep-th\]](#).
- [345] L. Adams, C. Bogner, and S. Weinzierl, *The two-loop sunrise graph in two space-time dimensions with arbitrary masses in terms of elliptic dilogarithms*, J. Math. Phys. **55** (2014) 102301, [arXiv:1405.5640 \[hep-ph\]](#).
- [346] L. Adams, C. Bogner, and S. Weinzierl, *The iterated structure of the all-order result for the two-loop sunrise integral*, J. Math. Phys. **57** (2016) 032304, [arXiv:1512.05630 \[hep-ph\]](#). [arXiv:1512.05630](#).
- [347] S. Bloch, M. Kerr, and P. Vanhove, *Local mirror symmetry and the sunset Feynman integral*, [arXiv:1601.08181 \[hep-th\]](#).
- [348] J. Bosma, M. Sogaard, and Y. Zhang, *Maximal Cuts in Arbitrary Dimension*, JHEP **08** (2017) 051, [arXiv:1704.04255 \[hep-th\]](#).
- [349] M. Harley, F. Moriello, and R. M. Schabinger, *Baikov-Lee Representations Of Cut Feynman Integrals*, JHEP **06** (2017) 049, [arXiv:1705.03478 \[hep-ph\]](#).